



Université Pierre et Marie Curie

Ecole doctorale d'Astronomie et Astrophysique d'Ile-de-France

Institut d'Astrophysique de Paris

Overdense regions in the intergalactic medium and the environments of high-redshift quasars

Par Hayley Finley

Thèse de doctorat d'Astronomie et Astrophysique

Directeur : Patrick Petitjean

Co-encadrant : Pasquier Noterdaeme

Présentée et soutenue publiquement le 25 septembre 2014

Devant un jury composé de :

Eric Aubourg	Directeur de Recherche	Examinateur
Patrick Boissé	Professeur	Président
Nicolas Bouché	Chargé de Recherche	Examinateur
Pasquier Noterdaeme	Chargé de Recherche	Invité
Bruno Milliard	Directeur de Recherche	Rapporteur
Patrick Petitjean	Astronome	Invité
Philipp Richter	Professeur	Examinateur
David Turnshek	Professeur	Rapporteur

Abstract

Overdense regions in the intergalactic medium and the environments of high-redshift quasars

Damped Lyman-alpha absorbers (DLAs), the highest column density H I Lyman-alpha (Lyα) absorptions, can be used to study the environments of high-redshift ($z > 2$) quasar host galaxies. This is essential for determining how feedback mechanisms from active galactic nuclei (AGN), including high-velocity winds and intense ionizing radiation, impact the host galaxies. Thanks to the large number of quasar sight-lines from the Sloan Digital Sky Survey III Baryon Oscillation Spectroscopic Survey, I implement two techniques to characterize AGN environments by using DLAs at the quasar redshift.

Along the sight-line, these DLAs act as natural coronagraphs and completely absorb the broad Lyα emission from the central AGN. In some cases, a narrow Lyα emission line from the quasar host galaxy is superimposed on the DLA trough. I compare coronagraph DLAs that reveal narrow Lyα emission with those that do not in a statistically complete sample and characterize the emission. DLAs with the most luminous narrow Lyα emission peaks may arise from dense, compact clouds in the host galaxy, while the others may be due to neighboring galaxies.

With a second technique, I use pairs of quasars with small angular separations to investigate host galaxy environments at distances of less than 90 kpc in the transverse direction. I analyze the gas properties for pairs where a DLA appears in the background quasar spectrum coincident with the foreground quasar Lyα emission peak.

In one of the pairs, I also detect an overdensity of Lyman-limit system absorbers at $z = 2.69$ in a region spanning 2 000 km s^{-1} (6.4 Mpc proper distance) along the two sight-lines. The overdense region properties suggest an intergalactic medium filament.

Keywords: cosmology – quasars – absorption systems – active galactic nuclei (AGN) – Lyman-alpha – large-scale structure (filaments)

Résumé

Régions sur-denses du milieu intergalactique et environnements de quasars à grand décalage spectral

Les systèmes d'absorption Lorentziens, conséquence de la présence de gaz neutre à haute densité de colonne sur la ligne de visée d'une source lumineuse, peuvent être utilisés pour sonder les environnements de galaxies hôtes de noyaux actifs à grand décalage spectral ($z > 2$). Ceci permet d'étudier l'effet des mécanismes de rétroaction des noyaux actifs sur les galaxies hôtes, tel que les vents à haute vitesse et le rayonnement ionisant intense. Pour cela, j'implémente deux techniques utilisant les systèmes Lorentziens au décalage spectral du quasar dans les données du *Sloan Digital Sky Survey III Baryon Oscillation Spectroscopic Survey*.

Un tel système Lorentzien fait office de coronographe naturel puisqu'il absorbe complètement le rayonnement provenant du noyau actif. Parfois une raie Lyα étroite émise par la galaxie est superposée à l'absorption. J'étudie un échantillon statistiquement complet et je caractérise l'émission. Les systèmes Lorentziens qui révèlent les raies étroites d'émission Lyα les plus lumineuses proviennent vraissemblablement de nuages denses et compacts dans la galaxie hôte, tandis que les autres seraient dûs à des galaxies voisines du quasars.

Une deuxième technique consiste à observer des paires de quasars ayant une petite séparation angulaire pour sonder les environnements des galaxies hôtes à des distances transverses inférieures à 90 kpc. J'analyse les propriétés du gaz pour des paires où un système Lorentzien apparait dans le spectre du quasar d'arrière plan coïncident avec le pic d'émission Lyα du quasar de premier plan.

Dans une des paires, je détecte également une sur-densité de systèmes absorbants à $z = 2.69$ dans une région correspondant à 6.4 Mpc en distance propre. Les propriétés de cette région suggèrent que nous avons détecté un filament du milieu intergalactique.

Mots-clés : cosmologie – quasars – systèmes d'absorption – noyau actif de galaxie – raie Lyman-alpha – structure à grande échelle (filaments)

Remerciements

Tout d'abord, je souhaite remercier Patrick de m'avoir orienté vers des sujets aussi intéressants et de m'avoir introduit au monde des systèmes d'absorption. Merci d'avoir été aussi présent et disponible pendant ces trois dernières années, pour regarder un fit, discuter d'une prochaine étape, donner des commentaires sur un brouillon, ou suggérer comment améliorer une présentation. Ayant une tendance à me perdre dans les détails, j'ai apprécie aussi ton expérience et ta vison à grande échelle.

Je remercie Pasquier qui, avec son esprit critique, m'a aidé à améliorer mes fits, mes figures, mes calculs, mon raisonnement, ainsi que mon français. J'ai bien profité de nos discussions, et essayer d'accorder les avis de Patrick et Pasquier a aussi été un exercice intéressant.

En particulier, je vous remercie tous les deux de m'avoir toujours poussé dans mon travail. Un des grands avantages d'avoir fait ma thèse en France est que j'ai dû apprendre à aboutir à des résultats dans un délai de temps fixe.

Etant loin de ma famille, je suis heureuse d'avoir pu m'appuyer sur des amis qui m'encouragent et m'inspirent.

Je remercie aussi toutes les personnes qui m'ont aidée pour des questions petites et grandes tout au long de mon séjour en France. J'apprécie beaucoup votre patience ainsi que l'accueil que j'ai trouvé parmi vous.

Thank you to the members of my jury, Eric Aubourg, Nicolas Bouché, and Philipp Richter, the president, Patrick Boissé, and the two reviewers, Bruno Milliard and David Turnshek. I'm very happy that you were all able to be present for my Ph.D. defense, and I appreciated your thoughtful questions and comments.

Finalement, merci à Lapo Fanciullo qui s'est porté volontaire pour assister à une dernière répétition que je pensais faire pour moi-même la veille de ma soutenance. Cet entrainement m'a préparé pour un bon déroulement le jour J.

Long Résumé

Les propriétés des galaxies hôtes de quasars sont d'un intérêt particulier à l'époque $z = 2 - 3$, quand la fonction de luminosité des quasars est maximale (e.g., Richards et al. 2006; Ross et al. 2013). Accéder à l'environnement galactique est essentiel pour déterminer l'effet des mécanismes de rétroaction des noyaux actifs sur l'évolution de leurs galaxies hôtes. Au début, l'accrétion par le trou noir central et la formation d'étoiles se font de concert, puisque les deux processus utilisent du gaz provenant de la fusion de galaxies et/ou d'instabilités dans le disque (e.g., Lutz et al. 2008). Ensuite, il est possible que la phase de noyau actif se termine quand les deux processus ont épuisé le réservoir de gaz. Une autre possibilité est que le gaz soit expulsé de la galaxie par les forts vents du noyau actif, stoppant ainsi la formation d'étoiles (e.g., Fabian et al. 2006). Ce deuxième scénario implique que la force vers l'extérieur provenant de la pression de radiation surmonte la force gravitationnelle vers l'intérieur, ce qui nécessite une certaine luminosité pour le quasar.

Les observations de galaxies hôtes de quasars à grand décalage spectral permettent d'étudier les effets des mécanismes de rétroaction afin de distinguer entre ces deux possibilités. Rauch et al. (2013) ont obtenu des spectres de l'émission Lyman-alpha (Lyα) étendue autour d'un quasar obscurci à $z = 3.045$ et ont détecté une population de jeunes étoiles proches du quasar qui se sont probablement formées quand le noyau de galaxie est entré en phase active. Des images profondes obtenue à l'aide d'optique adaptative en proche infrarouge ont révélé des galaxies hôtes de quasars à $z = 2-3$ avec des morphologies elliptiques (Falomo et al. 2008; Wang et al. 2013b). Des systèmes Lorentziens qui sondent le gaz aux alentours des galaxies hôtes de quasars nous informent sur l'extension de l'ionisation provenant du noyau actif, ainsi que sur la composition et la cinématique du gaz dans l'environnement du noyau actif de galaxie.

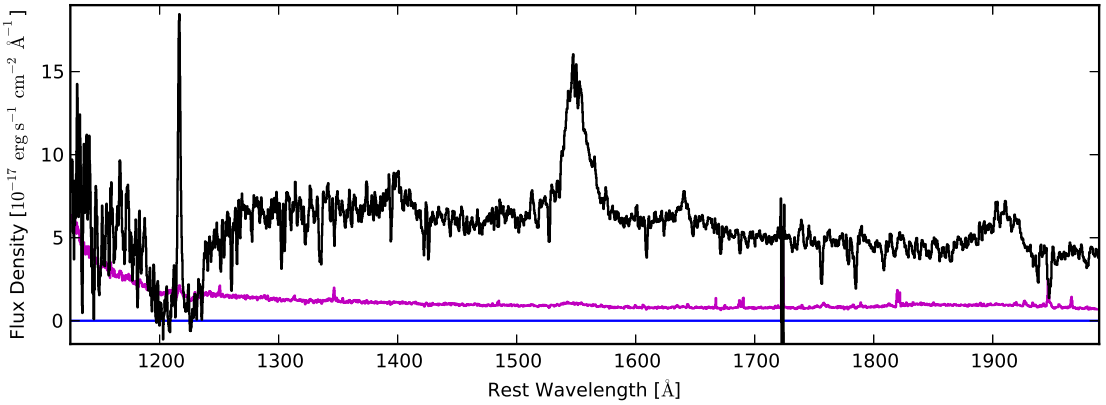

FIGURE 1: Exemple d'un spectre SDSS-III BOSS de quasar (SDSS J1256+3506) où le système Lorentzien à $z_{\rm abs} \simeq z_{\rm em}$ fait office de coronographe et révèle une raie d'émission étroite de Lyα. L'erreur (1σ) sur le flux est tracée en magenta.

Un relevé à grande échelle, le *Sloan Digital Sky Survey III Baryon Oscillation Spectroscopic Survey* (SDSS-III BOSS; Dawson et al. 2013; Eisenstein et al. 2011) a augmenté considérablement le nombre de quasars à grand décalage spectral confirmés spectroscopiquement et a ainsi ouvert de nouvelles possibilités pour étudier leurs environnements galactiques. À partir des premiers 61 931 quasars à $z > 2.15$ de la *Data Release 9* (DR9; Ahn et al. 2012), j'ai identifié des configurations particulières qui permettent d'éviter le rayonnement dominant et éblouissant issu de la région émettrice de raies larges s'étendant sur 1 pc autour du trou noir central, et d'accéder à l'environnement galactique. J'implémente deux techniques qui utilisent ces systèmes Lorentziens pour sonder le gaz au décalage spectral du quasar soit le long la ligne de visée (Chapitre 3), soit dans la direction transverse (Chapitre 4).

Des systèmes Lorentziens forts qui se trouvent le long la ligne de visée et au décalage spectral du quasar font office de coronographes naturels puisqu'ils absorbent complètement les raies d'émission larges de Lyα provenant du noyau actif de la galaxie. Dans certains cas, quand le nuage absorbant est petit par rapport à la galaxie, une raie Lyα étroite émise par la galaxie est superposée à l'absorption (Figure 1). Ces absorbants peuvent être des nuages denses et compacts situés dans la galaxie hôte elle-même. En revanche, quand la raie étroite de Lyα n'est pas détectée, les systèmes Lorentziens peuvent être dûs à des galaxies voisines du quasar qui agissent comme des écrans et bloquent même l'émission des régions plus étendues de la galaxie hôte.

Pour tester ce scénario, j'identifie un échantillon statistiquement complet de 31 systèmes Lorentziens forts avec une densité de colonne en hydrogène neutre $N(\mathrm{H\,I}) \geq 10^{21.3}$ cm^{-2} et à moins de 1 500 km s^{-1} du décalage spectral du quasar, parmi lesquels huit révèlent une raie étroite de Lyα. Je compare leurs propriétés, y compris les décalages en vitesse,

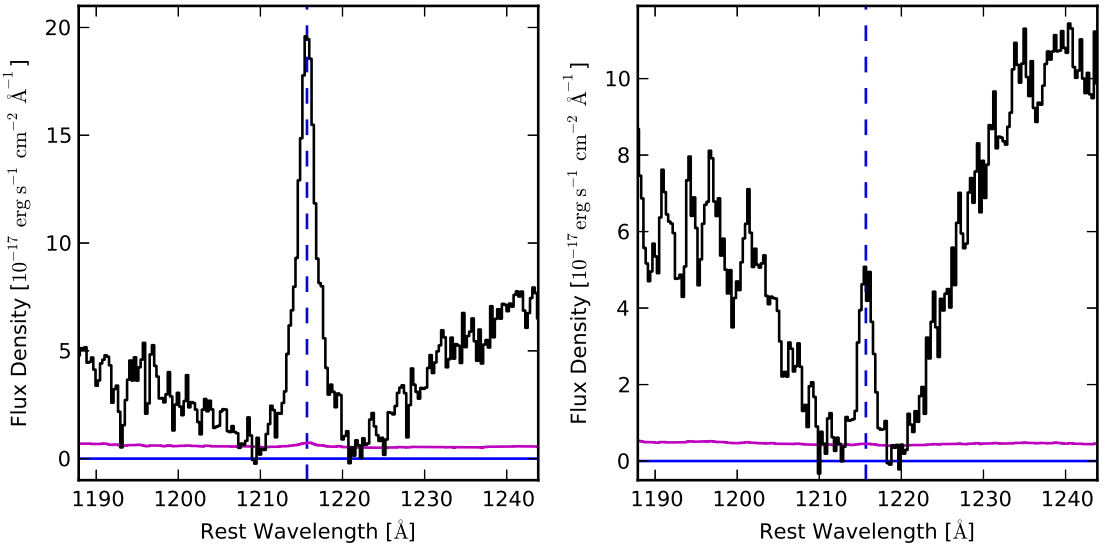

FIGURE 2: Résultat de la co-addition de onze raies étroites fortes (à gauche) et de quinze raies modérées (à droite) révélées par des systèmes Lorentziens coronographes. Les spectres sont combinés par une moyenne pondérée par l'inverse de la variance.

les largeurs équivalentes de raies d'absorption par les métaux, les couleurs et le rougissement du quasar. Bien que les nuages dans les galaxies hôtes de quasars puissent avoir des propriétés différentes de celles des galaxies voisines du fait d'une cinématique et d'un enrichissement en métaux augmentés par le noyau actif de galaxie, aucune différence nette n'est mise en évidence par l'analyse des spectres BOSS.

Pour caractériser la raie étroite de Lyα, dont la présence ou l'absence reste la différence la plus frappante entre les systèmes, j'ajoute d'autres détections de telles raies d'émission étroite (tirées de la Data Release 10, Ahn et al. 2014) à ceux de l'échantillon complet, accumulant ainsi un total de 26 systèmes qui révèlent une raie étroite de Lyα. En considérant les valeurs de flux intégré, cet échantillon peut être séparé en un groupe de 11 systèmes avec des raies étroites fortes dont le flux intégré est $\mathcal{F} > 40 \times 10^{-17}$ erg s^{-1} cm^{-2} et un groupe de 15 systèmes avec des raies modérément fortes ($\mathcal{F} < 26 \times 10^{-17}$ erg s^{-1} cm^{-2}). Le résultat de l'addition des spectres a un profil symétrique (Figure 2), contrairement à ce qu'on voit dans les galaxies *Lyman-break* (Shapley et al. 2003). La forme symétrique du profil d'émission Lyα indique que des processus de transfer Lyα n'interviennent pas, et donc que les régions d'émission manquent de gaz H I. Ceci impliquent que le gaz des systèmes Lorentziens n'est pas d'associé directement avec les régions en émission.

Finalement, comparer la luminosité en Lyα des raies étroites superposées sur les systèmes Lorentziens à celle d'émetteurs Lyman-alpha et de radiogalaxies (Figure 3) aide à contraindre la taille relative des régions en émission et en absorption. Environ la moitié

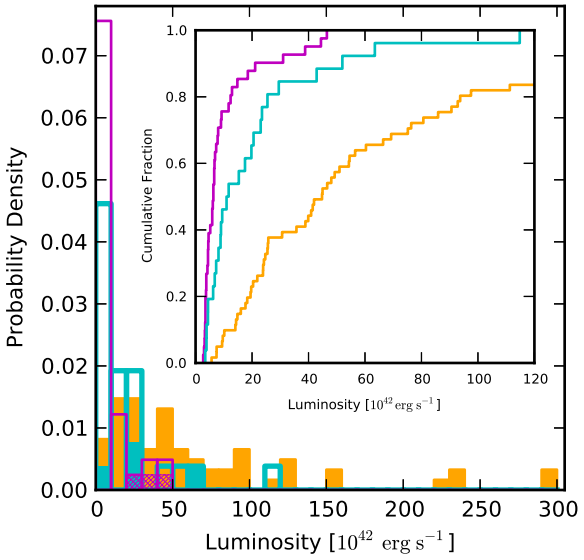

FIGURE 3: Distribution de la luminosité associée à la raie étroite de Lyα vue dans les systèmes Lorentziens coronographes (cyan épais), les émetteurs en Lyman-alpha (magenta), et les radiogalaxies (jaune). Les croisillons magentas indiquent trois émetteurs en Lyman-alpha qui ont aussi une contribution d'un noyau actif de galaxie. Les parties cyan pleines montrent des quasars de l'échantillon de systèmes Lorentziens coronographe qui sont aussi émetteur radio. Le sous-graphe donne la distribution cumulée (test statistique de Kolmogorov-Smirnov) jusqu'à 120×10^{42} erg s^{-1} avec les mêmes couleurs.

des raies étroites de Lyα détectées en utilisant des systèmes Lorentziens comme coronographes ont des luminosités qui sont cohérentes avec celles des émetteurs Lyman-alpha typiques. Pour ces galaxies hôtes de quasars, le gaz en absorption est suffisamment étendu pour couvrir la majeure partie de la région autour du noyau actif et réduire ainsi la luminosité à une valeur plutôt typique d'une galaxie présentant une activité soutenue de formation d'étoiles. Les luminosités de l'autre moitié des raies étroites de Lyα dépassent des valeurs caractéristiques des émetteurs Lyman-alpha. Elles sont comparables à, mais plus petites que, celles des radiogalaxies, dont les jets injectent de l'énergie loin de leurs centres. Trouver des luminosités qui approchent celles de radiogalaxies n'est pas surprenant, vu que les noyaux actifs de galaxies ionisent le gaz environnant et que ce dernier émet en Lyα. Quand la luminosité en Lyα est forte, le gaz en absorption n'obscure pas la région d'émission étroite de façon significative, qui fait que ces systèmes Lorentziens peuvent aussi être dûs à des nuages compacts dans les galaxies hôtes.

En plus de cette première technique consistant à sonder une galaxie hôte de quasar le long de sa propre ligne de visée avec un système Lorentzien servant de coronographe, j'ai utilisé une deuxième technique consistant à observer des paires de quasars de petite séparation angulaire afin d'étudier les environnements des galaxies hôtes à des distances transverses inférieures à 90 kpc (Figure 4). Dans la DR9, j'ai identifié trois de ces paires avec des lignes de visée proches, où un système Lorentzien apparait dans le spectre du quasar d'arrière-plan coïncidant avec le pic d'émission Lyα du quasar de premier

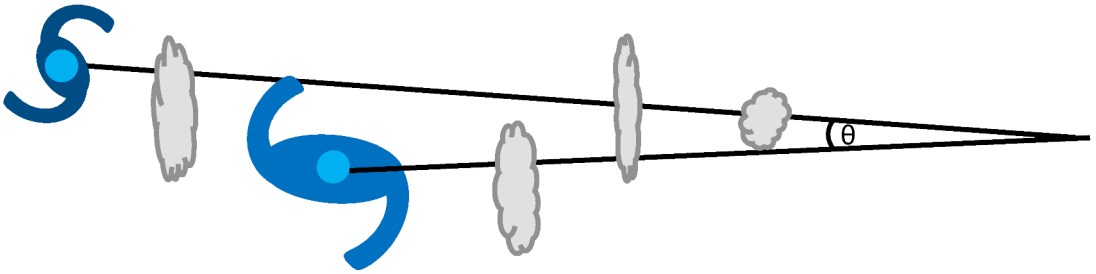

FIGURE 4: Pour les paires ayant une séparation angulaire (θ) très petite, la ligne de visée du quasar d'arrière-plan sonde l'environnement galactique du quasar de premier plan.

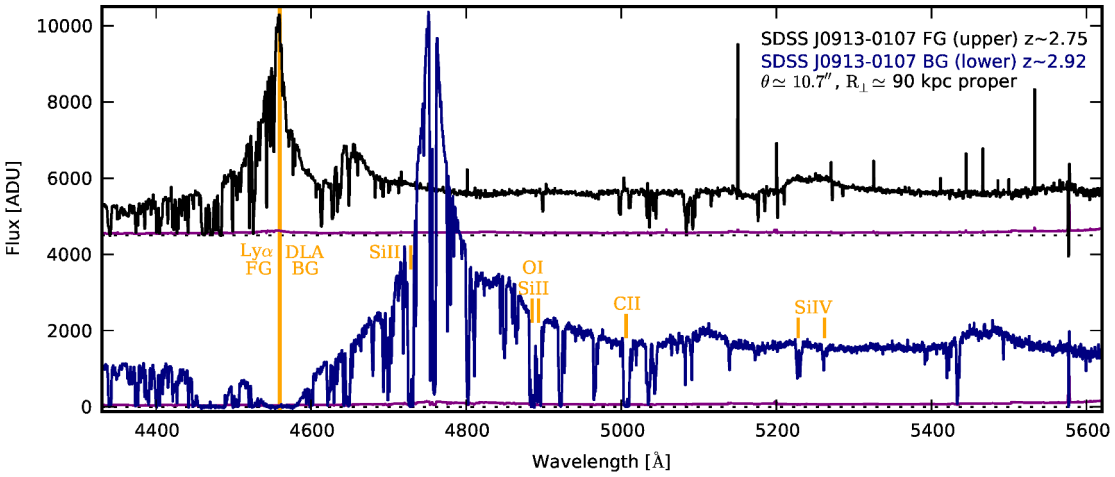

FIGURE 5: Spectres X-shooter pour la paire SDSS J0913-0107. Les marques verticales en jaune indiquent d'une part la raie d'émission Lyα du quasar de premier plan (*foreground*, FG) coïncidant avec le système Lorentzien (*damped Lyman-alpha absorption*, DLA) dans le spectre du quasar d'arrière-plan (*background*, BG), et d'autre part les absorptions métalliques associées avec ce système. Un autre système d'absorption forte est notable autour de 4475 Å.

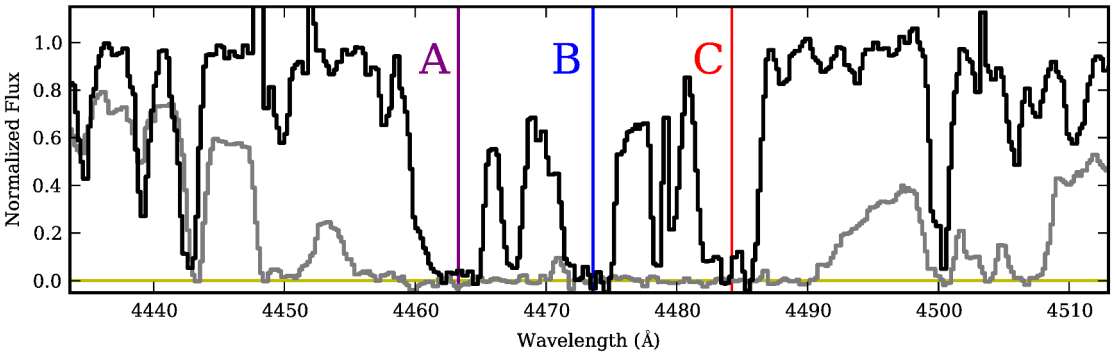

FIGURE 6: Une portion de la forêt Lyα dans la paire SDSS J0913-0107 avec d'importantes absorptions en H I coïncidant entre elles le long les deux lignes de visée. Le spectre X-shooter du quasar de premier plan est en gris et celui du quasar d'arrière plan est en noir. Les trois régions principales d'absorption sont nommées par A (violet), B (bleu), et C (rouge).

plan. J'ai ensuite obtenu des observations supplémentaires avec l'instrument X-shooter du VLT (Figure 5). Pour ces trois paires, des systèmes Lorentziens ont révélé du gaz principalement neutre, étendu sur plus de 250 km s^{-1} et regroupé dans deux ou trois régions principales. Ce gaz neutre ou faiblement ionisé, qui se trouve dans la direction transverse, montre que des quasars émettent de façon anisotrope, ce qui est en accord avec des études antérieures (Hennawi & Prochaska 2007, 2013; Hennawi et al. 2006a; Prochaska et al. 2013a). Étonnamment, le gaz diffus dans le halo du quasar, sondé par la ligne de visée ne présente que très peu d'absorption C IV. Le manque de fortes absorptions en C IV sur des lignes de visées aussi proches des galaxies hôtes de quasars s'explique si la température des halos est trop élevée pour permettre des absorptions associées à du gaz de température intermédiaire (T = 10^{4-5} K), comme le C IV. Le gaz dans les halos semble être soit dans une phase froide, sondé par les systèmes Lorentziens, soit dans une phase très chaude, que l'on pourrait éventuellement détecter grâce à son émission en rayons X.

Les paires de lignes de visées proches sont également un outil puissant pour étudier les structures du milieu intergalactique (Chapitre 5). J'ai inopinément détecté une surdensité d'absorbants avec log N(H I) > 18.0 à z = 2.69 le long des lignes de visées vers la paire SDSS J0913-0107 (Figure 6), dont les membres sont séparés de ∼90 kpc en distance propre transverse. Trois régions d'absorption sont présentes et s'étendent sur 2 000 km s^{-1} (ce qui correspond à 6.4 Mpc en distance propre), coïncidant sur les deux lignes de visées (Figure 7). Deux de ces régions ont une métallicité [Fe/H] < -1.9 et correspondent à des faibles surdensités du gaz du milieu intergalactique. Cependant, la troisième région est juste en-dessous de la limite des systèmes Lorentziens avec log N(HI) = 20.2 et [Fe/H] = −1.1, ce qui indique qu'elle est probablement associée à une galaxie. La probabilité d'intercepter trois systèmes avec log N(H I) > 18.0 dans une région de 2 000 km s^{-1} le long du chemin observé n'est que de 0.07%. Ces lignes de visées sondent donc à l'évidence une région surdense faisant éventuellement partie d'un proto-amas de galaxies, ou bien d'un filament du milieu intergalactique. Le gaz pauvre en métaux dans les deux régions et le manque de C IV impliquent que la région surdense n'est pas très enrichie, ce qui évoque la structure et le caractéristiques d'un filament du milieu intergalactique. Grâce aux mécanismes de croissance de structure, la région surdense pourrait néanmoins s'effondrer et devenir un amas de galaxies à faible décalage spectral.

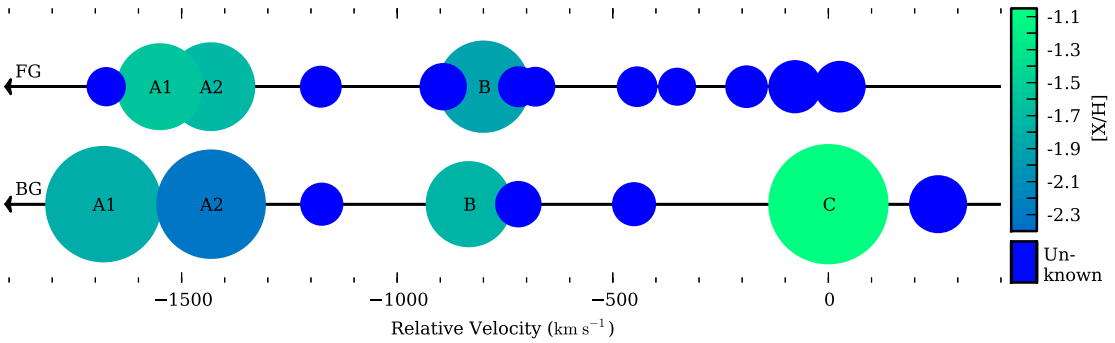

FIGURE 7: Diagramme représentant les nuages de H I communs aux deux lignes de visée vers la paire SDSS J0913-0107, l'une associée au quasar de premier plan (*foreground*, FG, partie haute), et l'autre au quasar d'arrière plan (*background*, BG, partie basse). Les absorbants principaux dans les trois régions sont désignés par A1, A2, B, et C. La taille des cercles est à l'échelle de la densité de colonne en HI, de telle sorte que le double de la surface représente huit fois plus de $N(\mathrm{H\,I})$ (Surface = $N(\mathrm{H\,I})^{1/3}$). Des nuages de basse densité de colonne, pour lesquels la métallicité est inconnue, sont en bleu foncé, tandis que les couleurs plus vives et plus vertes indiquent des nuages de plus haute métallicité (voir échelle de couleurs à droite). L'origine de l'échelle en vitesse est à $z = 2.6894$.

Contents

Abstract iii

Résumé v

Remerciements vii

Résumé (Long) viii

Contents xvii

1 Introduction 1
- 1.1 A Brief Cosmic History . . . 1
  - 1.1.1 Growth of Galaxies . . . 3
- 1.2 Absorption Systems . . . 5
  - 1.2.1 N(HI) Frequency Distribution . . . 5
  - 1.2.2 Characterizing Strong Absorbers . . . 7
    - 1.2.2.1 Neutral Hydrogen Mass Density . . . 9
    - 1.2.2.2 Metallicity . . . 12
- 1.3 Relating Absorption Line Systems and Galaxies . . . 18
  - 1.3.1 Mg II Systems . . . 18
  - 1.3.2 CGM . . . 18
  - 1.3.3 DLA Systems . . . 20
  - 1.3.4 DLA Galaxies in Simulations . . . 24
  - 1.3.5 Observing DLA Galaxies . . . 27
- 1.4 Thesis Work . . . 36

2 SDSS-III Baryon Oscillation Spectroscopic Survey 39
- 2.1 Survey Goals . . . 39
- 2.2 Telescope and Spectrograph . . . 42
- 2.3 Data Processing and Quasar Redshift Estimation . . . 44
- 2.4 Data Releases . . . 47
- 2.5 Value-Added Catalogs . . . 48
- 2.6 Quasar and Absorption System Science . . . 52
- 2.7 Survey Results . . . 55
- 2.8 Future Prospects . . . 57

3 A glance at the host galaxy of high-redshift quasars using strong damped Lyman-alpha systems as coronagraphs 59
3.1 Introduction . . . 59
3.1.1 Observing Quasar Host Galaxies . . . 61
3.1.2 Associated DLAs . . . 63
3.2 Sample Definition . . . 64
3.2.1 Strong associated DLAs . . . 64
3.2.2 Measuring DLA column densities and emissions . . . 65
3.2.3 The Statistical Sample . . . 68
3.2.4 The Emission Properties Sample . . . 69
3.2.5 The Redshift Distribution . . . 69
3.3 Anticipated Number of Intervening DLA Systems within 1 500 km s^{-1} of zQSO . . . 69
3.3.1 Anticipated Number in DR9 . . . 70
3.3.2 The Effect of Clustering near Quasars . . . 70
3.4 Characterizing the Statistical Sample . . . 71
3.4.1 Scenario . . . 71
3.4.2 Kinematics . . . 72
3.4.3 Metals . . . 72
3.4.4 Reddening . . . 75
3.5 Characterizing the Narrow Lyα Emission . . . 76
3.5.1 Correlation with other properties . . . 78
3.5.2 Position and profile of the emission line . . . 78
3.5.3 Comparison with Lyman Break Galaxies . . . 81
3.5.4 Comparison with Lyman-Alpha Emitters . . . 82
3.5.5 Comparison with Radio Galaxies . . . 83
3.6 DLAs with partial coverage . . . 83
3.7 Discussion and Conclusions . . . 86
3.8 Follow-Up Projects . . . 95
3.8.1 Observations with Magellan/MagE . . . 95
3.8.2 Observations with VLT/X-shooter . . . 96
3.8.3 Observations with HST/WFC3 . . . 97

4 Close Line-of-Sight Pairs 99
4.1 Introduction . . . 99
4.2 Close Line-of-Sight Pairs in SDSS-III BOSS . . . 100
4.2.1 The Transverse Correlation Function for Lyα Forest Absorptions . . . 102
4.2.2 Quasar Host Galaxy Environments . . . 108
4.3 VLT/X-shooter Follow-Up Observations . . . 109
4.3.1 Pair SDSS J0239-0106 . . . 112
4.3.2 Pair SDSS J2338-0003 . . . 117
4.3.3 Pair SDSS J0913-0107 . . . 124
4.4 Preliminary Conclusions . . . 131

5 A $\sim$6 Mpc overdensity at $z \simeq 2.7$ detected along a pair of quasar sight lines: filament or protocluster? 133
5.1 Introduction . . . 133

5.2 Data . . . 135
5.3 Absorption Systems . . . 136
5.3.1 Background Quasar Line-of-Sight . . . 138
5.3.1.1 H I Absorption Systems . . . 138
5.3.1.2 Abundances . . . 140
5.3.2 Foreground Quasar Line-of-Sight . . . 141
5.3.2.1 H I Absorption Systems . . . 141
5.3.2.2 Abundances . . . 142
5.4 Discussion and Conclusions . . . 144

6 Conclusions and Prospects **149**
6.1 Conclusions . . . 149
6.2 Prospects . . . 152
6.2.1 Follow-Up Projects . . . 152
6.2.2 Future Work . . . 152

Bibliography **155**

To all my friends whose weddings I've missed...

Chapter 1

Introduction

1.1 A Brief Cosmic History

In the standard model of the hot Big Bang (Lemaître 1931), the universe is in expansion, causing its temperature to cool. When the temperature decreased to about 3 000 K, protons and electrons in the primordial plasma combined to form atoms, primarily hydrogen. With their mean free path no longer impeded by charged particles, photons decoupled from matter. These photons from the recombination epoch have since been propagating through the universe and stretching to longer wavelengths as it expands. Today, we detect the photons as cosmic microwave background (CMB) radiation. Their surface of last scattering is imprinted in the CMB temperature map (Figure 1.1), which reveals small fluctuations on the order of 1 part in 100 000. Slightly colder CMB temperatures correspond to regions that were slightly overdense at the time of decoupling, since photons emanating from these regions used slightly more of their energy to escape the gravitational attraction of their denser-than-average surroundings.

The small density variations apparent in the CMB map are the seeds of larger structures, like galaxies and clusters. In the dark ages, after the primordial photons decoupled, no astrophysical objects existed that could radiate new photons (see Figure 1.2.) Slightly overdense regions gravitationally attracted more matter, growing until they collapsed. The first ionizing sources, possibly stars formed out of primordial gas or black holes, irradiated their surroundings and created pockets of ionized hydrogen (Figure 1.3). Over the course of the Epoch of Reionization, gas dispersed between radiating sources became predominantly ionized, while gravitational attraction continued to encourage the build-up of structure. Matter appears to be distributed in a cosmic web (Bond et al. 1996), with filaments and sheets outlining vast underdense regions known as voids before meeting at nodes that coincide with highly overdense galaxy clusters.

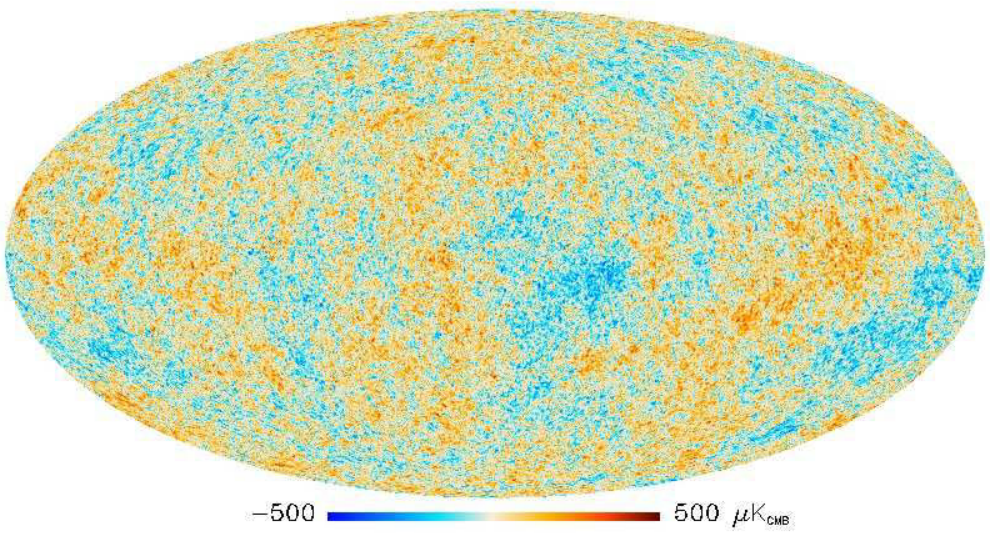

FIGURE 1.1: The Planck CMB temperature map shows temperature variations on the order of μK, which correspond to regions with slightly different densities. The density fluctuations shape the formation of structure in the universe. (Planck Collaboration et al. 2013)

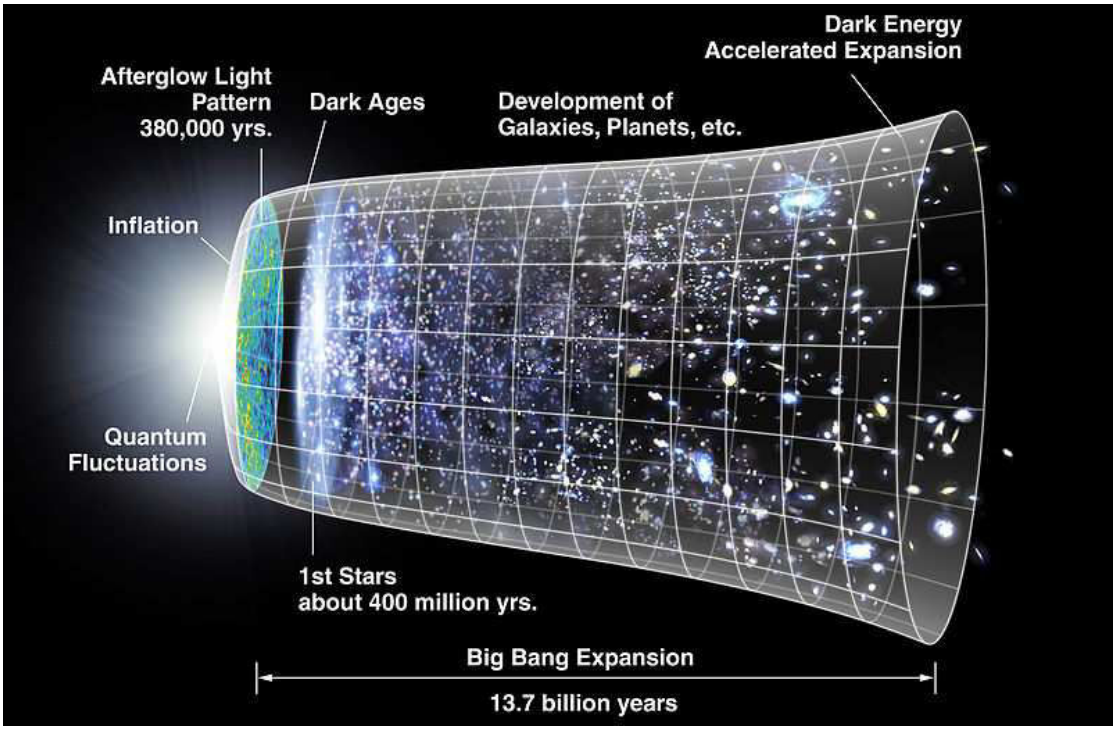

FIGURE 1.2: After recombination, when the CMB radiation was emitted, the universe was dark. Eventually, the build-up of structure produced ionizing sources, ending the dark ages. Structures continued to grow, with clouds of gas merging to form galaxies, small galaxies merging to form larger ones, and groups of galaxies forming clusters. Figure courtesy of NASA.

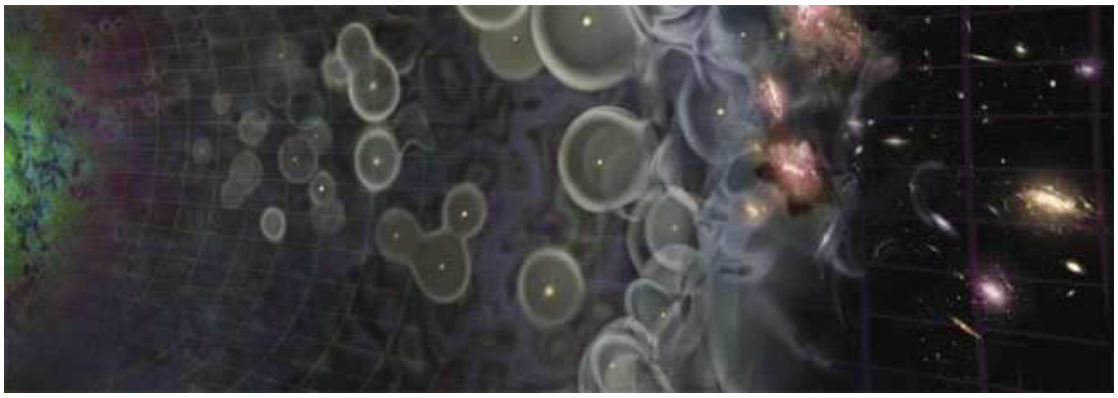

FIGURE 1.3: During the Epoch of Reionization, pockets of ionized gas form around radiating sources. From left to right, the gas is initially neutral, but becomes predominantly ionized. Figure adapted from Loeb (2006)

Low-density gas composed primarily of hydrogen permeates the space between galaxies. This intergalactic medium (IGM) can be detected in the spectra of bright background sources, such as quasars or gamma-ray burst afterglows.

Lynds (1971) was the first to recognize that absorptions at shorter wavelengths than the H I Lyman-α (Lyα) emission peak of a $z = 2.877$ quasar correspond to the Lyα transition at lower redshifts. Quasar lines-of-sight pass through intervening clouds of highly-ionized hydrogen, each of which imprints absorption features on the spectrum (Figure 1.4). For high-redshift quasars, the absorptions become so abundant that they create a Lyα forest. As such, quasar spectra are excellent probes of gas distributed in the IGM.

Gunn & Peterson (1965) predicted that given a sufficient amount of neutral hydrogen in the IGM, quasar spectra would be completely absorbed bluewards of the Lyα emission peak. This type of absorption signature, which indicates that the universe is opaque to Lyα photons, helps determine when the Epoch of Reionization ended. No quasars were identified at high enough redshift to show total absorption, until Becker et al. (2001) clearly detected a Gunn-Peterson trough in a $z = 6.28$ quasar spectrum. By analyzing a sample of quasars in the range $5.74 < z < 6.42$, Fan et al. (2006) found evidence that the neutral fraction decreased by a factor of $\gtrsim 10$ during this epoch, from $\sim 1\%$ at $z \sim 6.4$. By $z \simeq 2 - 3$, the neutral fraction $n_{\rm HI}/n_{\rm H}$ is $\sim 10^{-5}$.

1.1.1 Growth of Galaxies

In an explanatory scenario, the gas that galaxies gravitationally accrete from the IGM provides fresh material, which eventually collapses to form stars. Certain stars explode as supernovae and contribute to galactic winds that expel enriched gas into the IGM. As

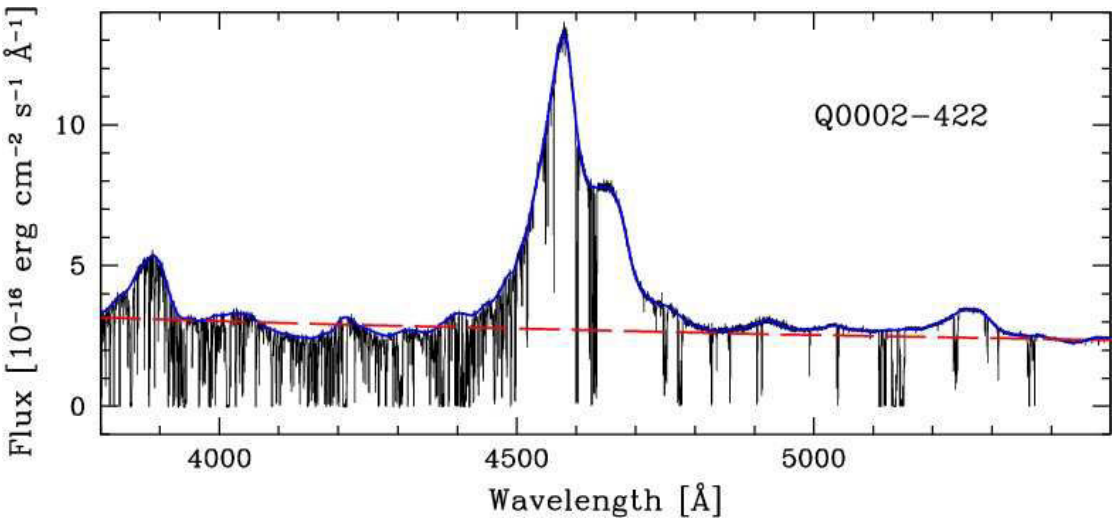

FIGURE 1.4: A typical high-resolution spectrum from VLT/UVES of the quasar Q 0002-422 ($z_{\rm em}$ = 2.768). The quasar continuum (solid blue line) follows a power law (dashed red line). Prominent emission peaks include Lyβ at 3880Å, Lyα at 4580Å with neighboring N V, and Si IV at 5275Å. The abundant absorptions blueward of the quasar Lyα emission peak constitute the Lyα forest. Metal absorption lines are apparent at redder wavelengths after the Lyα emission peak. (Figure from Dall'Aglio et al. (2008a).)

a result of this feedback cycle, enriched gas permeates the IGM near galaxies, earning the name "circumgalactic medium" (CGM).

Many avenues exist for studying galaxies. Identifying stellar populations reveals information about their ages, heavy element contents, and star formation histories (e.g., Gallazzi et al. 2005). Plus, galaxy masses can be inferred by analyzing the stellar kinematics (e.g., Ma et al. 2014). Star formation rates are estimated from the stellar UV continuum, Hα or [OII] emission in nebular regions, and thermal radiation due to dust that absorbs UV/optical photons from stars and re-emits in the far infrared. Comparing line ratios from excited gas detected in emission provides characteristic abundances, temperatures, and densities for ionized regions. The distribution of ionized gas is easily obtained from narrow-band images, barring dust extinction. When combined with IFU spectroscopy, the gas distribution can be converted into velocity and dispersion maps that trace gas masses and show evidence of rotation or recent interactions with another galaxy (e.g., Epinat et al. 2012). Finally, neutral gas detected in absorption adds additional insight into gas flows and abundances (e.g., Péroux et al. 2014). Analyzing the enrichment and kinematics for an absorption system can indicate whether gas is infalling or outflowing.

Consequently, absorption system analysis is well-placed to address fundamental questions about the growth and evolution of galaxies. Specifically:

- How do galaxies acquire fuel for continued star formation?
- What is the mass of the galaxy halo and how does the galaxy mass buildup?

- How much does feedback from star formation and AGN activity influence galaxy growth?
- In what ways do feedback processes (winds from SNe explosions and AGN activity) alter galaxies and the IGM?
- What is the physical state of the gas in the galaxy halo and the IGM?

1.2 Absorption Systems

1.2.1 N(HI) Frequency Distribution

The N(HI) frequency distribution, $f_{\rm HI}(N, X)$, describes the rate of occurrence of quasar absorbers with different neutral hydrogen column densities, N(HI), over an absorption path, X, since $f_{\rm HI}(N, X)dNdX$, gives the number of systems within (N, $N + dN$) and (X, $X + dX$). This is a convenient way to represent the whole population of absorbers (see Figure 1.5). When evaluated for a sample of absorbers,

$$f_{\rm HI}(N, X) = \frac{m(N,\, N + \Delta N)}{\Delta X}, \tag{1.1}$$

where m is the number of systems within a column density interval (N, $N + \Delta N$) observed along the total absorption path ΔX for a defined (X, $X + \Delta X$) interval. The absorption path along one quasar line-of-sight is:

$$dX \equiv \frac{H_0}{H}(1 + z)^2 dz, \tag{1.2}$$

which can be summed for all quasars in the sample to obtain ΔX.

Quasar spectra probe clouds of gas with neutral hydrogen column densities, N(HI), that range from $\sim 10^{12} - 10^{22}$ cm^{-2}. Absorption systems are classified based on their neutral hydrogen column density, which is related to the physical nature of the absorber.

The more abundant lower column density absorptions probe gas in the IGM, which is highly ionized. These weak absorptions with N(HI) $< 1.6 \times 10^{17}$ cm^{-2} constitute the Lyα forest. Resolution limits impose a threshold for detection, N(HI) $\sim 10^{12}$ cm^{-2}. The majority of Lyα forest absorption lines are in the optically thin regime, N(HI) $< 10^{14}$ cm^{-2}.

For N(HI) $> 1.6 \times 10^{17}$ cm^{-2}, clouds become optically thick to photons with rest frame wavelengths less than 912 Å, and they produce a decrement (or full absorption) in the quasar UV flux at this wavelength. Lyman limit systems (LLS) trace gas in galactic

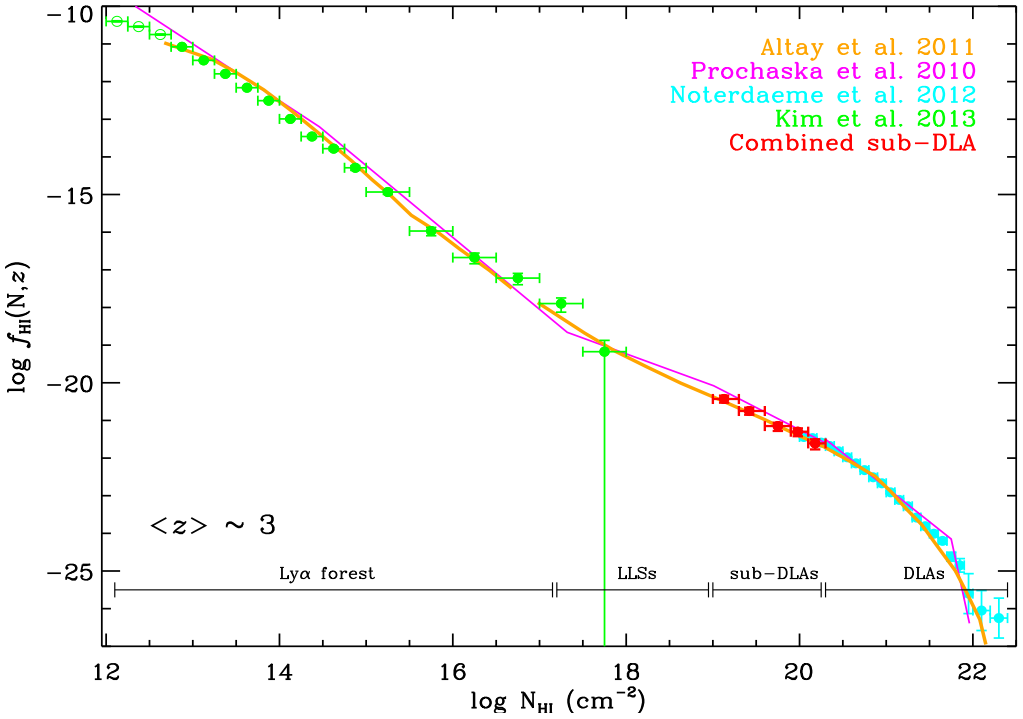

FIGURE 1.5: Differential column density distribution ($f_{HI}(N,z)$) plotted against log N_{HI}. The red data points indicate $f_{HI}(N,z)$ for sub-DLAs from the Zafar et al. (2013b) combined sub-DLA sample. The green filled data points represent $f_{HI}(N,z)$ for the Lyα forest from Kim et al. (2013). The green open circles are column densities from Kim et al. (2013) affected by incompleteness. The cyan data points represent the results from Noterdaeme et al. (2012b). The solid magenta line is the estimate of $f_{HI}(N,z)$ at $z \sim 3.7$ using a series of six power-laws by Prochaska et al. (2010). The solid orange line is hydrodynamic/analytical model prediction at $z \sim 3$ by Altay et al. (2011). (Figure from Zafar et al. (2013b).)

halos. The physical state of this gas varies widely, with temperatures ranging from T = $10^4 - 10^6$ K. LLS have associated metal absorption lines, but line strengths and ionization states can be very different from system to system. The column density for LLS with N(HI) $< 10^{19}$ cm^{-2} is difficult to determine if not enough other Lyman series lines are available, because it is degenerate with the Doppler parameter.

Sub-damped Lyman-α systems (sub-DLAs) span the range over which hydrogen becomes predominantly neutral, $10^{19} < N$(HI) $< 2 \times 10^{20}$ cm^{-2}. The upper limit is the historical cut-off for damped Lyα systems (DLAs; discussed below). Albeit weaker, damped wings appear for absorptions with N(HI) $> 10^{19}$ cm^{-2}. Certain authors (e.g. O'Meara et al. 2007) refer to this population of absorbers as super Lyman limit systems (SLLS) to set them apart from DLAs, since the gas may still be partially ionized. Ionization correction factors become increasingly important for absorbers with N(HI) $< 10^{19.5}$ cm^{-2} (Viegas 1995). The naming convention remains a matter of choice.

The rarer high column density absorptions, which include sub-DLAs, are associated with gas in galactic environments. Wolfe et al. (1986) introduced the definition of N(HI) $\geq$

2×10^{20} cm^{-2} for DLAs as part of a survey to observe galactic disks at high redshift. This threshold corresponds to typical N(HI) values measured in the disks of local galaxies from 21-cm observations (Bosma 1981). The corresponding equivalent width limit is also well adapted for detecting DLAs in low-resolution spectra.

The highest column density absorbers, extremely strong DLAs (ESDLAs) with $N(\mathrm{HI}) \geq 0.5 \times 10^{22}$ cm^{-2} (Noterdaeme et al. 2014), are the most likely to probe gas in the ISM of high-redshift galaxies.

1.2.2 Characterizing Strong Absorbers

An N(HI) measurement is more or less precise, depending on the optical depth in the center of the H I Lyα transition. The Lyα curve of growth, which relates the absorption profile equivalent width, W, to the HI column density, has three different regimes (Figure 1.6). For weak absorptions due to optically thin gas, the equivalent width increases linearly with the HI column density. As the gas transitions to optically thick, N(HI) and the Doppler parameter, b, quickly become degenerate. Lyα absorptions are already partially saturated starting at $N(\mathrm{HI}) = 10^{13}$ cm^{-2}. In the flat, saturated regime, a wide range of column densities are possible for a given equivalent width. At high column densities, $N(\mathrm{HI}) > 10^{19}$ cm^{-2}, damping wings appear and contribute substantially to the equivalent width. The curve of growth once again has a unique solution, independent of the Doppler parameter.

To measure N(HI) for an absorption system, the first step is to fit a continuum to the quasar spectrum. A precise redshift for the system can be determined by fitting low-ionization metal transitions associated with strong absorbers, if they are detected. Assuming that the low ions are kinematically associated with the neutral gas, they can be required to have the same redshift and tied Doppler parameters.

Then, fitting a Voigt profile centered on the system redshift to the HI absorption will give the column density, since the damping wings constrain the HI absorption profile for strong absorption systems. Any higher-order Lyman series absorptions available in the spectrum can help to further refine the fit. The continuum may also need to be readjusted to improve the Voigt profile fit.

The continuum placement is often uncertain in the Lyα forest, particularly near strong absorbers, and is usually the dominant source of error in an N(HI) measurement. Nonetheless, DLA column densities can be measured very reliably by iterating between

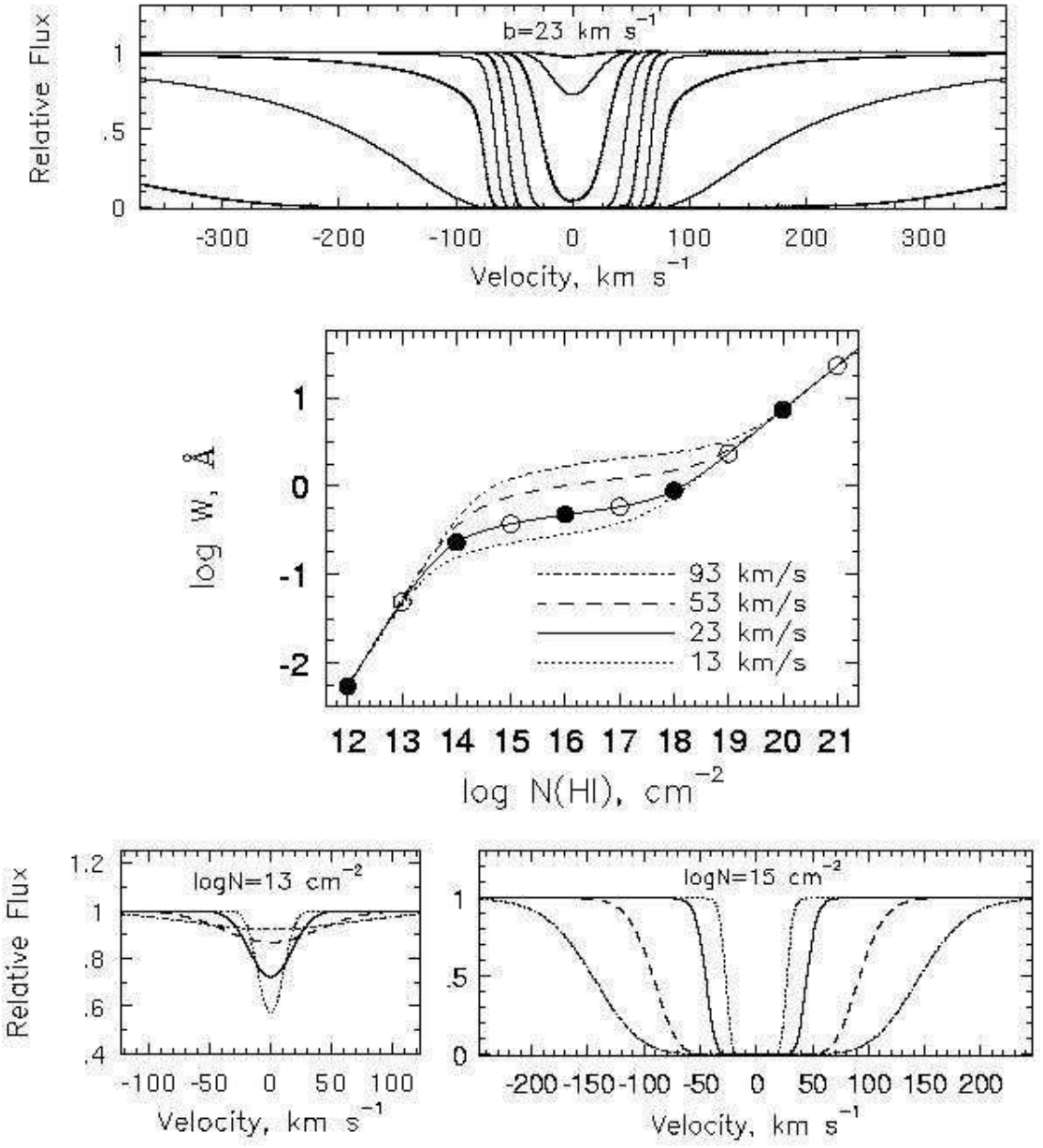

FIGURE 1.6: Illustration of the different regimes of the curve of growth. Middle panel: The curve of growth for the Lyα transition relates the equivalent width, W, of the absorption profile to the column density, N(HI). The different curves represent four different values of the Doppler parameter: b = 13, 23, 53, and 93 km s^{-1}. In the linear and damped regimes, the equivalent width does not depend on b. Upper panel: The absorption profile evolves as the HI column density increases from N(HI) = $10^{12} - 10^{20}$ cm^{-2} with a constant Doppler parameter, b = 23 km s^{-1}. The profile develops damped wings above N(HI) = 10^{19} cm^{-2}, which dominate the equivalent width. Lower left panel: At fixed N(HI) in the linear regime, the depth of the profile is smaller for large b, such that the equivalent width remains constant. Lower right panel: On the linear part of the curve of growth, profiles are saturated and the equivalent width increases with b for constant N(HI). (Figure from Charlton & Churchill (2000).)

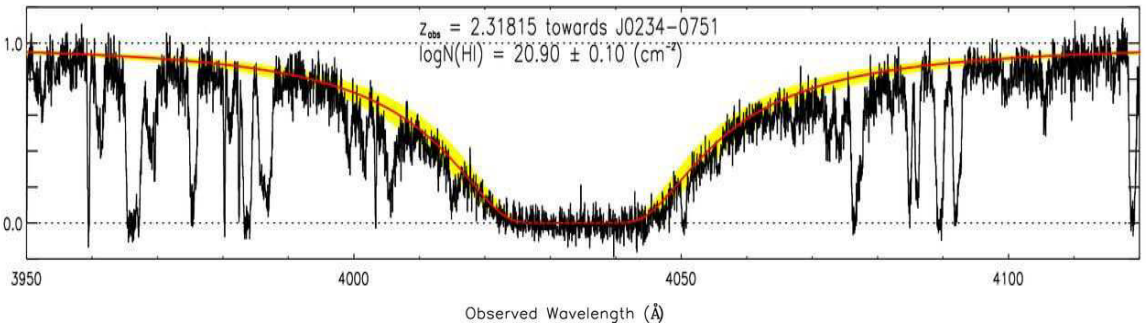

FIGURE 1.7: A normalized high-resolution (VLT/UVES) spectrum with a $\log N(\mathrm{HI}) = 20.90 \pm 0.10$ DLA. A red line traces the DLA profile, and the yellow shaded regions show the 1σ error on the fit. (Figure from Dutta et al. (2014).)

Voigt profile and continuum adjustments, since the damped wings are a strong constraint. Figure 1.7 shows an example of the Voigt profile fit to a $\log N(\mathrm{HI}) = 20.90 \pm 0.10$ DLA.

1.2.2.1 Neutral Hydrogen Mass Density

The various absorption systems (in order of decreasing importance), DLAs, sub-DLAs, LLS, and Lyα forest absorptions, contribute to the total mass density of neutral hydrogen, Ω_g, which can be evaluated over a column density range $N_{\rm min}$ to $N_{\rm max}$:

$$\Omega_g(X)\mathrm{d}X = \frac{\mu m_{\rm H} H_0}{c\rho_c} \int_{N_{\rm min}}^{N_{\rm max}} N(\mathrm{HI}) f_{\rm HI}(N, X)\mathrm{d}X \tag{1.3}$$

where $\mu = 1.3$ is the mean molecular mass and ρ_c is the critical mass density. In the discrete limit, the expression becomes:

$$\Omega_g(X) = \frac{\mu m_{\rm H} H_0}{c\rho_c} \frac{\sum N(\mathrm{HI})}{\Delta X} \tag{1.4}$$

Neutral hydrogen in Lyα forest absorptions is negligible, because the gas in these systems is highly ionized. As N(HI) is difficult to determine for LLS, their contribution to Ω_g is also uncertain. However, it is unlikely to be significant, since large surveys reveal that DLAs contain over 80% of the neutral gas in the Universe (e.g. Noterdaeme et al. 2012b, 2009; Zafar et al. 2013a). Systems with $N(\mathrm{HI}) \sim 10^{21}$ cm^{-2} contribute the most to $\Omega_g^{\rm DLA}$, and ∼10% of $\Omega_g^{\rm DLA}$ comes from gas in the highest column density absorption systems with N(HI) $\geq 0.5 \times 10^{22}$ cm^{-2} (Noterdaeme et al. 2012b, 2009). The gas is fully neutral for DLA column densities, and thanks to the damped wings N(HI) is easy to measure from the absorption profile.

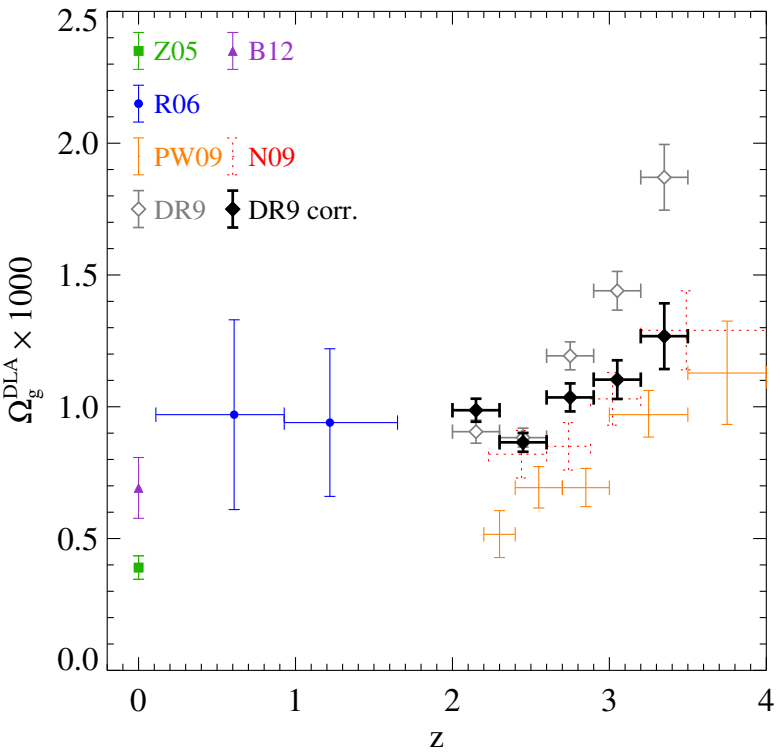

FIGURE 1.8: Cosmological mass density of neutral gas in DLAs as a function of redshift (Z05: Zwaan et al. (2005); B12: Braun (2012); R06: Rao et al. (2006); PW09: Prochaska & Wolfe (2009); DR9: Noterdaeme et al. (2012b)). (Figure from Noterdaeme et al. (2012b).)

Péroux et al. (2003) first emphasized the importance of sub-DLAs, noting that at $z > 3.5$ they may account for as much as ∼45% of Ω_g. Recent results indicate that sub-DLAs contribute no more than 20% to Ω_g, but confirm that they have a larger impact at $z \geq 3$ (Noterdaeme et al. 2012b, 2009; Zafar et al. 2013a). Including absorbers in the sub-DLA range permits a more complete census of Ω_g.

Since DLAs probe the most significant concentrations of neutral gas, these absorbers can be used to trace Ω_g as a function of redshift. The mass density of neutral gas in DLAs, $\Omega_g^{\rm DLA}$, decreases from $z = 3.5$ to $z \simeq 2$ (Figure 1.8; Noterdaeme et al. 2012b, 2009; Prochaska et al. 2005; Prochaska & Wolfe 2009), as could be expected if star formation draws on the gas reservoir. At all epochs, $\Omega_g^{\rm DLA}$ is significantly less than the amount of baryons in stars at $z = 0$, $\Omega_\star = (2.5 \pm 1.3) \times 10^{-3}$ (Cole et al. 2001). This indicates that DLAs represent a transition phase between the ionized gas in the IGM and the cold neutral gas in the ISM.

Péroux et al. (2003) advocated for including sub-DLAs, since their impact on Ω_g increases above $z > 3$. Prochaska et al. (2005) and Guimarães et al. (2009), who include both DLAs and sub-DLAs in their analysis, observe a decrease in Ω_g beyond $z = 3.5$. Indeed, some authors argue that Ω_g does not evolve significantly over $0.1 < z < 5$ when

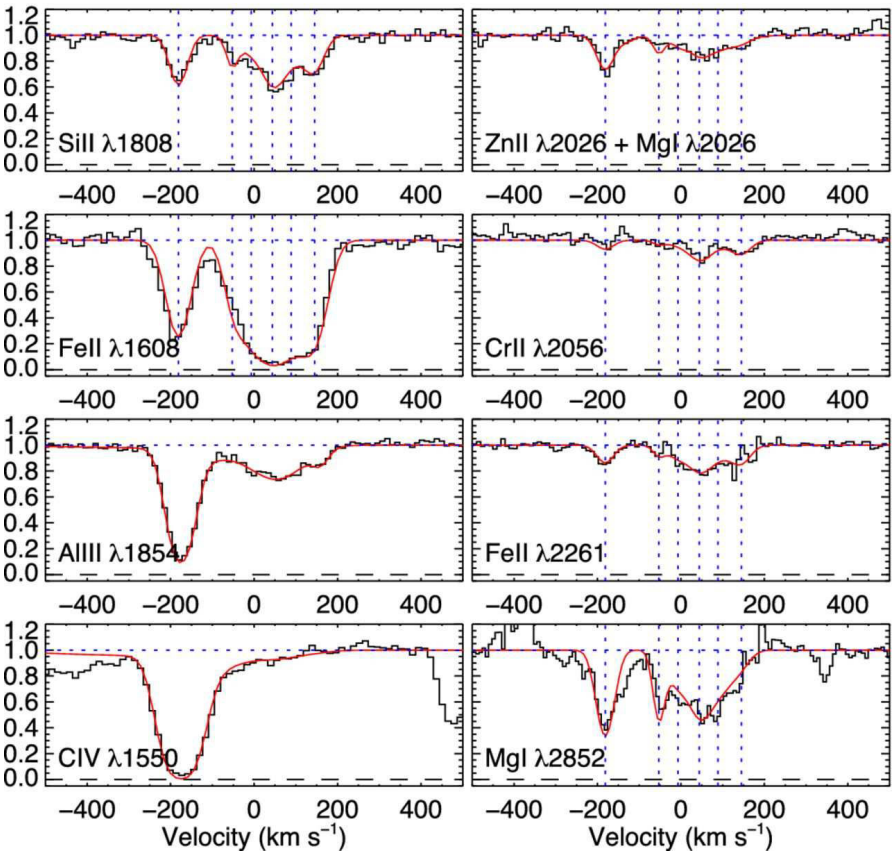

FIGURE 1.9: Voigt-profile fits to metal lines from a log N(HI)= 21.26±0.06 DLA at $z = 2.412$ in the Q0918+1636 quasar spectrum. Data are shown in black and the model fits in red. Vertical dotted lines mark the velocities for six subcomponents in the fit to the low-ionization lines. The left-hand column gives examples of weak and strong low-ionization lines (Si II and Fe II) and medium- and high-ionization lines (Al III and C IV) to illustrate the very different ionization states of the different subcomponents. The right-hand column shows low-ionization lines from Zn II, Cr II, Fe II and Mg I. (Figure from Fynbo et al. (2013).)

the contribution from sub-DLAs is included (Péroux et al. 2005; Zafar et al. 2013a). The decrease from $z = 3.5$ to $z \simeq 2$ is difficult to refute, but large error bars on $\Omega_g^{\rm DLA}$ measurements at low-redshift provide leeway for interpretation.

Samples of low-redshift DLAs are difficult to obtain, because Lyα is in the UV for $z < 1.65$ and requires space-based observations. Rao et al. (2006) greatly improved the statistics by detecting 41 DLAs in the range $0.11 < z < 1.65$ with a *Hubble Space Telescope* (*HST*) survey that targeted quasar lines-of-sight known to have strong Mg II absorptions (see also Turnshek et al. 2014). Whether the values for $\Omega_g^{\rm DLA}$ are biased by the Mg II selection or a statistical fluke has been discussed. Resolving these questions of selection bias would require a large blind survey for DLAs at $z \sim 1$, which is observationally expensive.

1.2.2.2 Metallicity

The chemical enrichment of an absorber can be measured from metals associated with the absorption system. The abundance of a species, X, is typically calculated relative to solar values:

$$[\mathrm{X/H}] \equiv \log\left(\frac{N(\mathrm{X})}{N(\mathrm{H})}\right) - \log\left(\frac{N(\mathrm{X})}{N(\mathrm{H})}\right)_{\odot} \tag{1.5}$$

where $\log(N(\mathrm{X})/N(\mathrm{H}))_{\odot}$ is the solar abundance and $N(\mathrm{H}) = N(\mathrm{H\,I}) + N(\mathrm{H\,II})$. Working with predominantly neutral absorption systems simplifies the analysis, since the contribution from ionized hydrogen, HII, is negligible and $N(\mathrm{H}) = N(\mathrm{H\,I})$. The $N(\mathrm{HI})$ is directly measured from fitting the damped absorption profile, as described above. Column densities for metal absorption lines are determined by fitting the available unsaturated transitions for a species.

Low ionization transitions, including OI, SiII, CII, AlII, FeII, and MgII, are usually readily apparent for strong absorption systems, as are several higher ionization transitions, like AlIII, SiIV, and CIV. Typically several transitions for the same species are redshifted to the visual portion of the spectrum, for example SiII $\lambda\lambda\lambda$1304, 1526, 1808 or FeII $\lambda\lambda\lambda\lambda\lambda\lambda$1608, 2344, 2374, 2382, 2586, 2600. Working with metal absorptions redward of the quasar Lyα emission peak is preferable, so as to avoid blends with HI in the Lyα forest. Since the multiple transitions have different oscillator strengths, it is possible to obtain a good measure of the ion column density. Even if some of the transitions are saturated, optically thin absorptions can often be detected. For the column density to be meaningful, it must be measured from metal absorption lines that are not saturated. High signal-to-noise (S/N) and/or high resolution spectra are particularly valuable for detecting weaker absorptions.

Figure 1.9 presents examples of metal absorptions that are part of a DLA system, including weak and strong lines. The low ions are fitted with six components and used to determine the metallicity for the system.

The best metallicity indicator is OI, because it is tightly related to HI. They have similar ionization energies, 13.618 eV for OI compared to 13.598 eV for HI, and consequently can exchange electrons during collisions (Stancil et al. 1999; Watson 1978). Due to this charge transfer, OI ionization is coupled to that of HI. However, OI λ1302 is almost always saturated for strong absorption systems, and lower wavelength transitions are typically blended with the Lyα forest.

After OI, favored species are those that are not strongly depleted onto dust grains. For Fe, Cr, and other refractory elements that are easily incorporated into dust, the gas-phase abundances do not reflect the total abundances (Jenkins 2009). If detected and

free of blends, Zn and S are robust metallicity indicators as they are nearly undepleted. Conveniently, the ZnII $\lambda\lambda$2026, 2062 absorption lines are often unsaturated and located redward of the Lyα forest. The ratio of depleted to undepleted elements provides a measure of the dust content of quasar absorbers (e.g., Khare et al. 2012; Pettini et al. 1997).

As with DLAs, N(HI) can be accurately determined for sub-DLAs from the damped absorption profile. However, since the gas may not be predominantly neutral in sub-DLAs, ionization effects could bias metallicity measurements toward higher values (e.g. Milutinovic et al. 2010). Metals with ionization potentials greater than 13.59 eV, such as FeII (ionization potential of 16.18 eV), may be associated with the ionized gas, rather than the neutral component. The observed FeII to HI ratio would thus be overestimated. Ionization corrections constrained from grids of photoionization models evaluated in CLOUDY (Ferland et al. 2013) are typically within errors on the metallicity, $\sim$0.15 dex (Dessauges-Zavadsky et al. 2003; Meiring et al. 2008, 2007). Péroux et al. (2007) used photoionization models to compute the ionization states for their sub-DLA sample and determined that the cosmological mass density from metals in sub-DLAs at $z \sim 2.5$ is $\Omega_{\mathrm{Z,\ sub\text{-}DLAs}} = 1.41 \times 10^{-6}$. At this redshift, sub-DLAs account for at most 6% of the total metal mass density, $\Omega_{\mathrm{Z}} = 2.47 \times 10^{-5}$.

One caveat for DLA metallicity measurements is that they are integrated over the entire absorption line profile. The metallicity cannot be calculated for individual components, since the HI is saturated. Fitting the DLA Lyα line gives only the total N(HI). Metallicity differences between components are therefore inaccessible, but it is still possible to compare the amount of depletion in each subsystem (Figure 1.10). In addition to depletion, nucleosynthesis can also affect metallicity measurements. An element may be prevalent or sparse depending on the dominant nucleosynthesis processes in the region where it was produced. Obtaining metallicities for as many species as possible and considering their relative depletion (Figure 1.11) helps to identify trends in the gas composition.

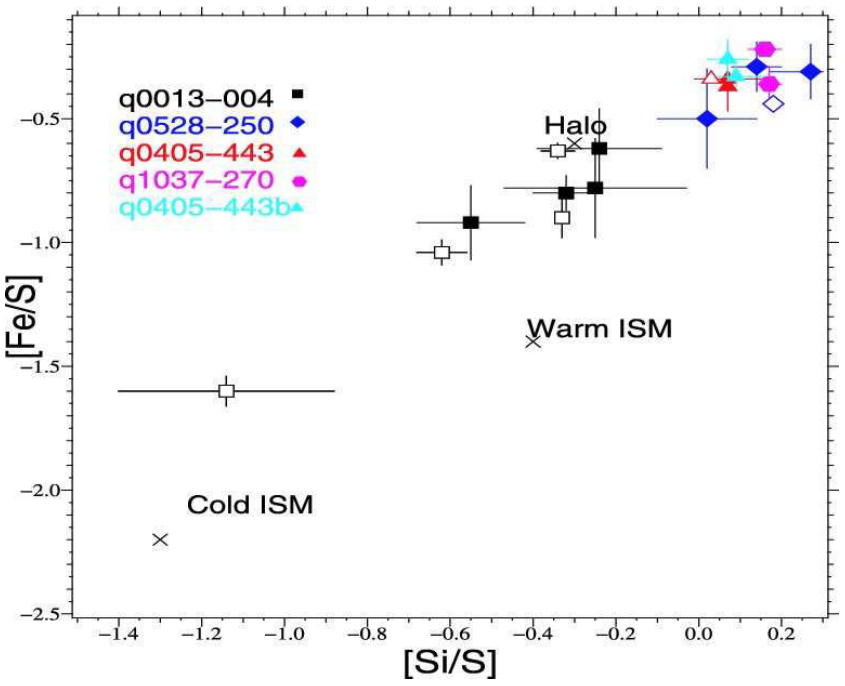

FIGURE 1.10: [Fe/S] vs. [Si/S] for all the subsystems analyzed in five high-redshift DLAs. Different symbols represent different DLA: squares for Q 0013-004, diamonds for Q 0528-250, triangles for Q 0405-443, and circles for Q 1037-270. Open symbols are used to distinguish subclumps where H_2 is detected. Otherwise symbols are filled. Typical [Fe/S] vs. [Si/S] values observed in the cold, warm ISM, and halo of our Galaxy (Welty et al. 1999) are given for comparison. (Figure from Rodríguez et al. (2006).)

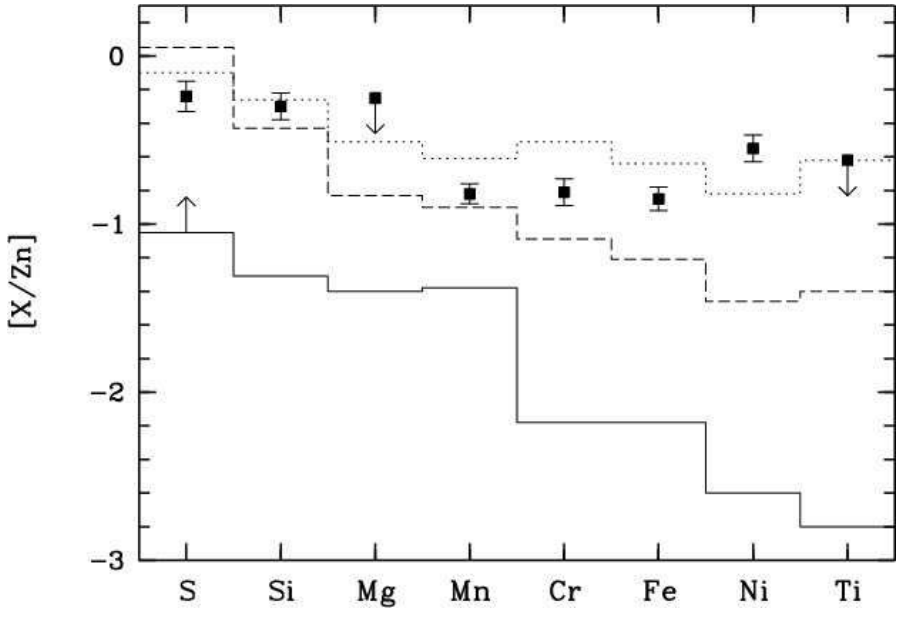

FIGURE 1.11: Depletion of heavy elements relative to zinc in the main subsystem (components at $z_{\rm abs} = 1.96203$, 1.96212 and 1.96225) of the near Solar-metallicity DLA system toward Q 0551-366. The histograms show the values observed in cold (solid line) and warm (dashed line) Galactic disc clouds, and warm Galactic halo clouds (dotted line; Savage & Sembach 1996). (Figure from Ledoux et al. (2002).)

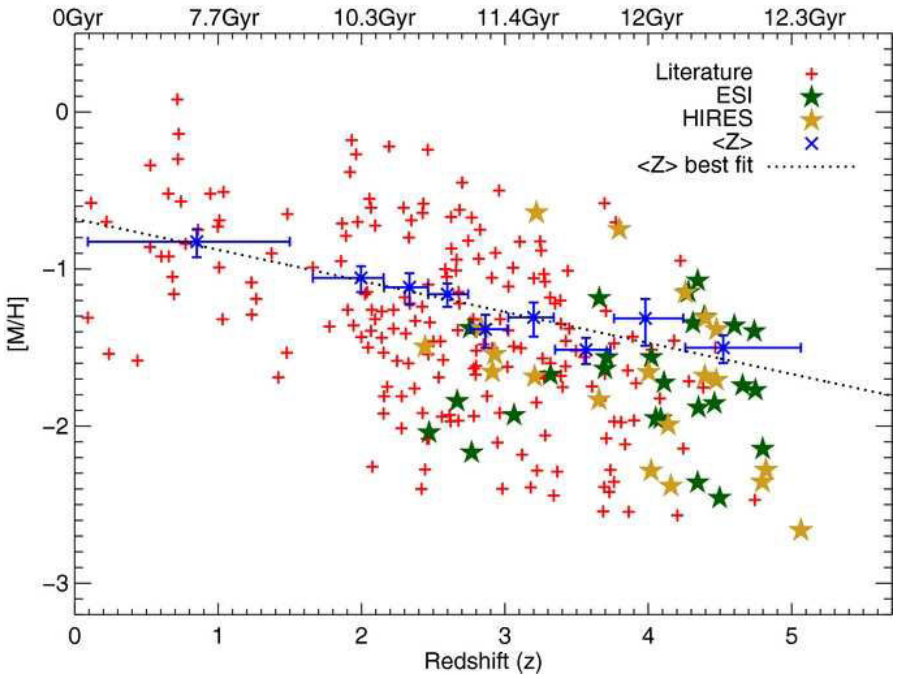

FIGURE 1.12: DLA metal abundance, [M/H], vs. redshift measured at the Keck telescope. Red plus signs are from the literature. The metallicities from ESI (lower spectral resolution) are green stars and those from HIRES (higher spectral resolution) are gold stars. The nine blue crosses with error bars show cosmic metallicity, $\langle \mathrm{Z} \rangle$, where horizontal error bars are determined such that there are equal numbers of data points per redshift bin. The vertical error bars represent 1σ confidence levels given from a bootstrap analysis. The black straight line is a linear fit to the $\langle \mathrm{Z} \rangle$ data points. (Figure from Rafelski et al. (2012).)

Mean Metallicity

The mean metallicity is defined as $\langle \mathrm{Z} \rangle = \log(\Omega_{\mathrm{Z}}/\Omega_{\mathrm{HI}})) - \log(\Omega_{\mathrm{Z}}/\Omega_{\mathrm{HI}}))_{\odot}$. It depends on the comoving densities of metals, Ω_{Z}, and neutral hydrogen, Ω_{HI}. Although Ω_{Z} cannot be measured directly, the mean metallicity for a redshift bin with i DLAs in a complete survey is calculated by summing over their metallicities and column densities (Lanzetta et al. 1995):

$$\langle \mathrm{Z} \rangle = \log\left(\frac{\sum_i 10^{[\mathrm{M/H}]_i} N(\mathrm{HI})_i}{\sum_i N(\mathrm{HI})_i}\right) \tag{1.6}$$

Up to $z \sim 5$, The mean metallicity for DLAs decreases with increasing redshift: $\langle \mathrm{Z} \rangle = (-0.22 \pm 0.03)z - (0.65 \pm 0.09)$ (Figure 1.12; Rafelski et al. 2012). Rafelski et al. (2014) observed that at $z > 4.7$ the mean metallicity drops significantly below the extrapolated linear fit. Although the mean metallicity evolves linearly with redshift, it is nonlinear in time. When viewed as a function of time, the most rapid change in metal abundances is at high redshift (see Figure 1.12, top axis).

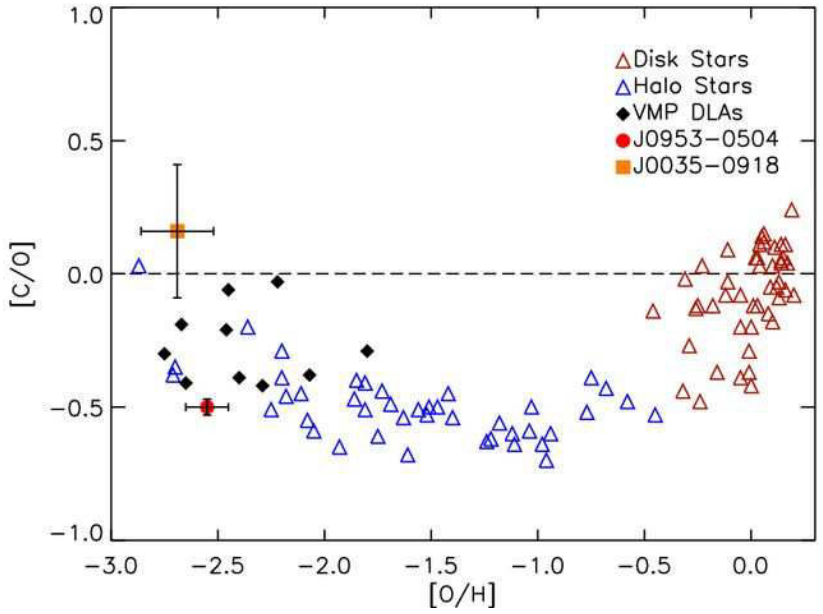

FIGURE 1.13: The [C/O] ratio versus [O/H] for very metal poor DLAs (Cooke et al. 2011; Dutta et al. 2014) compared with those of metal-poor stars (Frebel 2010) and disk stars (Bensby & Feltzing 2006). (Figure from Dutta et al. (2014).)

Samples have targeted DLAs at both the metal-strong (Herbert-Fort et al. 2006; Kaplan et al. 2010) and metal-poor (Cooke et al. 2011; Dutta et al. 2014) ends of the abundance range. Kaplan et al. (2010) measure a median abundance of [M/H] ≈ -0.67 for metal-strong DLAs at $z \approx 2$, which is 0.6 dex higher than a control sample of randomly selected DLAs. No DLAs with super-solar metallicities have been observed. The least enriched systems have [Fe/H] < -2, with some abundances as low as [Fe/H] $\simeq -3$ (Cooke et al. 2011; Dutta et al. 2014). The C/O ratio for these systems is nearly super-solar and follows a trend observed for halo stars in the Milky Way (Figure 1.13).

The Velocity-Metallicity Correlation

Ledoux et al. (2006) identified a correlation between the metallicity and the velocity width measured across $5\% - 95\%$ of the line optical depth, as per Prochaska & Wolfe (1997a), in a sample of 70 strong absorbers with $N(\mathrm{HI}) \gtrsim 10^{20}$ cm^{-2} and redshifts $1.7 < z_{\mathrm{abs}} < 4.3$ observed at high resolution with VLT/UVES. The velocity width is a proxy for the dark matter halo mass. The velocity-metallicity correlation (Figure 1.14) is likely the result of an underlying mass-metallicity relation for the DLA galaxies, which could imply that high metallicity systems are associated with more massive (and potentially brighter) galaxies. Møller et al. (2013) expanded the redshift range to $0.11 \leq z \leq 5.06$ with additional DLAs from literature to investigate tentative evidence in Ledoux et al. (2006) that the mass-metallicity relation evolves with redshift. They find that the correlation zero-point remains constant at high redshift during the early phases of galaxy growth,

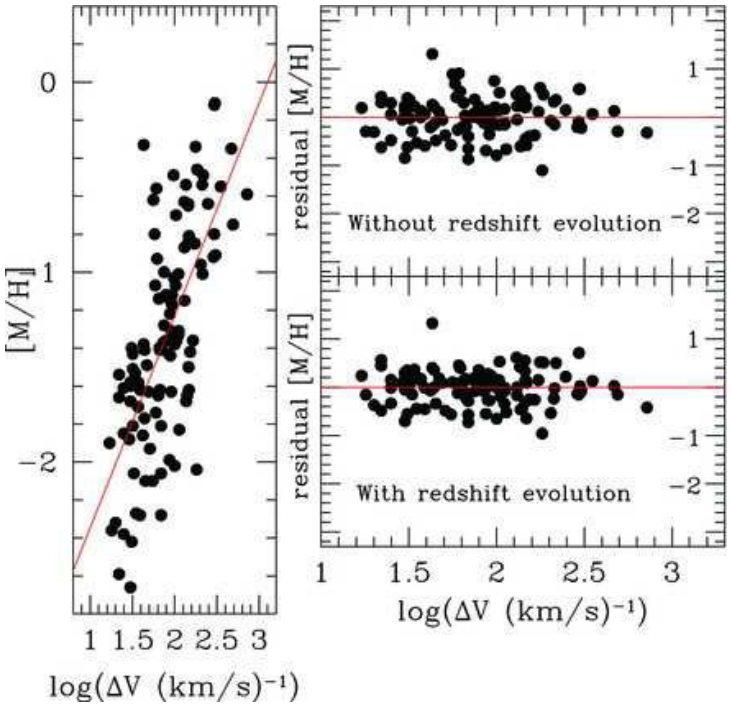

FIGURE 1.14: Left: Metallicity versus velocity width for 110 DLAs. The best-fitting linear relation with a slope of 1.12 is drawn as a red line. Upper Right: Residuals after subtracting the fit with no redshift evolution. Lower Right: Improved residual after subtracting the fit that includes redshift evolution. (Figure from Møller et al. (2013).)

but increases sharply with decreasing redshift below $z = 2.6 \pm 0.2$. DLA galaxies at low redshift are more metal-rich than those of equal mass at high redshift. Combining the velocity-metallicity and redshift-metallicity correlations, Neeleman et al. (2013) proposed a fundamental plane of DLA properties that relates their metallicity, redshift, and mass. The plane equation, which is based on data for 100 DLAs observed with Keck/HIRES, reduces the scatter around both correlations and suggests a mass-metallicity relationship with a zero-point that evolves from $z = 2 - 5$, in contrast to the Møller et al. (2013) results. Christensen et al. (2014) extended the mass-metallicity analysis to 12 confirmed DLA galaxies at $0.1 < z < 3.2$ for which it was possible to derive stellar masses from spectral energy distribution fits to multi-band photometry. They inferred metallicity gradients and provide a formalism for calculating the stellar mass (M^*_{DLA}) of the galaxy when the DLA metallicity and DLA galaxy impact parameter are known. Through these relations, the nature of DLA galaxies is becoming more clear.

1.3 Relating Absorption Line Systems and Galaxies

1.3.1 Mg II Systems

Early imaging studies established that quasar absorption line systems probe circumgalactic gas. By identifying galaxies associated with low-redshift MgII absorptions, Bergeron (1986) and Bergeron & Boissé (1991) demonstrated that large gaseous halos of enriched gas surround galaxies. The $z \sim 0.5$ absorbing galaxies were at impact parameters of $5'' - 12''$, which exceeded estimates of typical galactic radii by a factor of ∼3. Normal ($\sim L^*$) galaxies at intermediate redshifts ($0.5 \leq z \leq 1.0$) give rise to low-ionization MgII absorption with $W_0(2796) \geq 0.3$ Å out to projected distances of $\sim 40h^{-1}$ *kpc* (e.g., Steidel 1993). C IV absorption systems likewise appear to be related to gaseous galaxy halos (Petitjean & Bergeron 1994), with a tight correlation between Mg II kinematics and the C IV equivalent width (Churchill et al. 1999). Galactic halo models successfully reproduced a full range of absorption systems, including highly ionized systems, LLS with and without low ionization transitions, and DLAs (Srianand & Khare 1994).

Steidel et al. (1997) obtained extremely comprehensive data, including HST/FOS spectroscopy and very deep WFPC2 images, for the field centered on the 3C 336 quasar ($z_{\rm em} = 0.927$) with six intervening metal-line absorption systems in the range $z_{\rm abs} = 0.318 - 0.892$. They identified luminous ($L_{\rm K} \geq 0.1 L^*_{\rm K}$) galaxies for five of the six absorption systems (Figure 1.15) and observed that all bright galaxies ($L > 0.1 L_{\rm K}$) within 50 h^{-1} kpc produced detectable Mg II and/or C IV absorptions in the quasar spectrum. The systems exhibited a wide variety of absorption strengths and ratios of low to high ionization species, with C IV/Mg II equivalent widths that tend to increase with increasing galactocentric distance. Based on photoionization models for three systems with identified galaxies and HST/FOS spectra, Churchill & Charlton (1999) proposed that Mg II clouds are embedded in extended (10-20 kpc), highly ionized gas that gives rise to C IV, N V, and O VI absorptions.

Recent studies used the large statistics of SDSS for in-depth investigations of the relation between galaxies and the absorbing gas, either by detecting the galaxy directly (Noterdaeme et al. 2010) or through stacking methods (Ménard et al. 2011).

1.3.2 CGM

The CGM is composed of multiphase gas with different densities, temperatures, and ionization states, as evidenced by detections of Mg II, C IV, and O VI. While Mg II occurs in denser regions at lower temperatures, O VI appears in lower density gas at larger

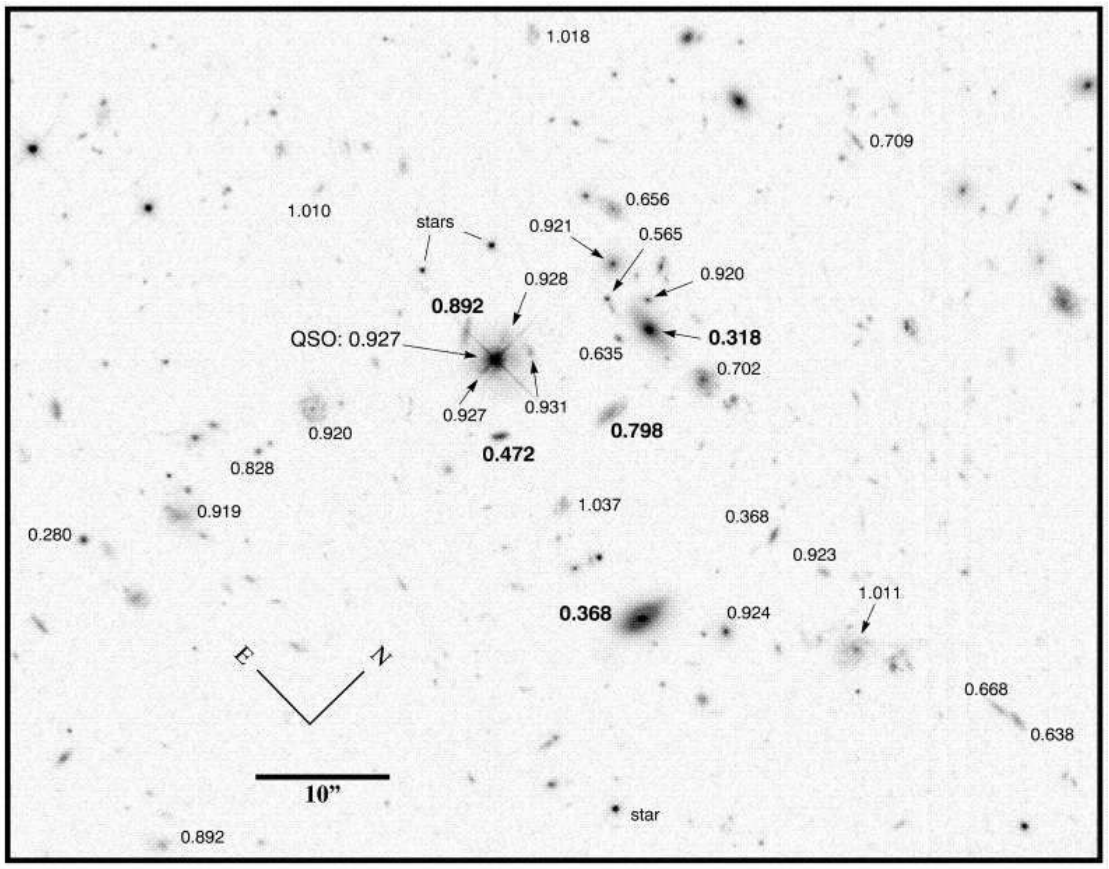

FIGURE 1.15: A portion of the 24 000 s HST/WFPC2 image of the field surrounding quasar 3C 336 ($z_{\rm em} = 0.927$), with the orientation indicated. Objects for which redshifts have been obtained are labeled, and galaxies that give rise to metal-line absorption systems in the quasar spectrum have bold redshift values. (Figure from Steidel et al. (1997).)

distances from galaxies or in gas at higher temperatures (e.g., Bergeron et al. 1994). The more tenuous O VI absorbers could be ionized by a hard UV background spectrum (photoionized), whereas the higher column density population could be shock heated and collisionally ionized. Detailed studies of individual O VI systems at low and high redshift revealed a variety of physical states (e.g., Bergeron et al. 2002; Carswell et al. 2002; Savage et al. 2002; Simcoe et al. 2002; Tripp et al. 2001).

By evaluating nearest neighbor distances between a sample of O VI absorbers at $z < 0.15$ and galaxy catalogs, Stocke et al. (2006) determined that $N(\mathrm{O\,VI}) \geq 10^{13.2}$ cm^{-2} absorbers are likely associated with galactic winds or halos. The gas has $10\% \pm 5\%$ solar metallicity and extends to median distances of $350-500\ h_{70}^{-1}$ kpc around L^* galaxies and $200-270\ h_{70}^{-1}$ kpc around $0.1L^*$ galaxies. Tumlinson et al. (2011b) created a model of a highly ionized, multiphase, low-metallicity gaseous halo that is photoionized by stars in nearby galaxies, consistent with observations of a LLS at $z_{\rm abs} = 0.3558$ with strong O VI absorptions. Similarly, Tumlinson et al. (2011a) detected ubiquitous, large (150 kpc) halos of ionized oxygen surrounding star-forming galaxies at $z = 0.10 - 0.36$, but found

much less ionized oxygen around galaxies with little or no star formation. Results from the COS-Halos Survey (Tumlinson et al. 2013; Werk et al. 2014) suggest that absorption systems within 160 kpc of $L \sim L^*$ galaxies at $z \sim 0.2$ are highly ionized ($n_{\rm H\,II}/n_{\rm H} > 99\%$) due to the extragalactic ultraviolet background. Werk et al. (2014) estimated a lower limit $M_{\rm cool}^{\rm CGM} > 6.5 \times 10^{10}$ $M_\odot$ for the volume within the virial radius, which implies that the cool, photoionized gas in the CGM accounts for over 25% of the baryon budget of an $L \sim L^*$ halo.

Indeed, fully accounting for baryons at $z \sim 0$ remains a major question. Baryons comprise nearly 17% of gravitational matter ($\Omega_{\rm b} = 0.167\Omega_{\rm m}$ Komatsu et al. 2011), whereas inventories of the gas and stars in galaxies contribute no more than ∼8% to $\Omega_{\rm b}$ (e.g., Baldry et al. 2008; Bell et al. 2003). In addition to the cool ($T < 10^5$ K) CGM gas, baryons can reside in a warm-hot intergalactic medium, (WHIM; $10^5 < T < 10^7$ K). The high temperatures in the WHIM are due to shock heating as structures form (Cen & Fang 2006; Cen & Ostriker 1999, 2006). The gas emits soft x-rays, and collisionally ionized oxygen lines can also be a tracer. Based on cosmological hydrodynamical simulations of the IGM evolution from z = 2 to z = 0, Davé et al. (2010) predicted that 35% of baryons are currently bound within galaxies and the CGM, leaving 41% in the IGM and 24% in the WHIM. By analyzing H I and O VI absorption systems in high-resolution HST/COS quasar spectra, Savage et al. (2014) identified 14 components associated with warm ($T \sim 10^6$ K) gas located 200 to 600 kpc beyond the closest galaxy. They estimated that this gas contains $(4.1 \pm 1.1)\%$ of $\Omega_{\rm b}$, which is nearly as many baryons as are found in galaxies. Stocke et al. (2014) re-evaluated the same sample and suggested that the warm absorbers are likely associated with galaxy groups, rather than individual galaxies. These recent investigations, which rely heavily on the unique capabilities of HST/COS, are closer to closing the gap between directly detected matter and $\Omega_{\rm b}$.

Lehner et al. (2013) identified a bimodal metallicity distribution for H I-selected LLS probing the cool CGM of galaxies at $z \lesssim 1$ with peaks at [X/H] $\simeq -1.6$ and -0.3 (or about 2.5% and 50% solar metallicities). The metal-rich absorptions systems likely trace winds, recycled outflows, and tidally stripped gas, whereas the metal-poor LLS may be consistent with cold accretion streams thought to provide fresh gas for star forming galaxies. (THIS IS OUT OF PLACE...)

1.3.3 DLA Systems

Wolfe et al. (1986) initially suspected that DLAs probe the disks of high-redshift precursors to local spiral galaxies. Early spectroscopic surveys (e.g., Lu et al. 1993; Turnshek

et al. 1989; Wolfe et al. 1993), focused on velocity signatures in the absorption line profiles (Figure 1.16) that could indicate a two-component model: a quiescent cloud with high H I column density gas and low velocity dispersion corresponding to the DLA and a turbulent lower column density halo with higher velocity dispersion corresponding to the associated metal lines. The kinematics for three DLA systems with high resolution spectroscopy supported the rotating disk interpretation, since their metal absorption line profiles showed leading-edge asymmetry Prochaska & Wolfe (1996, 1997b). Indeed, the first spectroscopically confirmed high-redshift intervening DLA galaxy, a $z_{\rm abs} = 3.150$ absorber toward Q2233+131, appeared to be a young, still-forming disk galaxy (Djorgovski et al. 1996). By extensively testing different protogalaxy models, Prochaska & Wolfe (1997a) determined that only rapidly rotating disks ($v_{\rm rot} \simeq 225$ km s^{-2}) were consistent with a statistical sample of DLAs at high confidence levels. Nonetheless, the number density of DLAs was greater than what is derived if they are associated with spiral galaxies, which raised the possibility that disks were larger in the past.

Alternatively, York et al. (1986) proposed that gas-rich dwarf galaxies could produce the complex structure and wide range of ionization states observed in quasar absorption line systems. Tyson (1988) determined that low surface brightness, gas-rich dwarf galaxies could account for the DLA number density. Moller & Warren (1993) tried to differentiate between possible morphologies for the spectroscopically confirmed galaxy associated with a $z_{\rm abs} \simeq z_{\rm em} \simeq 2.8$ DLA toward PKS 0528-250, but found evidence either for a compact group or a single large galaxy. By using strong Mg II absorption to predict damped Lyα absorption, Rao & Turnshek (1998) discovered two low-redshift DLAs at $z = 0.0912$ and $z = 0.2212$ toward the OI 363 quasar. Extended sources within $40''$ of the quasar were predominantly dwarf galaxies. The only luminous spiral galaxy in the field was at $z = 0.06$ and therefore not a candidate galaxy for either DLA. Additional imaging later confirmed that the $z = 0.0912$ and $z = 0.2212$ DLA galaxies are respectively a low surface brightness galaxy and an early-type dwarf (Turnshek et al. 2001). These low-redshift observations challenged the H I disk paradigm. Furthermore, abundance ratios for high-redshift DLAs also favored dwarf galaxies over spirals as the progenitors of DLA systems (Lu et al. 1996; Matteucci et al. 1997).

By studying galaxy formation in a cosmological context with hydrodynamic simulations, (Haehnelt et al. 1998) demonstrated that rotational and random motions in merging protogalactic clumps could reproduce the observed asymmetries in metal absorption line profiles and their velocity width distribution. Typical virial velocities for the haloes giving rise to the DLAs were on the order of 100 km s^{-1}. Ledoux et al. (1998) measured the velocity broadening, ΔV, in a sample of 26 DLAs and found a positive correlation with the line asymmetry for $\Delta V < 150$ kms^{-1}. Broader lines were more asymmetric, as could be expected if rotation dominates the line broadening. However, the kinematics

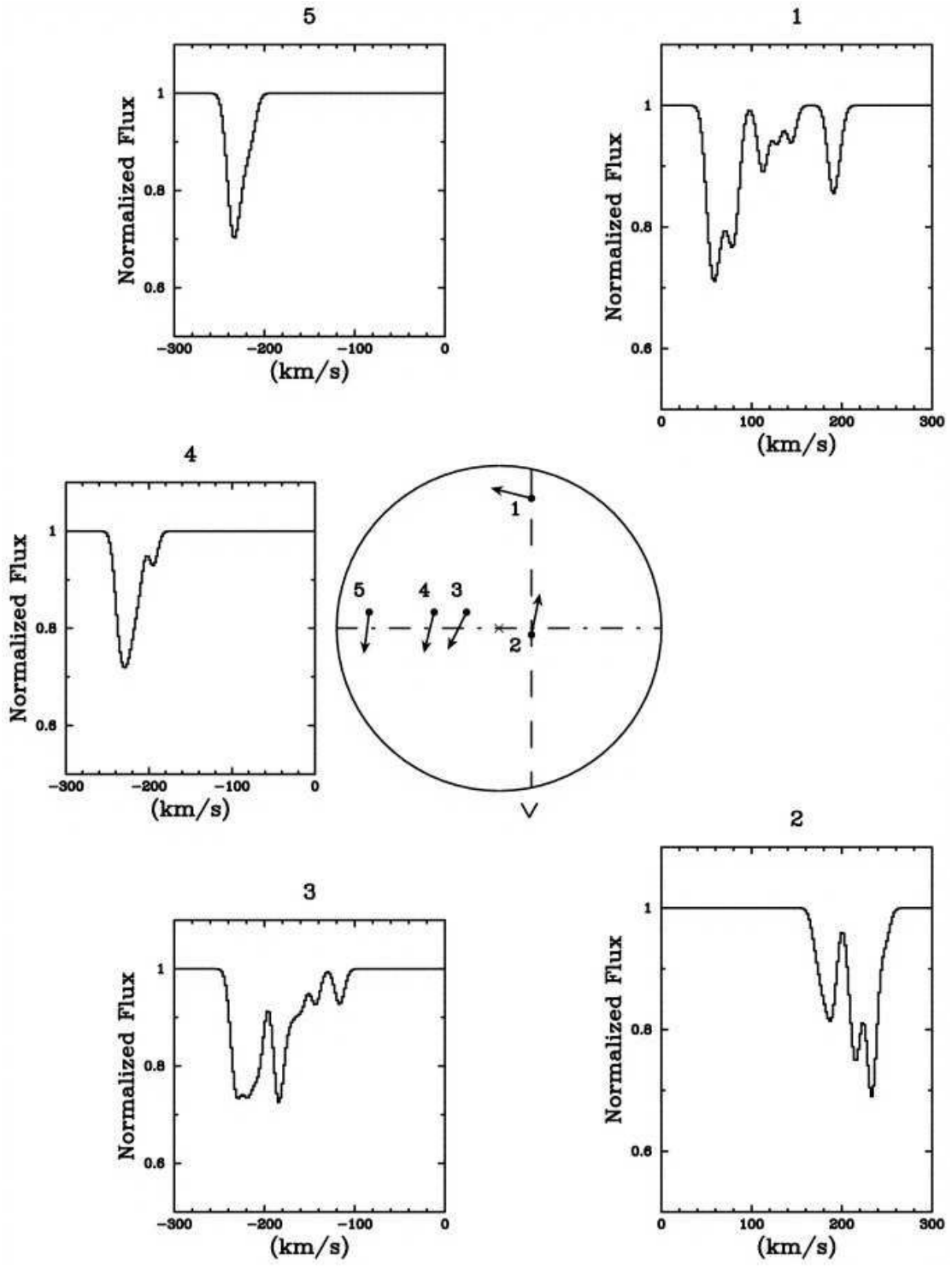

FIGURE 1.16: Metal absorption line profiles from discrete clouds rotating with a galactic disk. The center circle represents an inclined disk (top view) rotating counter clockwise with rotation speed $v_{\rm rot} = 250$ km s^{-1}. The solid dots represent the intersection points for five different sight lines with the midplane of the disk. The solid arrows indicate the direction of the rotation vector. The dashed vertical line represents the sight line for intersections 1 and 2. Finally, the dash-dotted line is the kinematic major axis, i.e., the intersection of the plane of the disk and the plane of the sky. The sight lines are inclined by 70° with respect to the normal of the disk and yield the profiles labeled $1-5$. Profile 1 exhibits reverse asymmetry because the midplane intersection is far from the major axis. Radial effects produce asymmetry in profile 2, where the midplane intersection is close to the major axis. Profiles $3-5$ show how changes in impact parameter, b, affect the velocity profiles. They arise at midplane intersections that have increasing impact parameters from the line-of-sight, but a constant offset from the major axis. The absorption intervals, Δv, decrease with increasing b, because the $v_{\rm rot}$ gradient projected along the line-of-sight decreases with increasing R. (Figure from Prochaska & Wolfe (1997a).)

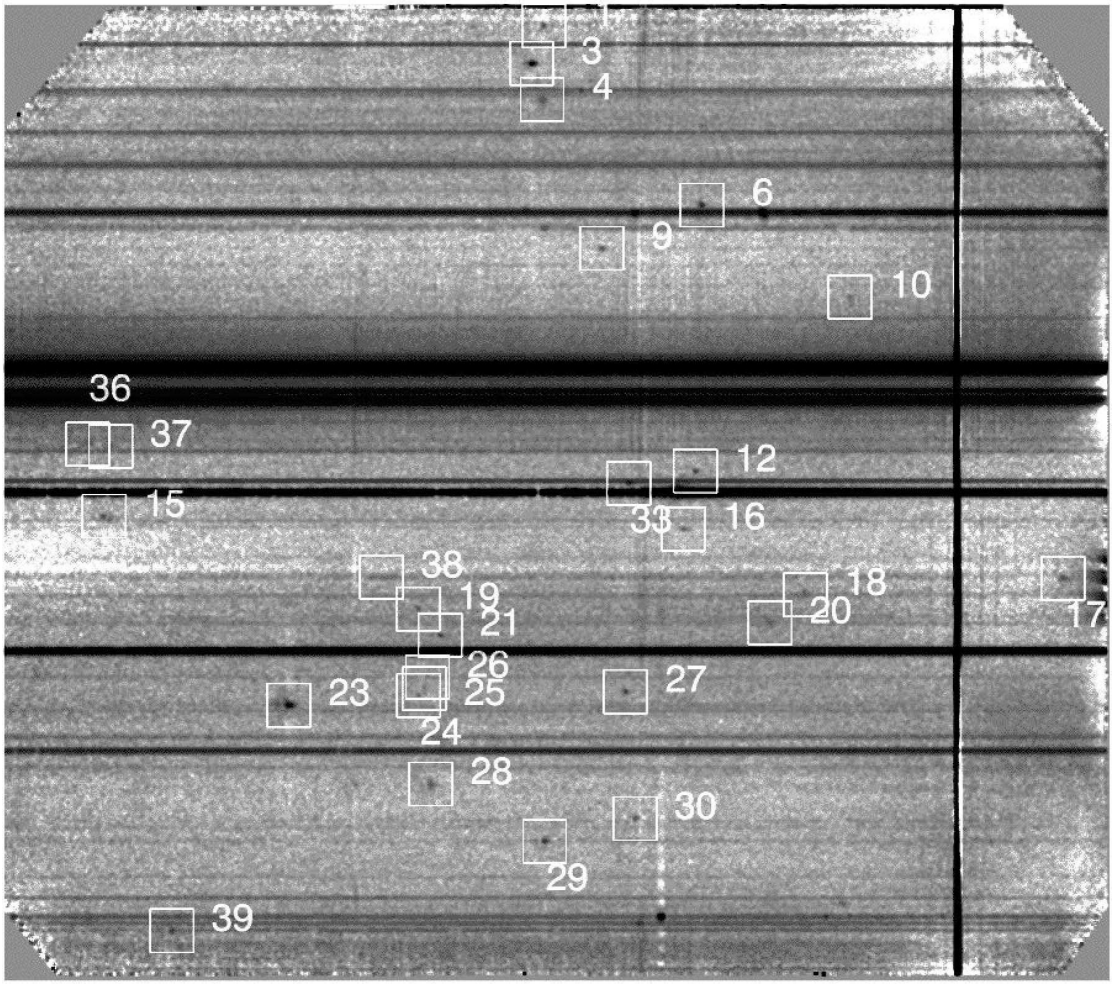

FIGURE 1.17: Two-dimensional spectrum obtained in 92 hr of exposure time with VLT/FORS2, showing the line emitter candidates for H I Lyα (boxes). The dispersion direction is horizontal, with blue to the left and red to the right; the spatial direction along the slit is vertical. The QSO spectrum (multiple absorption lines) is visible close to the center of the image. (Figure from Rauch et al. (2008).)

for DLAs with the largest velocity broadening, $\Delta V > 200$ kms^{-1}, were consistent with random motions and many showed evidence of sub-systems. Large, rapidly rotating disks were no longer the only plausible explanation for DLA kinematics.

Additional observations confirmed that galaxies with a variety of morphological types, including spirals, dwarfs, irregulars, and galaxies in groups, produced DLAs (e.g., Chen & Lanzetta 2003; Le Brun et al. 1997). Low-redshift galaxies associated with DLAs appear to be faint (Chun et al. 2006) and have low star formation rates (Wild et al. 2007). By stacking 341 DLAs at $\langle z \rangle = 2.86$ identified in SDSS spectra, Rahmani et al. (2010) measured Lyα flux in the DLA troughs emitted from galaxies within $\sim$1.5″ (12 kpc) of the quasar lines-of-sight. The 3σ upper limit of 3.0×10^{-18} erg s^{-1}cm^{-2} on the Lyα emission corresponds to galaxies with an average Lyα luminosity $\leq 2 \times 10^{41}$ erg s^{-1} or $0.03L^*$ (Lyα) and is deeper than the detection threshold for most Lyα emitter surveys.

Using VLT/FORS2 for the longest to date integration time focused on one quasar, Rauch et al. (2008) obtained 92 hours of on-source exposure with the $2'' \times 453''$ slit centered on the DMS 2139-0405 quasar (Figure 1.17), achieving a 1σ surface brightness detection limit of 8.1×10^{-20} erg cm^{-2} s^{-1} arcsec^{-2}. They detected 27 faint emitters at $2.66 < z < 3.75$ with line fluxes in the range $1.5 - 15 \times 10^{-18}$ erg s^{-1}cm^{-1}. The comoving density, large covering factor, and extended line profiles of these supposed Lyα emitters agree with the DLA rate of incidence and their characteristically low luminosities, metallicities, and dust content. This reinforced the idea that $z \sim 3$ DLA galaxies are protogalactic clumps that evolve into present day galaxies (Barnes & Haehnelt 2009). Although Rahmani et al. (2010) argued that they should have detected Lyα emission in their stacked spectrum if the Rauch et al. (2008) emitters were representative of DLA galaxies, Rauch & Haehnelt (2011) presented a refined treatment of the Lyα emission profile and concluded that the two flux measurements are consistent with the same populations: Lyα emitters overlap significantly with DLA host galaxies.

1.3.4 DLA Galaxies in Simulations

Simulations have been essential for relating absorbers to large-scale structure and characterizing the environments that give rise to DLAs (e.g., Fumagalli et al. 2011; Gardner et al. 1997, 2001; Haehnelt et al. 1998; Katz et al. 1996; van de Voort et al. 2012). Using either smooth-particle hydrodynamics or adaptive mesh refinement, most current simulations evolve dark matter and gas particles according to ΛCDM cosmology with hierarchical, bottom-up structure formation. Since implementing radiative transfer in N-body simulations is prohibitively computationally expensive, they are post-processed for absorption systems studies to include ionization processes and self-shielding effects. Absorber incidence rates and column density distributions help evaluate whether the simulations accurately represent the observed universe.

Pontzen et al. (2008) investigated the DLA population at $z = 3$ in simulations that produce galaxies with realistic physical properties at $z = 0$ (Figure 1.18) and were particularly successful at reproducing the metallicity distribution while respecting observational constraints. Across four redshift snapshots, $z = 0$, 1.6, 3.1, and 4.0, the peak of the DLA metallicity distribution in the Cen (2012) simulations decreases from $[\mathrm{Z/H}] \simeq -0.5$ at $z = 0$ to $[\mathrm{Z/H}] \simeq -1.5$ at $z = 4$, consistent with observations. Simulations have also emphasized the importance of galactic winds for recreating observed DLA properties, including column densities, kinematics, and metallicities (Cen 2012; Nagamine et al. 2004; Tescari et al. 2009). Recently, Altay et al. (2013) considered how physical processes, such as galactic outflows, molecular hydrogen formation, saturation of the neutral fraction, and self-regulated star formation, impact DLA statistics.

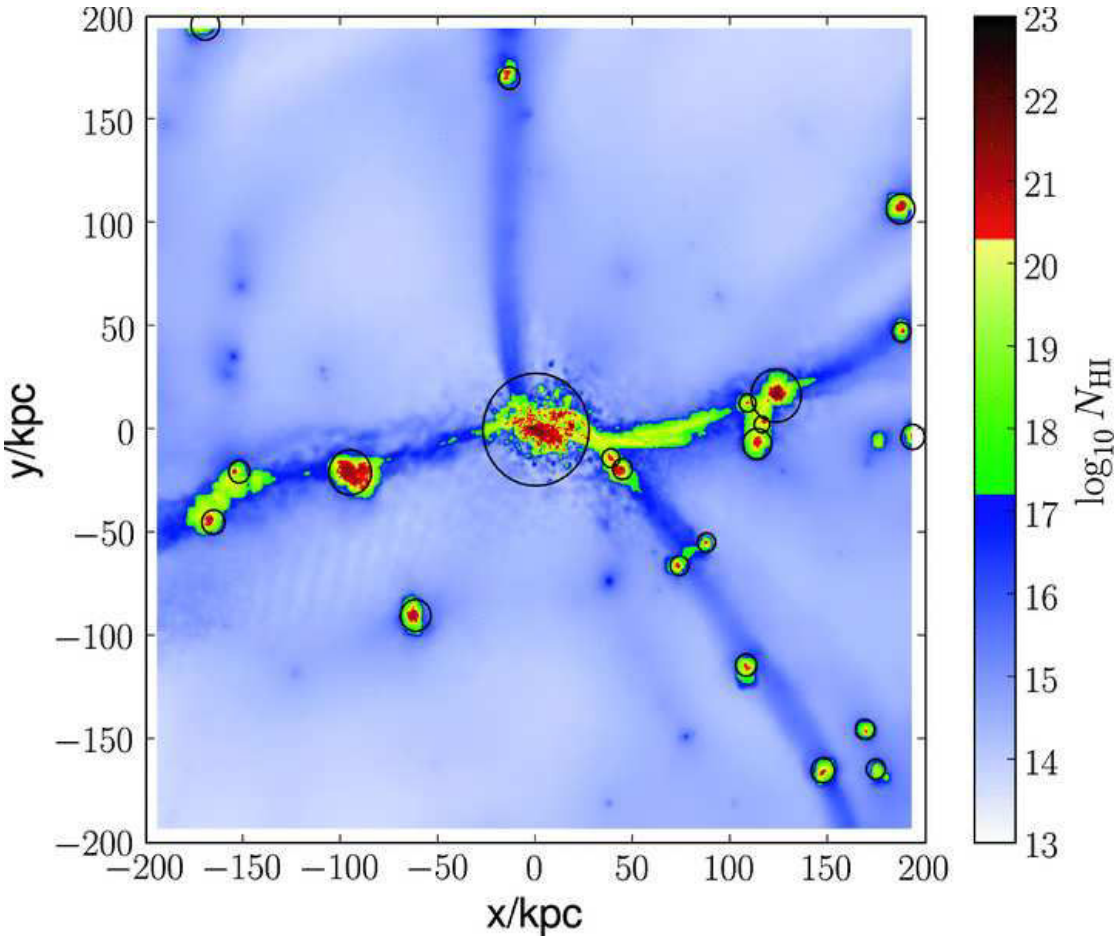

FIGURE 1.18: The $z = 3$ neutral column density of H I in a 400 kpc cube centered on the major progenitor to a $z = 0$ Milky Way type galaxy (box MW). The colors are such that DLAs ($\log_{10}N(\mathrm{HI})/\mathrm{cm}^{-2} > 20.3$) appear in dark red and Lyman limit systems ($20.3 > \log_{10}N(\mathrm{HI})/\mathrm{cm}^{-2} > 17.2$) appear in green and yellow. The circles indicate the projected positions and virial radii of all dark-matter haloes with $\mathrm{M} > 5 \times 10^8$ $\mathrm{M}_\odot$. All units are physical. A stereoscopic and an animated version of this plot are available at http://www.ast.cam.ac.uk/~app26/ (Figure from Pontzen et al. (2008).)

For each strong H I absorber ($N(\mathrm{HI}) \gtrsim 10^{17}$ cm^{-2}) at $z = 3$ in their cosmological hydrodynamical simulations (Figure 1.19), Rahmati & Schaye (2014) associated the absorber to the galaxy with the shortest transverse distance and a line-of-sight velocity difference within ± 300 km s^{-1}. They found that the DLAs and LLS have impact parameters on the order of 1 and 10 proper kpc, respectively. This anticorrelation between the H I column density and the impact parameter agrees with previous results from simulations and observations (e.g., Krogager et al. 2012; Pontzen et al. 2008). Similarly, Cen (2012) estimated that only 20-30% of DLAs are within 100 kpc of an L^* galaxy at $z = 3 - 4$, which increases to no more than 50% at $z = 1.6$.

Interestingly, Rahmati & Schaye (2014) predict that most DLA/sub-DLA systems are associated with very low mass galaxies, $M_\star \lesssim 10^8$ $\mathrm{M}_\odot$ (Figure 1.20), which are generally too faint for current instruments to detect. The galaxy mass increases with absorber

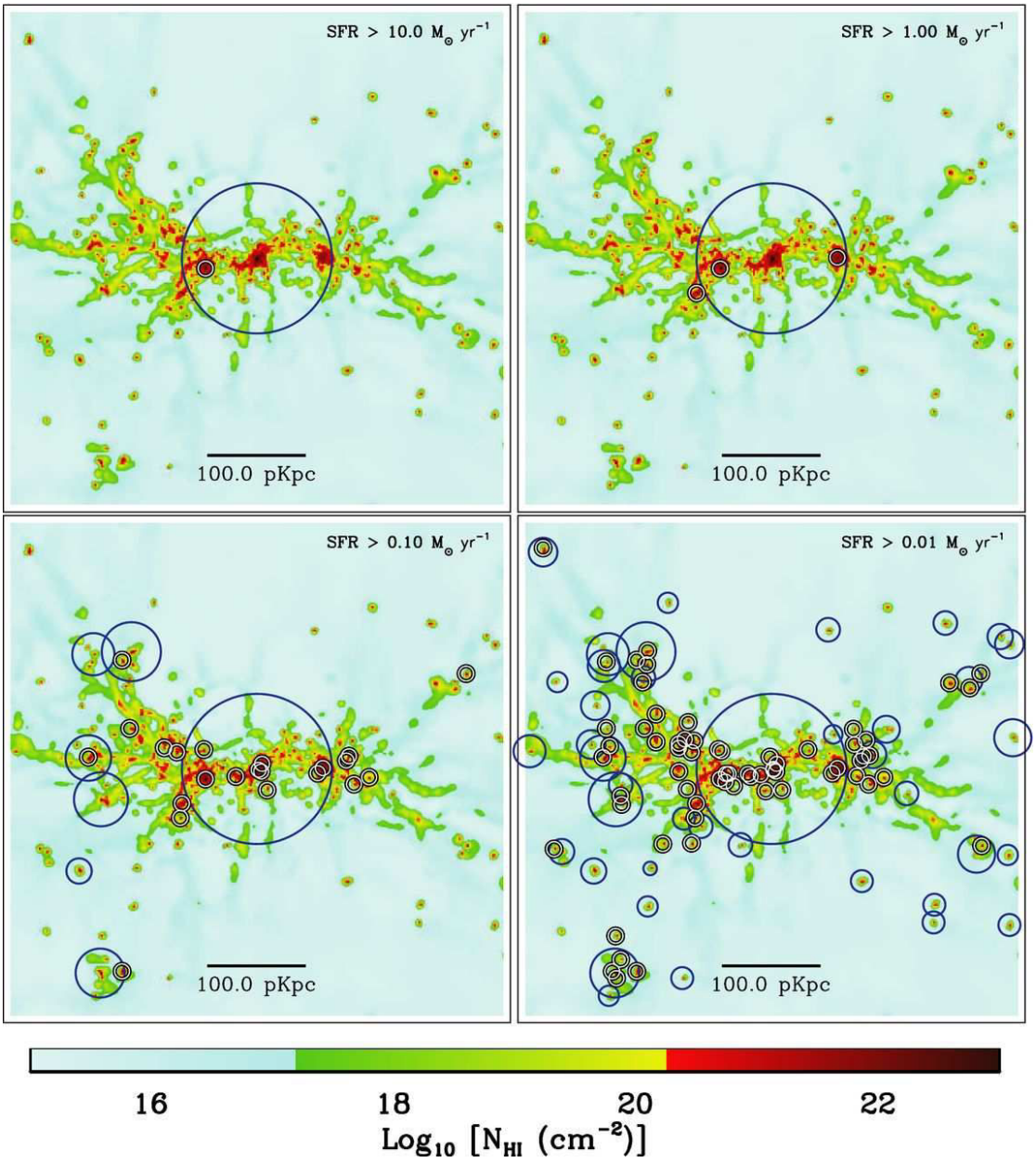

FIGURE 1.19: The simulated H I column density distribution around a massive galaxy with $M_* = 10^{10}$ $M_\odot$ and SFR = 29 $M_\odot$ yr^{-1} at $z = 3$. Circles indicate the positions of galaxies. The size of each dark circle indicates the virial radius of a central galaxy (R200) while the small white circles that all have the same size indicate the locations of satellite galaxies. Panels from top left to bottom right show galaxies with SFR > 10, > 1, > 0.1 and > 0.01 $M_\odot$ yr^{-1}, respectively. As the SFR threshold decreases, more galaxies are detected and the typical impact parameter between galaxies and absorbers decreases. (Figure from Rahmati & Schaye (2014).)

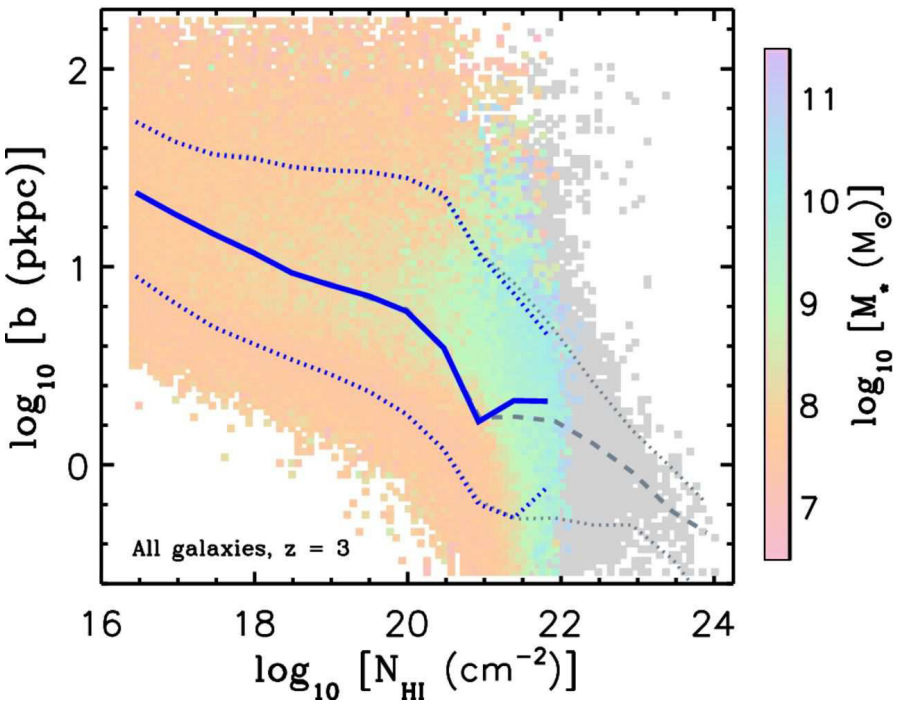

FIGURE 1.20: The predicted impact parameters (in proper kpc) of absorbers as a function of H I column density at $z = 3$. The color of each cell (in the b–N(HI) plane) indicates the median stellar mass of the galaxies associated with the H I absorbers in that cell. The blue solid curve traces the median impact parameter as a function of N(HI), and the dotted curves indicate the $15 - 85\%$ percentiles. The grey cells show the region where H_2 formation drains the atomic gas. The grey dashed and dotted curves trace the median impact parameter and the $15 - 85\%$ percentiles as a function of N(HI) if the conversion of high pressure gas into H_2 is neglected. (Figure from Rahmati & Schaye (2014).)

column density, such that the majority of strong DLAs, $N(\mathrm{HI}) \gtrsim 10^{21}$ cm^{-2}, are associated with $M_\star \gtrsim 10^9$ M$_\odot$ galaxies. (See also Tescari et al. (2009) and van de Voort et al. (2012).) Masses, SFRs, and impact parameters measured for the small sample of observationally confirmed DLA galaxies (see below) are in good agreement with the simulation predictions. The properties of observed DLA galaxies may be biased high, however, since the majority of DLAs are likely associated with faint galaxies at small impact parameters.

1.3.5 Observing DLA Galaxies

Candidate DLA galaxies have traditionally been identified by imaging quasar fields and following-up on promising targets with spectroscopy. See Steidel et al. (1995) and Djorgovski et al. (1996) for an early successful example or Kashikawa et al. (2014) for a more recent implementation. Confirming the redshift for a candidate galaxy is necessary to securely associate it with the DLA. Imaging DLA galaxies is often difficult, particularly at high redshift, due to surface brightness dimming that goes as $(1 + z)^4$. Furthermore, candidate galaxies at small impact parameters may only be seen after subtracting the

TABLE 1.1: Confirmed galaxies associated with $z \gtrsim 2$ intervening DLAs and sub-DLAs.

Quasar Name	$z_{\rm QSO}$	$z_{\rm abs}$	$\log N$(H I)	θ (arcsec)	$b_{\rm p}$ (kpc)	Spectroscopic Confirmation
Q2233+131	3.298	3.150	20.00	2.51	18.52	Djorgovski et al. (1996)
Q2206-1958	2.559	1.920	20.65	0.99	8.09	Møller et al. (2002)
PKS 0458-02	2.286	2.040	21.65	0.31	2.44	Möller et al. (2004)
Q2222-0946	2.926	2.354	20.65	0.80	6.67	Fynbo et al. (2010)
J0918+1636	3.086	2.583	20.96	1.98	16.20	Fynbo et al. (2011)
J0918+1636	3.086	2.412	21.26	< 0.25	< 2.0	Fynbo et al. (2013)
J1135-0010	2.888	2.207	22.10	0.1	0.9	Noterdaeme et al. (2012a)
J0338-0005	3.068	2.220	21.05	0.49	4.12	Krogager et al. (2012)
J0310+0055	3.782	3.115	20.05	3.80	28.0	Kashikawa et al. (2014)
J1110+0244	4.117	2.119	–	2.02	16.6	Bouché et al. (2012)
J1255+0305	2.530	2.114	–	1.68	14.1	Bouché et al. (2012)
HE 2243-6031	3.01	2.329	20.62	3.1	26	Bouché et al. (2012)

quasar PSF. Spectroscopy is preferred, although several slit positions may be necessary to detect the galaxy. Observing programs that target DLA galaxies were plagued by non-detections (e.g., Bunker et al. 1999; Kulkarni et al. 2006; Lowenthal et al. 1995; Prochaska et al. 2002), which were not always published. Recent selection criteria have been more successful.

At low redshift, where surface brightness dimming is less of a problem and galaxies are generally easier to detect, confirming the presence of a DLA is challenging. The atmospheric UV cut-off at 3000Å makes it impossible to observe the Lyman-series transitions from the ground for $z < 1.65$ absorbers. Measuring the H I column density for an absorber therefore requires spectra from a space-based instrument, such as HST/COS. Fortunately, Mg II absorption identified in ground-based quasar spectra can indicate a low-z DLA, especially when $W_0^{\lambda 2796} > 0.6$Å, thus making it possible to efficiently construct samples of UV DLAs (Rao & Turnshek 2000; Rao et al. 1995, 2006; Turnshek et al. 2014). Rao et al. (2011) obtained ground-based imaging for a sample of 80 absorbers at $0.1 \lesssim z \lesssim 1$ confirmed from HST spectra, including 27 DLAs, determined photometric redshifts for the field galaxies, and studied the absorbing galaxy properties. The surface density of galaxies falls off exponentially with increasing distance from the quasar line-of-sight, such that galaxies beyond an impact parameter of 100 kpc are statistically unrelated to the absorption system. The impact parameter decreases with increasing H I column density. DLA galaxies were found at a median distance of 17.4 kpc, a factor of two closer than sub-DLA galaxies, with a median luminosity of $0.33L^*$.

Bouché et al. (2007) likewise relied on the relationship between Mg II absorption and DLA systems to detect Hα emission from $z \sim 1$ DLA galaxies at impact parameters $0.25'' - 6.7''$ (2 – 54 kpc) with the VLT/SINFONI near-IR integral field spectrograph.

Their success rate was 67% (14/21 targets). A series of VLT/SINFONI studies investigated the properties of predominantly $z \sim 1$ DLA and sub-DLA galaxies (Péroux et al. 2013, 2011a,b, 2012, 2014). Overall the galaxies appeared to be rotation supported with inclined disc morphologies. The authors also measured neutral and ionized-phase metallicities and observed mildly negative or flat metallicity gradients, indicating evidence of outflows. Integral field units (IFUs) afforded a breakthrough for DLA galaxy detections, since the instruments simultaneously perform imaging and spectroscopy.

Despite the challenge of detecting faint galaxies at small impact parameters, observers have confirmed a handful of high-redshift DLA galaxies, with greater success in recent years. Table 1.1 summarizes published detections of $z \gtrsim 2$ DLA galaxies and their inferred properties. Taking advantage of the VLT/X-shooter spectrograph, Fynbo et al. (2010) developed a strategy to efficiently observe quasars with known DLAs at three different position angles, 60°, 0°, and -60° East of North, and predicted that only 10% of the galaxy counterparts would fall outside the slits. This technique has so far detected four DLA galaxies, ranging from $0.1 \pm 0.01''$ to $2 \pm 0.1''$ (0.9 to 16 kpc) from the quasar lines-of-sight (Fynbo et al. 2010, 2011; Krogager et al. 2012; Noterdaeme et al. 2012a). Indeed, the impact parameter for $z \gtrsim 2$ DLA galaxies appears to decrease with increasing H I column density (Krogager et al. 2012).

High-redshift absorber galaxies have also been the target of IFU observations. Following their $z \sim 1$ study, Bouché et al. (2012) targeted Hα emission from 18 $z \sim 2$ strong Mg II absorbers ($W_0^{\lambda 2796} > 2$ Å) with the VLT/SINFONI IFU. They detected only three new DLA galaxies, despite surveying an area of $10'' \times 10''$ (80 kpc × 80 kpc) around each quasar line-of-sight to a 5σ flux limit of $\sim 1.8 \times 10^{-17}$ erg s^{-1}cm^{-2}. While their SINFONI observing program focused mainly on $z \sim 1$ absorber galaxies, Péroux et al. (2011a) measured upper limits on the Hα flux for two $z > 2$ DLAs, and Péroux et al. (2013, 2012) included the $z = 2.354$ DLA toward Q2222-0946 (discussed below) in their investigation of ionized-phase metallicities and gas kinematics. Absorber galaxies at $z > 2$ remain more difficult to detect than their $z \sim 1$ counterparts.

The $z = 2.354$ DLA toward Q2222-0946 highlights how a variety of observations (ground-based, space-based, spectroscopy, imaging, and IFU) can compliment each other and create a nearly complete portrait of the associated galaxy.

$z_{\rm abs} = 2.354$ toward Q2222-0946

As part of a strategy to identify galaxies associated with high-metallicity DLAs using the VLT/X-shooter spectrograph, Fynbo et al. (2010) detected Lyα, Hα, and [O III] $\lambda\lambda$4959, 5007 emission at an impact parameter of $\sim 0.8''$ (6 kpc) from the $z = 2.354$ DLA toward

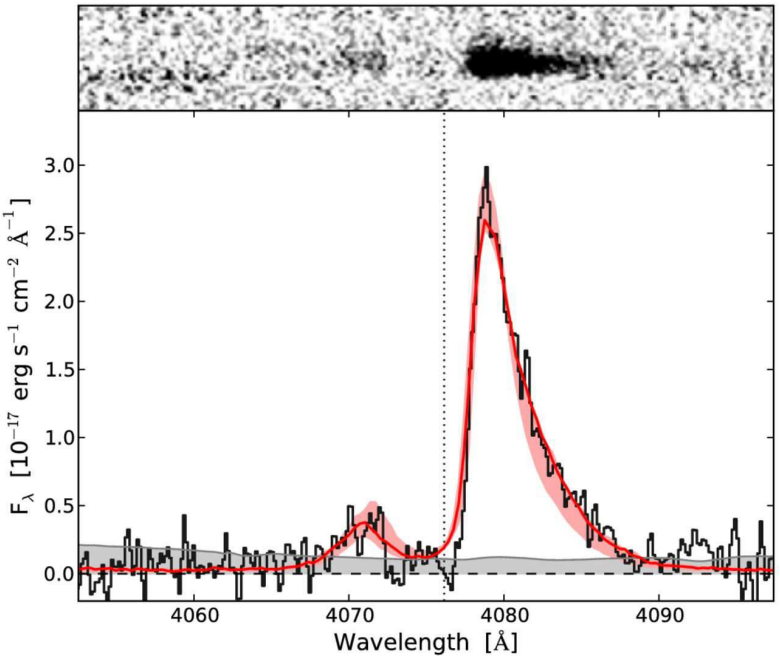

FIGURE 1.21: The Lyα emission line extracted from the Q2222-0946 DLA trough in the Krogager et al. (2013) X-shooter spectrum (S/N $\sim$ 100). The top panel shows the observed 2D spectrum and the bottom panel below shows the extracted 1D spectrum and 1σ uncertainty (grey shaded area). The dotted vertical line marks the systemic line center. The Lyα emission peak exhibits a common asymmetric profile, with a strongly absorbed blue wing. The best-fit model of the emission profile is plotted in red, along with the 68 percent confidence interval (red shaded area). (Figure from Krogager et al. (2013).)

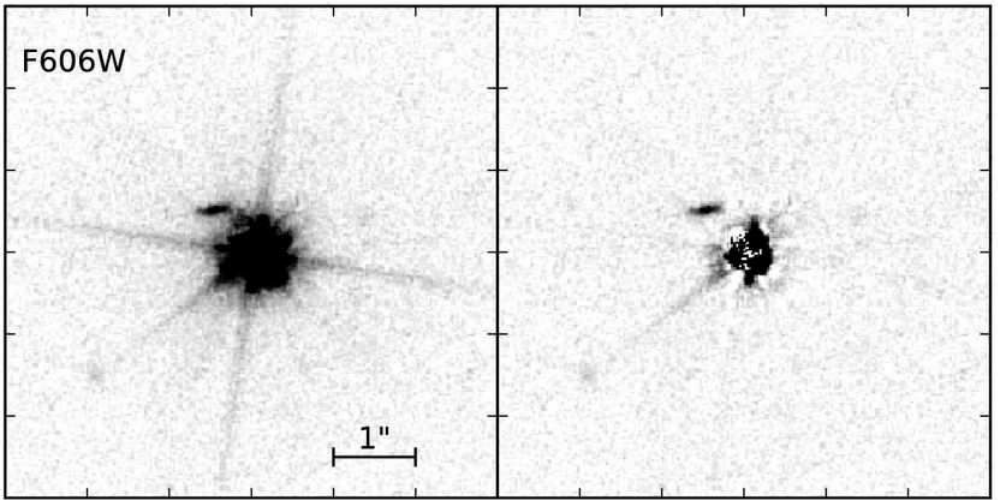

FIGURE 1.22: The data image (left) and PSF-subtracted residual (right) from GALFIT in the HST/F606W image of Q2222-0946. The image alignment is north up and east left. The galaxy causing the absorption is clearly visible even before PSF subtraction. (Figure from Krogager et al. (2013).)

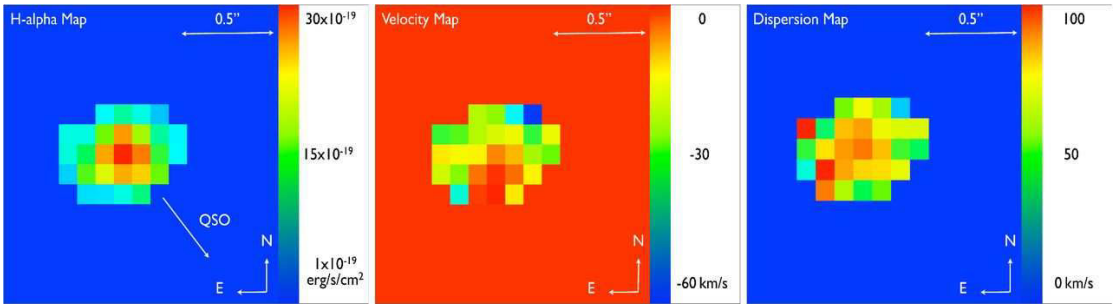

FIGURE 1.23: Left to right: Hα flux map, Hα velocity field, and Hα velocity dispersion maps from VLT/SINFONI observations of the DLA galaxy towards Q2222-0946 at $z$abs = 2.3543. Given the clear absence of a gradient, the velocity map suggests a dispersion-dominated system. In fact, the PSF dominates the dispersion at the center of the object. (Figure from Péroux et al. (2013).)

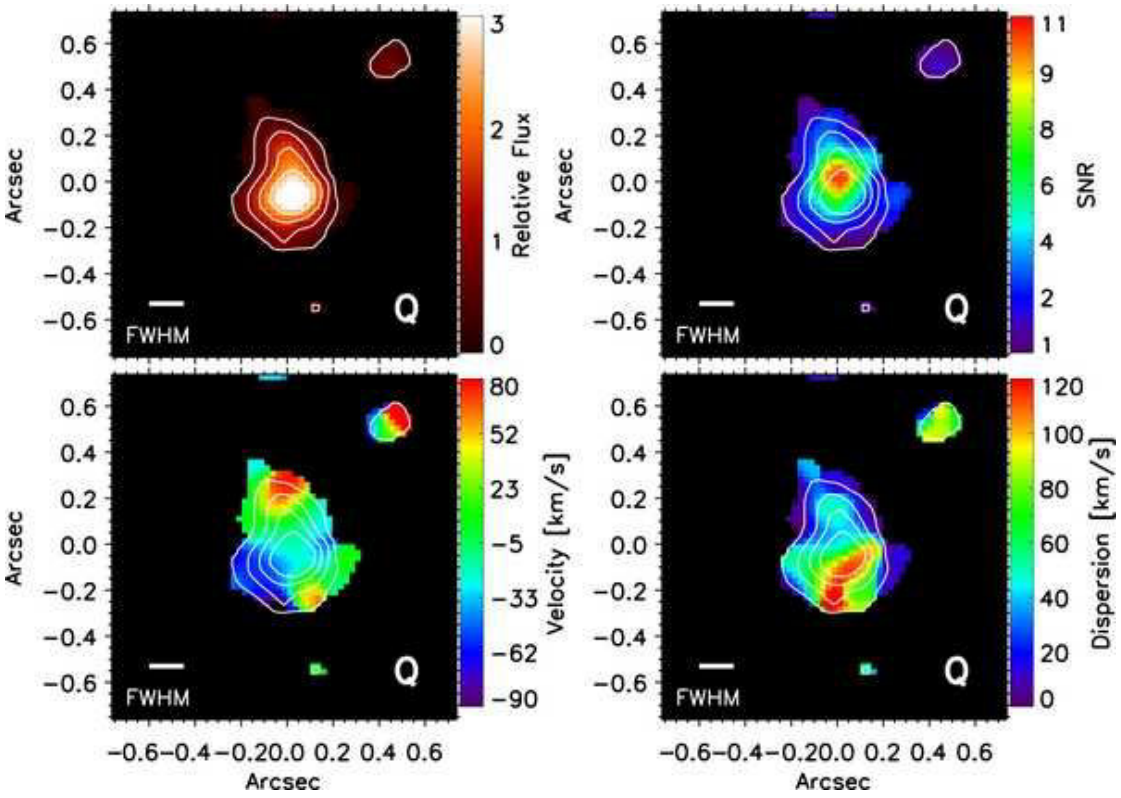

FIGURE 1.24: Hα intensity (top left), velocity (bottom left), velocity dispersion (bottom right), and S/N (top right) maps based on Keck/OSIRIS observations of the Q2222-0946 DLA galaxy with laser guide star adaptive optics. The maps are orientated with north up and east to the left. The velocity is relative to $z = 2.35391$, the best-fit redshift determined from a composite spectrum. Individual spaxels are 0.025 arcsec^2. The FWHM $\simeq 0.15''$ of the PSF after smoothing is shown in the lower left corner of the intensity map. At the redshift of the DLA $1''$ corresponds to $\sim$8.3 kpc. The quasar, indicated by a "Q," is located in the lower right-hand corner at approximately $x = 0''.5$ and $y = -0''.6$. (Figure from Jorgenson & Wolfe (2014).)

SDSS J222256.11-094636.2 (known as Q2222-0946; Herbert-Fort et al. 2006; Prochaska et al. 2007). By analyzing the low-ionization metal transitions, they measured a metallicity for the DLA gas of [Zn/H] $= -0.46 \pm 0.07$ and found evidence of significant dust depletion, consistent with previous results. The kinematical information indicates that the quasar line-of-sight is nearly parallel with the galaxy rotation axis (perpendicular to the galactic plane). The asymmetrical Lyα emission line profile (Figure 1.21) suggests that outflowing gas, perhaps due to a galactic wind, absorbs the blue side. Péroux et al. (2012) mapped the Hα emission from this DLA galaxy with VLT/SINFONI observations and estimated a SFR $= 17.1 \pm 6.0$ M$_\odot$ yr^{-1}, in agreement with the Fynbo et al. (2010) limit of SFR > 10 M$_\odot$ yr^{-1}. By comparing the metallicity of the neutral gas detected in absorption and the ionized gas seen in emission, the authors noted a potentially flat metallicity gradient.

Krogager et al. (2013) obtained HST/WFC3 imaging and additional deep (∼11 hrs) VLT/X-shooter spectroscopy of the Q2222-0946 DLA galaxy, with which they detected Lyα, Hα, Hβ, [O II] $\lambda\lambda$3726, 3729, [O III] $\lambda\lambda$4959, 5007, and [N II] λ6583. From the emission line ratios[1] R_{23} and N2, which are independent metallicity indicators, they measured [O/H] $= -0.30 \pm 0.13$ for the ionized gas. The revised neutral gas metallicity is [S/H] $= -0.49 \pm 0.05$, and this remains one of the most metal-rich $z \sim 2$ DLAs. Finding highly enriched neutral gas 6 kpc from the galaxy with a metallicity similar to that of the ionized gas is possible evidence of an outflow.

The Krogager et al. (2013) HST imaging revealed a compact (∼1 kpc), elongated, disc-like galaxy (Figure 1.22). Péroux et al. (2013) also re-observed Q2222-0946 with VLT/SINFONI at higher spatial resolution and from Hα velocity dispersion maps found that the DLA galaxy is dispersion dominated (Figure 1.23). Using laser guide star adaptive optics, Jorgenson & Wolfe (2014) mapped the Hα and [O III] flux and velocity fields with the Keck/OSIRIS IFU (Figure 1.24). The emitting regions have a roughly circular morphology that appear to conflict with the disc interpretation. The velocity dispersion is consistent with Péroux et al. (2013) and does not support a rotating disc scenario. Despite lingering questions about its morphology, the Q2222-0946 DLA galaxy showcases how much can be learned from a detailed study of absorber galaxies.

A DLA Arising from Infalling Gas

Bouché et al. (2013) concentrated follow-up VLT/SINFONI observations with adaptive optics on their DLA galaxy with the highest SFR and a large central velocity dispersion,

[1] R_{23} = ([O II] $\lambda\lambda$3726, 3729 + [O III] λ4959 + [O III] λ5007)/Hβ (Pagel et al. 1979) and N2 = [N II] λ6583/Hα (Denicoló et al. 2002; Pettini & Pagel 2004)

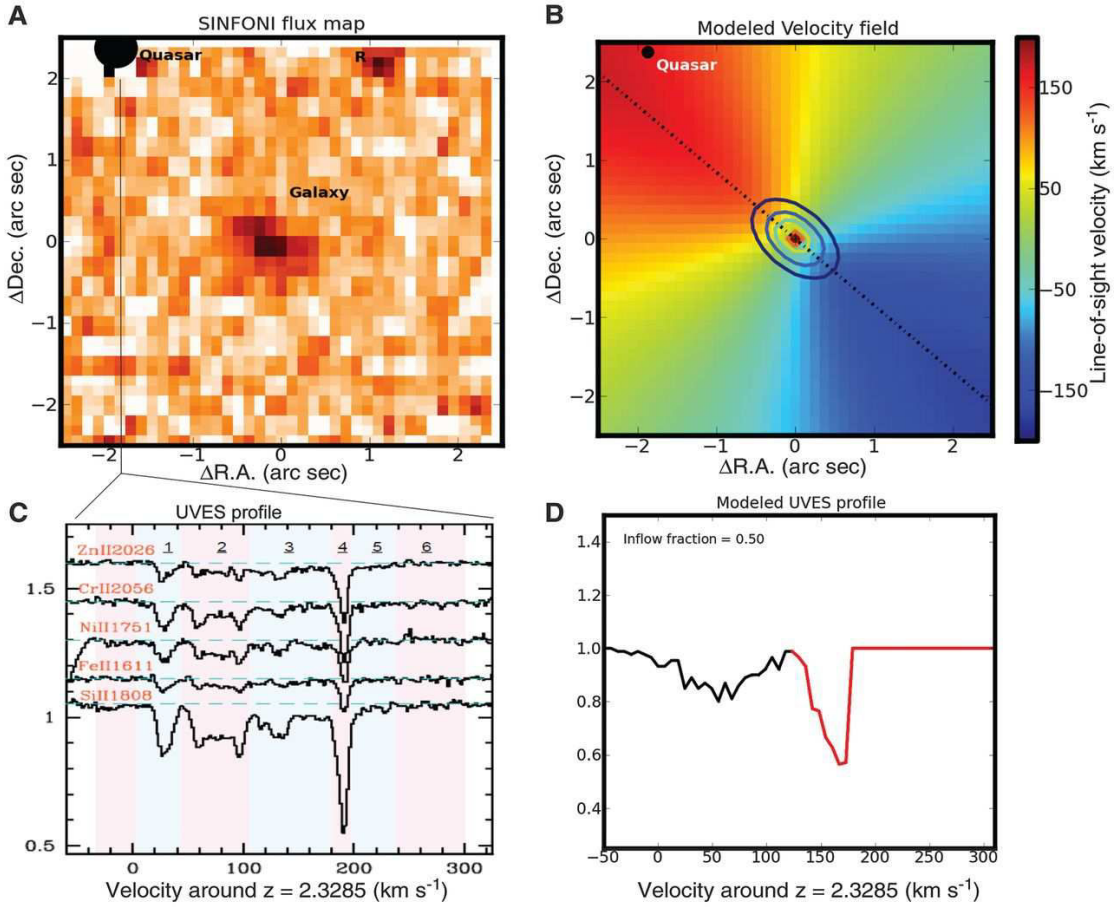

FIGURE 1.25: Emission and Absorption Kinematics. (a) The color scale represents a narrow band image (rest-frame Hα) with the continuum subtracted from the AO-assisted VLT/SINFONI datacube. The quasar HE2243-60 and the host $z \sim 2.328$ galaxy are marked. The residuals from the continuum subtraction are visible both near the QSO and near the position labeled R. The galaxy is detected in Hα with a maximum S/N of $\sim 5-8$ per pixel; no continuum emission is detected. The beam has a full-width-at-half-maximum (FWHM) of $0.25''$. (b) The fitted velocity field (extrapolated over the entire field) is shown along with the flux contours. The kinematic parameters were determined using our 3D analysis. The dotted line shows the kinematic major axis. At the quasar location (solid circle), the rotation speed is expected to be 160 to 180 km s^{-1}. (c) The absorption profiles from the VLT/UVES spectra showing the line-of-sight velocity of the various absorption components in the low-ionization ion (Zn II, Cr II, N III, Fe II, and Si II) where v = 0 km s^{-1} corresponds to the galaxy redshift. The main component (component 4) contains half of the Si II column density and appears to contain more dust. This component has a line-of-sight velocity $v = 180$ km s^{-1} consistent with that of the galaxy velocity field shown in (a). (d) A simulated line-of-sight profile for the geometry of this QSO-galaxy pair from a toy model that includes an inflow component (black) in addition to a component determined from the extended galaxy velocity field (red). (Figure from Bouché et al. (2013).)

located 3.1″ (26 kpc) from the HE 2243-6031 line-of-sight (discovered by the Hamburg/ESO QSO Survey; Reimers & Wisotzki 1997). With the enhanced IFU data, they detected all of the major nebular emission lines, [O II], [O III]+Hβ, and [N II]+Hα, and measured a metallicity for the DLA galaxy [O/H] = -0.35 ± 0.1 dex relative to solar. Lopez et al. (2002) had previously studied the HE 2243-6031 DLA in detail with a cloud-by-cloud analysis of the low-ionization ions detected in their VLT/UVES spectrum and observed no relative abundance gradient across the components, indicating that the clouds evolved under homogeneous physical conditions. From their measurements of [Zn/Cr] = -0.01 ± 0.05 and [S/Si]= -0.06 ± 0.03, these authors concluded that the DLA system harbors very little dust. Bouché et al. (2013) combined archival VLT/UVES spectra from three observing programs to obtain S/N of ∼110 near the Lyα, Zn II, and Cr II absorption lines. They measured N(HI) = $10^{20.62\pm0.05}$ cm^{-2}, consistent with the earlier value of $10^{20.67\pm0.02}$ cm^{-2}, and [Zn/H] = -0.72 ± 0.05, which is somewhat higher than the initial [Zn/H] = -1.10 ± 0.05 from Lopez et al. (2002). Nonetheless, since the gas detected in absorption has a metallicity that is ∼0.5 dex lower than that of the DLA galaxy detected in emission, it is unlikely that the quasar line-of-sight probes an outflow. The low-ionisation ions trace seven kinematically distinct components, which appear to be accreating and co-rotating with the DLA galaxy. The metallicity and kinematic properties are consistent with a model of recycled gas inflowing into the DLA galaxy (Figure 1.25).

Using a Higher-z LLS as a Blocking Filter

O'Meara et al. (2006) introduced a strategy to search for DLA galaxies without the glare of the background quasar by targeting lines-of-sight that have both a DLA and a higher-redshift optically thick absorber. If the DLA is located blueward of the Lyman limit from the higher-z system, then the LLS acts as a blocking filter, absorbing the quasar emission (Figure 1.26). With this technique, DLA galaxies at small impact parameters can be observed down to the sensitivity limits of the imaging data without any quasar contamination. From Magellan/MagIC imaging, the authors identified candidate galaxies for the $z = 2.033$ and $z = 1.690$ absorbers at distances of at 2.1″ (12.4 kpc) and 2.8″ (16.4 kpc) from the PKS 2000-3300 and SDSS J0322-0558 lines-of-sight, with a second potential source for the $z = 2.033$ DLA at 4.7″ (27.5 kpc).

Similarly, with VLT/FORS1, Christensen et al. (2009) imaged the fields toward two quasars that have strong Mg II absorptions detected in the spectra, suggesting that the lines-of-sight pass close to foreground galaxies at $z = 1.87$ and $z = 1.98$. In these lines-of-sight, the Lyman limit from higher-redshift DLAs fully absorbs the quasar flux at the location of the anticipated galaxies. However, no galaxies were detected within 5″

(∼40 kpc) of either line-of-sight to a point source limit of $U_{\rm AB} \sim 28.0$, which corresponds to SFR $= 0.6 M_{\odot}$ yr^{-1} at $z = 2$. The non-detections suggest that the Mg II absorbers are associated with low-metallicity, low-luminosity galaxies.

Implementing this technique on a larger scale, Fumagalli et al. (2014) imaged twenty quasar fields that have DLAs at $1.9 \lesssim z \lesssim 3.8$ with HST/WFC3 and twelve more from the ground with KECK/LRIS and LBT/LBC. They also obtained additional spectra with KECK/ESI and Magellan/MagE for twenty of the quasars to measure column densities and metallicities. A science analysis that uses this sample to investigate the connection between neutral gas, DLA galaxies, and star-formation rates is forthcoming.

When multiple galaxies are detected, the rule of thumb is to associate the closest candidate with the DLA. However, deep imaging searches may detect interlopers, in addition to - or instead of - the DLA galaxy. Fumagalli et al. (2010) explored statistical approaches to evaluating the most likely DLA galaxy, including a Bayesian approach that takes into account multiple candidates. Among galaxies with an 80% probability of being associated with the DLA, the procedure correctly identified spectroscopically confirmed DLAs ∼60% of the time and favored an interloper in ∼15% of the trials. While confirming candidate DLA galaxies is still only possible through follow-up spectroscopy, a Bayesian analysis may be helpful for allocating telescope time when multiple close candidates appear in the field.

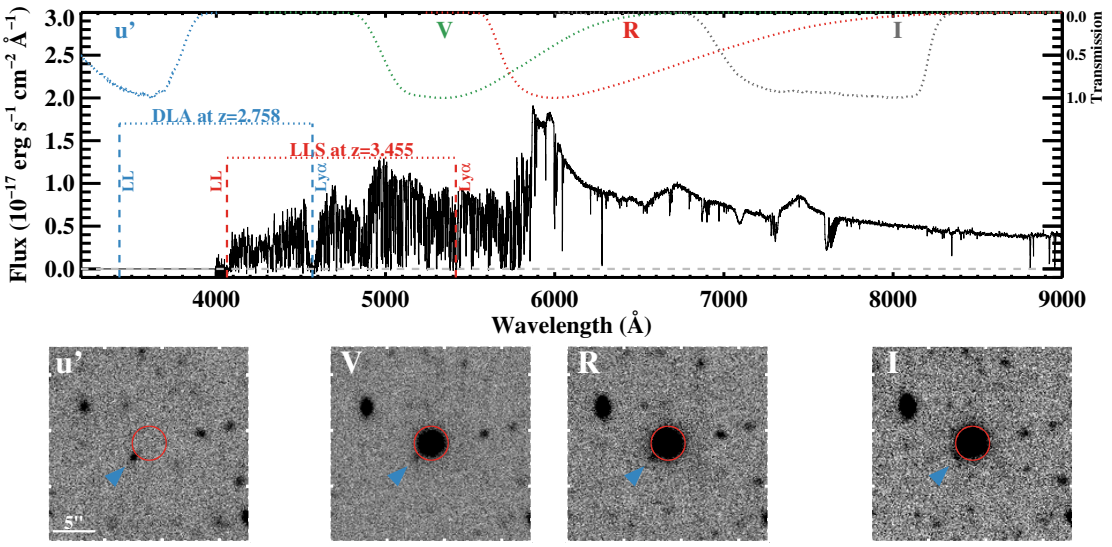

FIGURE 1.26: Top: Keck/ESI spectrum of the quasar J094927+111518 with mirrored transmission curves of the u', V, R, and I filters of LRIS at Keck superimposed. The corresponding y-axis of the transmission curves is on the top right. The Lyα transition and the Lyman limit of the targeted DLA and the LLS that acts as a blocking filter are also marked. Bottom: Keck/LRIS images of a $20'' \times 20''$ region centered at the quasar position in these four filters. Emission from the quasar dominates the inner $\sim 2''$(circles) in the red filters, but is completely absorbed in the u' band because of the intervening LLS. This allows for the detection of faint galaxies at all impact parameters, including objects that are aligned or in close proximity to the quasar line-of-sight (arrows). (Figure from Fumagalli et al. (2014).)

1.4 Thesis Work

My interest is in using absorption lines to probe quasar host galaxies and their environments. My thesis work addresses the following questions:

- What can strong DLAs at the quasar redshift reveal about the gaseous environments of bright AGN?
- How does ionization from the central AGN affect the host galaxy?
- What feedback mechanisms can be identified by probing gas in the host galaxy halo?
- What can we learn from overdense regions observed along pairs of sight lines?

Chapter 2 will give an overview of the SDSS-III BOSS survey. The following chapters will describe several techniques used to tackle the above problems:

Chapter 3 Thanks to the SDSS-III BOSS survey focused on high-redshift quasars, I was able to identify a complete sample of strong DLAs that occur at the redshift of

the quasar ($z_{\rm abs} \simeq z_{\rm em}$), such that the Ly$\alpha$ absorption trough completely absorbs the broad Lyα emission peak from the quasar. In some cases, a narrow Lyα emission peak can be detected in the DLA trough. I investigate whether there are intrinsic differences in the absorbers that reveal narrow Lyα emission and those that do not. Lines-of-sight that intersect dense, compact clouds in the host galaxy could explain associated DLA that reveal the strongest narrow Lyα emission, whereas neighboring galaxies may be the source of associated DLAs with less emission detected in their troughs.

Chapter 4 I evaluated the number of pairs in SDSS-III BOSS DR9 where the line-of-sight from a higher redshift background quasar passes through the galactic environment of a lower redshift foreground quasar, creating a strong absorption in the background quasar spectrum at the redshift of the foreground quasar. For three pairs with physical (angular) separations of 33 kpc (3.96″), 50 kpc (6.06″), and 90 kpc (10.74″), I proposed follow-up observations with the VLT/X-shooter spectrograph. Analyzing the kinematics and abundances for these DLA systems indicates large-scale gas motions in the immediate host galaxy environment, but relatively low ionization, with very little C IV detected in absorption. These lines of sight probe the host galaxy environment and investigate evidence of feedback mechanisms in the host galaxy environment.

Chapter 5 Lines-of-sight with small angular separations are likewise useful for identifying overdense regions that trace large-scale structure. Coincident absorptions in the lines-of-sight toward one of the quasar pairs observed with X-shooter span over 2 000 km s^{-1}, which corresponds to a proper distance of 6.4 h_{70}^{-1} Mpc at $z = 2.69$. I characterize the absorptions in common across the two lines-of-sight separated by 90 kpc. Two of the three main regions are concentrations of low-metallicity gas, whereas the third is a sub-DLA likely associated with a galaxy. Based on the metallicity, velocity differences, and weak probability of observing such an overdensity by chance, the lines-of-sight appear to pass along the length of a cosmic web filament.

Chapter 2

SDSS-III Baryon Oscillation Spectroscopic Survey

2.1 Survey Goals

A legacy project of the Sloan Digital Sky Survey (SDSS, York et al. 2000), the Baryon Oscillation Spectroscopic Survey (BOSS, Dawson et al. 2013) continued the SDSS tradition of investigating the underlying structure of the universe through observations of galaxies and quasars. As its name implies, the primary goal of BOSS was to measure the characteristic scale of baryon acoustic oscillations (BAOs) that arise from small variations in the density of the primordial universe. An overdensity of photons at points that had a slightly higher matter density created a sound wave driven by radiation pressure. Highly-ionized baryons were tightly coupled to the photons and traveled outward from their initial location with the sound wave. When photons decoupled during recombination, the baryons that were traveling with the acoustic oscillation remained at the final position of the sound wave. As gravity again became the dominant force, the baryon overdensity at this position skewed the dark matter distribution. When measuring the power spectrum of the baryon distribution, a peak should be seen at the typical scales corresponding to the sound waves. BOSS used these scales as standard rulers.

Eisenstein et al. (2005) first detected a BAO peak at the 100 h^{-1} Mpc (comoving) scale in the correlation function of $z \simeq 0.35$ luminous red galaxies from the SDSS-I (Figure 2.1). The original spectroscopic sample included 46 748 galaxies in the range $0.16 < z < 0.47$. The shape of the galaxy correlation function provides a constraint on the matter density that is independent of the measurement from the CMB anisotropies. Furthermore, when measured from the three-dimensional clustering of matter tracers at redshift z, the transverse BAO scale constrains the angular diameter distance $d_A(z)$,

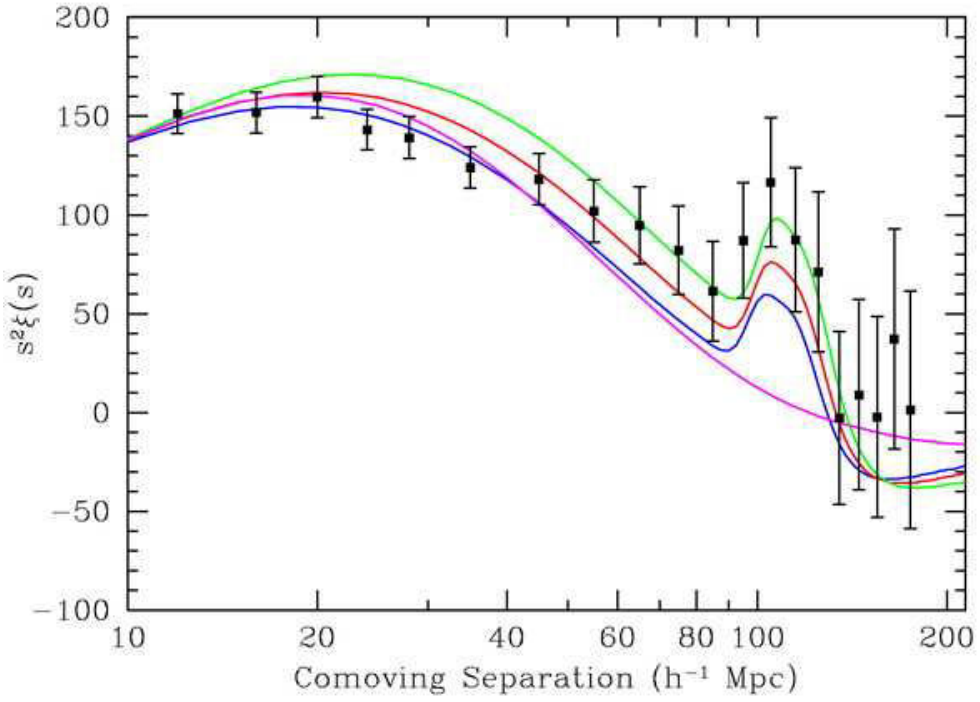

FIGURE 2.1: Large-scale redshift-space correlation function ($\xi(s)$) of the SDSS-I LRG sample multiplied by the square of the separation (s), so as to flatten out the result. The BAO peak is detected near 100 h^{-1} Mpc. The models are $\Omega_m h^2 = 0.12$ (green line), 0.13 (red line), and 0.14 (blue line), all with $\Omega_b h^2 = 0.024$. Varying $\Omega_m h^2$ alters the amount of large-to-small scale correlation, but boosting the large-scale correlations too much causes an inconsistency at 30 h^{-1} Mpc. The pure CDM model ($\Omega_m h^2 = 0.105$, magenta line) is actually close to the best fit due to the data points on intermediate scales. (Figure from Eisenstein et al. (2005).)

and the line-of-sight scale constrains the Hubble parameter $H(z)$ (Figure 2.2). Using the Hubble parameter and the comoving angular diameter distance evaluated at $z = 0.35$ with the LRG sample and at $z = 1089$ from WMAP results, Eisenstein et al. (2005) constructed a distance ratio for two extremely different redshifts. This distance ratio provided an argument for dark energy, based on a geometric comparison. The detection of BAOs in the galaxy correlation function laid the foundation for the SDSS-III BOSS project, which will expand the potential for the BAO measurement.

Over the course of five years, from Fall 2009 to Summer 2014, SDSS-III BOSS mapped the spatial distribution of luminous red galaxies and high-redshift quasars (Dawson et al. 2013; Eisenstein et al. 2011). The collaboration planned to obtain spectra of 1.5 million luminous galaxies extending to $z = 0.7$ and 160 000 quasars primarily in the range $2.15 \leq z \leq 3.5$. With this data, the goal was to measure the location of the BAO peak at low redshift from the galaxy correlation function and at high redshift from correlated absorptions in the Lyα forest. Since the Lyα forest absorptions indicate the amount of hydrogen along the quasar line-of-sight, the three-dimensional correlation function of the transmitted flux can reveal the underlying dark matter distribution. If

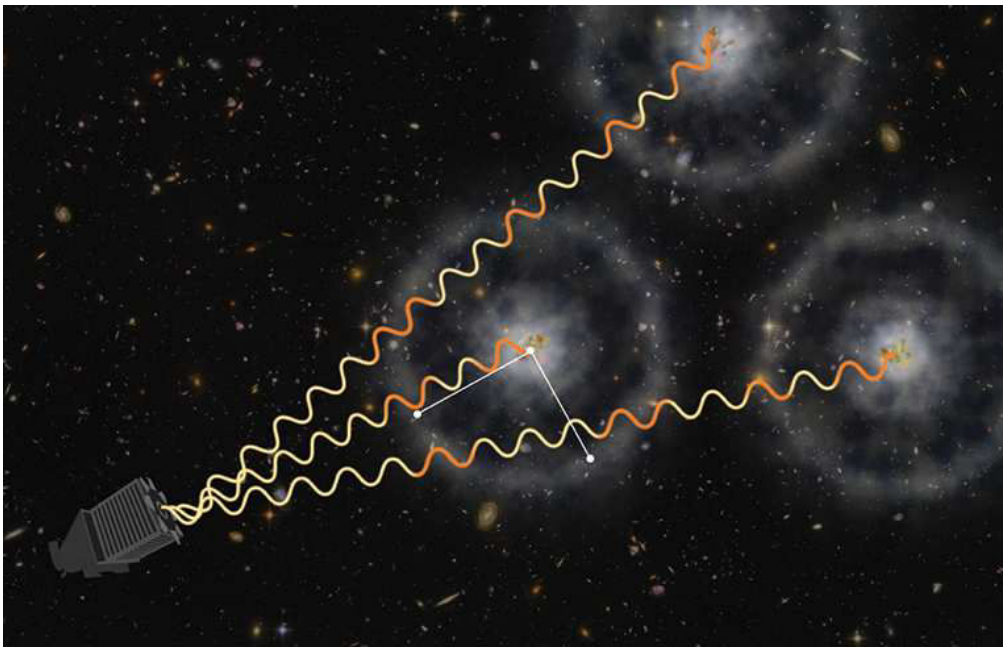

FIGURE 2.2: The BAO scale, illustrated here as a ring of gas, is imprinted in the distribution of the IGM. Quasar lines-of-sight (wavey orange lines representing the emitted light) probe the gas distribution. The BAO scale along the quasar line-of-sight constrains the Hubble parameter $H(z)$, and the transverse scale constrains the angular diameter distance $d_A(z)$. (Figure from www.sdss3.org, courtesy of Zosia Rostomian and Andreu Font-Ribera from Lawrence Berkeley National Laboratory.)

the sample of background quasars is sufficiently large and sufficiently dense, a peak in the distribution due to BAOs may be detected (McDonald & Eisenstein 2007). By measuring the BAO scale from many quasar and galaxy spectra at multiple epochs, BOSS intended to determine the distance scale and Hubble expansion rate at the one-percent level.

Obtaining a surface density of 15 quasars at $z \geq 2.15$ per square degree with $g_{PSF} < 22.0$ was crucial for adequately measuring the correlation function from transmitted flux in the Lyα forest. Although the surface density of $z \geq 2.15$ quasars to the BOSS magnitude limit is approximately 28 per square degree, (Palanque-Delabrouille et al. 2013a), correctly selecting targets was challenging. In *ugriz* color space, the quasar locus overlaps with the stellar locus in the range $2.2 < z < 3.5$ (e.g., Ross et al. 2012). A uniform sample was not necessary for the Lyα forest BAO analysis, since quasars are probes of the IGM and do not affect its large-scale distribution; however, statistical studies related to the quasars themselves, like measuring the quasar luminosity function or clustering analyses, do require a uniform sample. BOSS therefore incorporated multiple target selection strategies optimized to produce (primarily) CORE and BONUS samples. Additional samples, including previously known quasars, radio-loud quasars, and ancillary programs made up ∼6% of targets. The CORE sample is uniform, whereas the BONUS sample was designed to maximize the spectroscopic quasar density. Initially, the CORE sample was targeted from a likelihood method (Kirkpatrick et al. 2011), which used the

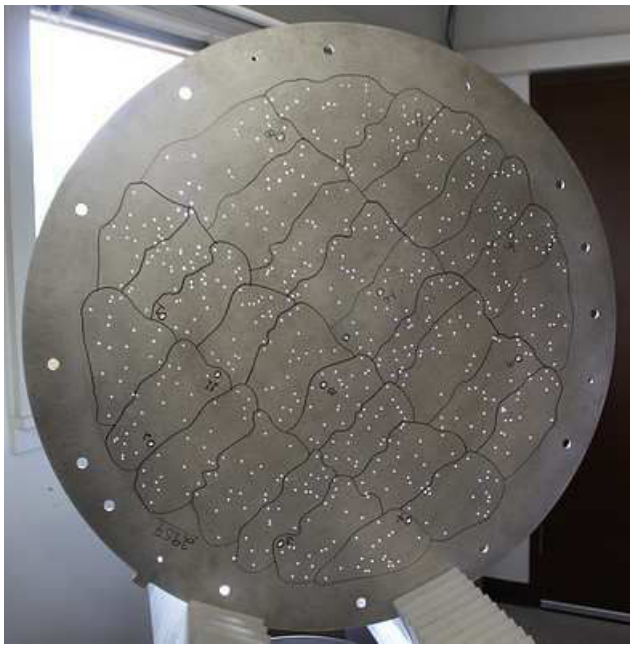

FIGURE 2.3: An example of a BOSS plate drilled and waiting to be observed. The aluminum plates are $^1/_8$ in. thick with a 32 in. diameter. (Figure from www.sdss3.org.)

photometry and models for the stellar and quasar locus to determine the likelihood that each object is a quasar. After the first year of operations, an extreme deconvolution method (Bovy et al. 2011) that incorporates photometric uncertainties into a density estimation of stars and quasars took over the CORE sample targeting. The BONUS sample was based also on the likelihood and extreme deconvolution methods, as well as kernel density estimator (Richards et al. 2009) and neural network (Yèche et al. 2010) techniques. The target selection strategy for the first two years of BOSS is presented in Ross et al. (2012).

The full SDSS-III collaboration included over 330 people with groups from France, Germany, Spain, and Brazil contributing to the projects. The French Participation Group, of which I am a member, focused on the quasar component of the BOSS project and was particularly invested in target selection, visual inspection, quasar catalogs, and the Lyα forest analysis.

2.2 Telescope and Spectrograph

The 2.5 m SDSS-III telescope and 1,000-fiber BOSS twin spectrographs are located at Apache Point Observatory in New Mexico, where the median seeing is $0.9''$. Aluminum plates with a 3° diameter were drilled with the position of target galaxies, stars, quasars, or blank sky areas to a accuracy of 9 μm (Figure 2.3). About 10% of holes on a plate were dedicated to sky calibration. In preparation for observing, plates were mounted

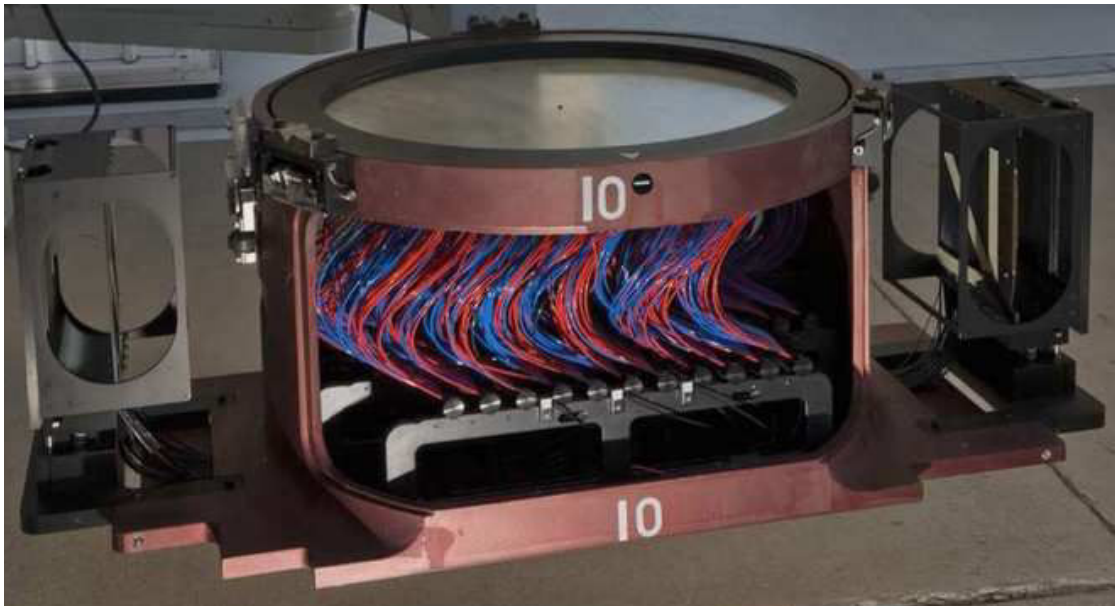

FIGURE 2.4: In preparation for observing, each plate is loaded into a cartridge and 1,000 optical fibers are plugged into the target holes. The fibers are routed in bundles to the slit-heads (the two boxes standing upright on either side of the cartridge) that interface with the twin spectrographs. (Figure from Smee et al. (2013).)



FIGURE 2.5: The cartridge is brought to the 2.5 m SDSS telescope and installed on the focal plane. (Figure from www.sdss3.org.)

on interchangeable cartridges that attach to the telescope, and the spectroscopic fibers, which have a 2″ diameter, were plugged by hand (Figure 2.4). The observing time for one BOSS plate was about an hour under excellent conditions, which included three fifteen minute science exposures, calibration observations, and the time required to swap one plate cartridge for another on the back of the telescope. On exceptional nights, up to nine plates could be observed. However, under typical conditions, usually four to six science exposures were required to obtain sufficient S/N per pixel at a fiducial magnitude, and the observing time per plate was longer. More than 2,000 unique plates were observed over the course of the survey.

The spectra have a wavelength range of 3600 Å to 10 000 Å, and the spectral resolution varies from ∼1500 – 3000, such that the instrument velocity dispersion is consistently ∼150 km s^{-1}. The two BOSS spectrographs each received 500 fibers, which were treated identically, regardless of which spectrograph they fed. To achieve a consistent spectral resolution across the entire wavelength range, a beamsplitter in each spectrograph sent incident light to two CCDs optimized separately for the red and blue ends of the spectrum. The blue CCD covered ∼3600 – 6350 Å, while the red CCD detected light at ∼5650 – 10 000 Å. The two ends of the spectrum then had to be reconciled by calibrating the flux at the overlapping wavelengths. Smee et al. (2013) fully characterize the two double spectrographs.

2.3 Data Processing and Quasar Redshift Estimation

Each BOSS spectrum has a unique identifier based on the PLATE, MJD, and FIBERID. The PLATE number specifies the plate drilled for a particular target. Since the same plate may have been plugged and observed on multiple occasions, with different mappings between fibers and target holes, MJD indicates the modified Julian date for a unique fiber configuration. Additionally, the spectroscopic pipeline (Bolton et al. 2012) numbered each fiber arriving at the slit-head with the sequential index FIBERID, 1 to 500 for one side and 501 to 1000 for the other. During the spectroscopic data reduction process, all good data from a unique plugging were co-added together.

In order to classify the targeted objects, the BOSS pipeline fit each spectrum with a library of stellar templates, a PCA decomposition of galaxy spectra, and a PCA decomposition of quasar spectra. A range of redshifts was tested for each class of templates: $z = -0.004$ to 0.004 ($\pm$1200 km s^{-1}) for stars, $z = -0.01$ to 1.00 for galaxies, and $z = 0.0033$ to 7.00 for quasars. The pipeline gave a spectral classification and redshift measurement based on the template and redshift combination that produced the lowest

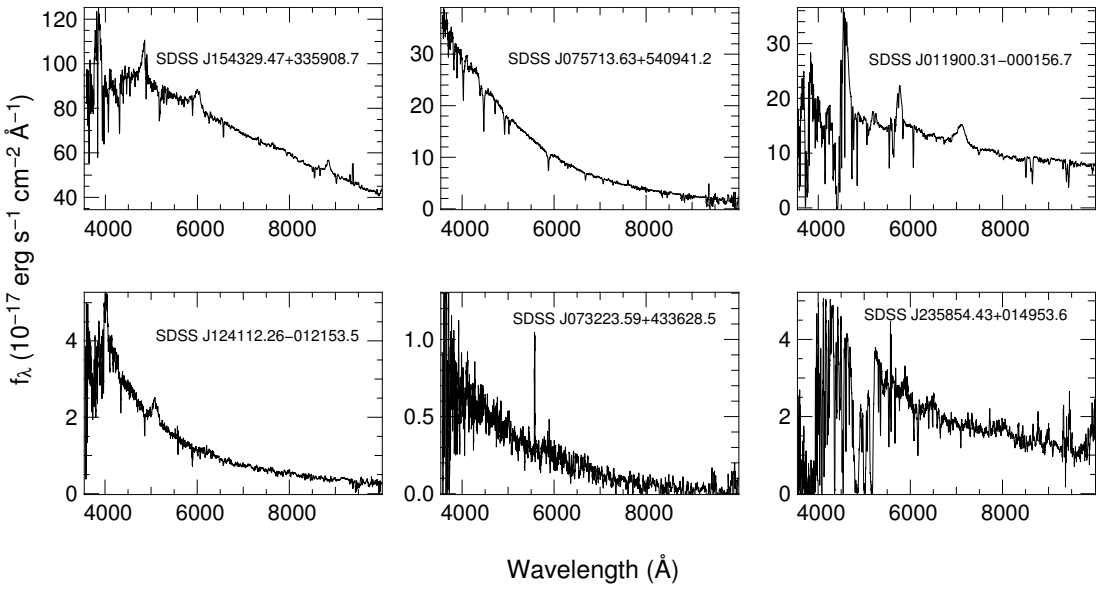

FIGURE 2.6: First column: examples of $z > 2$ quasars that the BOSS pipeline classified as stars. The overall shape of the spectrum is similar to the spectrum of F stars. Second column: examples of stars that the BOSS pipeline identified as quasars. Strong absorption lines or wiggles in the spectrum can mimic quasar features. Third column: examples of $z > 2$ quasars for which the BOSS pipeline provided an inaccurate redshift estimate that was corrected during the visual inspection. The strong absorption lines confused the pipeline. The spectra were boxcar median smoothed over 5 pixels. (Figure from Pâris et al. (2012).)

reduced chi-squared. A warning flag (ZWARNING) indicates problems with the spectrum or the template fit, including poor wavelength coverage, negative star template fits, broken or dropped fibers, fibers assigned to measure sky background, and fits that are within $\Delta\chi^2/\text{d.o.f.} = 0.01$ of the next best fit. The most common cause for a ZWARNING flag is the reduced chi-squared threshold. If ZWARNING = 0, the pipeline determined a classification and redshift with no apparent problems (Bolton et al. 2012).

After the pipeline evaluation, all spectra from targeted quasars were visually inspected. Although the pipeline identifications were very good, about 12% of all quasar targets had a non-zero ZWARNING flag. Visual inspection reduced this number to 4% and helped recover spectra useful for the BOSS Lyα forest analysis. Figure 2.6 gives examples of the types of corrections made during the visual inspection, which is fully described in (Pâris et al. 2012). The pipeline occasionally mixed-up quasar and star classifications, particularly for spectra that had low S/N and could be fitted equally well with either template. Visual inspection also corrected redshift estimates based on misidentified emission lines. The most common pipeline error for quasar redshift identification was mistaking Mg II λ 2800 for Lyα. In some spectra, strong absorption features, such as a DLA or intrinsic broad absorption lines, cut into the profile of an emission line and made it difficult for the pipeline to identify. Spectra with these features were flagged during the visual inspection.

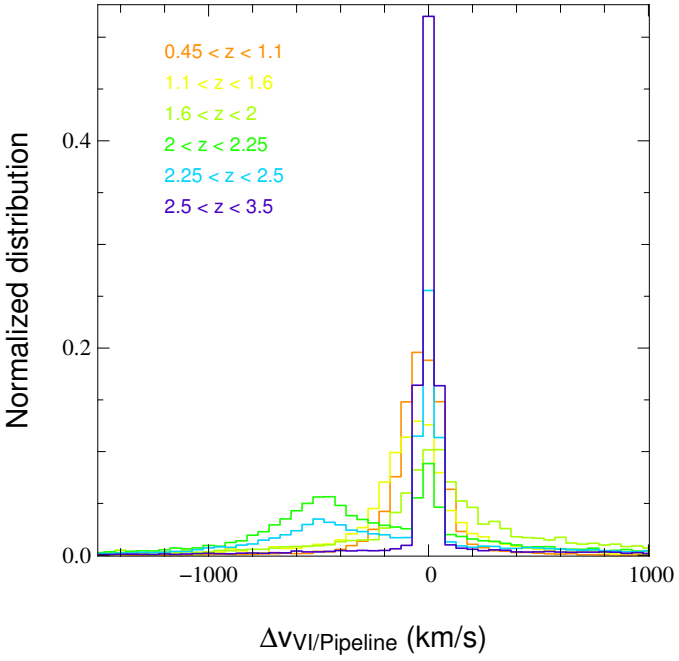

FIGURE 2.7: Normalized (to unit integral) distribution of the velocity difference between the pipeline and visual inspection redshift estimates for different redshift bins. About half of the pipeline redshifts were corrected during the visual inspection. Most of the corrections were for quasars with $2 < z < 2.5$, where the pipeline redshift estimate did not correspond to the peak of the Mg II emission line. (Figure from Pâris et al. (2012).)

Figure 2.7 shows the distribution of velocity differences between redshifts estimated from visual inspection and the pipeline. Most redshift corrections were minor, and the difference between the pipeline and visual inspection redshifts was larger than 0.1 for only ∼2% of quasars. At $z \leq 2$, the pipeline estimate did not require significant adjustments. About half of the redshifts in the range $2.0 < z < 2.3$ were modified to correct offsets from the Mg II emission line, which is considered the most robust redshift indicator of the broad emission lines (e.g., Hewett & Wild 2010). At $z \geq 2.3$, 10% of the redshifts were corrected. By fixing misidentifications and adjusting redshifts, the visual inspection resulted in a net gain of high-redshift quasars, at the level of $\sim 1 - 3$ objects per 7 square degree plate.

The visual inspection redshifts are not accurate to better than $\Delta z \sim 0.003$, but they served as a reliable initial guess for an automatic redshift determination based on principal component analysis (PCA). A linear combination of four principal components was fitted to each spectrum to determine the quasar redshift. The components reproduced the quasar spectrum between 1410 and 2900 Å in the rest frame, which covers most of the prominent emission lines, including C IV, the C III] complex, and Mg II. Well-known systematic shifts between emission lines (e.g., Hewett & Wild 2010) are intrinsically imprinted in the components, and the PCA method takes into account variations from

quasar to quasar (e.g., Pâris et al. 2011). The pipeline, visual inspection, and PCA redshifts are all included in the BOSS quasar catalogs (Pâris et al. 2012, 2014, see Section 2.5 for details).

2.4 Data Releases

SDSS-III maintained the tradition of almost yearly public data releases, which are always cumulative. Three other surveys, in addition to BOSS, were part of SDSS-III. Their goals were to understand the structure and evolution of the Milky Way through optical and infrared spectroscopy of stars in the Galactic bulge, bar, disk, and halo (SEGUE-2 and APOGEE), and to search for gas giant extrasolar planets with orbital periods that range from several hours to two years (MARVELS). SDSS-III data releases include products from these surveys, as well as from BOSS. Data access tools are linked from the SDSS website[1].

The first SDSS-III data release, which was the eighth overall, (DR8; Aihara et al. 2011a) was made public in January 2011. DR8 included new five-band imaging data of over 2500 deg^2 across the Southern Galactic Cap and stellar spectra from the SEGUE-2 project, in addition to all the data from SDSS-I and II (Abazajian et al. 2009). BOSS used the DR8 imaging data to select spectroscopic targets.

Data Release 9 (DR9; Ahn et al. 2012) became public on 31 July 2012 and included all survey-quality data from BOSS gathered through July 2011: ∼102,000 new quasar spectra, ∼91,000 new stellar spectra, and ∼536,000 new galaxy spectra. The effective area of the DR9 spectroscopic footprint is 3275 deg^2 (Figure 2.8, top). DR9 also corrected problems with astrometry identified in DR8 (Aihara et al. 2011b) and updated the SEGUE-2 stellar properties.

The most recent public data release, DR10 (Ahn et al. 2014), occurred on 31 July 2013 and added over 670,000 new BOSS spectra of galaxies and quasars. DR10 also presented the first results from the APOGEE project, including more than 57,000 high-resolution, high S/N infrared spectra of stars in the Milky Way. The DR10 BOSS spectroscopic footprint is 6373.2 deg^2 (Figure 2.8, center).

The SDSS-III project will produce two more public data releases, DR11 and DR12, which will both be released in 2014 December. DR11 includes BOSS data taken through the summer of 2013 over an effective area of 8377 deg^2 (Figure 2.8, bottom). DR11 was an internal release, since a separate public release would have occurred only six months prior to that of DR12. Instead, the DR11 version of the data will be made public at the

[1] http://www.sdss.org/data/

same time as DR12. The final data through Summer 2014 from all observations with BOSS, SEGUE-2, APOGEE, and MARVELS will be presented in DR12.

2.5 Value-Added Catalogs

In addition to the survey data, SDSS also produces value-added catalogs that contribute to the science analysis. The SDSS website lists value-added catalogs from the different projects for each data release[2]. Of particular interest for the BOSS Lyα forest analysis are the DR9 and DR10 quasar catalogs (Pâris et al. 2012, 2014), and the DR9 DLA catalog (Noterdaeme et al. 2012b). Both the quasar and DLA catalogs will be updated for DR12.

The DR9 quasar catalog contains 87 822 quasars, almost 90% of which were new discoveries. Within this sample, 61 931 quasars are at $z > 2.15$. The DR10 catalog added 74 454 new discoveries since DR9 and totals 166 583 quasars. As of DR10, BOSS had observed 117 668 quasars at $z > 2.15$, more than five times greater than what was known prior to BOSS. Figure 2.9 shows that the statistics continued to grow, particularly at $z > 2.15$. BOSS also inadvertently increased the number of known quasars at $z \sim 0.8$ as a consequence of degeneracies in the SDSS color space used to select spectroscopic targets. The $z \sim 0.8$ quasars were targeted as $z > 2.15$ quasars, but turned out to be a lower redshift. Nonetheless, the average surface density for quasars at $z > 2.15$ in DR10 is 16.3 per square degree, which exceeds the minimum surface density requirement for the Lyα forest BAO analysis of 15 per square degree.

The quasar catalogs give the coordinates and the PLATE-MJD-FIBERID identifier created when each target was observed. They also contain the magnitudes measured from five-band (u, g, r, i, z) CCD-based photometry, a morphology flag, and information about the target selection method. Redshift estimates from the pipeline, visual inspection process, and PCA procedure (discussed in Section 2.3) are all included, along with their errors where appropriate. The quasar catalogs consider that the PCA redshift is definitive. Redshifts and FWHMs measured during the PCA procedure are also provided for the C IV, C III], and Mg II emission lines. The overall S/N for the spectrum is given, along with the S/N in particular wavelength windows. The catalogs also present X-ray, ultraviolet, near-infrared, and radio emission properties of the quasars matched from other large-area surveys, when available.

Additionally, BAL quasars were identified both from visual inspection and from automatic detection of C IV BALs. The visual inspection flag was based primarily on C IV

[2] https://www.sdss3.org/dr10/data_access/vac.php

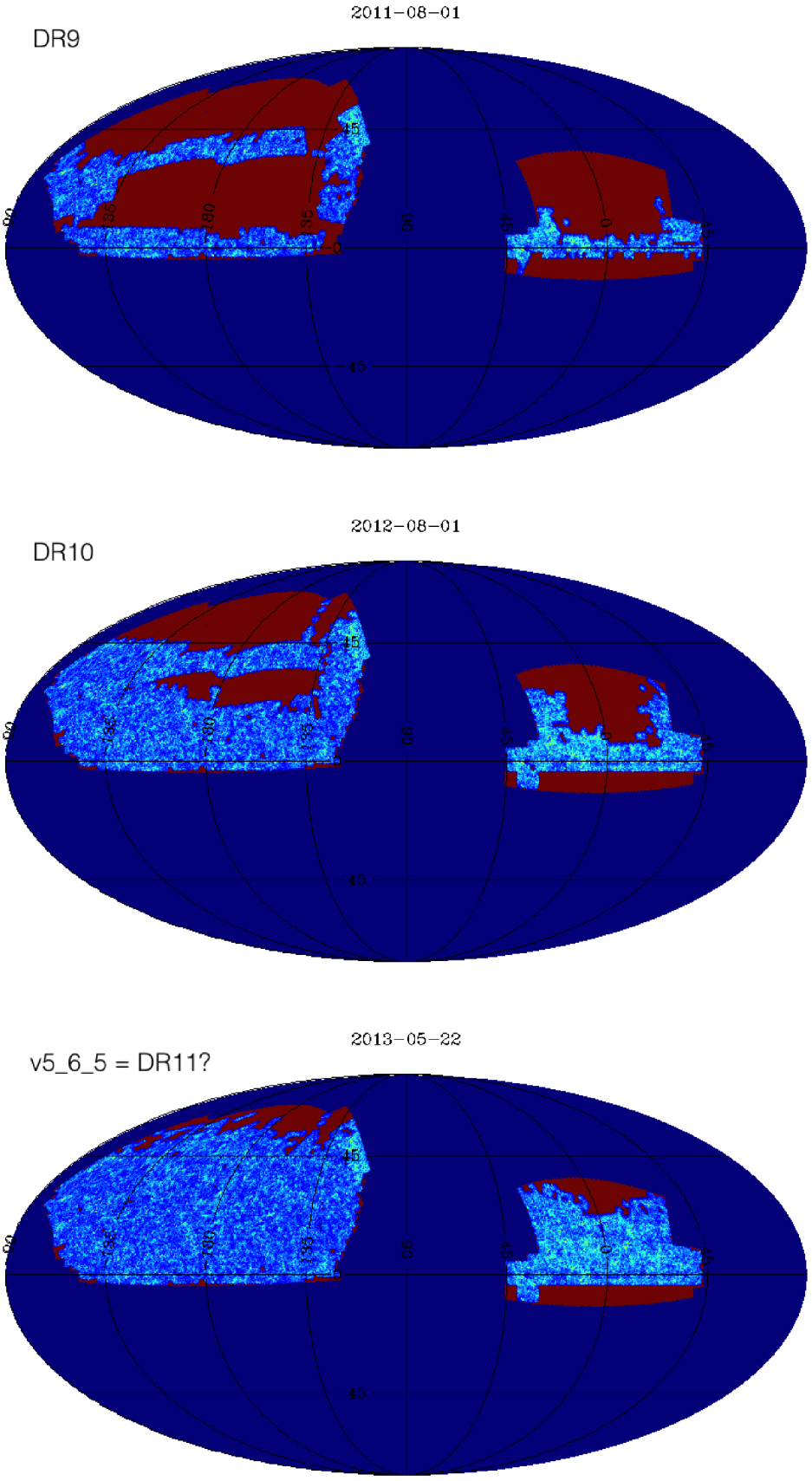

FIGURE 2.8: Mollweide projections of the targeted BOSS survey area (red) with completed regions in light blue showing the progress for DR9, DR10, and DR11. Note that $\alpha = 0^\circ$ is offset to the right. (Figure courtesy of S. Bailey.)

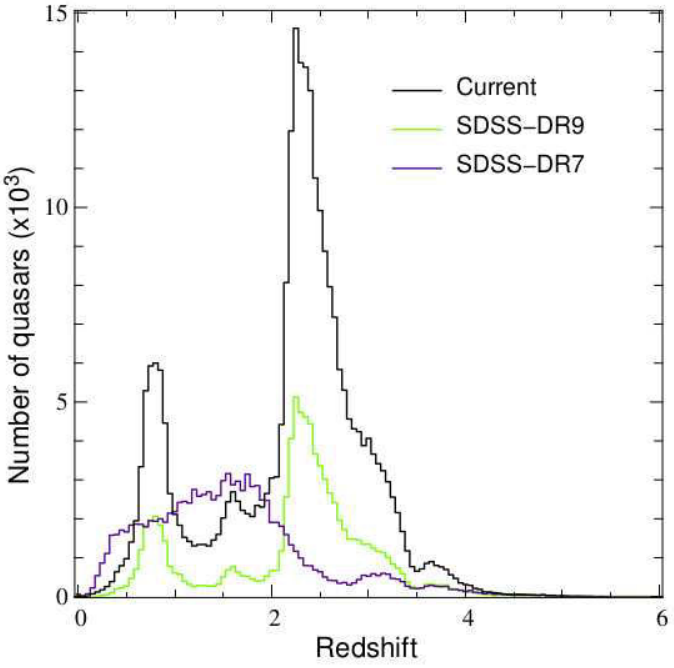

FIGURE 2.9: Redshift distribution for the quasars observed as of Winter 2013 (black histogram), SDSS-DR9 (green histogram; Pâris et al. 2012) and SDSS-DR7 (purple histogram; Schneider et al. 2010) over the redshift range $0 < z < 6$. The BOSS survey has substantially increased the number of observed high-redshift quasars. The secondary peaks in the BOSS redshift distributions around $z \sim 0.8$ and $z \sim 1.6$ are due to known degeneracies in the SDSS color space used for selecting targets. (Figure courtesy of I. Pâris.)

BALs, but also Mg II BALs. There is no a priori limit on the strength of the absorption, since the visual inspection process does not measure the BAL trough. Instead, several indices that characterize BALs, the balnicity index (BI; Weymann et al. 1991), the detection index (DI; Pâris et al. 2012), and the absorption index (AI; Hall et al. 2002), were calculated for each quasar in the catalog with $z > 1.57$ to measure the strength of the C IV BALs. This quasar redshift limit includes the Si IV emission line in the spectra, thereby ensuring that C IV BALs could be measured across the full range of velocities for the balnicity index, up to 25 000 km s^{-1}. Figure 2.10 shows examples of C IV BALs with a variety of BI values.

Based on comparing indices measured from BAL quasars flagged during visual inspection with other catalogs of BAL quasars (Allen et al. 2011; Trump et al. 2006), the DR9 sample appears to be pure at the 95% level, but is likely incomplete below BI $\sim$ 500 km s^{-1}. The BI measurements are robust for lines-of-sight with S/N > 5 and BI > 500 km s^{-1}. In the choice between visual inspection and automatic detection, the tradeoff is that visual inspection conservatively flag only easily apparent BALs, while automatic detection depends on the continuum placement. Visual inspection has fewer false positives, but is less complete. The DR10 catalog includes 16 461 BAL quasars flagged during visual inspection (7 533 in DR9).

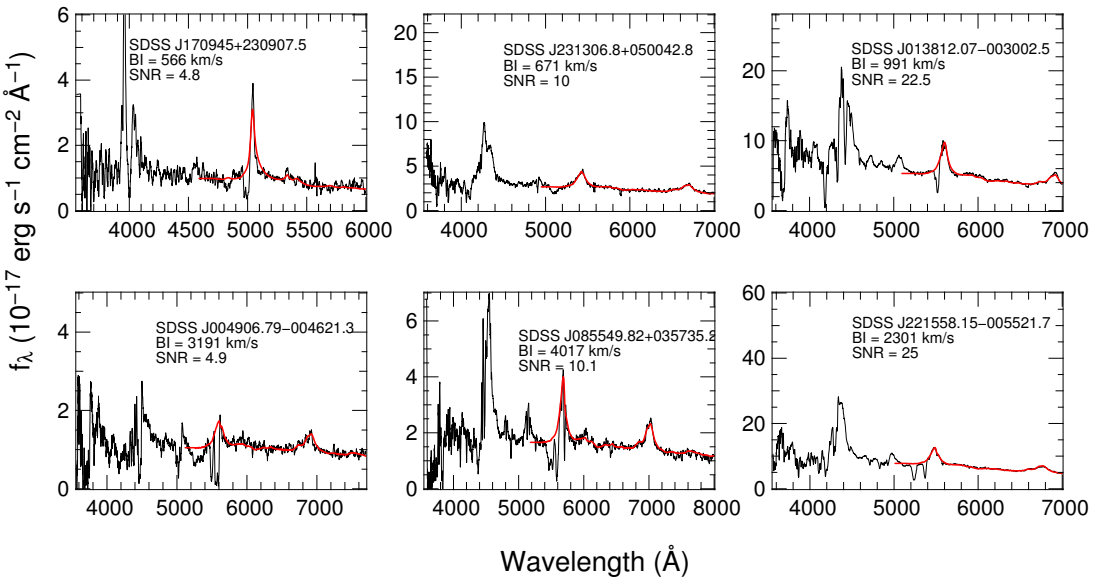

FIGURE 2.10: Examples of high-redshift quasar spectra with C IV BALs across a range of S/N and BI values. The fit to the continuum redwards of the Si IV emission peak is overplotted in red. (Figure from Pâris et al. (2012).)

Approximately 10% of high-redshift quasars have BAL features (Allen et al. 2011). These absorptions are intrinsic to the quasar and do not reflect the structure of the IGM. The BAO Lyα forest analysis must therefore avoid BALs, either by excluding the quasar line-of-sight or masking the BAL region. The same is true for DLAs, which arise when the quasar line-of-sight passes near an intervening galaxy. The BAL measurements in the quasar catalogs are valuable for the BOSS survey, as is the DLA catalog.

Noterdaeme et al. (2012b) implemented a fully automatic search along the DR9Q lines-of-sight to detect strong absorption systems and compiled the DR9 DLA catalog from DLAs and sub-DLAs with $\log N(\mathrm{H\,I}) \geq 20.0$. It contains 12 081 systems with $\log N(\mathrm{H\,I}) \geq 20.0$, 6 839 of which have $\log N(\mathrm{H\,I}) \geq 20.3$, and is available through the CDS[3]. After rejecting lines-of-sight that have BALs with balnicity index BI > 1000 km s^{-1}, the automatic procedure identified DLAs by correlating the Lyα forest portion of the quasar spectrum with synthetic profiles of increasing H I column density. DLA candidates, each with a column density and redshift, were determined from the strength of the Spearman's rank correlation coefficient. To improve the DLA redshift estimate, the quasar spectrum redwards of the Lyα emission line was cross-correlated with a mask representing metal absorption lines. Lastly, a Voigt profile fit to the DLA measured $N(\mathrm{H\,I})$. The DLA catalog thus provides a column density and redshift for each DLA, as well as the equivalent widths (or limits on the equivalent widths) of associated metal lines redwards of the Lyα emission line.

[3] http://cdsarc.u-strasbg.fr/viz-bin/qcat?J/A+A/547/L1
See also http://www2.iap.fr/users/noterdae/DLA/DLA.html

2.6 Quasar and Absorption System Science

The unprecedented number of quasar spectra observed for SDSS-III BOSS has made possible a variety of studies about quasars and the absorbing gas along their lines-of-sight. Notably, Ross et al. (2013) measured the quasar luminosity function from the uniform (CORE) sample of DR9 quasars. Members of the collaboration have identified unusual populations in the BOSS data, including high-redshift Type II quasars (Alexandroff et al. 2013) and reddened quasars (Glikman et al. 2012, 2013; Ross et al. 2014). Among the BAL quasars, Hall et al. (2013) discovered strong redshifted absorption troughs, and Filiz Ak et al. (2012) identified quasars that transition from BAL to non-BAL on timescales of several years. Noterdaeme et al. (2012b) evaluated the $N(\mathrm{H\,I})$ distribution at $z = 2.5$ using a statistical sample of $\log N(\mathrm{H\,I}) \geq 20.0$ absorption systems in the DR9 DLA catalog, and Noterdaeme et al. (2014) explored the properties of the strongest ($\log N(\mathrm{H\,I}) \geq 21.7$) DLAs. By selecting DLAs that occur at the quasar redshift and block the broad quasar the Lyα emission peak, Finley et al. (2013) detected narrow Lyα emission in several DLA troughs (Chapter 3).

By calculating the cross-correlation of DLAs with the Lyα forest transmitted flux fraction, Font-Ribera et al. (2012) determined the bias factor of DLAs at a mean redshift of $z = 2.3$. The bias factor, which is measured from the amplitude of the cross-correlation, constrains the host halo mass distribution; higher values imply that most DLAs are associated with massive halos. The cross-correlation revealed excess Lyα absorption around DLAs on scales up to 40 h^{-1} Mpc, consistent with linear theory predictions that halos hosting DLAs will grow via large-scale gravitational mass inflow. The bias factor implies that the majority of DLAs at $z \sim 2-3$ arise in atomic gas surrounding typical galaxies in dark matter halos with masses $\sim 10^{12}$ $\mathrm{M}_{\odot}$, much larger than expected from hydrodynamical simulations of galaxy formation. If metal abundances could be estimated for the DLAs (a challenge due to saturated metal absorption lines and the low S/N in BOSS data), this technique could constrain the halo mass - metallicity relation.

In another approach to probing the characteristics of gas distributed around high-redshift galaxies, Pieri et al. (2014) constructed composite spectra of Lyα forest absorbers in the redshift range $2.4 < z < 3.1$. The normalized Lyα forest flux was evaluated in bins 138 km s^{-1} wide (close to the BOSS resolution), and absorbers were divided into five samples with transmitted flux fractions, F, in the range $-0.05 \leq F \leq 0.45$. Note that when $F = 1$ no absorption is detected. Individual absorbers were shifted to the rest frame and stacked with both a median and an arithmetic mean procedure (details in Pieri et al. 2010). A comparison with high-resolution spectra indicated that 60% of absorbers in the three lowest transmitted flux samples would probe CGM regions (300 kpc proper transverse distance, $\Delta v \leq 300$ km s^{-1} line-of-sight separation) if noise in the spectra did

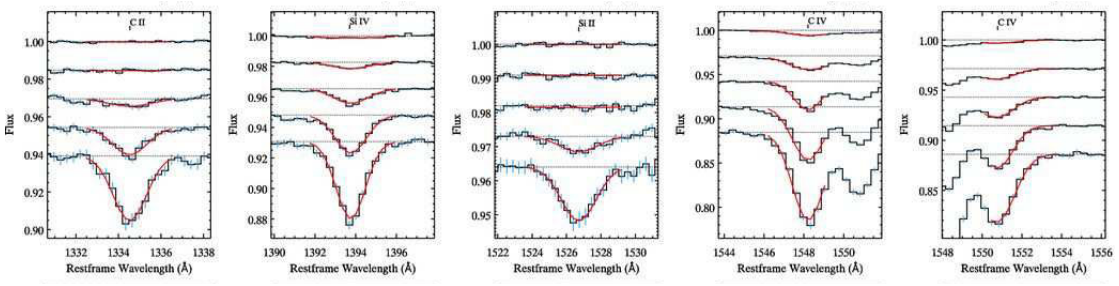

FIGURE 2.11: Metal absorption line profiles (with error bars shown in blue) and fits (shown in red) for C II, Si IV, Si II, and C IV in the median composite spectra. In each panel, the top profile corresponds to the sample with Lyα forest transmitted flux fractions $0.35 \leq F < 0.45$, and composite spectra from increasingly strong Lyα absorbers are offset downwards. Horizontal dashed lines indicate $F = 1$. (Figure from Pieri et al. (2014).)

not decrease the sample purity. Ionization models showed that the high-ionization metal absorptions in the composite spectra from all samples (Figure 2.11) have a metallicity of approximately [X/H] $= -2$ and are consistent with physical conditions associated with the IGM. Low-ionization lines are detected in the three samples more closely related to the CGM. Reproducing these lines in the ionization models required much higher densities and metallicities, which when combined with the column density measurement imply that the CGM absorbers have typical sizes $\sim$30 kpc and [X/H] $= -0.4$.

Using stacked spectra of background quasars, Zhu et al. (2014) measured the Mg II rest equivalent width as a function of impact parameter, $W_0^{\mathrm{Mg\,II}}(r_p)$, from foreground luminous red galaxies (LRGs) at $\langle z \rangle \sim 0.52$ and obtained values for 30 kpc $< r_p <$ 18 Mpc. The authors then calculated the spatial cross-correlation between the position of the LRGs and $W_0^{\mathrm{Mg\,II}}(r_p)$. The galaxy - gas correlation function changes slope on scales of $\sim$1 Mpc, consistent with the expected transition from the dark matter halo of a galaxy to an environment where halo - halo correlations have the most influence on the clustering (Figure 2.12). This transition is also reflected in the velocity dispersion of the Mg II gas clouds, estimated from line widths, as a function of impact parameter, indicating that the clouds are gravitationally bound to their host halos. The standard halo model appears to provide an accurate description of the Mg II gas distribution across distances that span three orders of magnitude.

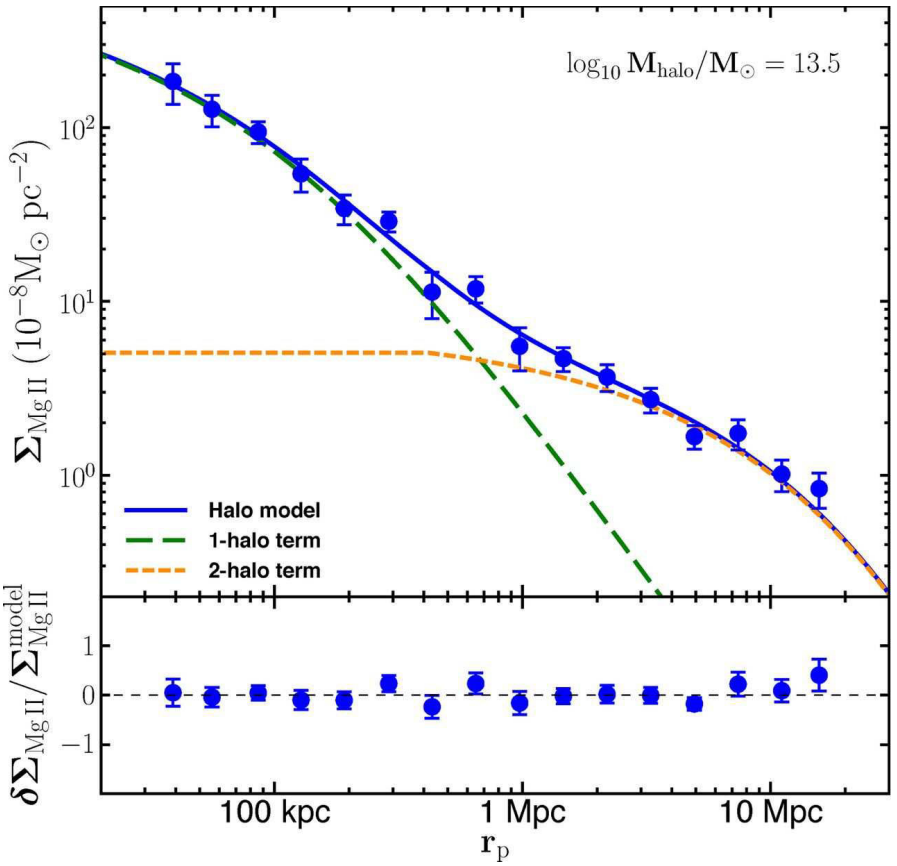

FIGURE 2.12: The galaxy - gas correlation with the best fitting halo model. The upper panel shows the best fitting halo model, decomposed into one-halo and two-halo terms. The lower panel shows the fractional residuals. The halo model has three parameters: the average LRG host halo mass $M_{\rm halo}$, the Mg II gas-to-mass ratio in the host halo $f^{\rm 1h}_{\rm Mg\,II}$, and the mean Mg II gas-to-mass ratio from all galaxies $f^{2h}_{\rm Mg\,II}$. (Figure from Zhu et al. (2014).)

2.7 Survey Results

Mapping correlations in the distribution of matter in the IGM at $z \sim 2.5$ is a new technique for studying the BAO scale and constraining cosmological parameters. Results based on preliminary samples appear promising and have already contributed important insights.

From the first year of data, Slosar et al. (2011) investigated the three-dimensional structure in the Lyα forest for over $14,000$ $z > 2.1$ quasars and measured correlations in the transmitted flux out to comoving separations of 60 h^{-1} Mpc. The analysis agreed with theoretical predictions about IGM structure that suggest it arises from the gravitational instability of primordial density fluctuations (Bi & Davidsen 1997; Cen et al. 1994; Hernquist et al. 1996; Miralda-Escudé et al. 1996; Zhang et al. 1995). The shape of the correlation function also followed predictions of a standard ΛCDM cosmological model. The good agreement with theoretical expectations reinforced the potential for using the Lyα forest as a tool to map the high-redshift universe, measure its expansion via BAOs, and thereby constrain the origin of cosmic acceleration.

A peak in the 3D correlation function of transmitted flux in the Lyα forest due to BAOs was detected in two separate analyses of DR9 spectra (Figure 2.13; Busca et al. 2013; Slosar et al. 2013). Based on the spectra of 48 640 quasars in the redshift range $2.1 \lesssim z \lesssim 3.5$, Busca et al. (2013) constrained the angular diameter distance D_A and the expansion rate H at the mean redshift, $z = 2.3$. By including constraints from the CMB, they

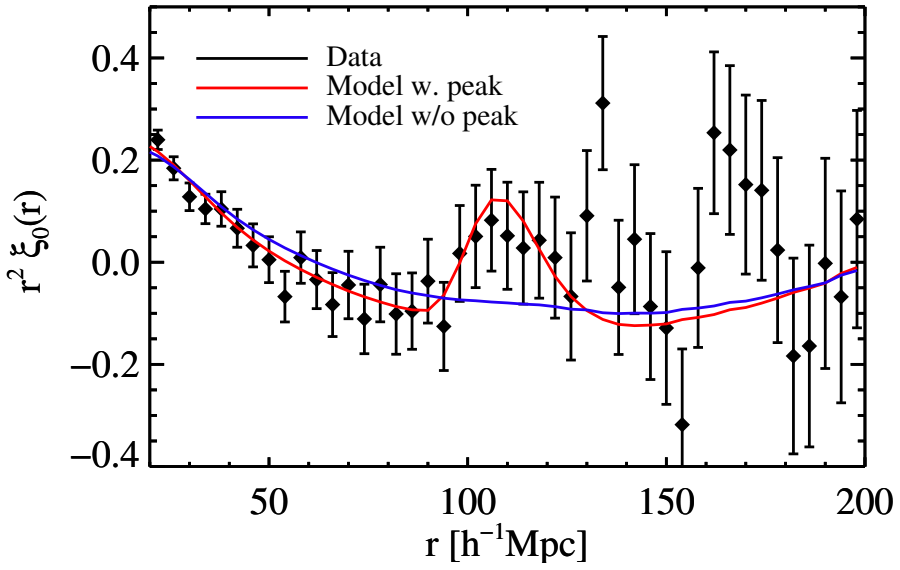

FIGURE 2.13: Fits to the transmitted flux correlation function monopole with a BAO peak (red line) and without a BAO peak (blue line). The fitting range is $20h^{-1} < r < 200h^{-1}$ Mpc. (Figure from Busca et al. (2013).)

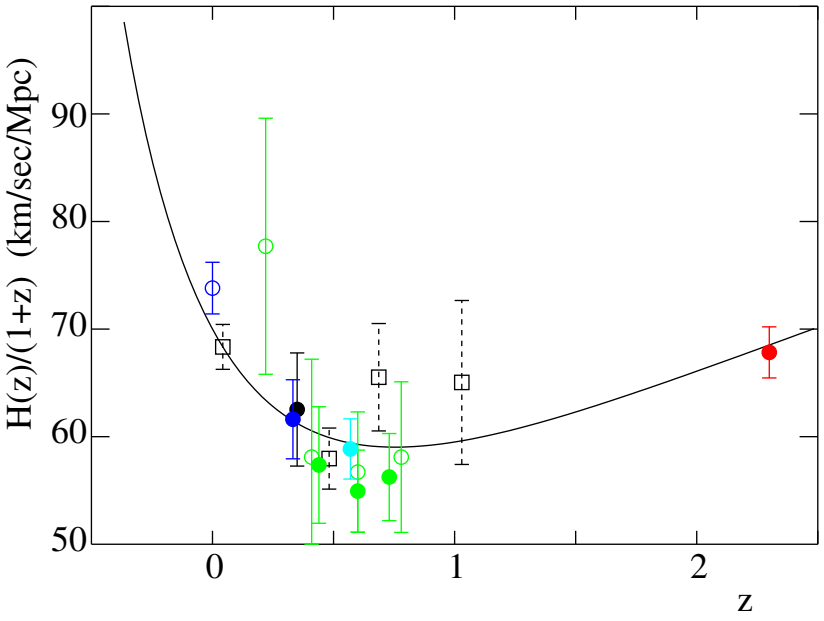

FIGURE 2.14: Measurements of $H(z)/(1+z)$ vs. z demonstrating the acceleration of the expansion for $z < 0.8$ and deceleration for $z > 0.8$. The BAO-based measurements are the filled circles: this work: (red), Xu et al. (2013, black), Chuang & Wang (2012, blue), Reid et al. (2012, cyan), and Blake et al. (2012, green). The open green circles are from WiggleZ (Blake et al. 2011) Alcock-Paczynski data combined with supernova data yielding $H(z)/H_0$ (without the flatness assumption) plotted here assuming $H_0 = 70$ km s^{-1} Mpc^{-1}. The open blue circle is the H_0 measurement of Riess et al. (2011). The open black squares with dashed error bars show the results of Riess et al. (2007) which were derived by differentiating the SNIa Hubble diagram and assuming spatial flatness. (For visual clarity, the Riess et al. (2007) point at z = 0.43 has been shifted to z = 0.48.) The line is the ΛCDM prediction for (h, Ω_M, Ω_Λ) = (0.7, 0.27, 0.73). (Figure from Busca et al. (2013).)

measured $H(z = 2.3) = (224 \pm 8)$ km s^{-1} Mpc^{-1} and determined that the cosmological expansion was decelerating in the range $0.7 < z < 2.3$ (Figure 2.14). The expansion appears to decelerate during the matter-dominated epoch and then accelerate as the universe becomes dominated by dark-energy, in agreement with ΛCDM cosmological models.

Slosar et al. (2013) confirmed these results with higher precision, using a different statistical method. They applied less stringent cuts to the underlying DR9 data set and analyzed sight lines from 58 227 quasars again within $2.1 \lesssim z \lesssim 3.5$, but at an average redshift $z = 2.4$. The larger data sample contributed significantly to the improved precision. The BAO peak is detected at a significance of between 3 and 5 sigma, depending on the error estimation method. Analyzing the DR9 spectra helped establish data treatment protocols and statistical techniques that will allow the BOSS collaboration to get the most out of the full quasar sample.

A joint analysis of the DR12 quasar and galaxy samples will be the capstone to the SDSS-III BOSS project. Results from preliminary samples at both $z \sim 0.5$ and $z \sim 2.5$

have already exceeded expectations for the full survey (e.g, Anderson et al. 2014). The total number of observed quasars at $z > 2.15$ is 183 345, a more than 12% increase over the targeted 160 000 quasars. The joint analysis results are anticipated around December 2014, concurrent with DR11 and DR12.

2.8 Future Prospects

June 30, 2014 was the last night of observations for SDSS-III, and SDSS-IV began operations as of July 1, 2014. Three surveys, eBOSS, APOGEE-2, and MaNGA, will run until 2020. APOGEE-2 will continue taking infrared stellar spectra to address questions about the structure and formation of the Milky Way, while MaNGA will use fiber IFUs to make spatially resolved maps of individual nearby galaxies. The goal for eBOSS is to fill in epochs not well-probed with the BOSS survey by taking spectra of galaxies at $0.6 < z < 1.0$ and quasars at $0.9 < z < 3.5$ (Figure 2.15). The eBOSS data will thereby constrain the BAO scale when the expansion of the universe transitioned from decelerating to accelerating. The survey plans to obtain 740 000 quasar spectra over 7500 square degrees, including variability selected and X-ray selected quasars. Rich data sets await those interested in quasar science and the IGM, both with the impending SDSS-III DR12 data release in December 2014 (over 180 000 quasars at $z > 2.15$) and the newly launched eBOSS project.

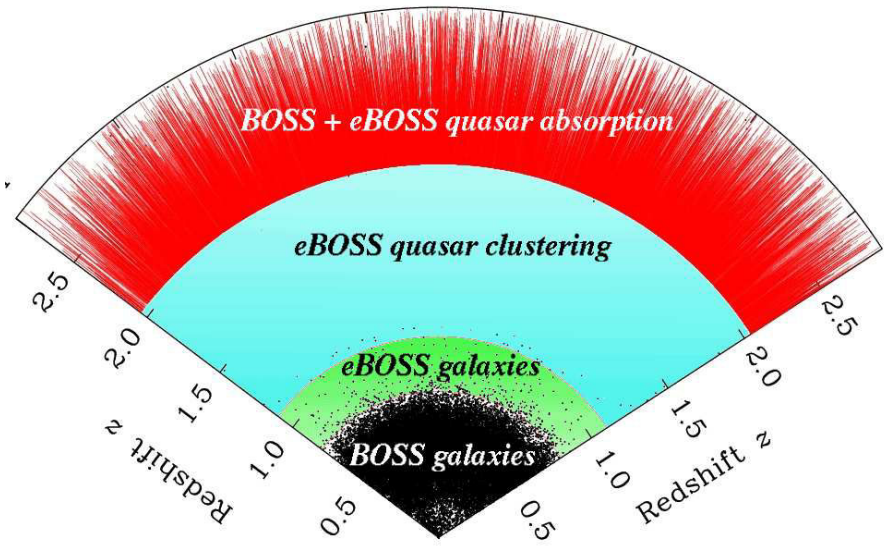

FIGURE 2.15: eBOSS plans to fill in redshift ranges not well-probed with BOSS or other large-scale structure surveys by obtaining galaxy spectra to $z \sim 1$ (green area) and quasar spectra at $z > 0.9$ (light blue and red areas). (Figure from www.sdss3.org.)

Chapter 3

A glance at the host galaxy of high-redshift quasars using strong damped Lyman-alpha systems as coronagraphs

3.1 Introduction

Quasar host galaxy properties may provide important constraints on active galactic nucleus (AGN) feedback mechanisms (Cattaneo et al. 2009; Fabian 2012) and information to better understand the relationship between the growth of the central black hole and the growth of the galaxy (e.g. Ferrarese & Merritt 2000). The black hole mass, $M_{\rm BH}$, scales with the stellar mass in the host bulge, $M_{\rm bulge}$, and the stellar velocity dispersion, σ. The star formation history of galaxies is therefore liked to the evolution of their supermassive black holes (Gebhardt et al. 2000). The bulk of star formation in the bulge may occur simultaneously with the maximum black hole growth (Lutz et al. 2008), since both processes rely on reservoirs of gas brought to the center by gas-rich mergers and disk instabilities. The growth phase ends when no gas remains, if, for example, star formation consumes all the gas. Alternatively, the AGN may blow the gas outside its host galaxy (Fabian et al. 2006), curtailing star formation. In this case, the AGN must have sufficient luminosity for the radiation-pressure force outwards to exceed the gravitational force inwards. Untangling the black hole growth and star formation processes is crucial for explaining how galaxies arrive at their present-epoch characteristics.

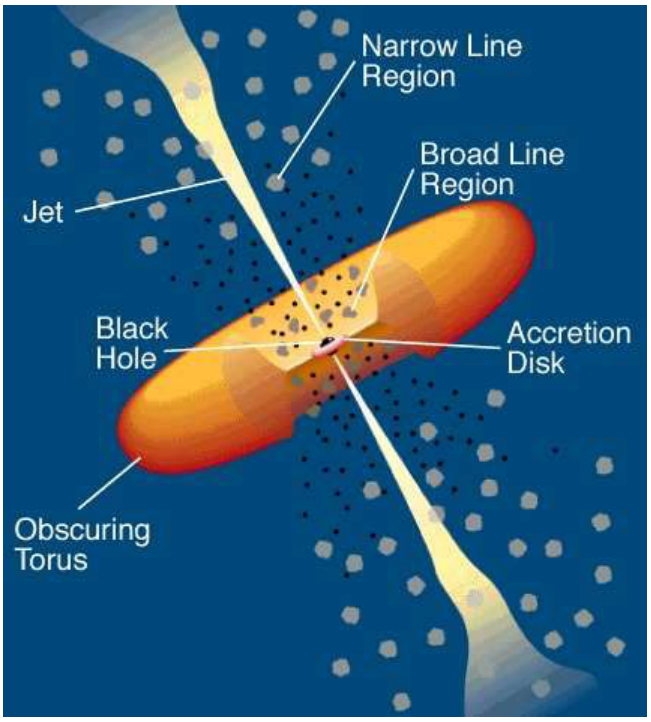

FIGURE 3.1: A schematic diagram of AGN structure. A luminous accretion disk surrounds the central black hole. Broad emission lines are due to clouds orbiting above the disk and perhaps the disk itself. A thick dusty torus obscures the broad-line region from transverse lines-of-sight, although some continuum and broad-line emission can be scattered into those lines-of-sight by hot electrons that pervade the region. Narrow emission lines originate from irradiated clouds much farther from the central source. In radio-loud AGN, jets emanate from the region near the black hole, initially at relativistic speeds. (Figure adapted from Urry & Padovani (1995).)

Galaxies with active galactic nuclei (AGN) are classified based on spectral features and whether or not they are radio-loud. The broad emission lines characteristic of quasar spectra originate from energetic gas clouds near to the accretion disk that surrounds the central black hole (Figure 3.1). In the broad line region, forbidden lines, like [O II] and [O III], are not emitted, because the density is so high (higher than the critical density) that their upper level is collisionally de-excited. These narrow emission lines arise in gas that is further from the central engine, where collisional de-excitation is no longer dominant. Ionizing radiation is thought to emanate from the AGN in a cone, and a thick dusty torus shields the plane aligned with the accretion disk. Spectral features vary widely depending on how an AGN is oriented with respect to the observer, producing a menagerie of AGN classifications. Certain quasars and radio galaxies have only narrow emission lines. Their AGN are thought to be shrouded behind the dusty torus. Unification models (e.g., Antonucci 1993) strive to explain how the many categories of objects (i.e, quasar, blazar, Seyfert galaxy, radio galaxy, etc.) can represent different aspects of the same AGN, depending on the viewing angle

Absorptions that occur closest to the redshift of the quasar probe gas associated directly with the AGN, its host galaxy, or the surrounding environment. High-velocity winds

from the central engine send material streaming across the line-of-sight in ∼10% of quasar spectra. The resulting broad absorption lines (BAL) can have troughs that extend several thousand km s^{-1} and outflow velocities that range from $\sim 1\,000 - 30\,000$ km s^{-1} (Weymann et al. 1991). They have metallicities close to solar (Hamann et al.) and they are highly ionized, leaving little doubt that they are intrinsic to the AGN. The BAL troughs often vary on $\sim 1 - 10$-year timescales and can thereby help constrain the properties of quasar winds (e.g., Filiz Ak et al. 2013). Narrow absorption lines (NAL) that are within a few thousand km s^{-1} of the QSO emission redshift and typically have velocity widths less than a few hundred km s^{-1} may also trace gas that originates near the quasar. These absorbers often show evidence of partial coverage of the quasar accretion disc continuum and/or broad-line region, as well as strong N V absorption (e.g., Barlow & Sargent 1997; Finn et al. 2014; Gabel et al. 2006; Petitjean et al. 1994; Petitjean & Srianand 1999; Srianand & Shankaranarayanan 1999). They can be ejected by the quasar up to large distances. By analyzing the ionization state of the absorbing gas, Finn et al. (2014) found that the distance between the AGN and NAL clouds could be as large as ∼3 kpc. Another population of NAL with little N V absorption arise from material ejected in supernova explosions or probe gas that is part of the host galaxy halo (e.g., Ganguly et al. 2013; Tripp et al. 1996).

3.1.1 Observing Quasar Host Galaxies

For nearby quasar host galaxies, it is possible to obtain detailed observations. Using an integral-field spectrograph, Davis et al. (2012) traced the kinematics of ionized gas and identified an AGN-driven outflow disrupting the star-forming gas in NGC 1266 (D = 30 Mpc). Similar studies of nearby quasars are abundant enough to permit a statistical analysis of the $M_{\rm BH} - M_{\rm bulge}$, $M_{\rm BH} - \sigma$, and $M_{\rm BH} - L$ scaling relations in samples compiled from the literature (Graham et al. 2011; Gültekin et al. 2009; McConnell & Ma 2013).

Resolving more distant quasar host galaxies is a challenge that can be overcome through several approaches, including deep ground-based imaging, space-based imaging (Bahcall et al. 1997), adaptive optics, and modeling gravitational lenses. Kotilainen et al. (2013) took advantage of the deep (r ∼ 22.4) images from the Stripe 82 area in the SDSS DR7 to resolve the host galaxies for ∼350 $z < 0.5$ low-redshift quasars. Turning to space, the Wide-Field Planetary Camera 2 (WFPC2) on the Hubble Space Telescope (HST) allowed Floyd et al. (2013) to compare the star formation rate in a modest sample of $z \sim 1$ and $z \sim 2$ quasar hosts. Adaptive optics makes it possible to detect and characterize the properties of quasar host galaxies at $z \sim 2 - 3$ (Falomo et al. 2008; Márquez et al. 2001; Wang et al. 2013b). Targeting gravitationally lensed quasars is

a particularly effective method for accessing quasar host galaxies, since lensing models can be used to disentangle the bright central AGN from the extended host. Peng et al. (2006a,b) were able to determine the host galaxy structure, measure the $M_{\rm BH}/M_{\rm bulge}$ ratio, and compare samples across $1 \lesssim z \lesssim 4.5$. These observations at different epochs provide essential constraints on the evolution of quasar host galaxies.

Millimeter astronomy has been essential for probing quasar host galaxies at higher redshifts. The detection of CO emission in the z = 4.7 quasar BR1202-0725 (Omont et al. 1996), along with continuum emission due to dust, confirmed that high-redshift quasars are associated with galaxies. This same quasar host galaxy also shows strong Lyα emission (Petitjean et al. 1996), indicating enhanced star formation or elevated ionization from the quasar flux. Recent observations with the Atacama Large Millimeter/submillimeter Array (ALMA; Wootten & Thompson 2009) of [C II] line emission in the BR1202-0725 host galaxy suggest an outflow of gas ionized by the quasar (Wagg et al. 2012). At this early epoch, quasar hosts have both vigorous star formation and central black holes that accrete at the Eddington limit (Wang et al. 2013a). Comparing the star formation rate to the black hole accretion rate indicates which process is dominant. For example, Willott et al. (2013) found that the $z \sim 6.4$ quasar host galaxy J2329-0301 has an uncharacteristically low ratio of star formation to black hole accretion, implying that the quasar has shut off star formation in the galaxy, potentially by photo-ionizing the diffuse gas. Indeed, this quasar has extended Lyα emission across at least 15 kpc (Goto et al. 2009; Willott et al. 2011).

At the $z = 2 - 3$ epoch, when the quasar luminosity function peaks (e.g., Richards et al. 2006), spectroscopy remains the best tool for investigating host galaxies. An ultra-deep, blind, spectroscopic long-slit survey revealed a young stellar population in the host galaxy of a $z = 3.045$ quasar, the formation of which coincides with the quasar activity (Rauch et al. 2013). With spectroscopy, it is also possible to study absorption systems, such as associated narrow absorption lines (NALs), that probe the gaseous environments close to quasars. Associated NAL systems at $z \sim 2.4$ tend to have solar or super-solar metallicities and potentially arise from AGN-driven outflows of gas from the interstellar medium (ISM; D'Odorico et al. 2004; Petitjean et al. 1994). However, it is difficult to differentiate between gas associated with the AGN, gas from the ISM of the host galaxy, and gas located in galaxies clustered around the AGN host galaxy. Proximate DLAs, which are within $\Delta v < 3\,000$ km s^{-1} of the background quasar, can be used to investigate this last category. Sixteen high-redshift proximate DLAs studied in detail have sub-solar metallicities ranging from $\rm Z \sim 1/3 - 1/1000\ Z_{\odot}$ and show evidence of enhanced ionization due to the nearby quasar (Ellison et al. 2010).

3.1.2 Associated DLAs

In a newly exploited technique for accessing the quasar host galaxy, DLAs at the redshift of the quasar, hereafter called associated DLAs, can act as natural coronagraphs, completely absorbing the broad Lyα emission from the central AGN. In the absence of broad Lyα emission, it is possible to observe a narrow Lyα emission line from a source at approximately the same redshift as the quasar in the DLA trough. For this situation to occur, the absorber must cover the $\sim$1 pc Broad Line Region (BLR) without also obscuring extended Lyα emission, which can be a result of both UV flux from the AGN that ionizes surrounding gas in the Narrow Line Region (NLR) and star formation activity within the host galaxy. A striking individual detection of this phenomenon is presented in Hennawi et al. (2009); the four other previous detections of narrow Lyα emission in the trough of a DLA near the quasar redshift all have lower Lyα luminosities (Ellison et al. 2002; Moller & Warren 1993; Moller et al. 1998; Pettini et al. 1995).

The serendipitous alignment of a DLA absorber along the quasar line-of-sight near enough to the host galaxy to reveal narrow Lyα emission in the DLA trough is a rare occurrence. Ellison et al. (2011) exploited the statistical power of the Sloan Digital Sky Survey (SDSS; York et al. 2000) to investigate the characteristics of $\Delta v < 10\,000$ km s^{-1} proximate DLA absorbers in a sample compiled from Data Release 5 (Adelman-McCarthy et al. 2007). Only one DLA in the sample revealed narrow Lyα emission (reported in Hennawi et al. 2009), and no emission signal was seen in the stacked spectrum of 29 $\Delta v \leq 3\,000$ km s^{-1} DLAs.

Thanks to the increased sample size of quasar spectra in the SDSS-III (Eisenstein et al. 2011) Baryon Oscillation Spectroscopic Survey (BOSS, Dawson et al. 2013), several associated DLAs with unprecedentedly strong narrow Lyα emission superimposed on their troughs were discovered. In this article, we construct a statistical sample of associated DLAs from the SDSS Data Release 9 (DR9; Ahn et al. 2012). We study the emission and absorption properties of systems in our sample with the goal of characterizing any differences between the populations with and without emission detected in the BOSS spectra. We also characterize the emission properties of a sample of associated DLAs that reveal narrow Lyα emission identified thus far in the survey by visual inspection.

Section 2 describes the definition of a complete statistical sample. We then calculate how many intervening DLAs we expect to find at the quasar redshift and consider the possibility of an overdensity (Section 3). Sections 4 and 5 respectively characterize the two DLA populations and the emission properties. In Section 6, we present several associated DLAs with a covering factor unequal to one and consider the implications. We discuss the results in the context of our two-population scenario in Section 7.

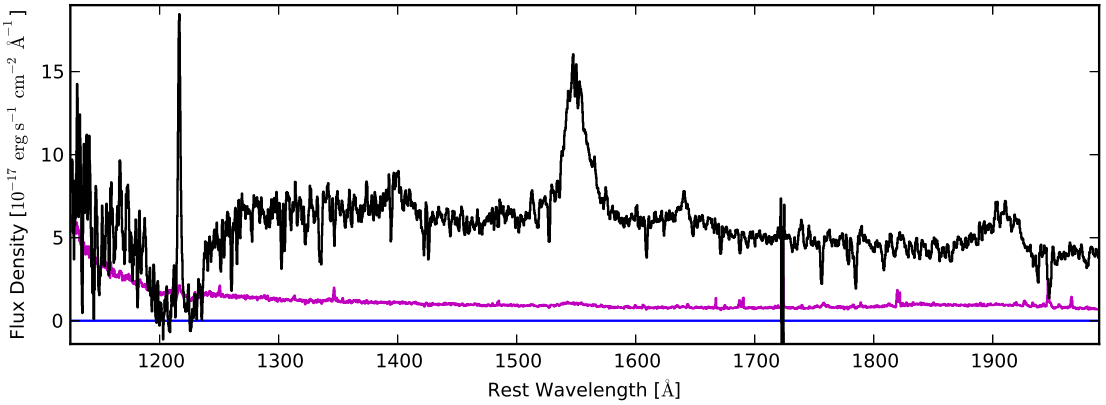

FIGURE 3.2: Example of a quasar spectrum (SDSS J1256+3506) with an associated DLA that reveals narrow Lyα emission. The 1-σ error on the spectral flux density is shown in magenta.

We use a ΛCDM cosmology with $\Omega_\Lambda = 0.73$, $\Omega_\mathrm{m} = 0.27$, and $\mathrm{H}_0 = 70$ km s^{-1} Mpc^{-1} (Komatsu et al. 2011).

3.2 Sample Definition

3.2.1 Strong associated DLAs

The quasar lines-of-sight were observed as part of SDSS-III BOSS. From 2009 – 2014, this survey will take spectra of over 150 000 quasars at $\langle z \rangle \sim 2.5$ and 1.5 million galaxies at $\langle z \rangle \sim 0.7$ with the primary goal of detecting baryon acoustic oscillations at different cosmological times. A dedicated 2.5 m telescope (Gunn et al. 2006) conducts the imaging and spectroscopy. SDSS-III uses the same camera (Gunn et al. 1998) as its predecessor surveys (York et al. 2000) to obtain images in five broad bands, *ugriz* (Fukugita et al. 1996). Twin multi-object fiber spectrographs designed for BOSS collectively span ∼3 600 – 10 000 Å with cameras individually optimized for observing at blue and red wavelengths (Smee et al. 2013). Their resolving power varies from ∼1500 – 3000 across the wavelength range, such that the instrument velocity dispersion is consistently ∼150 km s^{-1}. Bolton et al. (2012) describe the spectroscopic data reduction pipeline.

The Data Release 9 Quasar (DR9Q) catalog (Pâris et al. 2012) includes 87 822 quasars detected over 3 275 deg^2, 61 931 of which are at $z > 2.15$. A combination of target selection methods (Ross et al. 2012) achieved this high surface density of high-redshift quasars. The spectra are publicly available as part of DR9. Noterdaeme et al. (2012b, hereafter N12) provide a catalog of DLAs and sub-DLAs with $\log N(\mathrm{H\,I}) \geq 20.0$ detected from an automatic search along the DR9Q lines-of-sight. We use an extended version of the N12 catalog that includes automatic detections up to +3 000 km s^{-1} beyond the quasar redshift.

We select strong associated DLAs so that the Lyα trough is large enough to completely mask the broad Lyα emission line from the quasar (Figure 3.2). To gather candidates for a statistical sample of these strong associated DLAs, we search the extended N12 catalog for DLAs that are within $\pm 3\,000$ km s^{-1} of the quasar, have log N(H I) ≥ 21.2, and arise in lines-of-sight with balnicity index zero and BAL_FLAG_VI=0 (see Weymann et al. (1991) for a discussion of the balnicity index). We exclude quasar spectra with Broad Absorption Lines (BALs), since they could blend with the DLA and contaminate our H I column density measurements. N12 uses quasar redshifts assigned during the visual inspection, which have an uncertainty of about 500 km s^{-1} (Pâris et al. 2012). Due to this uncertainty on the quasar redshift, we allow the velocity difference limit to extend redward of the quasar, so as not to miss any associated DLAs by stopping the automatic search at the quasar redshift. The column density lower limit was chosen because the zero-level in the trough of the Voigt profile fit spans 1 000 km s^{-1} for log N(H I) ≥ 21.2. Extending to lower column densities would obscure our ability to clearly detect Lyα emission from the host galaxy in the trough. Applying these criteria returns 41 DLAs.

When an associated DLA reveals strong narrow Lyα emission, the N12 automatic search may wrongly identify two consecutive DLAs. To recover these split DLAs, the extended N12 catalog is searched for lines-of-sight that have more than one DLA detected within $\pm 3\,000$ km s^{-1} of the quasar, balnicity index zero and BAL_FLAG_VI=0. No limit is placed on the column density. Potential split DLAs must be confirmed by visually examining the associated metal absorption lines. Genuine split DLAs have one set of absorption lines that approximately align with the narrow Lyα emission peak, whereas two sets of metal lines are present for consecutive DLAs. This procedure finds 9 associated DLAs split by narrow Lyα emission, bringing the total number of log N(H I) ≥ 21.2 DLAs within $\pm 3\,000$ km s^{-1} of the quasar to 50.

3.2.2 Measuring DLA column densities and emissions

The zero-level in BOSS spectra tends to be slightly higher than the true zero (Pâris et al. 2012); this can impact the column density measurement for DLAs (Figure 3.3). Using the Voigt profile fit to the DLA, we identify the zero-flux density region in the DLA trough and calculate the average spectral flux density across these pixels to determine the zero-level offset for each spectrum. We correct the observed spectral flux density with this offset, ensuring that the spectral flux density is truly at zero in the DLA trough.

Column densities were re-measured for all DLAs according to the following process. Associated low-ionization transitions redwards of Lyα are identified and fitted as an absorption system to obtain the DLA redshift. For all absorption line fits we use the

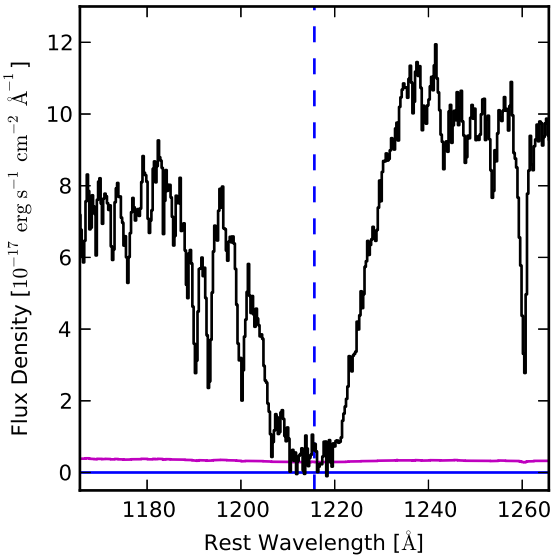

FIGURE 3.3: Combined spectrum for the twenty-three DLAs in the statistical sample with no Lyα emission detected at the 4-σ level. The spectra are combined with an inverse variance weighted average. The zero-flux density level in the DLA trough is approximately at the level of the error on the spectral flux density, $\sim 0.30 \times 10^{-17}$ erg s^{-1} cm^{-2} $^{-1}$ above zero.

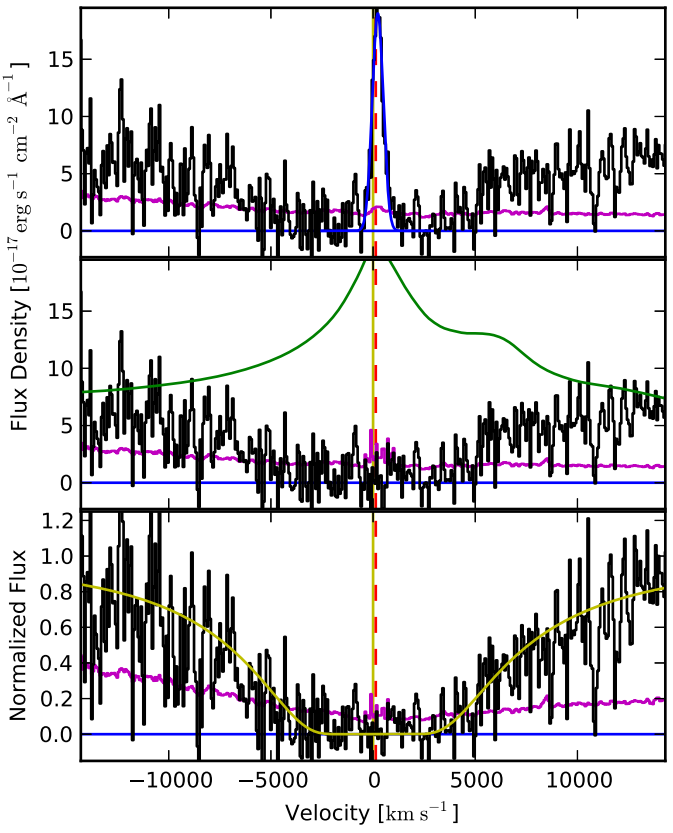

FIGURE 3.4: Top: Gaussian fit (blue) to the narrow Lyα emission revealed by the associated DLA toward SDSS J1256+3506. Center: The narrow Lyα emission is subtracted, and a quasar continuum template (green) is fitted to the spectrum. Bottom: The spectrum is normalized and the H I column density is fitted (yellow). SDSS J1256+3506 has log N(H I) = 22.1. The dashed red line marks the DLA redshift, and the solid vertical yellow line indicates the velocity offset for the quasar.

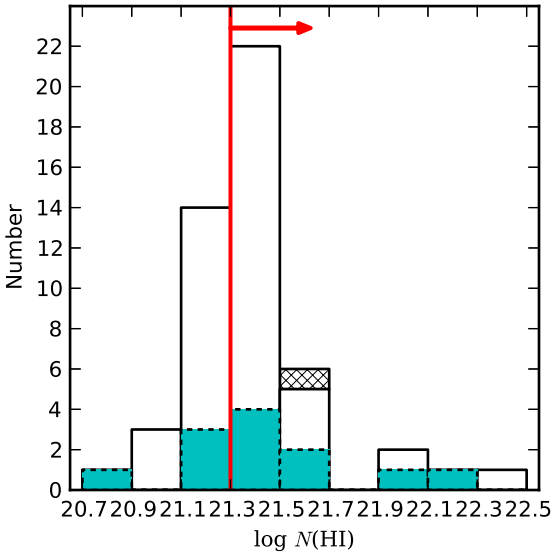

FIGURE 3.5: H I column density distribution for re-measured DR9 DLAs initially identified with log N(H I) $\geq$ 21.2 and $\Delta v \leq 3\,000$ km s^{-1}. Cyan shading indicates DLAs that reveal narrow Lyα emission. The sample is complete above log N(H I) = 21.3 (red arrow), and systems with lower column densities are not included in the statistical sample. One log N(H I) $\geq$ 21.3 DLA (marked with cross-hatching) is also not included in the statistical sample because of the velocity difference between the DLA and the quasar.

VPFIT package[1]. If narrow Lyα emission is present in the DLA, the peak is fitted with a Gaussian profile and removed (Figure 3.4, top). A template spectrum from the mean principal component analysis (PCA) quasar continuum (Pâris et al. 2011) is adjusted with a power-law fit to each spectrum and scaled to provide the quasar continuum near the Lyα emission line (Figure 3.4, center). The column density is measured from the normalized spectrum by fitting the DLA with the redshift fixed to the value measured from the metals (Figure 3.4, bottom). Column density errors are on the order of 0.1 dex. Figure 3.5 shows the resultant column density distribution in our sample. The absorption system redshift and the H I column density are listed in Table 3.1.

The noise level in the spectrum is the 1-σ error on the spectral flux density. We have checked that the noise level is consistent with the scatter in the bottom of the DLA troughs by examining five DLAs with noise levels $\sigma < 0.3 \times 10^{-17}$ erg s^{-1} cm^{-2} $^{-1}$ where narrow Lyα emission is not detected (Figure 3.6). The average noise level for 217 pixels from the five DLAs is $\sigma = 0.233 \times 10^{-17}$ erg s^{-1} cm^{-2} $^{-1}$ with 0.030×10^{-17} erg s^{-1} cm^{-2} $^{-1}$ standard deviation. The BOSS pixel size increases logarithmically from 0.82 to 2.39 Å over the wavelength range 3610 – 10 140 Å (Pâris et al. 2012), such that the pixel size is $\sim$1 Å at the typical observed wavelength for our DLAs, $\sim$4000 Å. The σ value from the Gaussian fit to the spectral flux density distribution,

[1]Carswell http://www.ast.cam.ac.uk/~rfc/vpfit.html

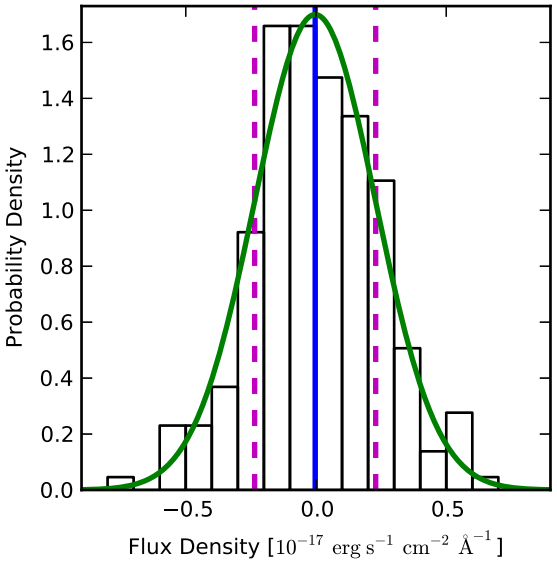

FIGURE 3.6: Spectral flux density distribution for pixels in the trough of five DLAs with $\langle \text{Noise} \rangle = 0.233 \times 10^{-17}$ erg s^{-1} cm^{-2} $^{-1}$. A Gaussian fit to the spectral flux density distribution (solid green line) gives $\sigma = 0.232 \times 10^{-17}$ erg s^{-1} cm^{-2} $^{-1}$ (dashed magenta lines), which is in excellent agreement with the measured average noise. The zero-level spectral flux density correction has been applied to these DLAs.

0.232×10^{-17} erg s^{-1} cm^{-2} $^{-1}$, is in excellent agreement with the average observed noise level.

We define the n-σ detection level for the narrow Lyα emission (prior to its removal) as:

$$\text{n} = \frac{\langle f_\lambda \rangle \sqrt{\text{N}_{\text{pix}}}}{\langle \text{Err} \rangle} \tag{3.1}$$

where N_{pix} is the number of pixels within 3-σ (1.27 FWHM) of the Gaussian fit. The average spectral flux density, $\langle f_\lambda \rangle$, and average error, $\langle \text{Err} \rangle$, are calculated for the pixels within this range. While we can determine Gaussian fits for narrow Lyα emission down to the $\sim$2-σ level, we are confident about emission features detected at and above 4-σ. The DLAs that have $\geq$ 4-σ narrow Lyα emission detections are shaded in cyan in Figure 3.5.

3.2.3 The Statistical Sample

The typical 1-σ column density error in the N12 catalog is 0.20 dex. Since our more precise column density estimates do not differ from the automatic detections by more than this error, we consider that our associated DLA sample is complete for systems with log $N(\text{H I}) \geq 21.3$. The shape of the column density distribution (Figure 3.5) further justifies this cut-off. We impose a velocity difference limit of $\Delta v = 1\,500$ km s^{-1} (stricter than the initial search criteria), which excludes one DLA with log $N(\text{H I}) \geq 21.3$

that is 2 530 km s^{-1} below the PCA quasar redshift. (See section 4.2 for a discussion of kinematics.) The statistical sample includes 31 DLAs that are within 1 500 km s^{-1} of the quasar and have log N(H I) $\geq$ 21.3.

The properties of these DLAs can be used to statistically look for differences between the systems that reveal narrow Lyα emission (detected at the 4-σ level, 8 DLAs) and those that do not.

3.2.4 The Emission Properties Sample

To characterize the properties of the narrow Lyα emission features, we examine all lines-of-sight for which the emission is detected at 4-σ, regardless of the DLA column density. We supplement the DR9 sample with additional cases of DLAs revealing narrow Lyα emission identified during the visual inspection of quasars for DR10 (Smee et al. 2013). Twenty-six DLAs are included in the emission sample. Although this dataset is not complete, it is currently the best possible sample for studying the narrow Lyα emission properties.

3.2.5 The Redshift Distribution

Figure 3.7 compares the redshift distributions for quasars in the statistical sample and DR9. The most noticeable difference is a possible excess of quasars at $z = 3.0 - 3.2$ in the statistical sample. The peak in probability density is also flatter for the statistical sample than for the DR9 quasars. Otherwise, the redshift distribution for quasars in the statistical sample generally follows that of the DR9 quasars. Based on a Kolmogorov-Smirnov test, it is 68% likely that the two distributions are the same. A K-S test comparing the eight quasars in the statistical sample that have detected narrow Lyα emission with the DR9 quasars indicates that it is 26% likely the two populations come from the same distribution. The quasar redshift distribution also shows that there is no preferred redshift for DLAs that reveal narrow Lyα emission.

3.3 Anticipated Number of Intervening DLA Systems within 1 500 km s^{-1} of zQSO

We explore the possibility of an overdensity of DLAs at the quasar redshift by calculating the anticipated number of intervening DLAs with $\Delta v \leq$ 1 500 km s^{-1} in DR9 and comparing this result to the number observed in our statistical sample of associated DLAs.

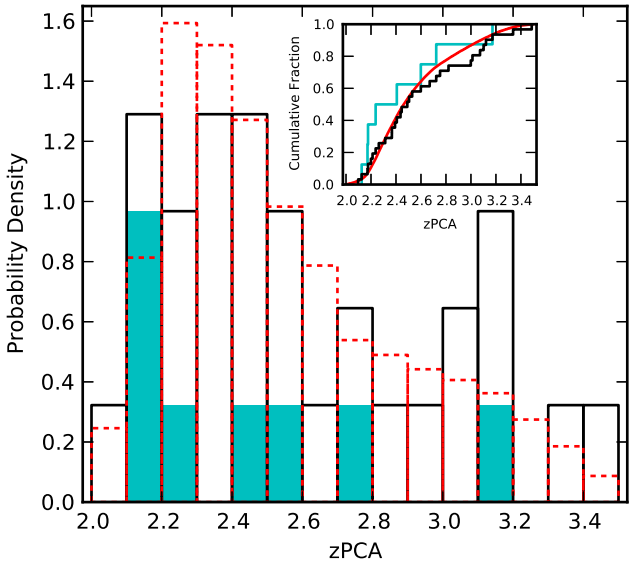

FIGURE 3.7: Distribution of quasar redshifts estimated from a principal component analysis for the statistical sample (solid black line) and the DR9 quasars (dashed red line). The relative portion of DLAs in the statistical sample that reveal narrow Lyα emission are shaded in cyan. The inset gives the cumulative fraction function using the same color scheme.

3.3.1 Anticipated Number in DR9

The absorption path is given by:

$$\frac{d\chi}{dz} = \frac{(1+z)^2}{\Omega_{\rm m}(1+z)^3 + \Omega_{\rm k}(1+z)^2 + \Omega_\Lambda} \tag{3.2}$$

(Bahcall & Peebles 1969) where $dz = (1+z)\frac{\Delta v}{c}$. We evaluate this expression with $\Delta v = 1\,500$ km s^{-1} and the PCA redshift for each non-BAL quasar in DR9 with $2.0 \leq z_{\rm PCA} \leq 3.5$, the redshift range covered in the statistical sample. Summing the absorption path for each of the 55 679 quasar lines-of-sight gives the total absorption path, $\Delta\chi$.

We use the N(H I) distribution function, $f(N_{H\,i}, \chi)$, given in N12 to integrate

$$\frac{N_{\rm DLA}}{d\chi} = \int f(N_{H\,i}, \chi)\, dN_{\rm QSO} \tag{3.3}$$

for $N_{H\,i} \geq 10^{21.3}$cm^{-2}, since our statistical sample is complete above this column density. The expected number of DLAs is then $N_{\rm DLA} = \frac{N_{\rm DLA}}{d\chi}\Delta\chi$, which predicts 12.93 associated DLAs in DR9.

3.3.2 The Effect of Clustering near Quasars

If the number density of associated DLAs is the same as that of intervening DLAs, then we anticipate finding ∼13 associated DLAs with log N(H I) $\geq$ 21.3 in DR9. Our

statistical sample contains 31 such DLAs, more than twice as many as expected. This observed overdensity can be attributed to the clustering properties of DLAs around quasars. It is well known that quasars occur in overdense regions. Measurements of quasar clustering, which is more pronounced at higher redshifts (Croom et al. 2005), indicate that a quasar is likely to be part of a group of galaxies. It has also been shown that an overdensity of neutral gas is present within ∼10 Mpc of the quasar (Font-Ribera et al. 2013; Guimarães et al. 2007). Not surprisingly, the incidence of DLAs within 3 000 km s^{-1} of the quasar is ∼2–4 times higher than that of intervening DLAs (Ellison et al. 2010). The number of associated DLAs that we observe is therefore consistent with what we expect due to clustering around the quasar host galaxy.

3.4 Characterizing the Statistical Sample

3.4.1 Scenario

The statistical sample breaks into two populations: associated DLAs that reveal narrow Lyα emission at more than the 4-σ level (8) and those with no emission detected at this level (23). The first category is such an unusual occurrence that we investigate whether these DLAs have specific properties.

We would like to test the hypothesis that the absorbers giving rise to associated DLAs with narrow Lyα emission superimposed on their troughs are intrinsically different than the absorbers responsible for the associated DLAs where no emission is detected. Narrow Lyα emission appears in the DLA trough only if the absorber blocks the ∼1 pc BLR without also covering more extended sources of Lyα emission, such as the NLR or star-forming regions. When no Lyα emission is observed, a galaxy near to the quasar host is likely acting as a screen, blocking the BLR, NLR, and any extended emission regions.

The impact parameters for ten confirmed $z \gtrsim 2$ galaxy counterparts to intervening DLAs are all on the order of ten kiloparsecs (Krogager et al. 2012). For very high column densities, such as those observed in our sample, impact parameters could be even smaller (e.g. Noterdaeme et al. 2012a). A neighboring galaxy would be sufficiently extended to obscure Lyα emission from the quasar host, but the absorber that allows narrow Lyα emission to pass unobscured must have a more compact size. Hennawi et al. (2009) suggest that the associated DLA towards SDSS J1240+1455 with a narrow Lyα emission peak could arise from small (∼10 pc), dense ($n_H \sim 100$ cm^{-3}) clouds of neutral hydrogen in the quasar host galaxy. Further supporting the idea that not all associated absorptions are due to galaxies clustered near the quasar host, Wild et al. (2008) found that upwards of 40% of $1.6 < z < 4$ $\Delta v \leq 3\,000$ km s^{-1} C IV absorbers

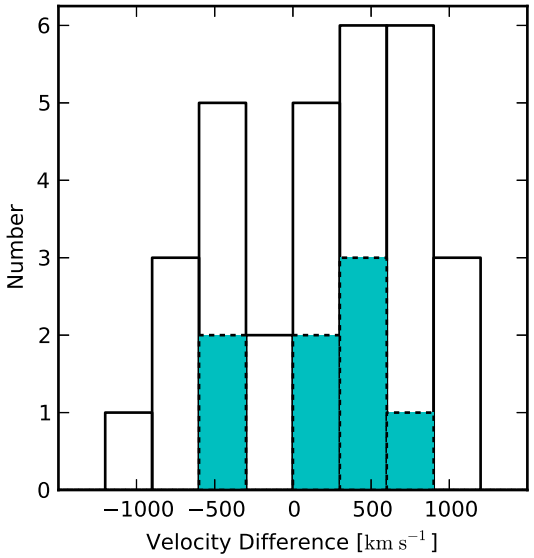

FIGURE 3.8: Velocity difference distribution for $z_{\rm DLA}$ with respect to $z_{\rm QSO}$. DLAs that reveal narrow Lyα emission are shaded in cyan. The preference for positive velocity differences may arise from uncertain quasar redshift estimates, rather than an abundance of DLAs falling into the quasar.

are directly related to the quasar. We likewise propose that the DLAs revealing narrow Lyα emission are due to dense clouds of neutral hydrogen in the quasar host galaxy.

3.4.2 Kinematics

The velocity difference of the DLA redshift, measured from the metals, with respect to the quasar redshift, determined from a PCA, is not distinct for systems with and without superimposed narrow Lyα emission (Figure 3.8). For both populations, nearly all DLAs fall within 1 200 km s^{-1} of the quasar.

The main uncertainty when studying the kinematics is that the quasar redshift is not well known. More than half of the DLAs appear to be at higher redshifts than the quasars (systems with positive velocity difference in Figure 3.8), which could indicate infalling absorbers. However, positive velocity differences are consistent with a known tendency for the PCA redshifts to be slightly bluer than the true quasar redshift (Pâris et al. 2012).

3.4.3 Metals

The rest equivalent width, W_0, of various metal transitions, C II λ1334, Si II λ1526, Al II λ1670, and Fe II λ2344, are measured for each DLA in the sample. These absorption features were chosen because they are typically not blended or redshifted out of the

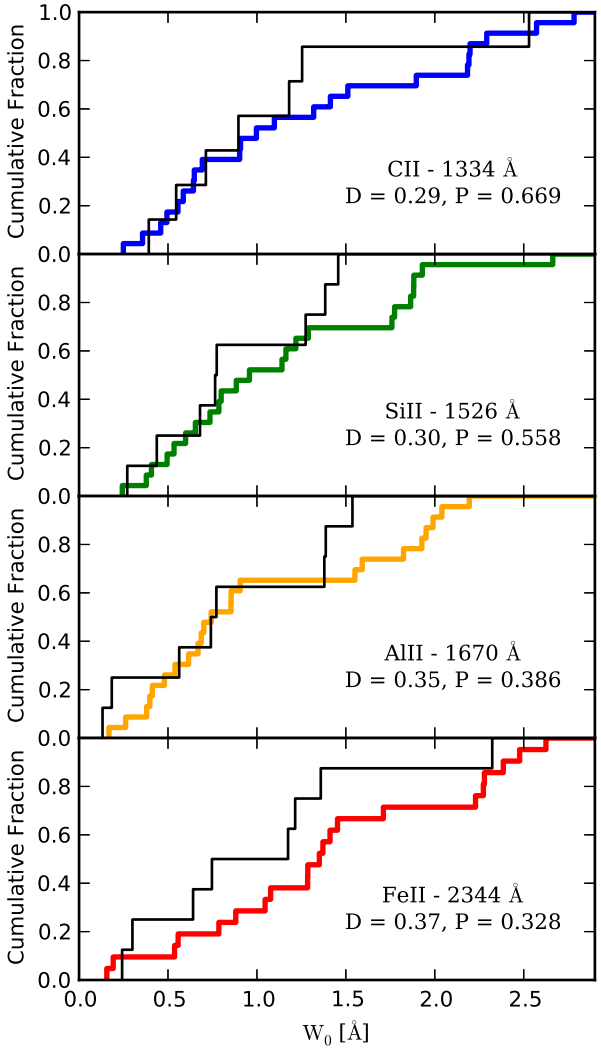

FIGURE 3.9: Kolmogorov-Smirnov tests comparing the DLAs with and without detected narrow Lyα emission using the rest equivalent widths for C II λ1334, Si II λ1526, Al II λ1670, and Fe II λ2344 absorption features. A black line traces the W_0 distribution for DLAs with narrow Lyα emission detected, and a thick colored line indicates the W_0 distribution for those without an emission detection. The K-S test statistic, D, gives the maximum vertical distance between the two distributions, and the P-value is the probability that the two distributions are drawn from the same population.

spectrum. The signal-to-noise ratio (S/N) is also best at wavelengths redward of Lyα. However, sky subtraction problems start to become noticeable after 7500 Å, and in some spectra the Fe II lines are subject to additional noise.

Table 3.2 gives W_0 values measured from a fixed-redshift Voigt profile fit to the absorption system (referred to as "Fit" in the Table). A second estimate of W_0 is directly measured from the normalized flux by integrating over the line profile (referred to as "$\mathcal{F}$" in the Table). We include both estimates of W_0 because of local problems in the spectra and/or complex blends that are difficult to disentangle at the spectral resolution

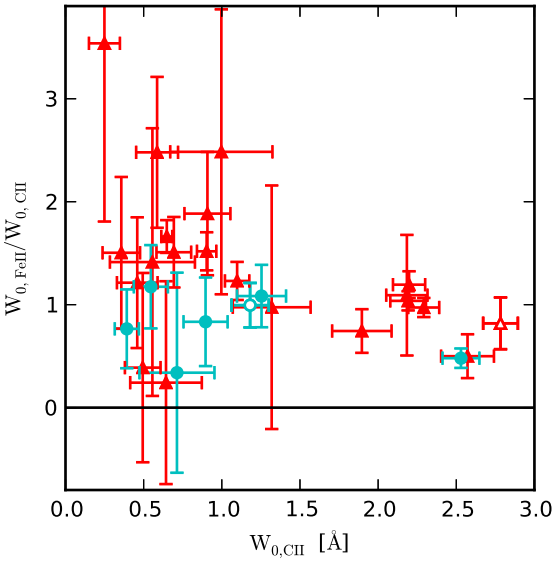

FIGURE 3.10: The equivalent width ratio $W_{0,\,\mathrm{Fe\,II}}/W_{0,\,\mathrm{C\,II}}$ is plotted as a function of $W_{0,\,\mathrm{C\,II}}$. DLAs where narrow Lyα is detected are marked by blue circles, and DLAs without a 4-σ detection are marked by red triangles. Filled symbols indicate that W_0 is measured from the fit to the absorption line, and empty symbols indicate that W_0 is estimated from the flux. One spectrum has flux problems at the location of the C II λ1334 absorption, and Fe II λ2344 is redshifted out of the spectrum in two cases. Twenty-nine of the 31 DLAs in the statistical sample are plotted here, 7 with an emission detection and 22 without.

and S/N typical of BOSS data. The error on W_0 is calculated using the error on the normalized flux across the six innermost pixels.

We performed a two-distribution K-S test with W_0 for the populations where emission is and is not detected (Figure 3.9). In general, the largest W_0 values are observed in systems where no emission is detected. However, the C II λ1334 and Fe II λ2344 distributions each have a strong absorption in a DLA system with emission detected. Overall, the W_0 values are less than ~67% likely to come from the same population. The maximum distance parameter is largest for Fe II λ2344, and for this absorption feature the probability that the populations are the same is only 33%.

Since most of these absorption features are saturated, it is reasonable to assume that W_0 is related to the width of the lines and not to column densities. Keeping this in mind, we nonetheless plot $W_{0,\,\mathrm{Fe\,II}}/W_{0,\,\mathrm{C\,II}}$ versus $W_{0,\,\mathrm{C\,II}}$ (Figure 3.10) to investigate any indication of species depleting onto dust grains. While some depletion is expected for C II, Fe II is expected to be ~50 times more depleted (Welty et al. 1999). The equivalent width ratios appear to decrease with increasing $W_{0,\,\mathrm{C\,II}}$. A linear fit indicates a slope of -0.39 ± 0.07 $^{-1}$ and a y-intercept of 1.74 ± 0.15. The systems where narrow Lyα emission is detected consistently have lower $W_{0,\,\mathrm{Fe\,II}}/W_{0,\,\mathrm{C\,II}}$ than the systems without a detection at the same $W_{0,\,\mathrm{C\,II}}$. We should be careful when interpreting this, but if the $W_{0,\,\mathrm{Fe\,II}}/W_{0,\,\mathrm{C\,II}}$ is related to depletion then this would indicate that dust content is

stronger in DLAs showing emission. Although somewhat surprising, this would at least support the idea that the gas in the DLA is not directly related to the Lyα emitting gas. Any correlations may become clearer with column densities, rather than W_0, but the BOSS spectral resolution and S/N are too low to permit this measurement.

3.4.4 Reddening

We explore reddening of the quasar spectra due to dust absorption from the associated DLAs by comparing their colors to the general population of quasars. All but one of the associated DLAs fall in the u or g band, so we are limited to the r-i and r-z colors. The left panel of Figure 3.11 shows the r-z color as a function of $z_{\rm QSO}$ and the right panel gives the distribution for color bins. Quasar spectra with an associated DLA and narrow Lyα emission are nearly all redder than the average r-z color for DR9 quasars with no DLA along their line-of-sight, while the r-z colors for associated DLAs without a narrow Lyα detection are more dispersed. The distribution reveals that the associated DLAs, both with and without an emission detection, have redder average r-z colors than the DR9 comparison quasars. A K-S test indicates that the associated DLAs with (without) narrow Lyα emission detected have a 3% (36%) probability of arising from the same r-z color distribution as the DR9 comparison quasars, and the associated DLAs with an emission detection have a 21% probability of arising from the same distribution as the

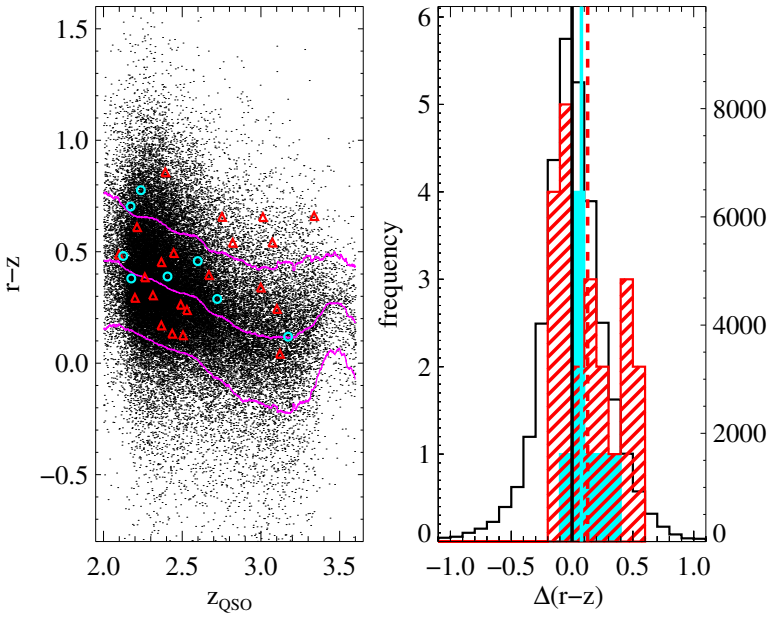

FIGURE 3.11: The r-z color as a function of the quasar redshift (left) and the r-z color distribution (right) for DR9 quasars without BALs or a DLA along the line-of-sight (black), associated DLAs without an emission detection (red), and associated DLAs with narrow Lyα emission detected (cyan). In the color plot, the median and 1-σ colors for the DR9 quasar sample are shown as magenta curves.

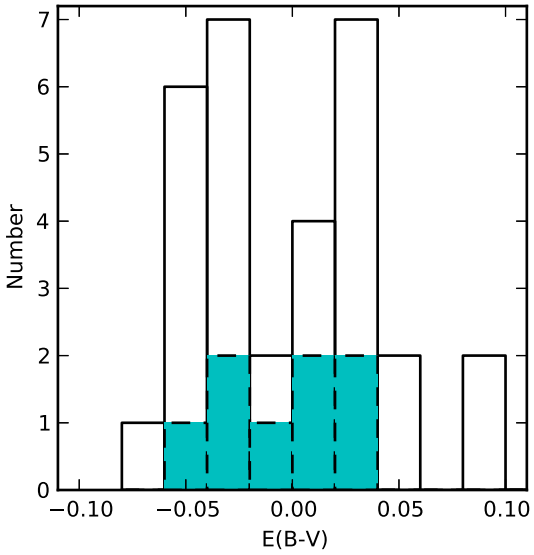

FIGURE 3.12: E(B-V) reddening distribution estimated from a Small Magellanic Cloud reddening law template. DLAs with narrow Lyα emission detected are shaded in cyan.

associated DLAs without a detection. A larger sample size would be needed to confirm that these are truly distinct populations.

We fit the quasar spectra with a Small Magellanic Cloud (SMC) reddening law template (Gordon et al. 2003) to further investigate potential differences between the associated DLAs that reveal narrow Lyα emission and those that do not. The SMC extinction curve is the best fit for the majority of the spectra, because they lack the 2175 Å bump characteristic of Large Magellanic Cloud or Milky Way extinction curves. In the E(B-V) reddening distribution (Figure 3.12), the most reddened systems (E(B-V) > 0.05) do not have a narrow Lyα emission detection. Otherwise, the distributions are similar for the two populations, and they are both consistent with no reddening on average.

3.5 Characterizing the Narrow Lyα Emission

In order to explore the properties of the narrow Lyα emission detected in the troughs of associated DLAs, we analyze the sample described in Section 3.2.4.

We fit a Gaussian profile to each narrow Lyα emission peak and derive $z_{\mathrm{Ly}\alpha}$, the integrated flux (IF), and the luminosity from the fit parameters. The integrated flux is calculated by summing the spectral flux density in the region within 3-σ of the Gaussian fit center (1.27 FWHM). The emission peaks all have IF values less than 70×10^{-17} erg s^{-1} cm^{-2}, except for two extremely strong emission peaks with IF $\sim$ 200×10^{-17} erg s^{-1} cm^{-2}. Since no IF values are in the range $26 <$ IF $< 40 \times$

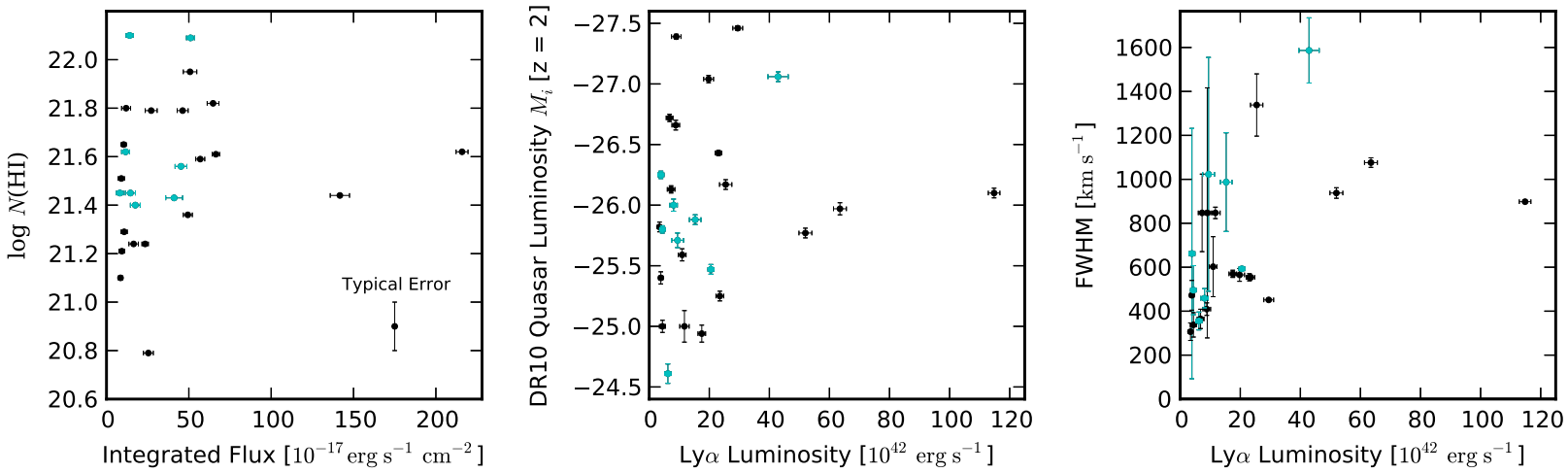

FIGURE 3.13: HI column density as a function of the integrated flux in the narrow Lyα emission peak (left), the quasar absolute luminosity as a function of the Lyα emission luminosity (center), and the deconvolved FHWM from a Gaussian fit to the narrow Lyα emission peak (right) as a function of the Lyα emission luminosity. DLAs that are part of the statistical sample are shaded in cyan.

10^{-17} erg s^{-1} cm^{-2}, we use these limits to distinguish strong and moderate narrow Lyα emission peaks.

We estimate the luminosity using the integrated flux and the luminosity distance calculated for $z_{\mathrm{Ly}\alpha}$. In Figure 3.13, we examine properties of the DLA, quasar, and emission peak as a function of the integrated flux and the luminosity.

3.5.1 Correlation with other properties

The H I column density increases mildly with integrated flux (Figure 3.13, left). An outlier with $\log N(\mathrm{H\,I}) \approx 20.8$ has moderate Lyα emission, and none of the $\log N(\mathrm{H\,I}) < 21.3$ DLAs show strong Lyα emission.
The quasar absolute luminosity, indicated by M_i $[z = 2]$, is calculated using the K-correction process outlined in Richards et al. (2006), with $\alpha_\nu = -0.5$ and $\mathrm{H}_0 = 70$ km s^{-1} Mpc^{-1}. No trend is apparent for the quasar absolute luminosity versus Lyα emission luminosity (Figure 3.13, center).
The FWHM from the Gaussian fit to the narrow Lyα emission peak is deconvolved from the BOSS spectrograph velocity resolution, 150 km s^{-1}, and the error depends on the error for the fit to the Gaussian σ parameter. Two narrow Lyα emission peaks have FWHM $> 1\,100$ km s^{-1}. Only one point at FWHM $= 662$ km s^{-1} with a large uncertainty falls between ~ 600 km s^{-1} and ~ 850 km s^{-1}.

Figure 3.14 shows the quasar absolute luminosity as a function of the FWHM. Narrow Lyα emission peaks with FWHM $\lesssim 660$ km s^{-1} are uniformly distributed across the luminosity range, while those with FWHM $\gtrsim 850$ km s^{-1} are concentrated at $\langle \mathrm{M}_i \rangle = -26.1$. The average FWHM for the narrower and wider Lyα emission peaks are $\sim$485 km s^{-1} and $\sim$1 000 km s^{-1} respectively. For the wider Lyα emission peaks, luminosity increases with increasing FWHM. Lyα emission peaks with large FWHM values are preferentially observed in high luminosity quasars.

3.5.2 Position and profile of the emission line

The center of the Gaussian fit to the narrow Lyα emission provides the Lyα emission redshift, $z_{\mathrm{Ly}\alpha}$. The velocity difference distribution for $z_{\mathrm{Ly}\alpha}$ with respect to z_{DLA} reveals that the narrow Lyα emission is within ± 500 km s^{-1} of the DLA for the majority of systems (Figure 3.15). The narrow Lyα emission peaks are blueshifted and redshifted in nearly equal numbers, and the mean velocity difference is 45 km s^{-1}.

Figure 3.16 shows the combined spectra for the associated DLAs with strong and moderate narrow Lyα emission (left and center panels respectively). The emission is symmetric,

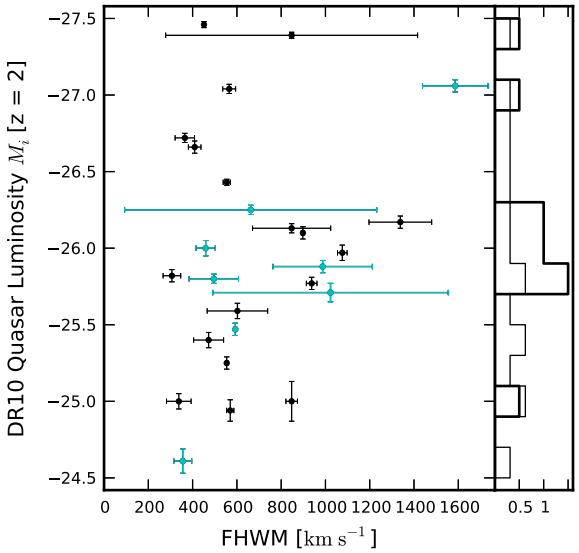

FIGURE 3.14: Quasar absolute luminosity as a function of the deconvolved FWHM from the Gaussian fit to the narrow Lyα emission. DLAs that are part of the statistical sample are shaded in cyan. The probability density distribution for the luminosity of quasars that have narrow Lyα emission peaks with FWHM $\lesssim$ 450 km s^{-1} (thin line) and FWHM $\gtrsim$ 600 km s^{-1} (thick line) is given to the right.

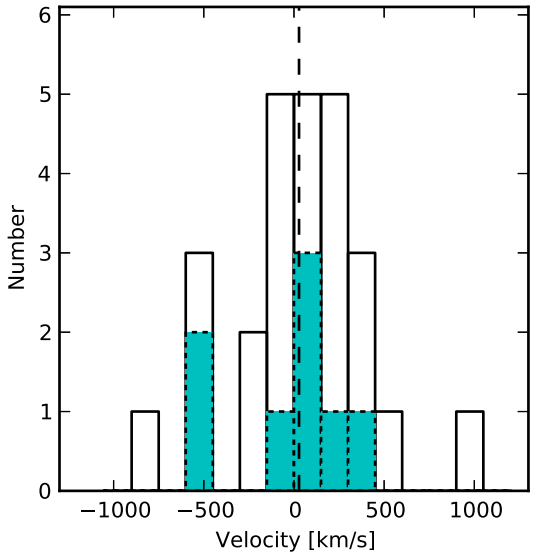

FIGURE 3.15: Velocity difference distribution for $z_{\mathrm{Ly}\alpha}$ with respect to z_{DLA}. A dashed line marks the mean velocity difference. DLAs that are part of the statistical sample are shaded in cyan.

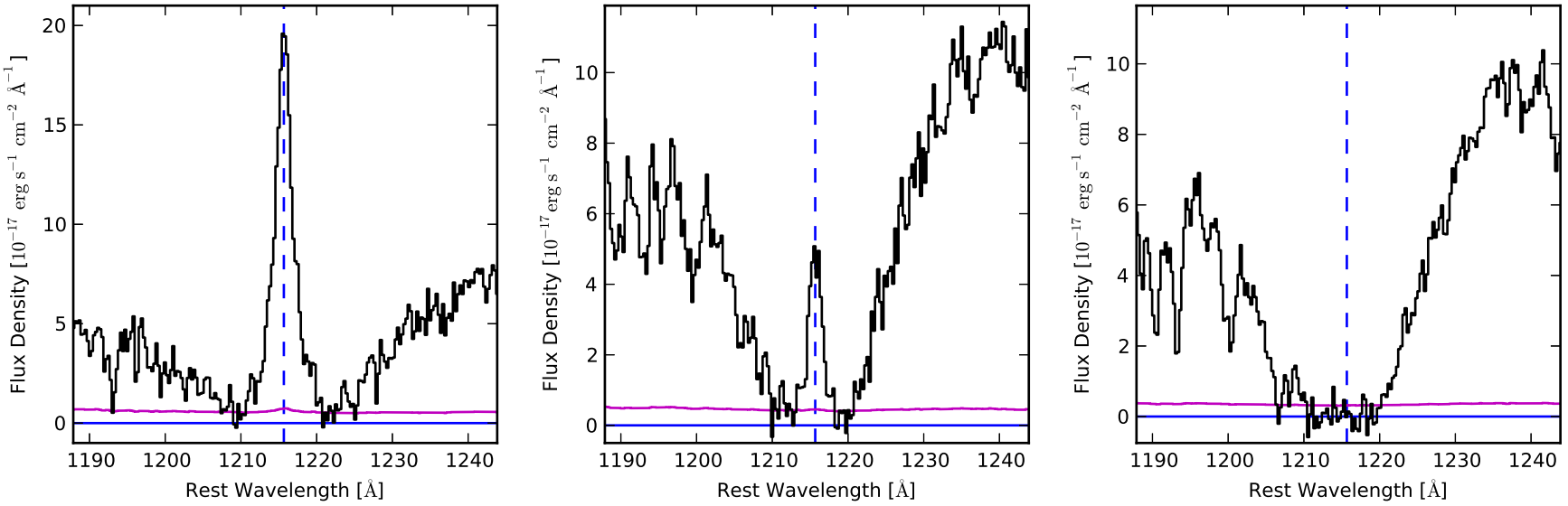

FIGURE 3.16: Left: Combined spectrum for eleven DLAs with strong Lyα emission (IF $> 40 \times 10^{-17}$ erg s^{-1} cm^{-2}). Center: Combined spectrum for fifteen DLAs with moderate Lyα emission (IF $\leq 26 \times 10^{-17}$ erg s^{-1} cm^{-2}). Right: Combined spectrum for fifteen DLAs that have an integrated Lyα emission line flux upper limit $\leq 5.5 \times 10^{-17}$ erg s^{-1} cm^{-2} and N(H I) ≥ 21.3. In all cases, the spectral flux density zero-level is corrected, and the spectra are combined with an inverse variance weighted average.

in contrast to the asymmetric line profile characteristic of Lyman Break Galaxies (LBGs; Tapken et al. 2007). This indicates that there is no H I gas in front of the emitting region to absorb the emitted Lyα photons. Small H I clouds in the host galaxy can explain the presence of the associated DLAs and also the symmetric narrow Lyα emission. Neutral hydrogen is located in front of the quasar line-of-sight, but does not fully cover the NLR or extended emission regions.

Figure 3.16 (right) presents the combined spectrum for the associated DLAs where the 4-σ upper limit on the integrated flux is $\leq 5.5 \times 10^{-17}$ erg s^{-1} cm^{-2}. At the 3-σ level, no Lyα emission is detected in the combined spectrum down to 0.79×10^{-17} erg cm^{-2} s^{-1}, which is surprising for such bright quasars. This implies that the entire host galaxy must be covered by a screen of gas unrelated to its own composition. We speculate that an independent nearby galaxy acts as a screen and blocks the Lyα emission from the quasar host galaxy.

3.5.3 Comparison with Lyman Break Galaxies

The narrow Lyα emission peaks superimposed on the troughs of associated DLAs can be compared with LBGs, which typically have redshifted emission and blueshifted absorption features at the Lyα transition. In LBGs, star-forming regions that emit Lyα photons are surrounded by H I gas. The Lyα photons are most likely to escape the galaxy when they scatter off of gas that is redshifted with respect to the emitting region.

Shapley et al. (2003) analyzed spectra from 811 LBGs at $z \sim 3$, and found that the average velocity difference between Lyα emission and low ionization interstellar absorption is 650 km s^{-1}. The deconvolved Lyα emission FWHM measured from a composite spectrum of the LBG sample, 450 ± 150 km s^{-1}, is in the range of deconvolved FWHM values measured for the narrow Lyα emission peaks observed in the associated DLAs. However, the FWHM values for this later category indicate two populations of Lyα emission peaks, one of which is comparable to and another that is more than twice as wide as the average FWHM observed in LBGs.

The narrow Lyα emission peaks revealed by associated DLAs are not systematically redshifted like those in LBGs. This, along with the symmetric emission peak profiles, is clear evidence that the emission is not significantly scattered and therefore that the emitting region is relatively void of H I gas. Lyα emission features in LBGs and associated DLAs appear to have different properties. The absorbing gas that gives rise to an associated DLA is separate from the emission region.

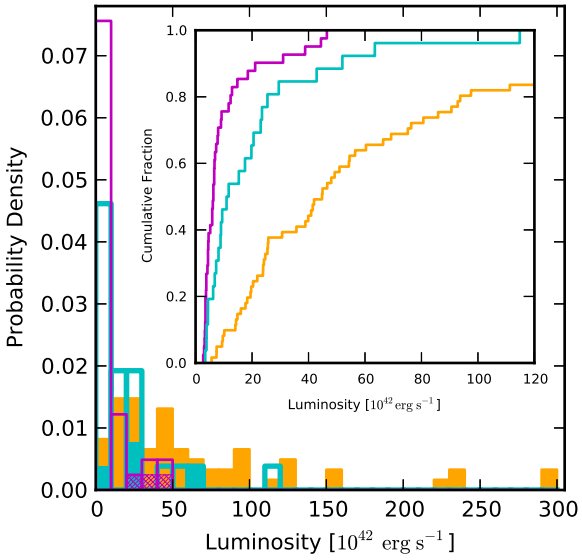

FIGURE 3.17: Distribution of Lyα emission luminosities for our sample (thick cyan), LAEs (magenta), and radio galaxies (filled yellow). Cross-hatched magenta shading denotes LAEs that have an AGN contribution (3). Cyan shading indicates quasars in our sample that are also radio-loud (4). The inset shows the K-S test cumulative fraction out to 120×10^{42} erg s^{-1} with the same color scheme. The cumulative fraction distribution is scaled for a comparison between our sample and LAEs and is truncated for the radio galaxies.

3.5.4 Comparison with Lyman-Alpha Emitters

Lyman-alpha emitters (LAEs) are objects detected on the basis of their Lyα emission. Their emission is primarily due to star formation, since these galaxies typically have negligible AGN activity except at the highest luminosities (log $L > 43.5$ erg s^{-1}, see Ouchi et al. 2008; Overzier et al. 2013). We therefore expect the luminosities for our sample of narrow Lyα emission peaks detected by using DLAs as coronagraphs to be consistently higher than what is observed in LAEs, due to the AGN ionizing gas in its host galaxy. Figure 3.17 compares the luminosities of our narrow Lyα emission peaks and a complete sample of 41 $z \sim 3.1$ LAEs from Ouchi et al. (2008), three of which have an AGN contribution. The majority of the LAEs have a luminosity less than 10^{43} erg s^{-1}. Although the luminosity distributions overlap, the two populations are only 0.85% likely to come from the same distribution, based on a K-S test (Figure 3.17, inset). Ionizing radiation from the AGN increases the average luminosity of Lyα emission in our sample beyond what is typically observed in LAEs. However, the luminosity distribution overlap indicates that the covering factor is significant for the NLR in approximately half of the quasar host galaxies in our sample with narrow Lyα emission detected. This favors the idea that the majority of associated DLAs ($\sim 3/4$) are extended and probably due to galaxies neighboring the quasar host. Only the most luminous Lyα emission peaks, where the high luminosity implies a low covering factor for the NLR, support the idea of compact associated DLAs.

3.5.5 Comparison with Radio Galaxies

Radio galaxies are known to be surrounded by extended Lyα nebulosities (van Breugel et al. 2006). The AGN is hidden, and consequently most of the emission is from surrounding gas ionized by the central AGN. Some radio galaxies also exhibit Lyα absorption but with H I column densities lower than those in our sample (Rottgering et al. 1995). We therefore compare the Lyα emission detected in our sample to that of 61 $2.0 \leq z \leq 3.5$ radio galaxies from the De Breuck et al. (2000) sample. The luminosities from our sample coincide in part with the luminosity distribution for radio galaxies, overlapping at moderate luminosities. However, the radio galaxy luminosities extend well beyond even the highest luminosity Lyα emission peak detected in our sample (Figure 3.17). It is not surprising that the radio galaxies have Lyα luminosities that surpass the luminosities we measure from narrow Lyα emission in quasar host galaxies, since the radio jet sends a huge amount of energy across several tens of kiloparsecs and provokes far-ranging Lyα emission. In quasar host galaxies, the AGN influence is predominantly at the heart of the galaxy in the NLR.

3.6 DLAs with partial coverage

If the DLA does not cover the whole BLR entirely, then some residual flux (apart from the narrow Lyα emission) could be seen in the bottom of the Lyα trough. Estimating the exact value of the spectral flux density in the DLA trough is difficult, since the zero-level is not well-defined in SDSS spectra (Pâris et al. 2012, 2011).

In a few specific cases, however, we are able to demonstrate that some residual flux is indeed present and not due to data calibration errors. The covering factor appears to be less than one for several associated DLAs. The troughs of three DLAs with detected narrow Lyα emission are well-above zero at their bottoms, while their associated Lyβ absorptions are consistent with zero within errors (Figure 3.18). The bottoms of the DLA troughs are flat, even though they are not at zero. Some BLR flux is probably transmitted, raising the spectral flux density level in the DLA and Lyβ absorptions. However, since the BLR Lyβ flux is more than five times weaker than the Lyα flux (Vanden Berk et al. 2001), this effect on the Lyβ absorption is lost in the noise. If the non-zero DLA trough were due to quasar continuum emission, which follows a power law, we would expect the Lyβ absorption to also be clearly above zero. The observations indicate that the covering factor is less than one for these DLAs.

Alternatively, if the BLR is fully covered, the residual flux could be continuum emission from the quasar host galaxy. Indeed, Zafar et al. (2011) suggest that this possibility

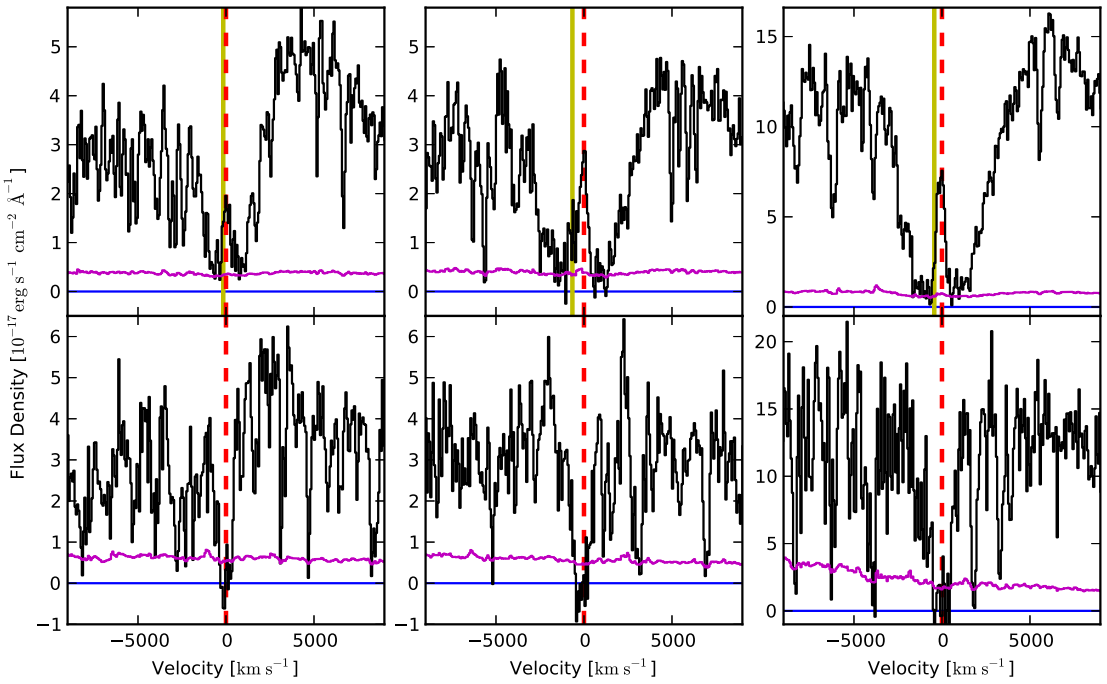

FIGURE 3.18: Damped Lyα (top) and Lyβ (bottom) absorptions in the SDSS J0839+2709 (left), J1253+1007 (center), and J1323+2733 (right) spectra. In each case, the spectral flux density in the DLA trough is well-above the zero-level, while the Lyβ absorption is at zero. No zero-level offsets are applied here. All three DLAs reveal narrow Lyα emission. A dashed red line marks the associated DLA, and a solid yellow line indicates the velocity offset of the quasar.

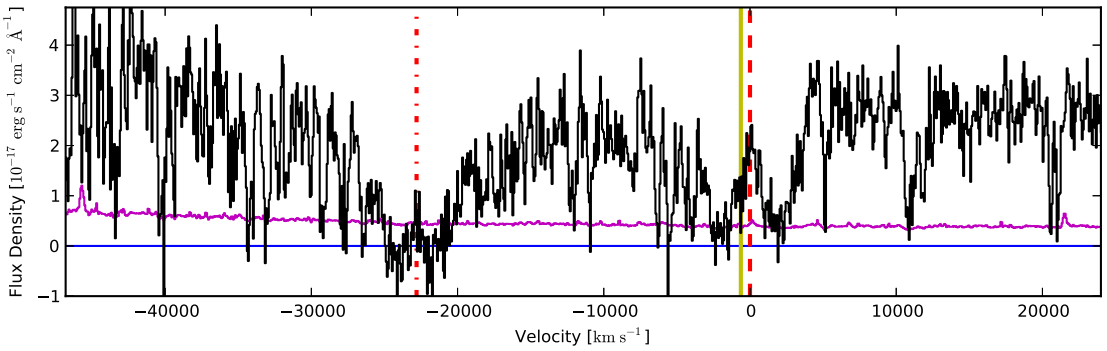

FIGURE 3.19: Two consecutive DLAs in the SDSS J0148+1412 spectrum that both reveal narrow Lyα emission. A dashed (dash-dotted) red line marks the associated (intervening) DLA, and a solid yellow line indicates the velocity offset of the quasar. The spectral flux density in the associated DLA trough is clearly above zero, whereas the trough of the intervening system at $\Delta\, v \sim -22\,800$ km s^{-1} goes to zero. No zero-level offset is applied in this Figure.

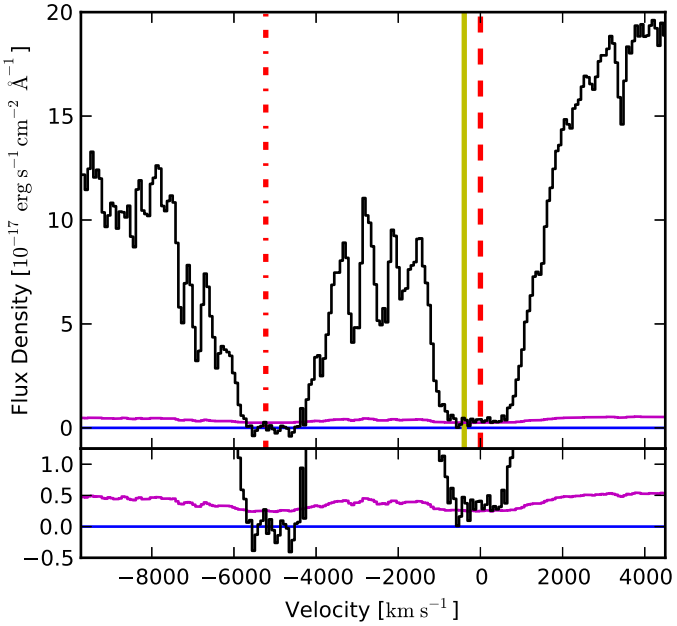

FIGURE 3.20: Two consecutive DLAs in the SDSS J1635+1634 spectrum, neither of which have narrow Lyα emission detected. The spectral flux density in the associated DLA trough is slightly above zero, in contrast to the trough of the intervening DLA at $\Delta\, v \sim -5025$ km s^{-1} (see lower panel zoom). Labeling is the same as in Figure 3.19.

could account for the trough of the associated DLA towards Q0151+048A not going to zero.

In the most striking example towards SDSS J0148+1412, an intervening DLA with a trough at zero occurs along the same line-of-sight as an associated DLA with a trough distinctly above zero (Figure 3.19). Remarkably, both the intervening and the associated DLA show narrow Lyα emission. The line-of-sight towards SDSS J1635+1634 (Figure 3.20) also has an associated and an intervening DLA, separated by only $\sim$5 025 km s^{-1}. However, no narrow Lyα emission is detected in either DLA trough. Again, the bottom of the intervening DLA trough is at zero, while the associated DLA trough is slightly above the zero-level. If this offset in the associated DLA flux is due to partial coverage, we would expect to also detect narrow Lyα emission. Potentially, the covering factor is one and the flux from the lower-redshift galaxy creates the small zero-level offset in the associated DLA. Another explanation could be that the quasar has no detectable Lyα emission.

Partial coverage of absorption systems is an interesting phenomenon that can constrain the relative sizes of the foreground and background objects (see e.g., Balashev et al. 2011). The absorber radius, $r_{\rm DLA}$, along with the column density, can then be used to estimate the H I number density, $n_{\rm H\,I}$, assuming a spherical absorber: $n_{\rm H\,I} = N({\rm H\,I})/r_{\rm DLA}$. The average H I column density for the associated DLAs with detected narrow Lyα emission is $10^{21.53}$ cm^{-2}. If the DLA absorber is on the order of 10 - 100 pc, then

$n_{\rm H\,I} \simeq 11 - 110$ cm^{-3}. For smaller-sized absorbers, we could expect to find H_2 gas, since it occurs in systems with $n_{\rm H\,I} \gtrsim 100$ cm^{-3} (Srianand et al. 2005). However, due to the low resolution and S/N in SDSS spectra, only rare systems with H_2 column density $\log N(H_2) \gtrsim 18.5$ cm^{-2} can be detected (Balashev et al., in prep).

3.7 Discussion and Conclusions

Thanks to the large number of $z > 2$ quasar lines-of-sight surveyed with SDSS-III BOSS, we have uncovered an unprecedented sample of strong associated DLAs that reveal narrow Lyα emission superimposed in their troughs. The number of associated DLAs in our statistical sample exceeds the anticipated number calculated from the N(H I) distribution function by ∼2.4. This overdensity of DLAs is consistent with expectations based on what we know about galaxy clustering.

We propose that when no narrow Lyα emission is detected in the trough of an associated DLA the absorber is a galaxy near to the quasar host, and when the absorber blocks the ∼1 pc BLR without also obscuring the extended Lyα emission the associated DLA arises from dense clouds of H I gas in the quasar host galaxy. However, efforts to distinguish two populations of DLA sources from the statistical sample are inconclusive. DLAs with the largest $W_{0,\,\rm Si\,II}$ and $W_{0,\,\rm Al\,II}$ have no Lyα emission, but this trend does not hold for $W_{0,\,\rm C\,II}$ and $W_{0,\,\rm Fe\,II}$. The low resolution and S/N of BOSS spectra limits our ability to investigate this issue. With higher resolution and higher S/N spectra, we would be able to measure the column densities and study properties, such as the depletion, in greater detail.

Geometrical effects between the quasar host and a nearby galaxy could produce a configuration that transmits the narrow Lyα emission. Potentially, the weakest narrow Lyα emission occurs when the absorber is a nearby galaxy and the strongest narrow Lyα emission occurs when the absorber is an H I cloud associated with the galactic environment. A continuum of such configurations would explain the lack of distinct characteristics for the two absorber populations.

Additionally, the NLR may be significantly extended in quasar host galaxies, beyond 10 kpc (Hainline et al. 2013; Netzer et al. 2004). Zafar et al. (2011) determined that a Lyα blob located more than ∼ 30 kpc from Q0151+048A is both the source of Lyα emission in the DLA trough and associated with the quasar host galaxy. With long slit spectroscopy, we could pinpoint the location of the narrow Lyα emission relative to the quasar and investigate the extent of emission regions in quasar host galaxies.

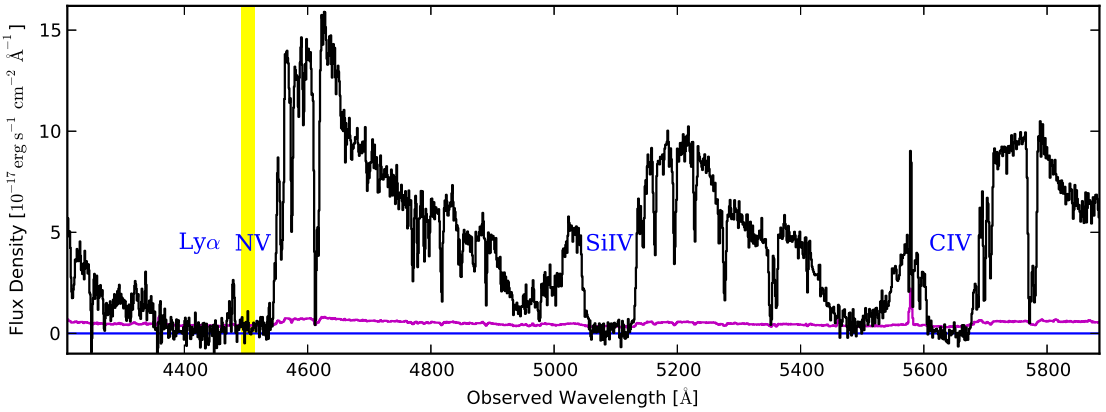

FIGURE 3.21: BAL quasar SDSS J1116+3205 where no narrow Lyα emission is detected, despite absorption troughs that go to zero (labeled). Yellow shading indicates the possible range for the quasar Lyα emission peak, which coincides with the N V BAL absorption trough.

The symmetrical profile of the narrow Lyα emission peaks, which is strikingly different from what is seen in LBGs, supports the idea that the gas in the DLA is not directly associated with the emission region and that the H I content of this emission region is low. The line profile symmetry and lack of velocity offset for the Lyα emission peak with respect to the DLA center indicate that there is not a continuous distribution of H I gas in the emission region to scatter the Lyα photons.

We have compared the Lyα luminosities in our sample to those of LAEs and radio galaxies. Roughly half of the narrow Lyα emission peaks detected by using DLAs as coronagraphs have luminosities consistent with standard LAEs. We argue that for these quasar host galaxies the DLA is extended enough to cover most of the NLR around the AGN and reduce the luminosity to a value more typical of a star-forming galaxy. The luminosities for the other half of our narrow Lyα emission peaks (25% of the total sample) are higher than what is typical for LAEs. They are comparable to, but smaller than, those of radio galaxies. This is consistent with the fact that the AGN ionizes the surrounding gas, which in turn emits Lyα photons. In these cases, the DLA probably occurs in a small cloud in the host galaxy. Radio galaxies have higher luminosities, since their jets inject energy further from the center.

Partial coverage in an associated DLA with no detected narrow Lyα emission raises the question of whether all quasars have a NLR, since a DLA absorber cannot leave the $\sim$1 pc BLR partially covered while simultaneously blocking emission across the entire NLR. We can potentially use BALs to investigate the possibility of quasars without emission from the NLR. Like associated DLAs, the gas clouds that create strong BALs in quasar spectra can serve as coronagraphs to obscure emission from the BLR and reveal NLR emission. The BAL clouds are located close to the central engine, so they cannot extend more than marginally into the NLR.

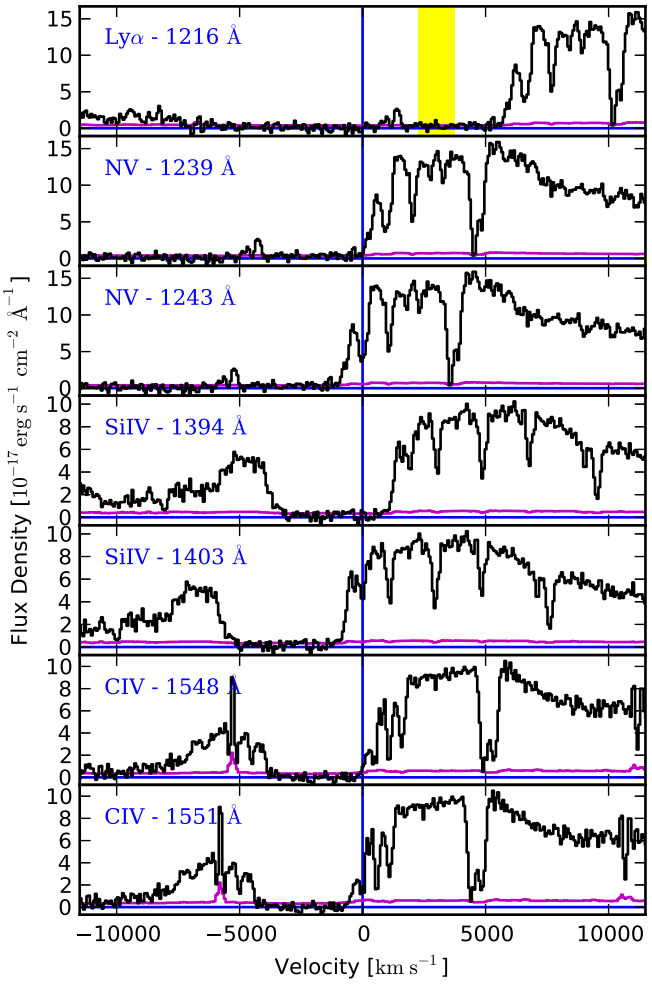

FIGURE 3.22: Velocity plots for BAL quasar SDSS J1116+3205. The absorption system that indicates the beginning of the BAL troughs is at zero velocity. The possible redshift range for the quasar is shaded in yellow in the Lyα panel (top). The flux density is consistent with zero inside this region, which coincides with the N V BAL trough.

The difficulty with using BALs as coronagraphs, however, is that the spectral flux density in their H I troughs seldom goes to zero, either because the optical depth is not high enough or because the cloud does not cover the BLR completely. We have searched for the very rare ideal occurrences where it is possible to measure Lyα flux from the NLR in a BAL trough. Figure 3.21 gives an example of a BAL quasar (SDSS J111629.37+320511.5) where no emission is detected. We identify the minimum possible quasar redshift from the C III] emission peak and limit the maximum to five times the typical blueshift for quasar C III] emission peaks, 300 km s^{-1} (Pâris et al. 2012). The small rise in flux density at ∼4480 Å corresponds to the transition between the N V and Lyα BAL troughs (Figure 3.22) and is unlikely to be narrow Lyα emission. This BAL quasar provides definite evidence that no Lyα emission is detected from the NLR of some quasars.

Before further speculating about this intriguing fact, we must check if [O III] emission is present in the BAL quasar spectra that lack narrow Lyα emission. X-shooter (Vernet et al. 2011) on the VLT would be the ideal instrument for obtaining additional spectroscopic data, since its wavelength coverage extends from the ultraviolet to the near-infrared.

Definitively interpreting why some associated DLAs reveal narrow Lyα emission while others do not is not possible with low-resolution spectra. Future observations with an Integral Field Unit (IFU) or higher resolution spectra taken with multiple position angles for each quasar are essential to make progress in this domain. Associated DLAs with narrow Lyα emission potentially offer a unique probe of the quasar host galaxy. The DLA provides a measure of the gas composition in the galactic environment, while emission from the NLR can be linked to ionization. Such systems could provide important insight into the effect of AGN feedback on their host galaxies.

TABLE 3.1: Associated DLAs

SDSS Name[a]	$z_{\rm QSO}$	M_i	E(B-V)	log N(H I) ($\rm cm^{-2}$)	$z_{\rm DLA}$	$z_{\rm Ly\alpha}$	Integ. Flux[b] $\left(\frac{10^{-17}\ \rm erg}{\rm s\ cm^2}\right)$
DR9 Associated DLAs							
Statistical Sample							
013654.00-005317.5	2.491	-26.43	-0.076	21.30	2.493	...	$\leq$ 4.6
014858.31+141235.4[c]	3.172	-27.06	-0.022	21.56	3.181	3.182	45.2
073446.02+322205.3	2.314	-26.51	0.029	21.35	2.308	...	$\leq$ 6.5
080523.32+214921.1	3.487	-28.08	0.032	21.55	3.477	...	$\leq$ 4.3
081626.02+351055.2	3.073	-26.68	0.033	21.31	3.071	...	$\leq$ 3.4
083716.51+195025.9	2.262	-24.70	-0.036	21.31	2.271	...	$\leq$ 5.2
084448.59+043504.7	2.367	-26.31	-0.058	21.33	2.379	...	$\leq$ 7.5
093859.15+405257.8	2.172	-25.88	-0.015	21.43	2.176	2.170	41.1
093924.71+430246.8	2.722	-25.71	0.014	21.45	2.717	2.722	14.5
095307.13+034933.8	2.599	-26.00	0.025	22.10	2.592	2.594	14.1
104939.76+433533.6	2.505	-25.01	-0.022	21.40	2.514	...	$\leq$ 5.1
105138.65+433921.5	2.670	-26.10	0.002	22.07	2.665	...	$\leq$ 5.3
115605.93+354538.5	2.125	-24.61	-0.042	21.40	2.126	2.128	17.5
121902.52+382822.1	3.012	-26.65	0.083	21.34	3.012	...	$\leq$ 4.4
125635.73+350604.8	2.237	-25.47	0.008	22.09	2.238	2.239	51.0
131309.25+392456.9	2.446	-25.96	0.043	21.42	2.447	...	$\leq$ 5.5
132922.21+052014.3	2.999	-26.36	-0.006	21.57	2.994	...	$\leq$ 4.2
133430.83+383819.1	2.176	-25.80	-0.028	21.62	2.181	2.180	11.6
141745.90+362127.4	3.338	-25.66	0.056	22.34	3.338	...	$\leq$ 3.0
142542.06+025701.4	2.199	-25.55	-0.046	21.35	2.205	...	$\leq$ 6.0
143253.28-005837.6	2.530	-26.50	-0.042	21.36	2.537	...	$\leq$ 5.5
143634.65+350553.8	2.212	-25.56	-0.032	21.42	2.220	...	$\leq$ 7.1
150016.39+070609.1	2.367	-26.08	0.024	21.33	2.379	...	$\leq$ 6.9
150049.63+053320.0	2.392	-26.76	0.085	21.36	2.398	...	$\leq$ 7.3
150227.84+054853.8	2.753	-26.69	0.037	21.40	2.738	...	$\leq$ 4.6
150812.79+363530.3	2.097	-25.50	-0.046	21.33	2.106	...	$\leq$ 16.1
151129.27+181138.7	3.120	-25.81	-0.020	21.39	3.134	...	$\leq$ 3.9
151843.30+050808.3	2.436	-26.79	-0.025	21.38	2.441	...	$\leq$ 6.5
154621.59+020102.9	2.821	-28.60	0.002	21.34	2.810	...	$\leq$ 3.3
163217.98+115524.3	3.101	-26.25	-0.049	21.51	3.092	...	$\leq$ 3.3
223037.78-000531.5	2.407	-26.25	0.039	21.45	2.412	2.406	8.1
020555.00+061849.3	2.223	-25.09	-0.084	20.91	2.223	...	$\leq$ 7.5
075556.95+365658.3	2.935	-25.65	-0.081	21.25	2.973[d]	...	$\leq$ 2.5
080045.73+341128.9	2.334	-26.13	-0.001	21.24	2.329	2.328	16.5
083523.26+141930.8	3.139	-28.01	-0.017	21.27	3.142	...	$\leq$ 3.8

TABLE 3.1: continued.

SDSS Name[a]	$z_{\rm QSO}$	M_i	E(B-V)	log N(H I) (cm^{-2})	$z_{\rm DLA}$	$z_{{\rm Ly}\alpha}$	Integ. Flux[b] $\left(\frac{10^{-17}\ {\rm erg}}{{\rm s\ cm^2}}\right)$
083954.59+270913.1	2.959	-26.72	-0.064	21.10	2.961	2.961	8.5
085600.89+030218.7	3.039	-25.55	-0.011	21.23	3.056	...	$\leq$ 2.9
100112.40-014737.9	2.188	-25.32	-0.038	21.21	2.199	...	$\leq$ 7.0
114639.00-010703.2	3.072	-25.23	-0.084	21.28	3.063	...	$\leq$ 2.9
115656.97+024619.8	2.377	-25.11	-0.017	21.28	2.383	...	$\leq$ 8.3
121716.25+012139.1	3.388	-26.34	-0.033	21.13	3.370	...	$\leq$ 4.0
135138.57+352338.8	2.078	-25.97	0.035[e]	21.26	2.074	...	$\leq$ 10.4
145155.59+295311.7	2.185	-25.50	0.013	21.18	2.169	...	$\leq$ 9.0
150806.90+283835.4	2.341	-25.39	-0.023	21.15	2.341	...	$\leq$ 7.1
152243.24+065138.2	2.146	-26.46	0.018	21.25	2.148	...	$\leq$ 11.3
155310.67+233013.3	3.022	-27.39	-0.001	21.29	3.023	3.025	10.7
221811.59+155420.1	2.294	-25.59	-0.023	20.79	2.302	2.304	25.4
222007.76+002331.8	2.432	-25.74	0.108	20.97	2.434	...	$\leq$ 4.8
225307.84+030843.1	2.327	-25.51	0.005	21.01	2.320	...	$\leq$ 3.9
234757.96+034910.7	2.182	-26.38	-0.072	21.52	2.155	...	$\leq$ 9.0
Additional Associated DLAs with Lyα Emission Detected							
005917.64+112407.7	3.030	-26.66	0.015	21.65	3.034	3.039	10.4
011226.76-004855.8	2.137	-25.25	-0.016	21.82	2.150	2.148	64.7
082303.22+052907.6	3.188	-25.97	0.090	21.61	3.191	3.193	66.4
083300.07+233538.5	2.459	-26.17	0.116	21.95	2.460	2.450	50.7
091137.46+225821.4	2.185	-25.82	0.000	21.51	2.188	2.190	9.0
103124.70+154118.1	2.151	-25.77	0.038	21.44	2.155	2.156	141.7
105823.73+031524.4	2.301	-25.00	-0.068	21.79	2.293	2.305	27.1
112829.38+151826.5	2.246	-26.43	0.076	21.59	2.251	2.245	56.9
115432.67-021538.0	2.187	-24.94	-0.078	21.79	2.186	2.184	46.2
125302.00+100742.3	3.023	-27.04	-0.000	21.24	3.032	3.031	23.5
132303.48+273301.9	2.625	-27.46	-0.003	21.36	2.631	2.630	49.4
150217.33+084715.4	2.264	-25.40	0.084	21.21	2.264	2.267	9.3
225918.46-014534.8	2.508	-26.10	-0.030	21.62	2.502	2.509	215.9
230709.81+020843.0	2.157	-25.00	0.000	21.80	2.165	2.164	11.9
Additional Associated DLA with No Detected Lyα Emission (Figure 3.20)							
163538.57+163436.9[c]	3.019	-28.63	-0.005	20.91	3.024	...	$\leq$ 3.4

[a] J2000 coordinates
[b] 4-σ upper limit on the integrated flux when no Lyα emission is detected.
[c] Additional intervening DLA along the line-of-sight
[d] $z_{\rm DLA}$ fitted with N(H I), not from metals
[e] An LMC, rather than SMC, reddening law may be preferred in this case.

TABLE 3.2: Rest Equivalent Widths[a]

SDSS Name	$z_{\rm DLA}$[b]	C II – 1334			Si II – 1526Å			Al II – 1670			Fe II – 2344Å		
		Fit ()	$\mathcal{F}$ (Å)	Err (Å)	Fit (Å)	$\mathcal{F}$ (Å)	Err (Å)	Fit (Å)	$\mathcal{F}$ (Å)	Err (Å)	Fit (Å)	$\mathcal{F}$ (Å)	Err (Å)
DR9 Associated DLAs													
Statistical Sample													
013654.00-005317.5	2.493	2.198	2.252	0.103	1.882	1.992	0.084	2.040	2.051	0.161	2.625	2.600	0.258
014858.31+141235.4	3.181	...	...	...	1.384	1.224	0.089	1.379	1.318	0.107	2.323	3.020	0.246
073446.02+322205.3	2.308	2.292	2.106	0.099	1.759	1.473	0.080	2.194	2.665	0.094	2.229	2.014	0.190
080523.32+214921.1	3.477	1.511	1.560	0.081	1.163	0.984	0.069	0.906	1.037	0.091	...	...	...
081626.02+351055.2	3.071	0.494	0.760	0.114	0.534	0.565	0.112	0.262	0.324	0.118	0.192	0.365	0.452
083716.51+195025.9	2.271	0.997	1.044	0.327	0.799	0.902	0.195	0.854	1.241	0.549	2.477	1.916	1.115
084448.59+043504.7	2.379	0.249	0.161	0.099	0.378	0.436	0.087	0.380	0.337	0.122	0.881	1.368	0.251
093859.15+405257.8	2.176	0.546	0.576	0.109	0.437	0.452	0.084	0.563	0.542	0.111	0.641	0.676	0.180
093924.71+430246.8	2.717	0.713	0.777	0.240	0.765	0.826	0.215	0.132	0.208	0.316	0.242	0.605	0.688
095307.13+034933.8	2.592	1.254	1.520	0.157	1.457	1.419	0.124	1.387	1.478	0.223	1.359	0.726	0.340
104939.76+433533.6	2.514	0.556	0.878	0.272	0.407	0.288	0.169	0.412	0.710	0.496	0.786	2.066	0.612
105138.65+433921.5	2.665	0.586	0.903	0.134	0.736	1.115	0.109	0.480	0.828	0.225	1.453	1.433	0.272
115605.93+354538.5	2.126	2.530	2.561	0.118	1.274	1.269	0.089	1.537	1.626	0.127	1.215	1.865	0.232
121902.52+382822.1	3.012	...	2.783	0.111	1.930	2.018	0.143	1.927	1.843	0.150	2.279	1.977	0.694
125635.73+350604.8	2.238	...	1.181	0.119	0.774	0.737	0.096	0.741	0.472	0.120	1.175	1.174	0.226
131309.25+392456.9	2.447	1.896	1.944	0.190	2.663	2.727	0.116	1.551	1.580	0.191	1.411	1.233	0.376
132922.21+052014.3	2.994	2.184	2.048	0.132	1.881	1.930	0.130	1.824	1.797	0.137	2.385	3.842	1.271
133430.83+383819.1	2.181	0.392	0.454	0.077	0.271	0.329	0.067	0.184	0.267	0.084	0.300	0.321	0.138
141745.90+362127.4	3.338	1.413	1.478	0.287	1.289	1.334	0.185	1.592	1.803	0.484	...	...	...
142542.06+025701.4	2.205	0.908	0.954	0.147	1.141	1.233	0.096	0.687	0.701	0.171	1.711	1.932	0.468
143253.28-005837.6	2.537	1.098	1.244	0.078	0.884	0.726	0.064	0.701	0.652	0.113	1.351	1.139	0.179
143634.65+350553.8	2.220	0.459	0.594	0.130	0.599	0.724	0.086	0.539	0.508	0.116	0.557	0.568	0.245

TABLE 3.2: continued.

SDSS Name	$z_{\rm DLA}$[b]	C II – 1334Å			Si II – 1526Å			Al II – 1670Å			Fe II – 2344Å		
		Fit (Å)	$\mathcal{F}$ (Å)	Err (Å)	Fit (Å)	$\mathcal{F}$ (Å)	Err (Å)	Fit (Å)	$\mathcal{F}$ (Å)	Err (Å)	Fit (Å)	$\mathcal{F}$ (Å)	Err (Å)
150016.39+070609.1	2.379	2.572	2.429	0.169	1.774	1.702	0.121	1.951	2.077	0.184	1.285	3.312	0.541
150049.63+053320.0	2.398	2.192	2.635	0.114	1.864	1.912	0.062	1.990	2.080	0.093	2.273	2.801	0.166
150227.84+054853.8	2.738	0.693	0.705	0.111	0.786	0.860	0.101	0.616	0.533	0.141	1.046	-0.150	0.168
150812.79+363530.3	2.106	0.357	0.460	0.120	0.243	0.181	0.087	0.168	0.155	0.097	0.537	0.300	0.191
151129.27+181138.7	3.134	0.643	0.649	0.229	0.495	0.288	0.193	0.669	0.621	0.285	0.156	1.131	0.631
151843.30+050808.3	2.441	0.903	1.009	0.062	0.958	1.014	0.087	0.855	0.895	0.065	1.371	1.473	0.138
154621.59+020102.9	2.810	0.648	0.720	0.035	0.654	0.644	0.038	0.743	0.809	0.050	1.077	0.977	0.085
163217.98+115524.3	3.092	1.319	2.150	0.249	1.219	1.969	0.168	0.398	2.005	0.268	1.286	-0.153	1.541
223037.78-000531.5	2.412	0.896	1.117	0.141	0.680	0.589	0.105	0.772	0.558	0.160	0.747	0.479	0.367
221811.59+155420.1	2.302	...	0.937	0.160	0.632	0.644	0.098	0.283	0.027	0.165	0.559	0.502	0.364
020555.00+061849.3	2.223	0.241	0.505	0.188	0.413	0.593	0.166	0.219	0.414	0.291	1.385	1.534	1.019
222007.76+002331.8	2.434	2.719	3.338	0.180	1.804	2.068	0.111	1.953	2.030	0.183	1.968	2.753	0.205
225307.84+030843.1	2.320	1.069	0.987	0.195	1.205	1.233	0.116	1.477	1.310	0.212	1.906	3.069	0.483
083954.59+270913.1	2.961	0.455	0.618	0.119	...	...	...	0.242	0.373	0.162	0.848	0.710	0.375
121716.25+012139.1	3.370	1.694	1.651	0.254	1.794	1.926	0.204	1.552	1.387	0.324	...	...	...
150806.90+283835.4	2.341	0.410	0.382	0.101	0.373	0.371	0.074	0.449	0.286	0.424	0.417	0.408	0.208
145155.59+295311.7	2.169	0.391	0.677	0.193	0.286	0.327	0.133	0.250	0.263	0.173	0.219	0.427	0.385
100112.40-014737.9	2.199	0.943	1.224	0.145	1.071	1.149	0.097	1.313	1.235	0.139	1.267	1.358	0.269
085600.89+030218.7	3.056	3.607	3.857	0.212	3.038	4.849	0.211	2.981	2.668	0.276	...	...	...
080045.73+341128.9	2.329	0.945	1.096	0.110	0.781	0.719	0.074	0.827	0.900	0.121	0.808	0.528	0.199
075556.95+365658.3[c]	...	...	...	...	...	...	...	...	...	...	...	...	...
152243.24+065138.2	2.148	2.031	2.748	0.103	1.211	1.071	0.061	1.159	1.210	0.082	1.412	1.397	0.114
135138.57+352338.8	2.074	1.517	1.567	0.114	1.368	1.428	0.068	1.514	1.479	0.081	2.150	2.190	0.135
083523.26+141930.8	3.142	0.725	0.778	0.045	0.701	0.685	0.041	0.710	0.675	0.054	1.050	0.565	0.197
114639.00-010703.2	3.063	0.893	1.108	0.283	0.467	1.328	0.379	0.414	0.805	0.420	...	...	...

TABLE 3.2: continued.

SDSS Name	$z_{\rm DLA}$[b]	C II – 1334Å			Si II – 1526Å			Al II – 1670Å			Fe II – 2344Å		
		Fit (Å)	$\mathcal{F}$ (Å)	Err (Å)	Fit (Å)	$\mathcal{F}$ (Å)	Err (Å)	Fit (Å)	$\mathcal{F}$ (Å)	Err (Å)	Fit (Å)	$\mathcal{F}$ (Å)	Err (Å)
115656.97+024619.8	2.383	1.303	1.551	0.180	1.052	0.983	0.111	1.357	1.401	0.197	0.513	1.172	0.346
155310.67+233013.3	3.023	0.205	0.191	0.084	0.188	0.239	0.079	0.287	0.286	0.080	0.331	0.378	0.212
234757.96+034910.7	2.155	1.583	1.813	0.082	1.395	1.336	0.072	1.307	1.305	0.076	2.042	1.825	0.238
Additional Associated DLAs with Lyα Emission Detected													
005917.64+112407.7	3.034	1.014	1.375	0.129	0.803	0.656	0.158	0.820	0.786	0.127	1.381	1.490	0.554
011226.76-004855.8	2.150	0.626	1.116	0.294	0.714	0.906	0.180	0.667	0.820	0.289	0.415	-0.096	0.614
082303.22+052907.6	3.191	2.666	2.809	0.328	1.569	1.683	0.197	2.479	2.108	0.281	...	...	...
083300.07+233538.5	2.460	1.066	1.350	0.206	...	...	...	1.239	1.251	0.201	1.501	1.349	0.199
091137.46+225821.4	2.188	1.853	1.806	0.119	1.307	1.367	0.081	1.007	0.918	0.133	0.791	1.057	0.315
103124.70+154118.1	2.155	1.342	2.089	0.158	1.022	0.922	0.104	1.115	1.189	0.120	1.124	1.388	0.247
105823.73+031524.4	2.293	0.580	1.138	0.279	0.420	0.771	0.245	...	...	...	0.887	3.283	0.776
112829.38+151826.5	2.251	3.052	3.148	0.096	2.547	2.382	0.067	2.353	2.379	0.087	2.631	2.325	0.288
115432.67-021538.0	2.186	...	2.186	0.248	0.200	0.672	0.309	0.563	0.661	0.350	0.074	-0.163	1.063
125302.00+100742.3	3.032	0.992	1.376	0.124	0.723	0.587	0.105	0.741	0.718	0.122	0.804	0.905	0.283
132303.48+273301.9	2.631	0.284	0.462	0.044	0.310	0.364	0.040	0.381	0.312	0.061	0.494	0.377	0.081
150217.33+084715.4	2.264	0.822	1.475	0.238	0.943	0.933	0.161	0.867	0.969	0.188	1.400	0.696	0.397
225918.46-014534.8	2.502	...	2.388	0.106	1.959	1.788	0.089	1.996	1.872	0.134	2.421	1.963	0.465
230709.81+020843.0	2.165	1.340	2.085	0.358	0.980	1.437	0.423	4.088	4.363	0.310	1.623	1.612	0.967
Additional Associated DLA with No Detected Lyα Emission (Figure 3.20)													
163538.57+163436.9	3.024	0.270	0.255	0.030	0.215	0.182	0.029	0.225	0.200	0.031	0.424	0.781	0.082

[a]Measured from the Voigt profile fit and from the normalized flux ($\mathcal{F}$)
[b]For systems with multiple components, $z_{\rm DLA}$ is the weighted average of the absorption redshifts.
[c]Spectrum too noisy to identify metal absorption lines.

3.8 Follow-Up Projects

The unprecedented sample of DLAs that reveal narrow Lyα emission (Table 3.1) are natural candidates for follow-up projects designed to investigate the extent of the NLR in high-redshift quasar host galaxies. Spectra taken at multiple positions angles can be used to determine the spatial extent of the narrow Lyα emission and constrain the size and geometry of the NLR. Since the gas is detected in both emission and absorption, the emission line strength can be correlated with metal abundances and depletion factors, placing constraints on stellar nucleosynthesis. The relative kinematics between emission and absorption lines may reveal evidence of outflows or gas infall. These measurements will provide a valuable comparison for lower-redshift samples.

Studies of low-redshift AGN revealed a correlation between the size of the NLR and its luminosity (e.g., Bennert et al. 2002; Schmitt et al. 2003). However, extrapolating the law to high-luminosity and high-redshift quasars gives NLR sizes larger than the host galaxy. Either the relation breaks down at high luminosity or the physical conditions in the NLR evolve with the luminosity (Netzer et al. 2004). Recent studies of obscured quasars at $z < 0.7$ find that the relationship between NLR size and quasar luminosity flattens at the high-luminosity end (Greene et al. 2011; Hainline et al. 2013, 2014; Liu et al. 2013). The NLR appears to reach a maximum size of $\sim$7 kpc, beyond which there is no longer enough gas with the correct density or ionization state to produce emission. The AGN may effectively ionize the interstellar medium over the full extent of the host galaxy. Despite several attempts to constrain the NLR size in high-redshift quasar host galaxies using lensed quasars (e.g., Yonehara 2006, and references therein), there are no direct constraints on the inner part of AGN at $z \sim 2$.

3.8.1 Observations with Magellan/MagE

Over three nights in 2012 and 2013, six quasars with associated DLAs and strong narrow Lyα emission were observed with the Magellan/MagE spectrograph. By observing the quasars at multiple position angles, the goal was to determine the extent of the narrow Lyα emission and triangulate its precise location on the sky. The instrument has excellent blue throughput, which makes it well-adapted for detecting Lyα emission around $z \sim 2.2$. The MagE spectral resolution (R = 4100 for the $1''$ slit) and spatial sampling are likewise suitable for this type of study. The quasars are generally faint, but integration times of one hour are sufficient to achieve science-quality spectra. Comparing the 2-D spectra taken at the different position angles indicates that the narrow Lyα emission is extended (Figure 3.23) for at least one of the orientations in all six cases.

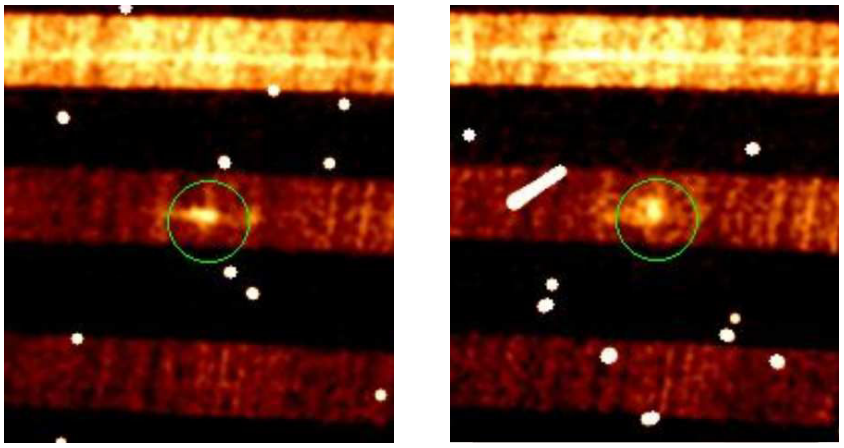

FIGURE 3.23: 2-D MagE spectra of the SDSS J1154-0215 quasar with the slit oriented North-South (left) and East-West (right). The spectral direction is horizontal, and orders closer to the top of the image cover redder wavelengths. The spatial direction is oriented along the width of each order. In the middle order, narrow Lyα emission (circled) is detected in the DLA trough. The quasar continuum is shown in the uppermost order for comparison. For the East-West slit orientation, the narrow Lyα emission is spatially extended (vertical direction in the image).

The emission region spans $\sim 10 - 20$ kpc, revealing the large-scale impact of the quasar on its environment.

3.8.2 Observations with VLT/X-shooter

The VLT/X-shooter spectrograph affords higher resolution and extended wavelength coverage. It has UVB, VIS, and NIR arms that allow simultaneous observations across the full wavelength range from 300 nm to 2.5 μm, with $R_{UVB} = 5100$ ($1.0''$ slit), $R_{VIS} = 8800$ ($0.9''$ slit), and $R_{NIR} = 5300$ ($0.9''$ slit). Unfortunately, orienting the slit at multiple position angles is not currently feasible, since the atmospheric dispersion correctors (ADC) were disabled as of August 1, 2012 after repeatedly failing. The position angle was therefore the parallactic angle at the start of the observations. X-shooter spectra for two of the quasars previously observed with MagE were obtained in Spring 2014 and will be used to investigate the relation between the absorbing gas and the host galaxy.

Accessing the narrow emission lines shifted to the near infrared will be complimentary to the Lyα analysis. The [O II] and [O III] emission lines are of particular interest, since unlike Lyα they are not affected by absorption. Furthermore, the narrow and broad components of Hβ and Hα emission in quasar host galaxies can be disentangled (see Oh et al. 2013). It will therefore be possible to measure the emission region metallicity from the [O II] and [O III] lines together with the narrow components of Hβ and Hα when the lines are present. Comparing the emission region metallicities to the metallicities of the associated DLA absorption systems can indicate whether the DLA gas is a component

of the quasar host galaxy or a different nearby galaxy. The DLA metallicity should be similar to that of the NLR if the absorbing gas is part of the same galaxy.

3.8.3 Observations with HST/WFC3

The technique of using an associated DLA like a coronagraph can also apply to an imaging analysis with narrowband filters, provided that narrow Lyα emission is detected in the DLA trough and falls within the range of one of the filters. Fortuitously, the HST/WFC3 UVIS FQ387N filter lies completely within the trough of the associated DLA towards the J1154-0215 quasar, covering only the narrow Lyα emission at $z = 2.186$ and excluding strong continuum emission from the quasar. This configuration creates an unprecedented opportunity to image a $z > 2$ quasar host galaxy while avoiding complications from PSF subtraction. Spatially-resolved observations will probe the distribution of photoionized gas in the host galaxy and potentially detect fluorescent emission in the surrounding environment, perhaps from the DLA absorber or streams of cold gas thought to fuel galaxy and black hole growth (e.g., Bournaud et al. 2011). In addition to investigating signatures feedback in the CGM, it may also be possible to constrain the host galaxy morphology. The proposal was submitted in Spring 2014 and six orbits were granted for Cycle-22 (October 1, 2014 to September 30, 2015) to obtain high-resolution deep imaging of the J1154-0215 host galaxy, which will compliment the existing MagE and X-shooter spectroscopy for this target.

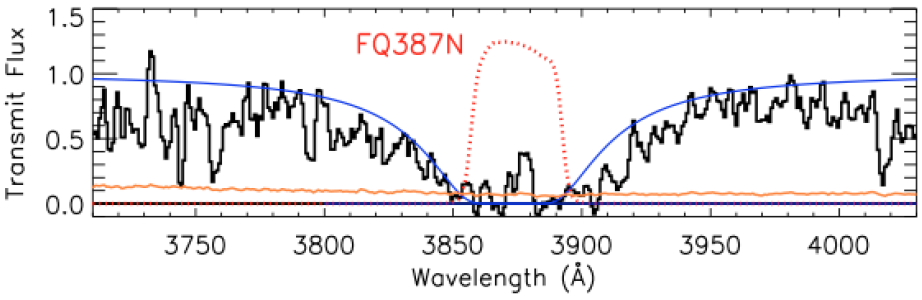

FIGURE 3.24: The BOSS spectrum of the J1154-0215 quasar with an associated DLA that reveals narrow Lyα emission from the host galaxy. The HST/WFC3 UVIS FQ387N filter (red dotted line) is well-centered on the narrow Lyα emission. Narrowband imaging will be unaffected by the quasar continuum emission.

Chapter 4

Close Line-of-Sight Pairs

4.1 Introduction

One difficulty with analyzing absorption systems along the quasar line-of-sight is that the physical distance between the quasar and the absorber is hard to constrain. Studies of narrow absorption lines with gas in a variety of ionization states observed in great detail have been able to derive limits on the distance between the quasar and the absorber using the results from photoionization models (e.g., Arav et al. 2013; Borguet et al. 2012; Edmonds et al. 2011; Finn et al. 2014; Srianand & Petitjean 2000). For DLA systems, which arise from multi-phase gas, the problem is even less constrained and any distance that can be derived is tenuous.

A technique complimentary to probing the quasar host galaxy environment with associated absorptions along the line-of-sight takes advantage of a second line-of-sight that passes close to the quasar host galaxy to detect gas in the halo at a known projected transverse distance. Accessing the quasar host galaxy environment nonetheless hinges on identifying line-of-sight pairs with small angular separations.

Fiber-fed spectroscopic surveys, like SDSS-I/II and SDSS-III BOSS, select against close pairs of quasars, since they must avoid fiber collisions. The fiber separations on a single plate are $> 55''$ and $> 62''$ for SDSS-I/II and SDSS-III BOSS respectively (Blanton et al. 2003; Dawson et al. 2013). To obtain spectra from quasars with smaller angular separations, the same area of the sky must be re-observed with a different plate. Fortunately, a significant portion of the SDSS-III BOSS footprint, 4643 deg^2 corresponding to 46% of the full survey area, is covered by two or more plates (Dawson et al. 2013). Overlapping plates covered only ∼30% of the SDSS-I/II survey area (Blanton et al. 2003), and SDSS-III BOSS has observed more than five times the number of previously known $z > 2.15$

quasars (Pâris et al. 2014). SDSS-III BOSS affords unprecedented opportunities for identifying quasar pairs.

When a higher-redshift background quasar and a lower-redshift foreground quasar have a small angular separation, the background quasar spectrum probes gas in the vicinity of the foreground quasar host galaxy. This scenario has been the focus of the "Quasars Probing Quasars" project (Hennawi & Prochaska 2007, 2013; Hennawi et al. 2006a; Prochaska & Hennawi 2009; Prochaska et al. 2013a,b).

The "Quasars Probing Quasars" analysis does not find evidence of strong ionization in the transverse direction from the host galaxies, and suggests instead that quasars emit anisotropically. Optically-thick H I absorbers are significantly more prevalent in samples of background quasar spectra at projected transverse distances $\lesssim 1$ Mpc from the foreground quasar than in the $z \sim 2$ Lyα forest (Hennawi & Prochaska 2007; Prochaska et al. 2013a). Conversely, optically-thick absorbers along a quasar line-of-sight are less common within $\sim$3 000 km s^{-1} due to a proximity effect (Dall'Aglio et al. 2008a,b; Faucher-Giguère et al. 2008a; Prochaska et al. 2008). Furthermore, Hennawi & Prochaska (2013) failed to detect large-scale diffuse Lyα emission near foreground quasars from optically-thick absorbers apparent in the background quasar spectra, implying that the absorbing gas is shadowed from the quasar radiation. Finally, based on a detailed study of a line-of-sight pair separated by 13.3″ (108 kpc), Prochaska & Hennawi (2009) estimate that the mass of cold $T \sim 10^4$ K gas is a non-negligible portion of the total baryon supply in the foreground quasar halo, and a larger sample analyzed in (Prochaska et al. 2013b) confirms the substantial presence of cold gas and metal enrichment from low-ionization transitions.

Note, however, that Adelberger et al. (2006) serendipitously discovered a faint background quasar 49″ from the quasar HS1549+1919 ($z \simeq 2.84$) while taking spectra for a galaxy survey. The DLA in the background quasar spectrum shows double-peaked Lyα emission that is potentially provoked by the the incident quasar radiation.

These results highlight what projected close line-of-sight pairs can reveal about quasar host galaxy environments.

4.2 Close Line-of-Sight Pairs in SDSS-III BOSS

In order to detect a BAO signal in the Lyα forest, SDSS-III BOSS focused on high-redshift quasars. The survey required a minimum surface density of 15 quasars deg^{-2} at redshifts $2.15 \leq z \leq 3.5$ to make the measurement (McDonald & Eisenstein 2007). After the first 2.5 years of operations, the mean density of $z > 2.15$ quasars in the

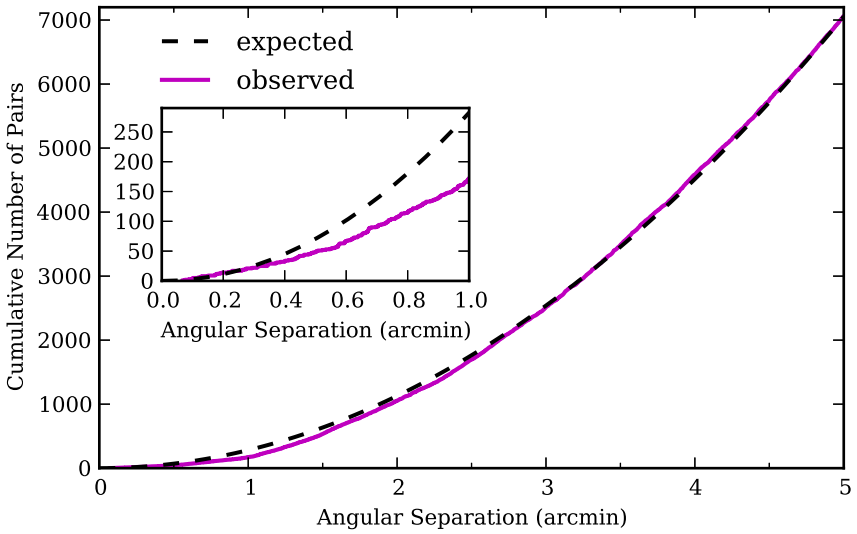

FIGURE 4.1: The number of line-of-sight pairs with angular separations $2.5' \lesssim \theta \leq 5'$ from a preliminary sample of ∼35 000 quasars at $z > 2.15$ (dashed magenta line) increases as R^2, as expected for a random distribution (solid black line). Fewer pairs than expected are observed below ∼2.5′, likely due to tiling constraints that select against close line-of-sight pairs. The minimum fiber separation is 62″, so the same region must be observed with two different plate to obtain spectra of close pairs. At the smallest scales (inset), the number of observed pairs again appears to follow R^2. Quasar clustering produces more pairs at small scales. (Figure to be updated using the DR12 quasar catalog)

DR10 catalog was 16.3 deg^{-2} (Pâris et al. 2014). Since SDSS-III BOSS is observing an unprecedented 160 000 quasars at $z > 2.15$, the prospects are good for identifying pairs of lines-of-sight with small angular separations.

Assuming that quasars are randomly distributed, the number of line-of-sight pairs increases with the square of their separation, R.

$$n_{\rm pairs} = \sigma_{\rm QSO} * \pi R^2 * N_{\rm QSO}/2 \tag{4.1}$$

where $\sigma_{\rm QSO}$ represents the surface density of quasars on the sky and $N_{\rm QSO}$ is the total number of quasars in the survey. Around 1 000 close line-of-sight pairs could be detected within 1′ for the expected values of 15 quasars deg^{-2} and 160 000 total quasars, including ∼30 pairs within 10 ″. The predictions based on a random distribution may be a lower limit, since small-scale quasar clustering (Hennawi et al. 2006b; Myers et al. 2008; Shen et al. 2010) will increase the number of observed close line-of-sight pairs. However, a comparison between the expected and observed distributions of close line-of-sight pairs from a preliminary sample of ∼35 000 quasars at $z > 2.15$ (Figure 4.1) illustrates the competing effects of tiling constraints that select against close line-of-sight pairs and quasar clustering that increases the number of pairs at small scales. The SDSS-III BOSS sample of close line-of-sight pairs should nonetheless be large enough to permit

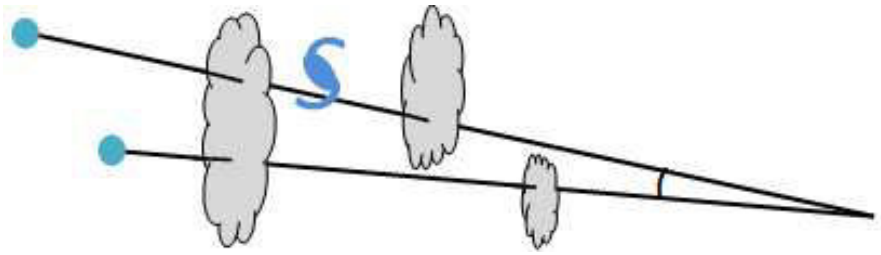

FIGURE 4.2: Lines-of-sight from two quasars traverse the same intervening structure when the angular separation between them is small.

statistically significant sub-samples. Additional selection criteria can then be applied, depending on the scientific goals for the analysis. One application of close line-of-sight pairs is to study correlations in the Lyα forest absorptions that occur at the same wavelengths in both spectra.

4.2.1 The Transverse Correlation Function for Lyα Forest Absorptions

Physical distances can be measured along the line-of-sight from recessional velocities due to the expansion of the universe, as well as in the transverse direction from angular separations. In both cases, a cosmological model is necessary to go from the measured quantity to a physical distance. If the universe is homogeneous, then the cosmological parameters that allow this transformation must be the same. The cosmological parameters, and thereby the geometry of the universe, can be constrained if the measured recessional velocities or angular separations are associate with a known physical distance. It is therefore of extreme interest to identify standard rulers.

The IGM is a source of standard rulers that can be used in an Alcock & Paczynski (1979) test, since IGM gas follows the dark matter gravitational potential and traces its structure. Correlating Lyα forest absorptions gives a measure of the clustering in the IGM (e.g., Rollinde et al. 2003). The correlation function can be calculated along the line-of-sight using velocity measurements and in the transverse direction with angular separations (e.g., Coppolani et al. 2006). The correlation function should be the same in both directions if the universe is homogeneous, and therefore serves as a standard ruler for the Alcock & Paczyński test.

The correlation function along the line-of-sight is easily obtained. With large numbers of quasar spectra available and so many absorptions in the Lyα forest, the statistic along the line-of-sight is good. Furthermore, this correlation function can be calculated for quasars observed at high spectral resolution.

Measuring correlations in the transverse direction is more complicated, because pairs of quasars are necessary. If the quasars in a pair have a small angular separation,

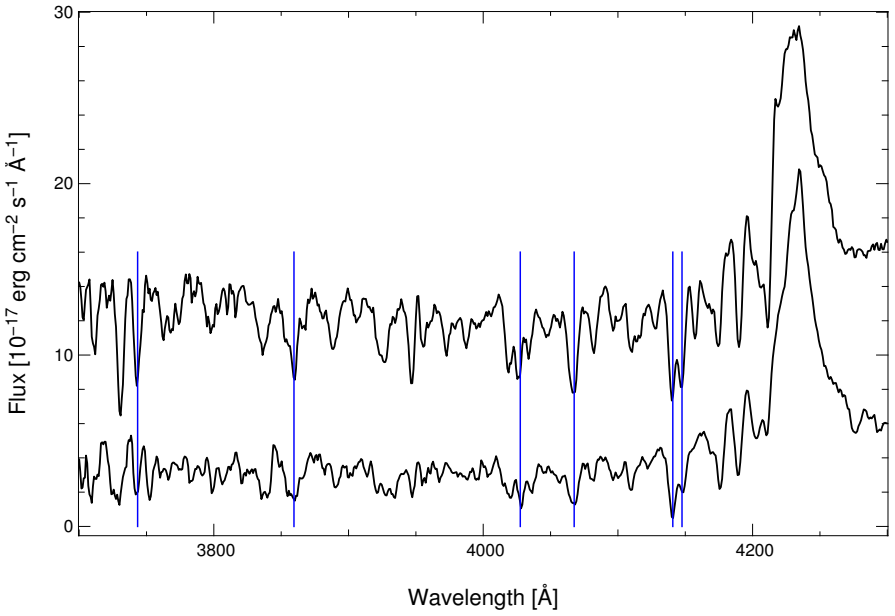

FIGURE 4.3: Blue markers indicate examples of correlated absorptions in the Lyα forests of two minimally-separated SDSS-III BOSS quasars at $z = 2.48$.

then it is possible for their lines-of-sight to pass through the same intervening structure (Figure 4.2; Petitjean et al. 1995). When this occurs, an absorption line appears at the same wavelength in each spectrum. In Figure 4.3, the marked absorption lines each represent intervening structures common to both lines-of-sight. Correlating the absorptions directly opposite in the two Lyα forests gives one measure of the correlation function per quasar pair.

The transverse correlation function (Equation 4.2) depends on the angular separation (θ) between a pair of quasars. The correlation coefficient (ξ) is determined from the normalized flux ($\mathcal{F}$) measured at the same wavelength (λ) in each spectrum. Since the flux for one quasar is compared to the flux directly opposite in the spectrum of its pair, the overlapping Lyα forests are at constant angular separation.

$$\xi_f(\theta) = \langle (\mathcal{F}(\theta, \lambda) - \langle \mathcal{F} \rangle)(\mathcal{F}(0, \lambda) - \langle \mathcal{F} \rangle) \rangle_\lambda \tag{4.2}$$

Absorptions at the same place in each spectrum produce positive values of ξ, while mismatched normalized flux levels contribute to a negative ξ. Averaging the values calculated pixel by pixel in the overlapping Lyα forest gives a measure of absorption line correlation. Each quasar pair yields one data point in the transverse correlation function. Many pairs are necessary to have a robust sample of standard rulers in the intergalactic medium, but these systems are relatively rare.

Coppolani et al. (2006) previously studied the transverse correlation function for a sample of 32 quasar pairs at an average redshift of $z \sim 2.1$ (Figure 4.4). The separation

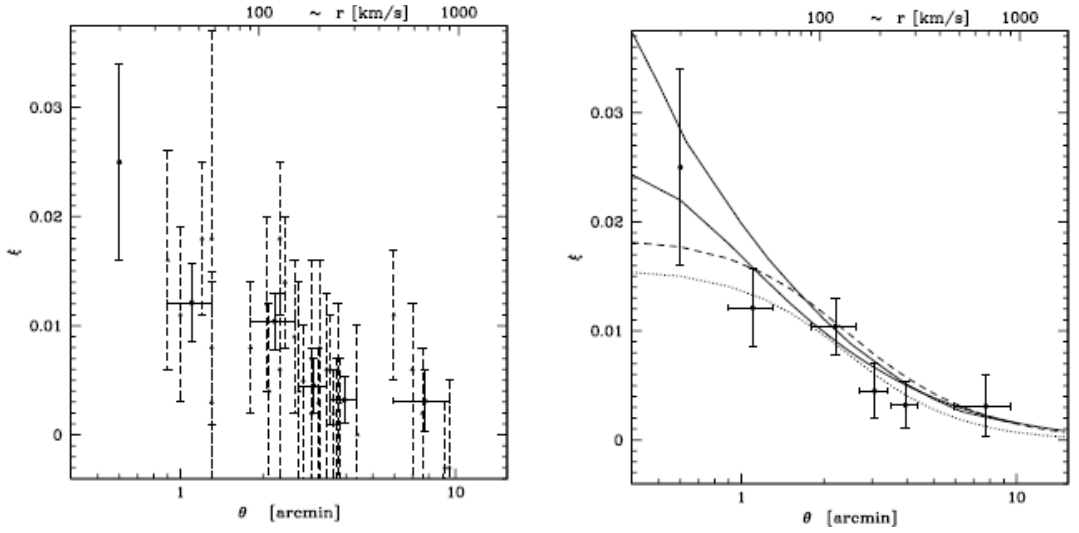

FIGURE 4.4: Left: The observed transverse correlation coefficient for 32 individual pairs (black triangles, dashed error bars) and a binned estimate of the transverse correlation function (solid error bars). Right: The binned estimate of the observed transverse correlation function is shown together with the estimate of the transverse correlation function from a hydrodynamical simulation (thick solid curve) and linear predictions for $\Omega_{\rm m} = 0.1$, 0.3 and 1 (thin solid, dashed and dotted lines, respectively, assuming a flat universe: $\Omega_\Lambda + \Omega_{\rm m} = 1$. (Figures from Coppolani et al. (2006).)

between the pairs ranged from 0.6 to 10 arcminutes, which corresponds to physical distances spanning 300 kpc to 5 Mpc. Although this was the best sample available at the time, the correlation function is nonetheless sparsely sampled, particularly at angular separations less than one arcminute, where there is only one data point. Obtaining more quasar pairs is essential to achieving a robust transverse correlation function that can place constraints on the cosmological parameters.

A preliminary investigation of close line-of-sight pairs in SDSS-III BOSS was based on 50 604 quasar spectra that were available as of February 24, 2011. The number of pairs with angular separations of less than five arcminutes was 14 583. Additional selection criteria were applied to identify a sample best-suited for evaluating the transverse correlation function:

- $z \geq 2.3$
- $\Delta z \leq 0.5$
- No DLA flagged during Visual Inspection
- No BAL flagged during Visual Inspection (BAL_FLAG_VI=0)
- S/N > 1.0
- $0.55 \leq \langle F \rangle \leq 0.95$

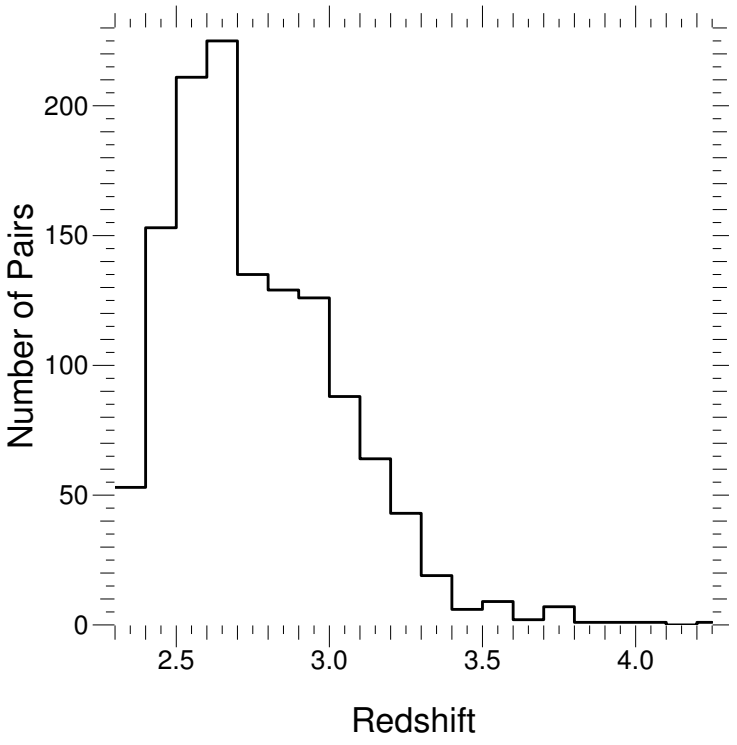

FIGURE 4.5: Number of quasar pairs within five arcminutes as a function of redshift.

The quasars are required to have a redshift greater than 2.3, so that spectrum sufficiently covers the Lyα forest. Additionally, the redshift difference for a pair must be less than 0.5. Otherwise, the purely Lyα forest of the higher-redshift pair will end as the Lyα forest of the lower-redshift pair begins, leaving no overlap. Once the Lyβ forest begins and Lyβ absorptions are interspersed with Lyα absorptions, it can no longer be assumed that corresponding absorptions are due to the same gas cloud. Broad absorption lines and DLAs likewise contaminate the correlation function measurement, since neither are related to IGM gas. The BOSS visual inspection processes, which is discussed in Pâris et al. (2012), identifies BALs and DLAs. The visual inspection flags were used to eliminate spectra with these absorption features from the pair sample. After these initial selection criteria, 1 197 pairs within five arcminutes remained. Figure 4.5 shows the redshift distribution for the subsample, which peaks at $z = 2.76$.

The S/N in BOSS spectra is often very low, particularly in the Lyα forest. Poor S/N contributes greatly to correlation function scatter; the dispersion is the highest when the S/N at blue wavelengths is the lowest. Having good S/N at red wavelengths is also important for estimating the quasar continuum and normalizing the spectra. Only spectra with signal-to-noise ratios greater than one at both red and blue wavelengths are retained for the correlation function calculation, but this reduces the number of pairs by 46.8%. Insufficient S/N in the Lyα forest is the main reason for rejecting pairs (Figure 4.6).

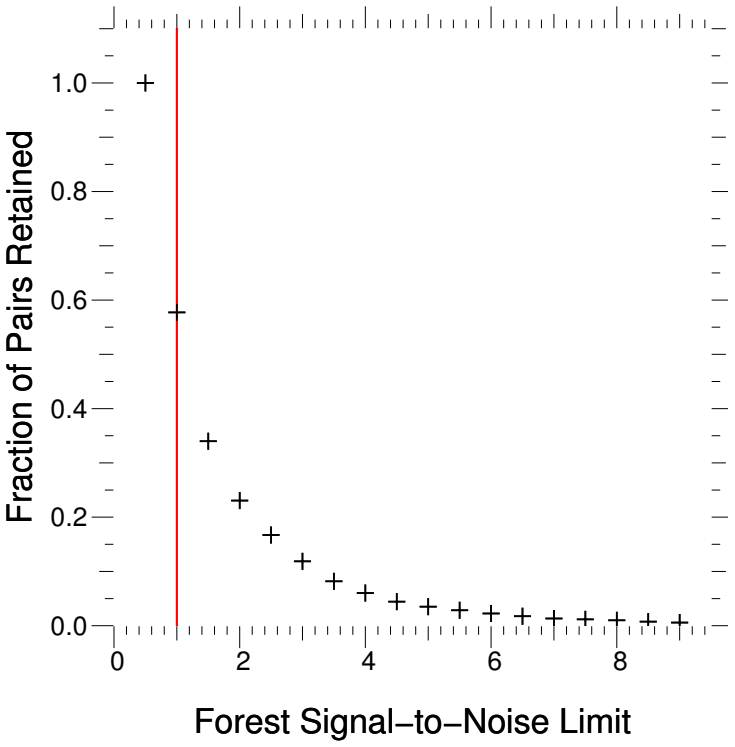

FIGURE 4.6: Keeping only quasar pairs that both have S/N > 1 in the Lyα forest reduces the total number of pairs by over 40%. The number of pairs decreases dramatically for stricter S/N cuts.

Choosing an appropriate continuum for normalizing the spectra is the most challenging aspect of the transverse correlation function calculation. The average normalized flux is a good indicator of whether a continuum is reasonable. For $z = 2.5$ quasars, $\sim$0.25 of the flux in the Lyα forest is absorbed, and the average normalized flux level should therefore be $\sim$0.75 (Faucher-Giguère et al. 2008b; Palanque-Delabrouille et al. 2013b). Continua are cut from the correlation function calculation if their average normalized flux is less than 0.55 or greater than 0.95. An average normalized flux of one implies that no absorptions are observed, which is not realistic in the Lyα forest. The number of pairs as a function of angular separation decreases dramatically after all the selection criteria are applied (Figure 4.7).

For each pair, the overlapping Lyα forest region was identified. A continuum was fitted to each spectrum, and the spectra were normalized. The average normalized flux across the overlapping pixels was determined. Then the correlation coefficient for the pair was calculated according to Equation 4.2. Individual correlation coefficients were binned to estimate the transverse correlation function out to five arcminutes for a total of 691 pairs (Figure 4.8). The transverse correlation function shows the expected general distribution of structure in the intergalactic medium. The scatter is large in the first bin ($\theta \leq 45''$), since it only contains 15 pairs. The statistics will improve further with

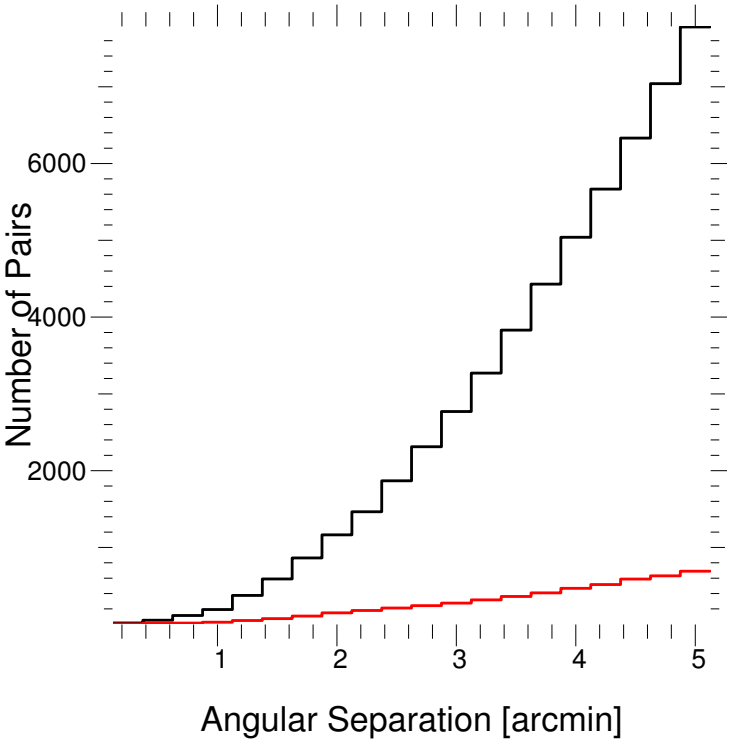

FIGURE 4.7: The total number of quasar pairs in the available sample (black) compared with the number of pairs after the selection criteria have been applied (red).

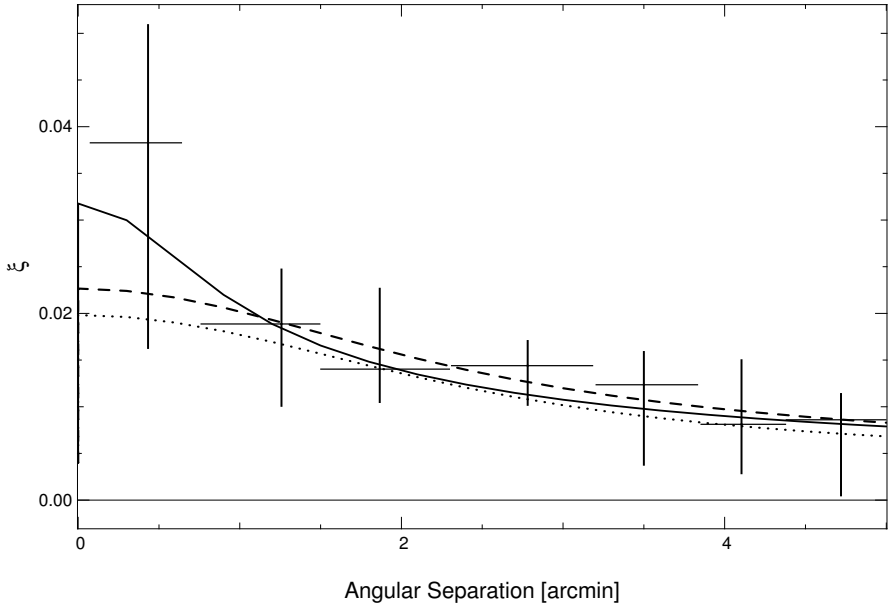

FIGURE 4.8: The transverse correlation function has fifteen pairs are in the first bin, ∼50 in the second, and ∼100–120 in the following bins. Error bars show the inner-quartile range of each bin. Curves represent the transverse correlation function estimated from a linear structure formation model with $\Omega_m = 0.1$ (solid line), $\Omega_m = 0.3$ (dashed line) and $\Omega_m = 1$ (dotted line).

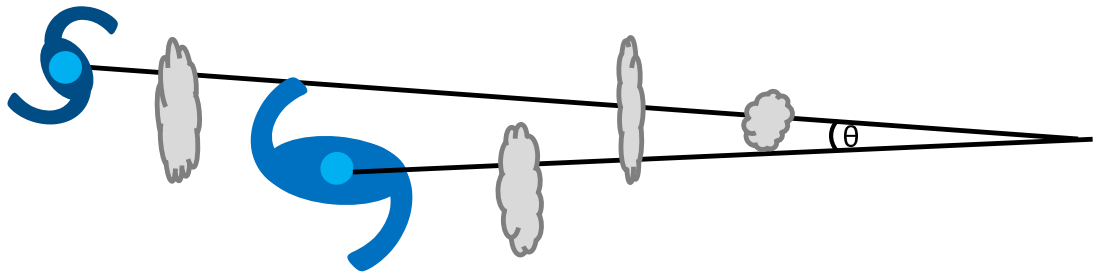

FIGURE 4.9: For pairs with the smallest angular separations (θ), the line-of-sight from the higher redshift background quasar may pass through the galactic environment of the lower redshift foreground quasar.

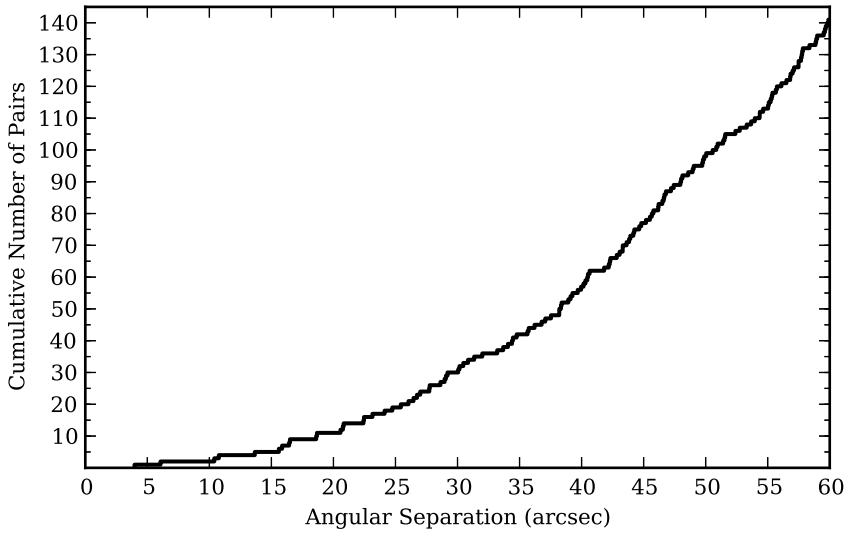

FIGURE 4.10: Cumulative number of close line-of-sight pairs at $z > 2.0$ with offset redshifts and a maximum angular separation of $60''$.

the full SDSS-III BOSS quasar sample, which has ∼3 times as many sight lines as this preliminary sample. A robust comparison with the correlation function along the quasar lines-of-sight, leading to constraints on cosmological parameters, will be possible.

4.2.2 Quasar Host Galaxy Environments

By applying different selection criteria, the same initial sample of 50 604 SDSS-III BOSS quasar spectra was used to identify pairs where the line-of-sight from a higher redshift background quasar probes the galactic environment of a lower redshift foreground quasar (Figure 4.9). First, only quasars with $z > 2.0$ were considered to ensure that the Lyα forest would begin before the blue spectral cutoff at 3 600 Å. Then a minimum redshift difference of $\Delta z \geq 0.04$ was imposed, since it needs to be obvious which quasar is in the foreground and which is in the background. Quasars with similar redshifts are therefore avoided. For line-of-sight separations $\theta \leq 1'$, 142 pairs that meet these criteria were identified (Figure 4.10).

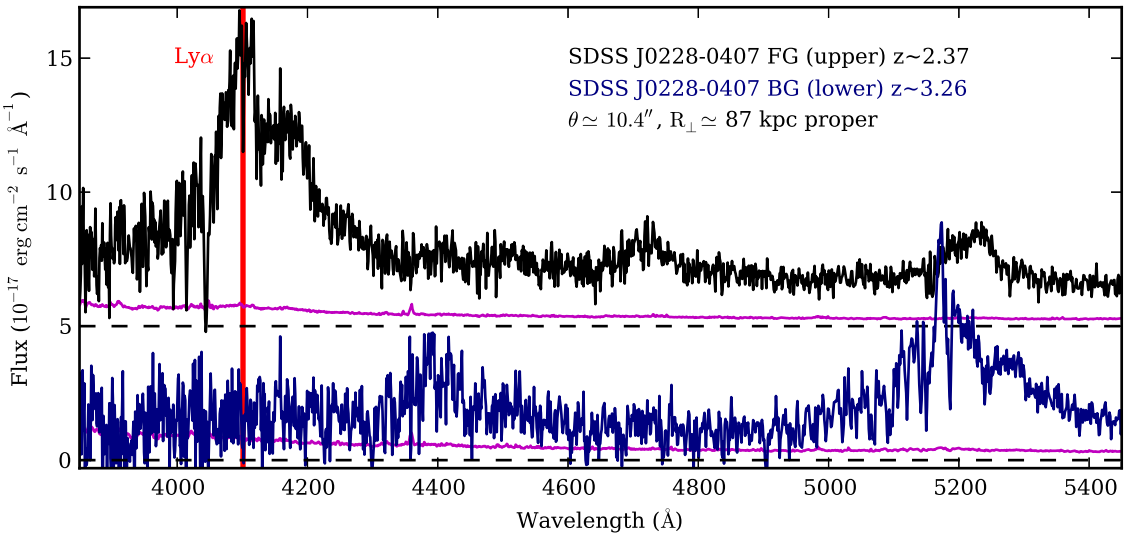

FIGURE 4.11: No significant Lyα absorption is detected in the SDSS J0228-040 BG quasar spectrum at the redshift of the FG quasar Lyα emission peak.

Four of the pairs have angular separations within $\theta \lesssim 10''$ and physical separations $<$ 100 kpc: SDSS J0239-0106, SDSS J2338-0003, SDSS J0228-0407, and SDSS J0913-0107. Three show significant Lyα absorptions (DLA or sub-DLA systems) in the background quasar spectrum at the redshift of the foreground quasar, suggesting that the background quasar line-of-sight passes near to the foreground quasar host galaxy. Surprisingly, there is no appreciable excess of Lyα absorption in the background quasar spectrum coincident with the foreground quasar Lyα emission peak for the SDSS J0228-0407 pair (Figure 4.11). For the three lines-of-sight that do show evidence of probing the quasar host galaxy environment, the N(HI) is estimated and associated metal absorption lines are identified in the BOSS spectra. These unusual systems are excellent targets for follow-up with a higher resolution instrument, because they offer an opportunity to study feedback processes, including the gas dynamics and enrichment, in detail at smaller transverse distances than have been probed so far.

4.3 VLT/X-shooter Follow-Up Observations

The three closest line-of-sight pairs with DLA/sub-DLA absorptions were proposed for follow-up observations with VLT/X-shooter. The X-shooter spectrograph has UVB, VIS, and NIR arms that allow simultaneous observations across the full wavelength range from 300 nm to 2.5 μm, making it uniquely adapted for the observing goals. With the 11″ slit length, both quasars in the pairs SDSS J0239-0106 ($\theta = 3.96''$) and SDSS J2338-0003 ($\theta = 6.06''$) can be observed simultaneously, efficiently using telescope time.

TABLE 4.1: Log of X-shooter observations for ESO program 089.A-0855. For pairs J0239-0106 and J2338-0003, the quasars were observed simultaneously, whereas the quasars were observed separately for pair J0913-0107. Observations were conducted in stare mode for all arms.

Pair	θ [arcsec]	Quasar Coordinates	Pos.	r Mag	$z_{\rm em}$	$z_{\rm abs}$	Observing Dates	Arm	$T_{\rm exp}$[s] $\times$ $N_{\rm exp}$	$T_{\rm exp,tot}$ [h]
J0239-0106	3.96	J023946.44-010644.1	FG	20.51	2.296	–	2012 Nov. 10 - 11,	UVB	4080×3	3.40
		J023946.42-010640.5	BG	20.08	3.127	2.296	2013 Jan. 2 - 3	VIS	4080×3	3.40
								NIR	600×18	3.00
J2338-0003	6.06	J233845.44-000331.8	FG	21.51	2.445	–	2012 Sept. 12 - 13,	UVB	3000×3	2.50
		J233845.18-000327.1	BG	19.62	2.979	2.445	Sept. 17 - 18	VIS	3000×3	2.50
								NIR	600×15	2.50
J0913-0107	10.74	J091338.30-010708.7	FG	20.49	2.750	–	2013 March 30 - 31,	UVB	3000×2	1.67
							March 31 - April 1	VIS	3000×2	1.67
								NIR	600×10	1.67
		J091338.30-010708.7	BG	20.38	2.916	2.750	2013 April 11 - 12,	UVB	3720×5	5.17
							April 29 - 30,	VIS	3720×5	5.17
							April 30 - May 1	NIR	600×30	5.00

The UVB and VIS arms cover the DLA absorptions at blue wavelengths and their associated metal lines at red wavelengths. The NIR arm gives access to the [O II] λ3727 and [O III] $\lambda\lambda$4959,5007 quasar emission lines that permit the most precise redshift determinations. The entire spectral range is necessary to best analyze gas kinematics and metallicities in the quasar host galaxy environments.

The BOSS data have spectral resolution $\sim$2 000 and average S/N $\sim$ 3.8. Although it is possible to measure equivalent widths for the metal absorptions, line blending and confusion with noise prevent serious metallicity estimates. X-shooter has more than twice the resolution of the BOSS spectrograph in the blue (R_{UVB} = 5 100 for the 1.0″ slit width) and over four times the resolution in the red (R_{VIS} = 8 800 for the 0.9″ slit width). Metallicities can be derived using several transitions of the same species, since the X-shooter spectral range covers many lines. High S/N ($>$ 25) is necessary to decompose the absorption profiles and measure column densities, given the intermediate resolution of X-shooter spectra. At R $\simeq$ 5 000 $-$ 9 000, components in the absorption system are often blended and/or saturated. Nonetheless, fitting the absorption profiles from multiple transitions will constrain the gas kinematics.

The proposal was awarded 15 h of observing time for the Spring 2012 semester and carried over into Fall 2012 (ESO program 089.A-0855). Table 4.1 gives a log of the observations. For the pairs with the two smallest separations, J0239-0106 and J2338-0003, the quasars were observed simultaneously. The J0913-0107 quasars were observed separately, since they could not both be placed in the slit at the same time.

The seeing was estimated by fitting a Gaussian to the quasar trace in the 2-D spectrum and measuring the FWHM. Across a wavelength range, the trace was averaged with inverse variance weighting. The seeing was calculated for the individual exposures and then averaged to get a final estimate. Note that the seeing measured this way may not reflect exactly what happens in the spectral direction. Figure 4.12 presents the individual and weighted average seeing measurements for the J0913-0107 BG quasar sprectra in the three arms. The average seeing is smaller than the slit widths (1″ in the UVB and 0.9″ in the VIS and NIR arms), especially in the optical. The seeing in the NIR is somewhat larger than anticipated, compared to the values for the UVB and VIS, probably due to flexure in the instrument. The measured seeing may therefore be enlarged compared to the true seeing.

The spectral resolution is likely higher than the nominal value for the UVB and VIS arms, since the average seeing is smaller than the slit widths. Fitting telluric absorption lines in the VIS spectrum with a double Gaussian profile constrains the resolution for this arm. In the UVB, a lower limit on the resolution can be estimated by fitting the most narrow absorption lines observed in the spectrum with a Gaussian profile.

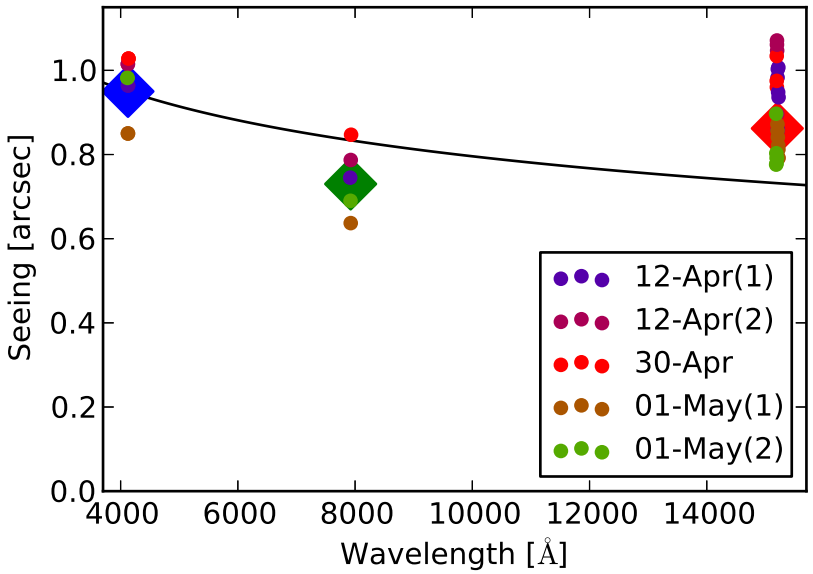

FIGURE 4.12: Average seeing estimated from the five exposures (30 in the NIR) of the J0913-0107 BG quasar. Large blue, green, and red diamonds indicate the average seeing for the UVB, VIS, and NIR arms. Individual points mark the seeing for individual exposures with dates as indicated. The black line traces the expected seeing ($\propto \lambda^{-0.2}$) based on the average value in the VIS arm.

For components with small intrinsic Doppler parameters, the absorption line width is dominated by the resolution.

4.3.1 Pair SDSS J0239-0106

The SDSS J0239-0106 line-of-sight pair has the smallest separation currently known for projected quasar pairs, $\theta = 3.96''$. The corresponding physical distance is 33 kpc at $z = 2.30$. A DLA due to gas associated with the foreground quasar galactic environment occurs at this redshift in the spectrum of the background quasar (Figures 4.13, 4.14). Because of the redshift difference between the two quasars, $\Delta z = 0.83$, the DLA is in the Lyβ forest. Only the Lyα transition appears in the spectrum before a higher redshift LLS fully absorbs the quasar flux. The DLA column density estimated from the BOSS spectrum is log N(H I) = 20.4, and log N(H I) = 20.26 ± 0.14 is measured from the higher resolution X-shooter spectrum (see below).

Hennawi et al. (2006a) identified this pair in the SDSS Data Release 3 quasar catalog (Schneider et al. 2005) and observed the background quasar with Keck/LRIS. In their low resolution spectrum with FWHM $\simeq$ 500 km s^{-1}, they identified metal absorptions at $z = 2.3025$ and measured log N(H I) = 20.45 ± 0.2 for the DLA. The higher resolution X-shooter spectrum provides better constrains on the H I column density and on the system redshift from more detailed absorption line fits.

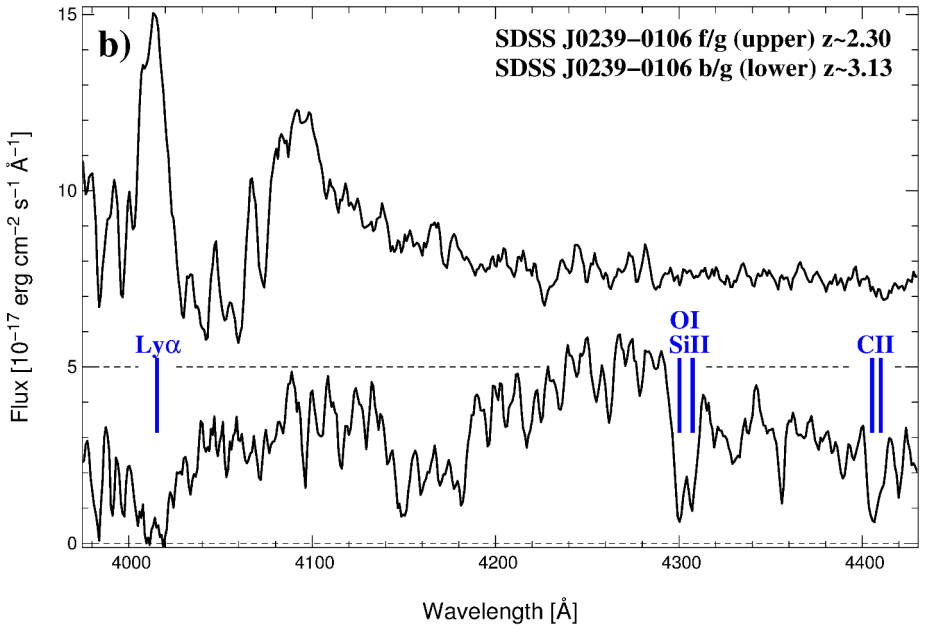

FIGURE 4.13: BOSS spectra for the SDSS J0239-0106 pair with an angular (physical) separation of 3.96″ (33.0 proper kpc). In the upper spectrum, the foreground quasar at $z = 2.30$ has intrinsic broad absorption lines that cut into the Lyα emission peak. Due to the redshift difference, $\Delta z = 0.83$, the DLA in the lower spectrum appears in the Lyβ forest of the background quasar at $z = 3.13$. Metal absorption lines associated with the DLA are indicated with blue labeling.

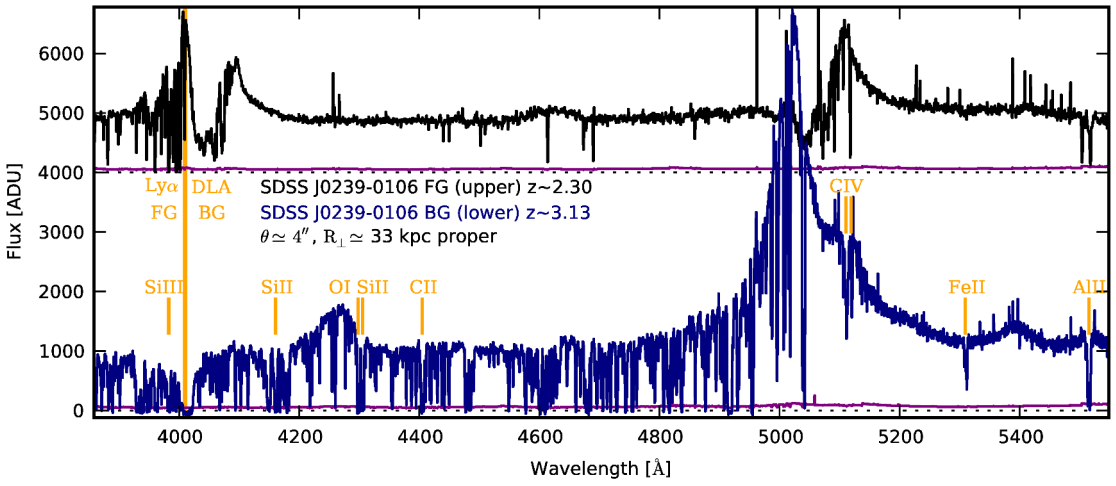

FIGURE 4.14: X-shooter spectra for the SDSS J0239-0106 pair. The Lyα emission peak from the FG quasar at $z = 2.30$ and the coincident DLA in the BG quasar spectrum, along with the associated metal absorption lines, are labeled in yellow. The higher resolution improves the level of detail for the absorptions compared to Figure 4.13.

TABLE 4.2: Column densities for the J0239-0106 DLA components. Velocities (km s^{-1}) are calculated relative to $z = 2.301002$.

v	N(Si II)	$\sigma_{N(\mathrm{Si\,II})}$	N(Al II)	$\sigma_{N(\mathrm{Al\,II})}$	N(Fe II)	$\sigma_{N(\mathrm{Fe\,II})}$	N(Mg II)	$\sigma_{N(\mathrm{Mg\,II})}$
-273	13.53	0.13	12.51	0.48	13.00	0.20	13.17	0.36
-99	14.74	0.15	14.07	1.04	14.05	0.10	15.32	0.95
-39	14.45	0.12	13.54	0.76	14.01	0.10	14.55	12.87
0	13.64	0.35	–	–	12.74	0.90	13.31	22.25
52	14.37	0.14	13.14	1.00	13.94	0.12	14.25	9.69
115	14.66	0.14	14.01	0.81	14.21	0.14	15.01	2.40
154	14.59	0.25	–	–	14.47	0.15	14.16	10.00
Total	15.30	0.08	14.43	0.56	14.89	0.07	15.58	1.57

Many of the associated metal absorption lines, including O I λ1302, Si II λ1304, and C II λ1334, are in the Lyα forest and are potentially blended with H I absorptions. Transitions that occur redward of the Lyα emission peak are favored for identifying components and measuring column densities. A tied fit of the Fe II $\lambda\lambda\lambda$ 1608, 2374, and 2586 transitions fixes the redshift and Doppler parameter for each component. The values are then imposed on the other species, and only their column densities are allowed to vary. Figure 4.15 presents metal absorption lines fitted for the J0239-0106 DLA system with zero velocity relative to the central component at $z = 2.3010$. Six main components spanning $\sim$250 km s^{-1} are identified, along with a weak blue component at -273 km s^{-1}. The individual column densities for each component are given in Table 4.2, and they are summed to obtain the total column density for each ion.

The metal absorption line profiles suggest two main clumps, each with three components. The DLA Lyα profile is fitted with two components, corresponding to the two main clumps. The redshift values for the DLA are determined by averaging the three component redshifts in each main clump, weighted by their Fe II column densities. A fit with a single H I component was also tested, but did not reproduce the profile as well as two H I components. A weak H I component at 563 km s^{-1} helps fit the asymmetrical profile along the red wing. Two additional H I components near 1 400 km s^{-1} are associated with C IV absorptions (Figure 4.17). Any C IV associated with the H I component at 563 km s^{-1} is blended both with the DLA C IV λ 1550 absorption and a N V λ 1242 absorption that is part of a high-ionization system at $z = 3.1282$. The C IV associated with the DLA has the same velocity extent as the low-ionization metals, but the absorptions are relatively weak.

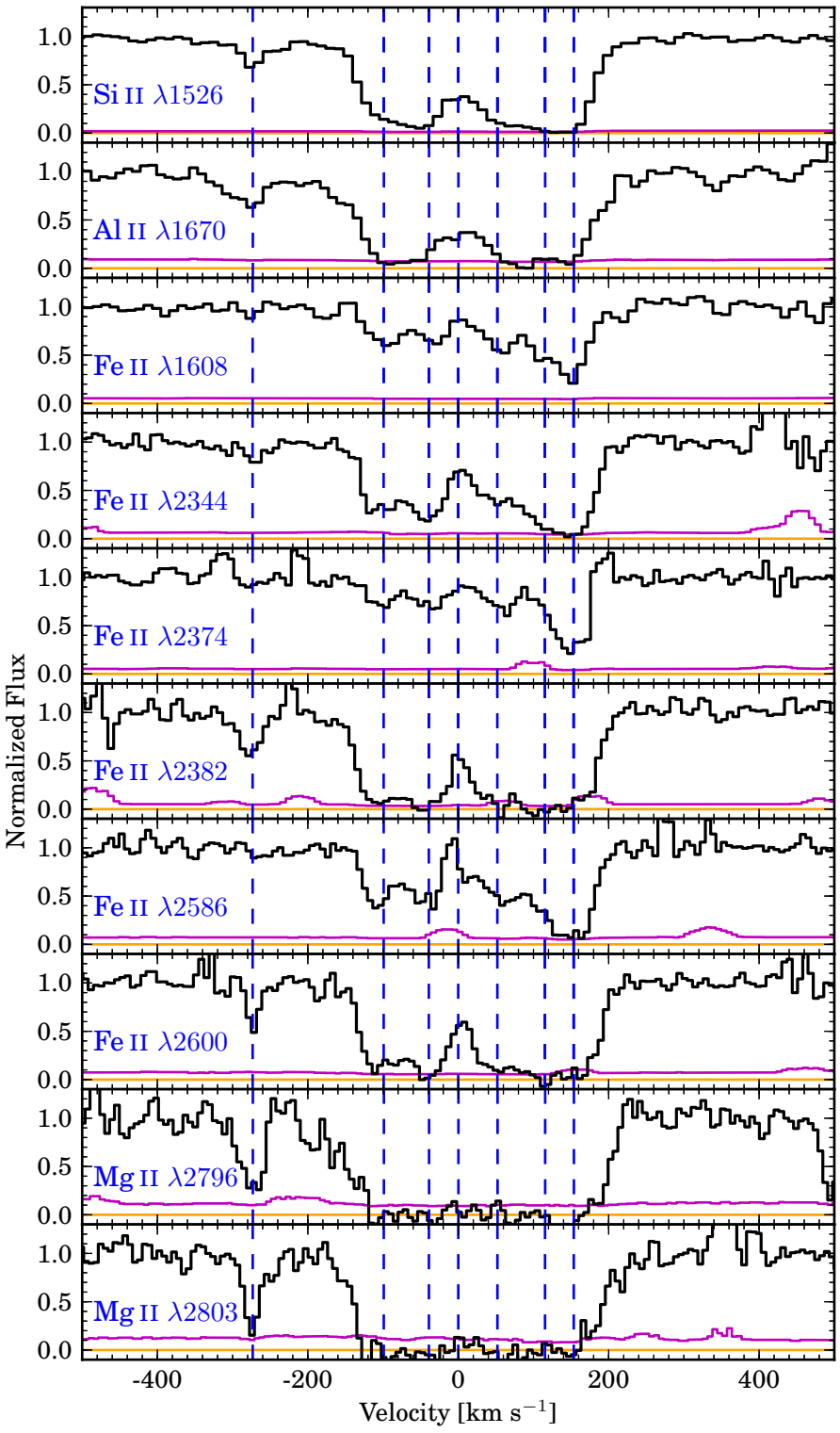

FIGURE 4.15: Metal absorption lines associated with the DLA detected in the spectrum of the J0239-0106 BG quasar. Dashed blue lines indicate six components identified in the main absorption profile, plus an additional component at -273 km s^{-1}. Zero velocity corresponds to $z = 2.301002$.

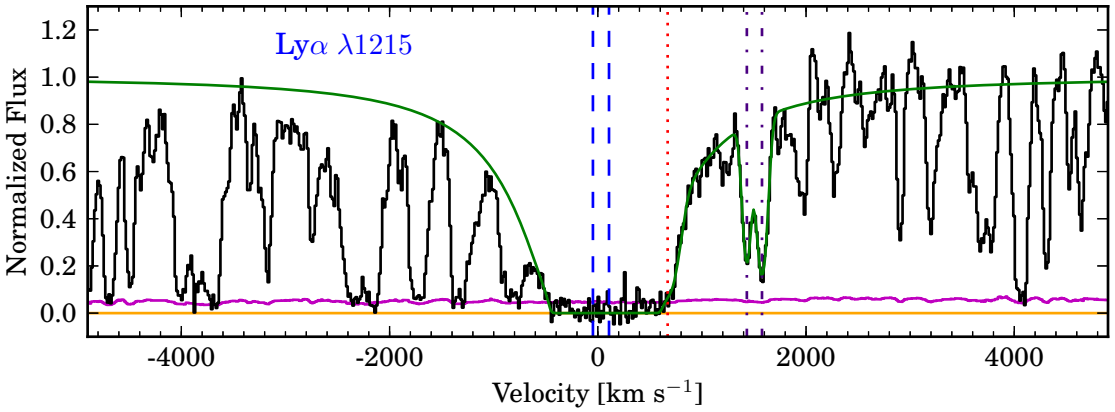

FIGURE 4.16: DLA in the J0239-0106 BG quasar spectrum fitted with two components (dashed blue lines). A weak intervening component (dotted red line) is also included in the fit. Two H I absorptions along the red wing of the DLA (dash-dotted purple lines) are associated with C IV absorptions. Zero velocity corresponds to $z = 2.301002$.

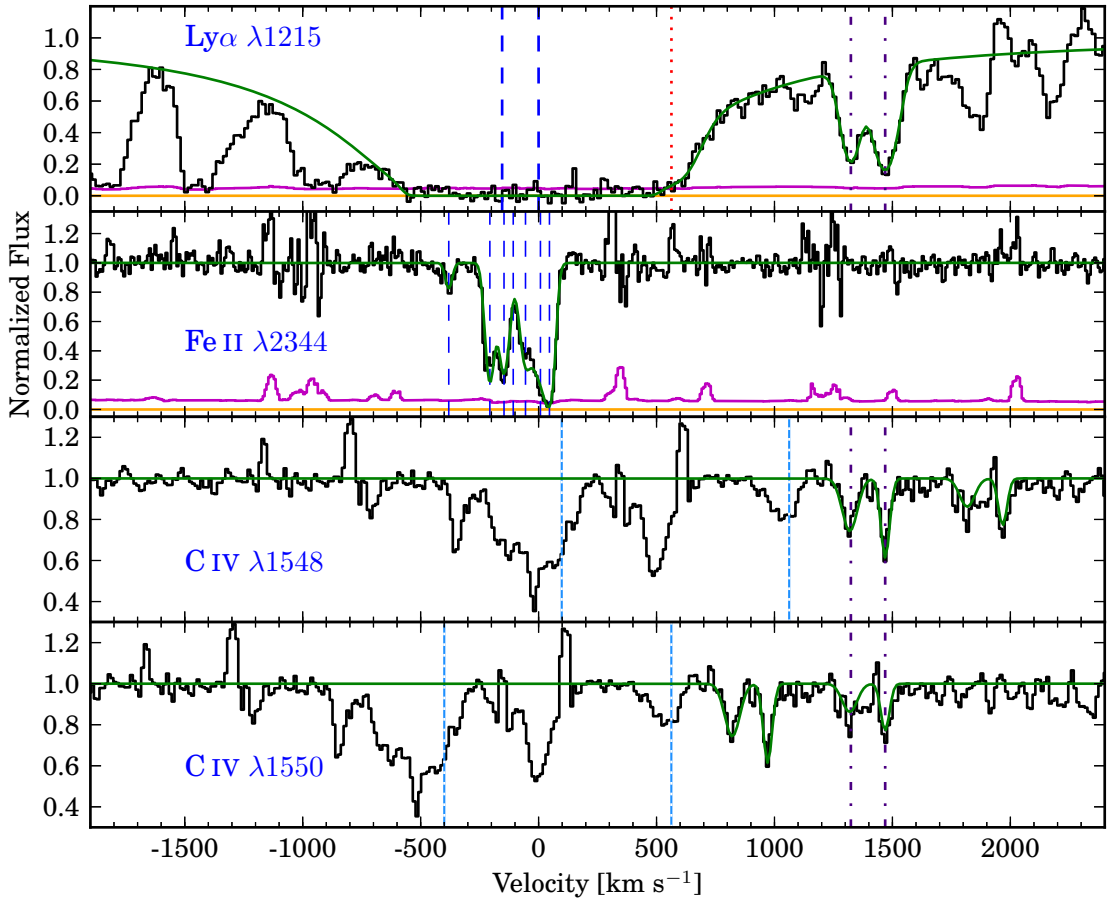

FIGURE 4.17: Lyα absorptions near the DLA in the J0239-0106 BG quasar spectrum compared with low-ionization Fe II λ 2344 and C IV transitions. A C IV absorption system associated with the DLA has the same velocity structure as the low-ionization transitions. Two single-component C IV absorptions near 1 400 km s^{-1} are associated with H I absorptions along the red wings of the DLA. No other C IV systems are apparent within ~2 000 km s^{-1} of the DLA. A N V $\lambda\lambda$ 1238, 1242 high-ionization system at $z = 3.1282$ (light blue short dashed lines) is blended with the DLA C IV λ 1548 and may mask C IV λ 1550 absorption associated with the H I component at 670 km s^{-1}. Note that the vertical scale is altered for the C IV panels to show detail. Zero velocity corresponds to $z = 2.301002$.

TABLE 4.3: H I and C IV column densities for the J0239-0106 DLA and nearby absorptions. Velocities (km s^{-1}) are calculated relative to the metal absorption component at $z = 2.301002$. (WILL MEASURE N(C IV) FOR THE DLA.)

v	z	N(H I)	$\sigma_{N(\mathrm{H\,I})}$	N(C IV)	$\sigma_{N(\mathrm{C\,IV})}$
-47	2.300484	20.18	0.14	–	–
108	2.302186	19.47	0.44	–	–
671	2.308395	14.37	0.30	–	–
1431	2.316800	13.97	0.16	13.43	0.13
1577	2.318410	14.14	0.13	13.61	0.11

4.3.2 Pair SDSS J2338-0003

The lines-of-sight toward the foreground and background quasars in the SDSS J2338-0003 quasar pair are separated by 6.06″, which corresponds to a physical distance of 50.5 kpc at $z = 2.46$. A DLA coincident with the Lyα emission peak of the foreground quasar occurs in the Lyα forest of the background quasar spectrum (Figures 4.18, 4.19). The column density estimate from the BOSS spectrum is log N(H I) $\simeq$ 20.0, placing the absorber in the sub-DLA range. However, the re-evaluated column density from the higher resolution X-shooter spectrum is log N(H I) $= 20.32 \pm 0.06$ (see below). The Lyβ transition observed at ∼3550 Å is not detected in the BOSS spectrum, since the wavelength coverage begins at 3600 Å. Both the Lyα and Lyβ transitions for the DLA are visible in the X-shooter spectrum before a higher-redshift LLS completely absorbs the quasar flux.

Some of the associated metal absorption lines, O I, Si II λ1304, and C II, occur in the Lyα forest and may be blended with H I absorptions. However, the Si II λ1526, Al II, Fe II, Mg II, and Mg I absorptions redwards of the background quasar Lyα emission peak place good constraints on the individual components (Figure 4.20). The absorption system can be fitted with six components that span over 250 km s^{-1}. Two main clumps, each with three individual components, are centered on $v = 0$ km s^{-1} ($z = 2.439933$) and $v = 166$ km s^{-1}. The column densities for the six components are given in Table 4.4, along with the total column density for each ion.

Since the metal absorption lines are distributed into two main clumps, the DLA is fitted with two H I components (Figure 4.21). Each H I component redshift is the average of the three metal absorption components in the corresponding clump weighted by the Fe II column densities. Their redshifts, velocity offsets relative to $z = 2.439933$, and column densities are given in Table 4.5. A weaker log N(H I) $\simeq$ 16.9 component at $z = 2.433427$ is blended with the blue wing of the DLA. No metal absorptions are detected for this component. The C IV absorptions associated with the DLA have the same velocity span as the low-ionization transitions (Figure 4.22). The C IV absorption is strongest at

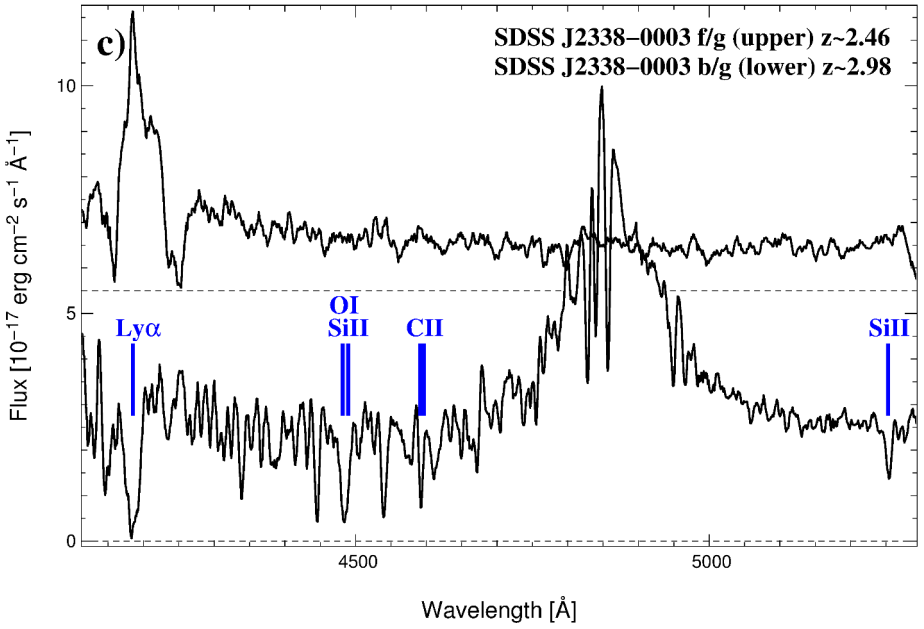

FIGURE 4.18: BOSS spectra for the SDSS J2338-0003 pair with an angular (physical) separation of 6.06″(50.5 proper kpc). The upper spectrum shows the Lyα emission peak of the foreground quasar at $z = 2.46$, and the lower spectrum shows the background quasar at $z = 2.98$. A sub-DLA (blue labeling) appears in the background quasar spectrum at the same wavelength as the foreground quasar Lyα emission peak. Metal absorption lines associated with the absorption system are indicated. The O I, Si II λ1304, and C II metal absorption lines associated with the sub-DLA fall in the Lyα forest.

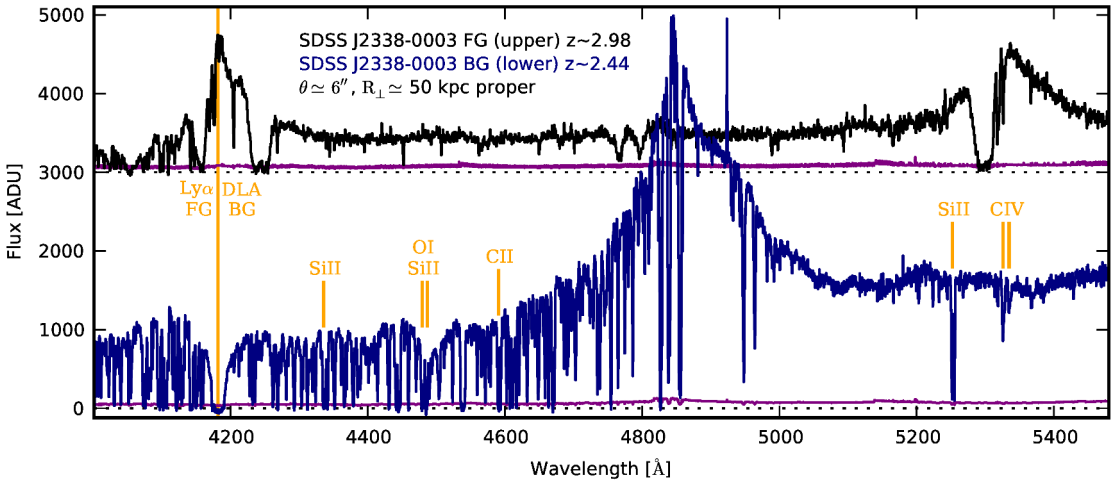

FIGURE 4.19: X-shooter spectra for the SDSS J2338-0003 pair. The Lyα emission peak from the FG quasar at $z = 2.46$ and the coincident DLA in the BG quasar spectrum, along with the associated metal absorption lines, are labeled in yellow. Lyα, N V, and C IV broad absorption lines are apparent in the FG spectrum.

$v = 0$ km s^{-1}. The absorption strength gradually decreases as the velocity separation increases in the positive direction, and C IV absorption does not follow the two-clump dichotomy observed for the low-ionization transitions. As with the J0239-0106 pair, the C IV absorption is relatively weak compared to the low-ionization metals.

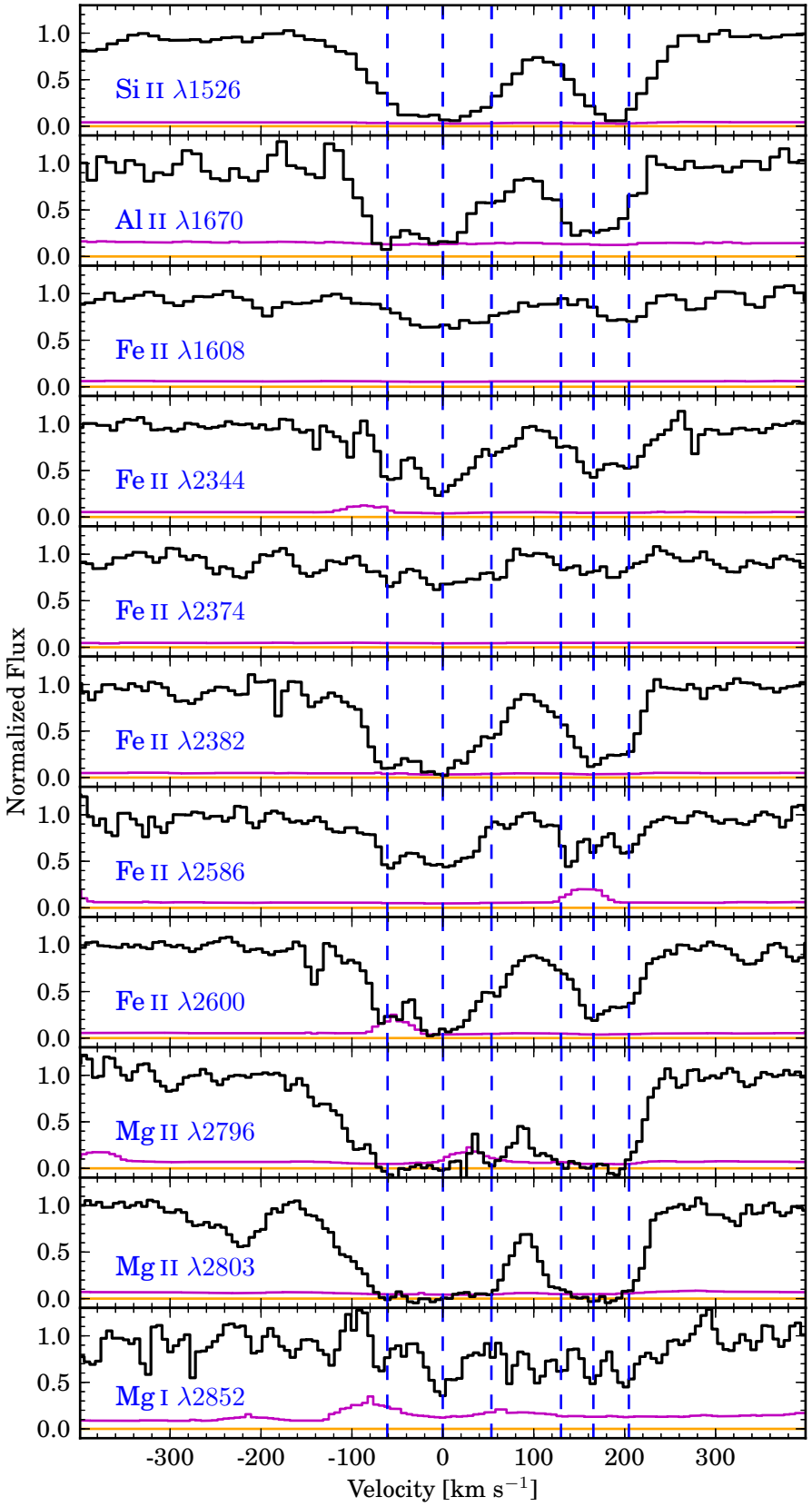

FIGURE 4.20: Metal absorption lines associated with the DLA detected in the spectrum of the J2338-0003 background quasar. Blue dashed lines indicate six components identified in the absorption profile, grouped into two main clumps. Zero velocity is relative to $z = 2.439933$.

TABLE 4.4: Column densities for the J2338-0003 DLA components. Velocities (km s^{-1}) are calculated relative to $z = 2.439933$.

v	N(Si II)	$\sigma_{N(\mathrm{Si\,II})}$	N(Al II)	$\sigma_{N(\mathrm{Al\,II})}$	N(Fe II)	$\sigma_{N(\mathrm{Fe\,II})}$	N(Mg II)	$\sigma_{N(\mathrm{Mg\,II})}$	N(Mg I)	$\sigma_{N(\mathrm{Mg\,I})}$
-61	14.19	0.05	13.24	0.23	13.79	0.03	15.62	0.15	11.61	0.74
0	14.75	0.10	13.19	0.20	14.06	0.02	14.42	0.41	12.46	0.12
54	14.10	0.05	12.46	0.25	13.28	0.03	13.60	0.08	11.89	0.35
130	13.62	0.08	12.61	0.22	12.93	0.06	13.59	0.09	12.26	0.18
166	14.10	0.09	13.10	0.34	13.68	0.04	16.15	1.04	11.87	0.36
205	15.97	0.28	12.47	0.33	13.59	0.05	14.09	0.33	12.41	0.23
Total	16.02	0.25	13.74	0.12	14.46	0.02	16.27	0.78	12.96	0.10

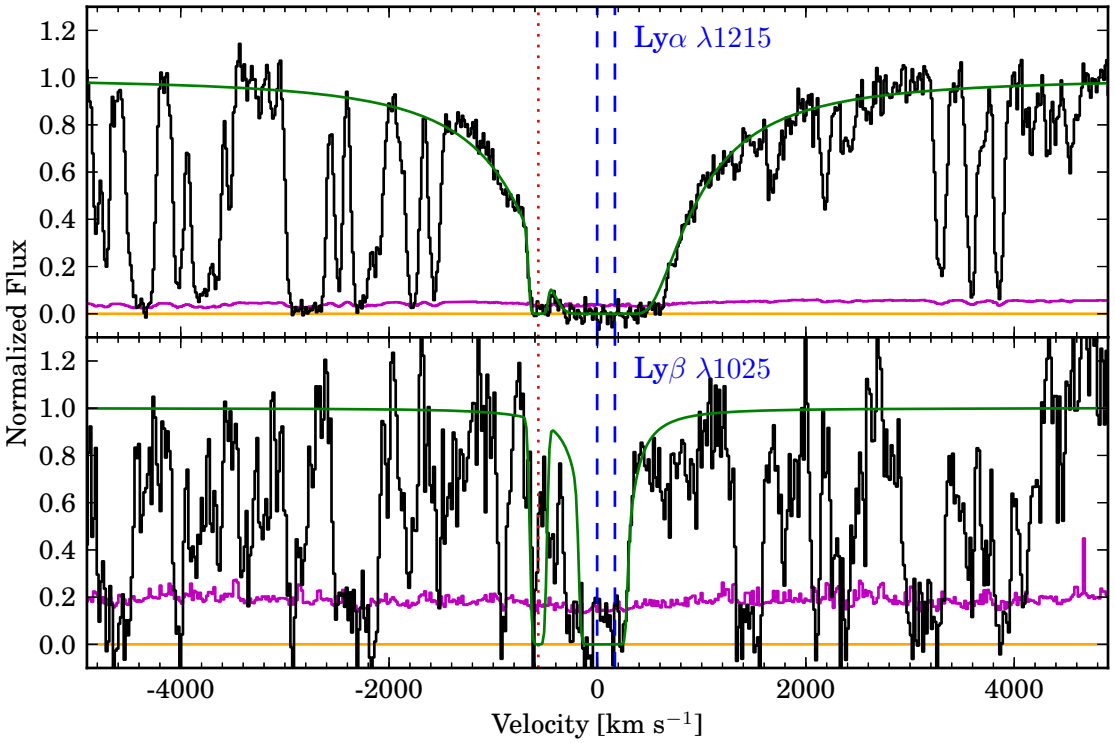

FIGURE 4.21: Preliminary fits to the Lyα and Lyβ absorptions associated with the DLA in the J2338-0003 BG quasar spectrum. The DLA is fitted with two components (dashed blue lines), and an intervening component (dotted red line) is also included in the fit. Zero velocity is relative to $z = 2.439933$.

TABLE 4.5: H I column densities for the J2338-0003 DLA and nearby absorptions. Velocities (km s^{-1}) are calculated relative to the strongest metal absorption component at $z = 2.439933$.

v	z	N(H I)	$\sigma_{N(\mathrm{H\,I})}$
-568	2.433427	16.87	0.28
-3	2.439897	20.04	0.09
167	2.441855	20.01	0.08

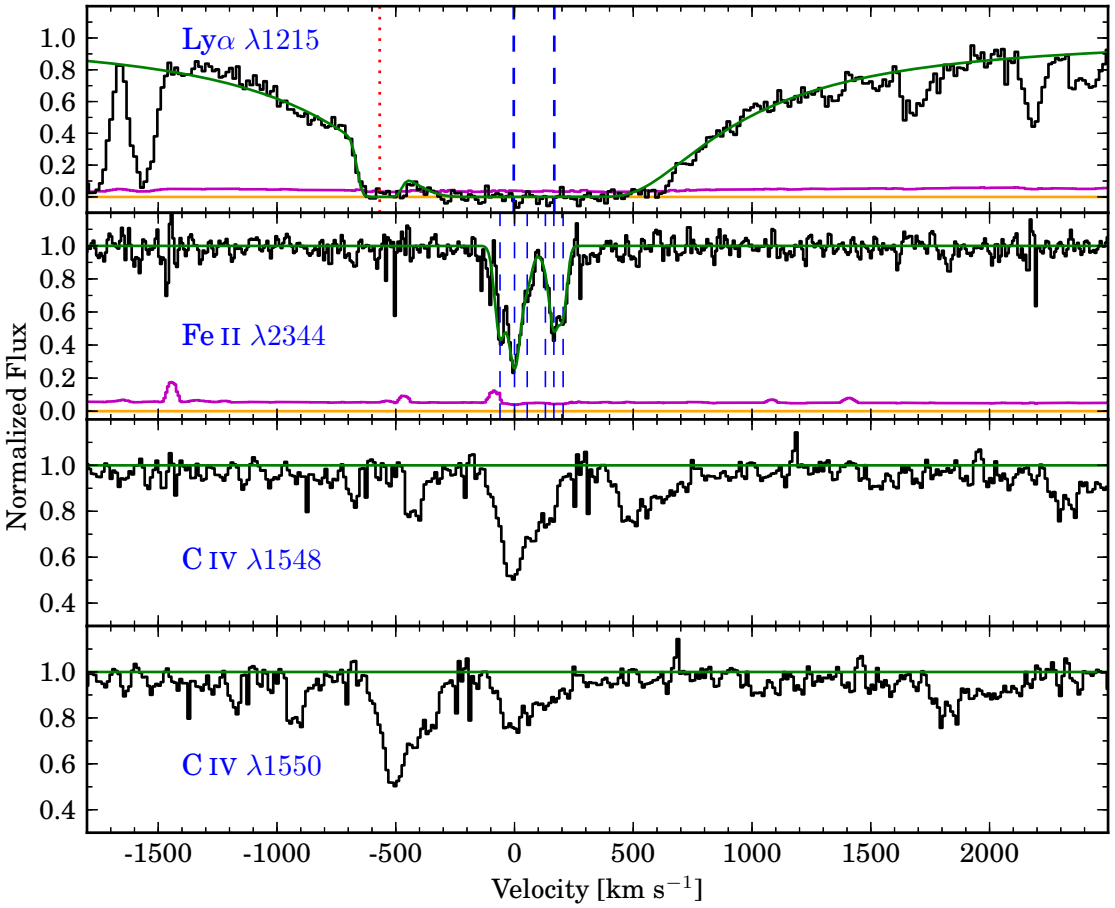

FIGURE 4.22: DLA absorptions (dashed blue lines) in the J2338-0003 BG quasar spectrum compared with low-ionization Fe II λ 2344 and C IV transitions. No metals associated with the weaker H I component (red dotted line) are detected. The C IV absorption associated with the DLA has the same velocity spread as the low-ionization components (thin dashed blue lines). Note that the vertical scale is altered for the C IV panels to show detail. Zero velocity is relative to $z = 2.439933$.

4.3.3 Pair SDSS J0913-0107

The lines-of-sight in the quasar pair SDSS J0913-0107 have an angular separation of $10.74''$, which implies a physical distance of 89.5 kpc at $z = 2.75$. As with the previous two pairs, the Lyα emission peak in the foreground quasar spectrum corresponds to a DLA in the background quasar spectrum (Figure 4.23, 4.24). The J0913-0107 DLA is strong, with an H I column density that is a factor of ten larger than the DLAs associated with the two other quasar host galaxy environments, despite their smaller line-of-sight separations. The H I column density estimate from the BOSS spectrum is $\log N(\mathrm{H\,I}) \simeq 21.0$, and the higher resolution X-shooter spectrum gives $\log N(\mathrm{H\,I}) \simeq 21.37 \pm 0.15$ (see below).

Remarkably, a second lower-redshift absorption system also appears at the same wavelength in both spectra (Figure 4.23), blueward of the Lyα emission peak/first DLA. Based on the absorber metallicities, velocity distribution, and overdensity, this lower redshift coincident absorption system may correspond to a cosmic web filament. Chapter 5 describes the full analysis.

Nearly all of the low-ionization metal transitions associated with the DLA that probes the foreground quasar host galaxy environment occur redwards of the background quasar Lyα emission peak. The O I λ 1302, Si II λ1304, and C II λ1334 transitions are all saturated, and the first two are blended with other metal absorption systems. Thanks to higher S/N due to a longer integration time for this LOS, several weaker transitions are detected, including Si II λ1808 and Al III $\lambda\lambda$1854, 1862 (Figure 4.25). A tied fit to these transitions, along with Fe II λ2374, determines the redshift and Doppler parameter for the components. The weaker Fe II λ1608 transition is also detected, but blended with C IV absorptions associated with the background quasar. Once the components are fitted, their values are imposed on the other transitions and only the column densities are allowed to vary. Table 4.6 gives the column density for each component as well as the total column density for the ion. The metal absorptions are fitted with eight components, spanning over 400 km s^{-1}. To fix the DLA H I component redshifts, the redshifts for the first four and second four metal absorption components are averaged by weighting their Fe II column densities.

Fitting the quasar continuum near the DLA to normalize the spectrum is not straightforward, since the red damping wing overlaps with the blue wing of the background quasar Lyα emission peak. The blue damping wing extends into the lower redshift absorption system. Consequently, the H I components for the DLA and the lower redshift absorption system must all be fitted simultaneously (Figure 4.26). The plentiful Lyman

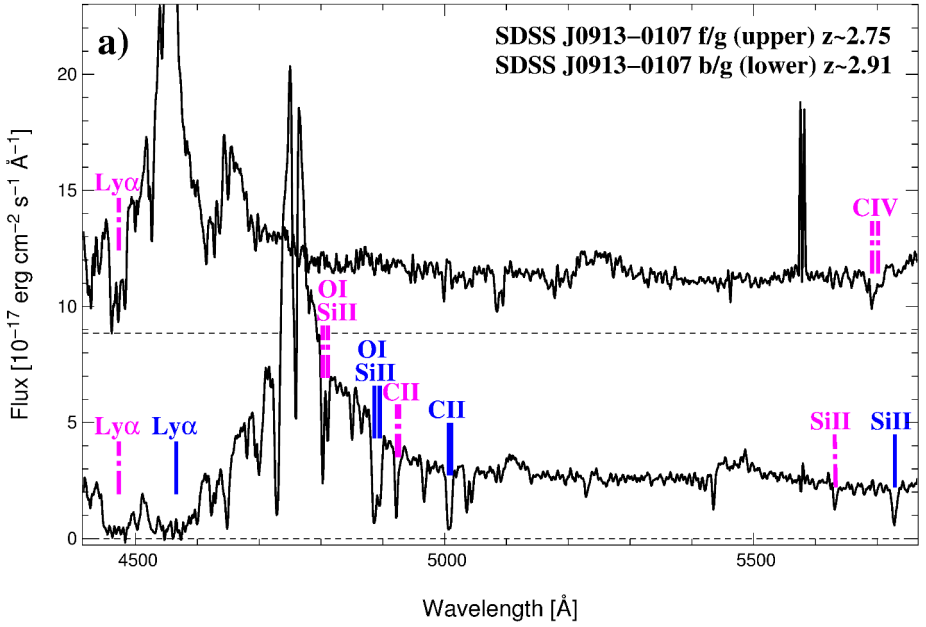

FIGURE 4.23: BOSS spectra for the SDSS J0913-0107 pair with an angular (physical) separation of 10.74″(89.5 proper kpc). The upper spectrum shows the Lyα emission peak of the foreground quasar at $z = 2.75$. A DLA (blue labeling) appears in the lower spectrum at the same wavelength, indicating that the line-of-sight from the background quasar passes close to the galaxy hosting the foreground quasar. A second lower redshift absorption system (pink labeling) is coincident in both spectra.

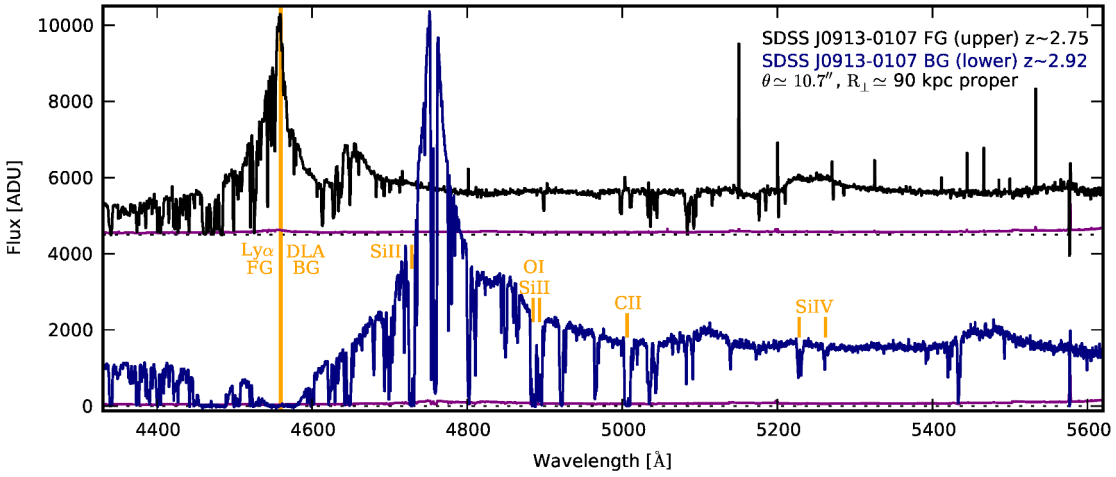

FIGURE 4.24: X-shooter spectra for the SDSS J0913-0107 pair. Yellow labeling indicates the foreground quasar Lyα emission peak and the coincident DLA in the background quasar spectrum, along with associated metal absorption lines. The lower redshift absorption system is apparent near 4475 Å, but is not labeled.

TABLE 4.6: Column densities for the J0913-0107 DLA components. Velocities (km s^{-1}) are calculated relative to $z = 2.752314$.

v	N(Si II)	$\sigma_{N(\mathrm{Si\,II})}$	N(Al II)	$\sigma_{N(\mathrm{Al\,II})}$	N(Al III)	$\sigma_{N(\mathrm{Al\,III})}$	N(Fe II)	$\sigma_{N(\mathrm{Fe\,II})}$
-151	14.46	0.05	13.15	0.03	12.77	0.05	13.99	0.02
-58	14.79	0.08	13.52	0.14	12.75	0.06	14.28	0.03
0	15.31	0.05	15.08	1.30	12.94	0.05	16.00	0.39
78	14.54	0.08	12.98	0.05	12.54	0.08	13.85	0.03
144	14.36	0.20	13.78	0.51	11.79	0.33	13.94	0.07
171	14.82	0.13	13.42	0.57	12.19	0.17	14.13	0.06
203	15.01	0.08	13.18	0.27	12.57	0.08	14.39	0.03
234	14.72	0.13	13.18	0.43	11.94	0.24	13.94	0.06
Total	15.74	0.03	14.55	0.16	13.48	0.13	15.20	0.02

series absorptions, Lyα - Ly7, detected in the background quasar spectrum help constrain the H I component fit (Figure 4.27). Beyond the red wing of Ly7, the higher order transitions completely absorb the quasar flux. The DLA Lyman series absorptions are saturated, and Lyδ as well as Ly6 are blended with Lyman series transitions from the intervening system, again highlighting the need to fit both systems together.

A predominent C IV absorption component is aligned with the first DLA H I component (Figure 4.28). However, the C IV absorption from $0 - 200$ km s^{-1} is very weak and does not correspond to the H sc i or low-ionization components. Given the significant H I absorption, log N(H I) $\simeq 21.4$, associated with a quasar host galaxy environment, it is surprising that the C IV absorption is not stronger.

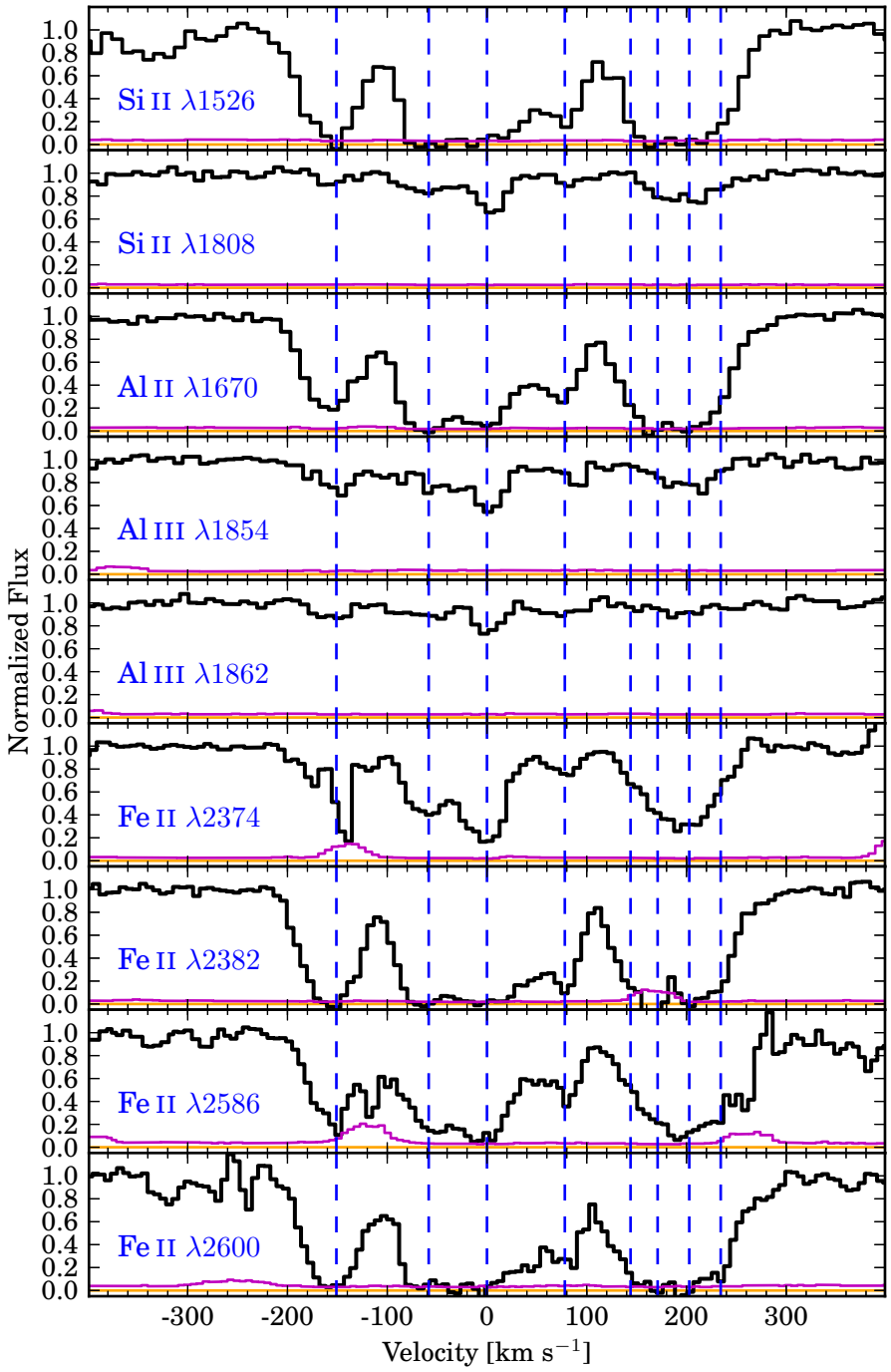

FIGURE 4.25: Metal absorption lines associated with the $z_{\rm abs} \sim 2.75$ DLA detected in the spectrum of the J0913-0107 BG quasar. Dashed blue lines indicate eight components identified in the absorption profiles, which span ∼400 km s^{-1}. Zero velocity corresponds to $z = 2.752314$.

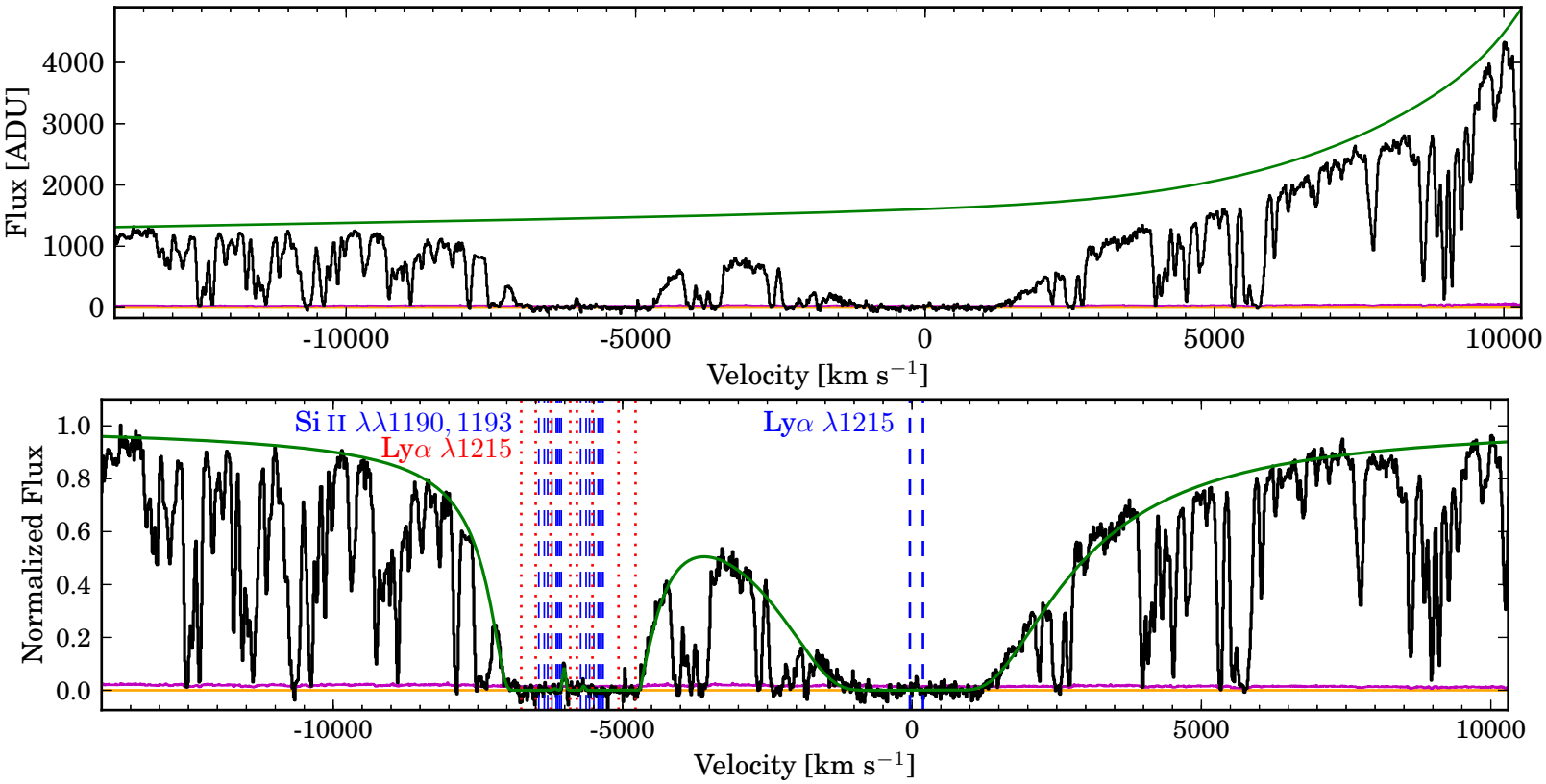

FIGURE 4.26: Top: Continuum fit near the DLA in the J0913-0107 BG quasar spectrum. The DLA is near the blue wing of the quasar Lyα emission peak. Bottom: The wings of the DLA at $z_{\rm abs} \sim 2.75$ ($v \sim 0$ km s^{-1}, dashed blue lines) overlap with another strong absorption system (8 components, dotted red lines). Si II $\lambda\lambda 1190, 1193$ absorptions associated with the DLA are blended with the lower-redshift H I absorptions (8 components, thin dashed blue lines). Zero velocity corresponds to $z = 2.752314$.

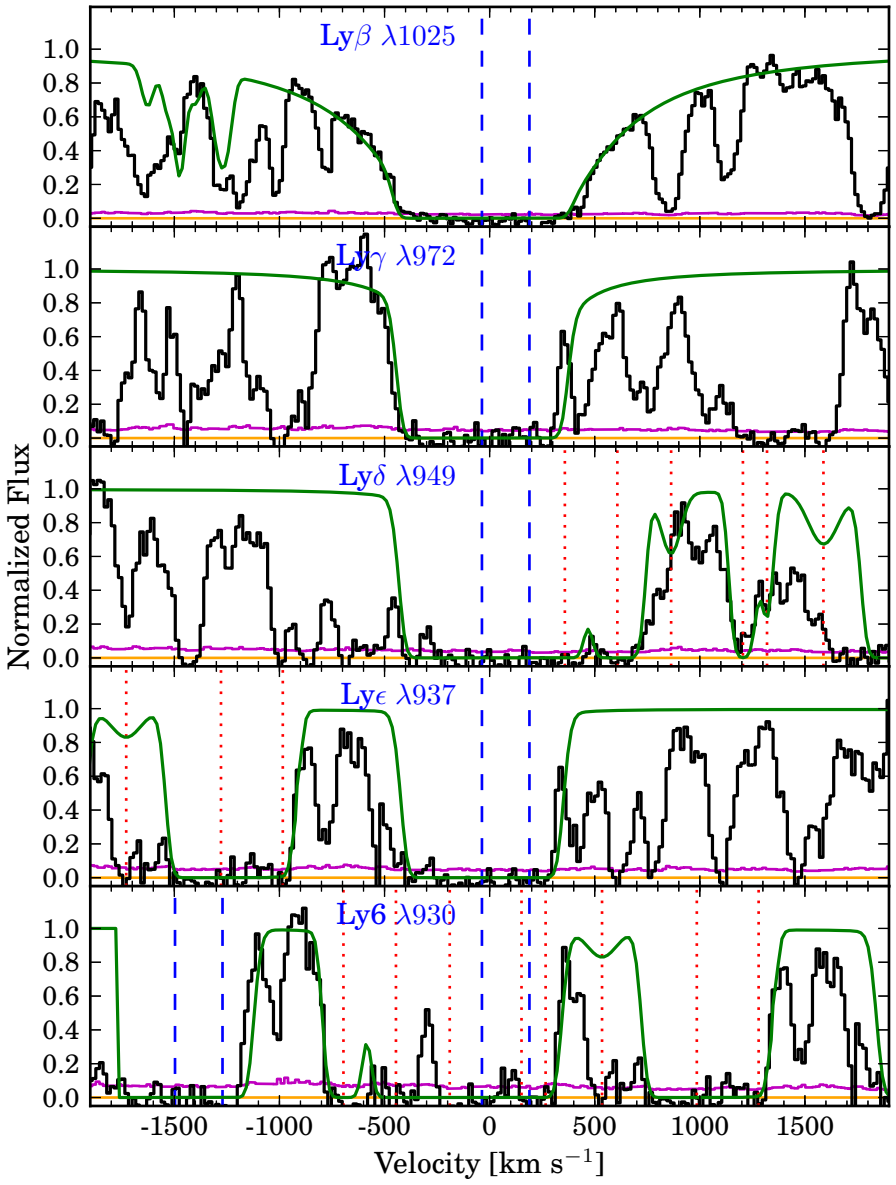

FIGURE 4.27: Lyman series absorptions the J0913-0107 BG quasar spectrum help constrain the (preliminary) DLA fit (two components, dashed blue lines). The Lyman series is detected down to Ly7 λ926 before the flux becomes completely absorbed. Lyman series absorptions from the lower-redshift intervening H I system (dotted red lines) are blended with some of the DLA transitions. Intervening Lyγ components are blended with the DLA Lyδ absorption. Intervening Lyδ components appear in the DLA Lyϵ panel and are blended with the DLA Ly6 absorption. The DLA Ly7 absorption also appears in the DLA Ly6 panel. Zero velocity is relative to $z = 2.752314$.

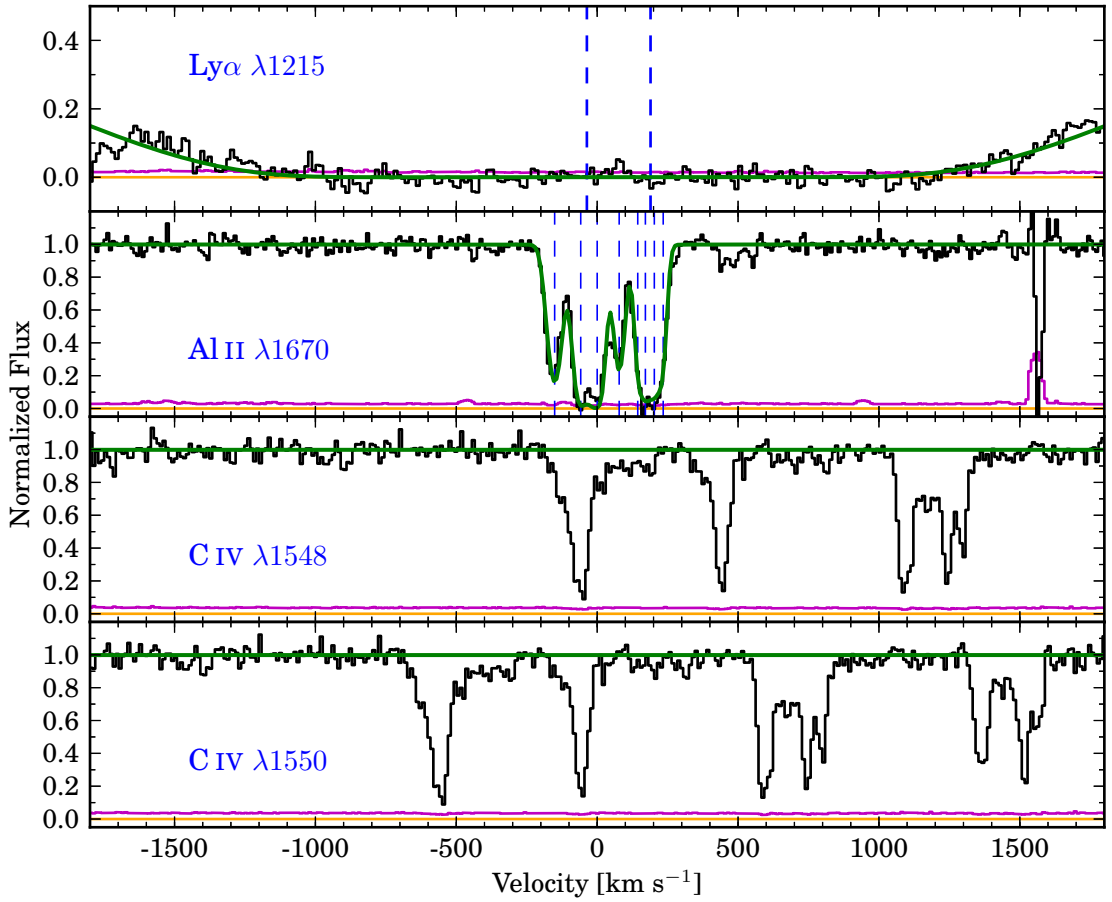

FIGURE 4.28: Lyα absorptions near the DLA (preliminary fit) in the J0913-0107 BG quasar spectrum compared with low-ionization Al II λ 1670 and C IV transitions. The C IV absorption is prominent only in one component near $v = 50$ km s^{-}1 and weak across the remaining extent of the low-ionisation components. No other C IV absorptions are detected within ~2000 km s^{-1} of the DLA, implying that strong H I components unlikely to be blended with the DLA. The absorptions redwards of the C IV associated with the DLA is Mg II at $z = 1.086$. Zero velocity is relative to $z = 2.752314$.

4.4 Preliminary Conclusions

The three line-of-sight pairs are separated by physical distances of ∼33, 51, and 90 kpc. In each case, a DLA occurs in the background quasar spectrum coincident with the foreground quasar Lyα emission peak. Table 4.7 summarizes the DLA H I column densities and metal abundances. The two absorption systems closest to the quasar host galaxies have metal absorptions that span ∼250 km s^{-1} and DLAs with log N(H I) $\simeq$ 20.3. Despite the larger transverse distance between the third line-of-sight pair, both the H I column density (log N(H I) $\simeq$ 21.4) and the metal absorption line velocity spread (∼400 km s^{-1}) are significantly larger.

Prochaska & Hennawi (2009) study a similar close line-of-sight pair separated by 13.3″, corresponding to 108 kpc at the foreground quasar redshift $z = 2.436$, with a Keck/HIRES spectrum of the background quasar. The metal transitions span ∼650 km s^{-1} and are separated into three distinct regions. An H I component is fitted for each region and constrained from the Lyα and Lyβ absorption profiles. Each H I component is in the sub-DLA range, and the total column density for the system is log N(H I) $\simeq$ 19.7. The derived [O/H] abundances for the three regions are high, similar to that of the J0239-0106 DLA. Passing through the halo within ∼ 100 kpc of the quasar host galaxies, the background quasar lines-of-sight detect significant reservoirs of cold (T ∼ 10^4 K) metal-enriched gas predominantly in low-ionization states. These observations are in contrast with the associated and proximate absorption systems along quasar lines-of-sight that typically show higher-than-average ionization levels.

The foreground quasar line-of-sight probes only the gas that lies between the quasar and the observer, where material in the "proximity zone" is exposed to strong ionization from the quasar. The proximity effect along the line-of-sight is an observed decrease in the median optical depth of the IGM surrounding quasar host galaxies because of enhanced photoionization due to emission from the quasar. However, the optical depth near quasar hosts does not decrease as rapidly as expected, which suggests H I overdensities out to distances of ∼10 Mpc (Font-Ribera et al. 2013; Guimarães et al. 2007). Samples of line-of-sight pairs with optically thick absorbers detected in the background quasar

TABLE 4.7: Total H I column densities and metal abundances relative to solar values (Lodders 2003) for the three DLAs in the close line-of-sight pairs. The projected transverse distance (kpc) and velocity spread (km s^{-1}) for the main component of the metal absorption lines are also noted.

Pair	$R_\perp$	Δv	N(H I)	$\sigma_{N(\mathrm{H\,I})}$	Si	σ_{Si}	Al	σ_{Al}	Fe	σ_{Fe}
J0239-0106	33.0	253	20.26	0.14	-0.50	0.16	-0.29	0.57	-0.84	0.16
J2338-0003	50.5	266	20.33	0.06	–	–	-1.04	0.14	-1.33	0.07
J0913-0107	89.5	385	21.37	0.15	-1.17	0.14	-1.25	0.16	-1.63	0.13

spectra reveal excess H I absorption relative to the average IGM extending ∼1 Mpc in the transverse direction from $z \sim 2$ foreground quasar host galaxies (Hennawi et al. 2006a; Prochaska et al. 2013a). The incidence of strong H I absorbers is much higher in the transverse direction than along the line-of-sight (Hennawi & Prochaska 2007), and fluorescent Lyα emission is not detected to a 1σ surface brightness limit of $\sim 3 \times 10^{-18}$ erg s^{-1} cm^{-2} arcsec^{-2} in the transverse direction at scales of ∼100 kpc (Hennawi & Prochaska 2013). These results suggest that the quasar emits anisotropically. The background line-of-sight passes through gas that is associated with the host galaxy halo, but shadowed from the foreground quasar emission.

Given that the background quasar lines-of-sight see slices of the foreground quasar halos, the most surprising aspect of the absorption system analysis for the three close line-of-sight pairs presented here is the lack of strong and extended C IV absorption. C IV enrichment is detected in the Lyα forest for absorptions with log N(H I) > 15 (Kim et al. 2013), and strong C IV absorptions are commonly associated with the CGM of intervening galaxies on scales of several hundred kpc (Adelberger et al. 2005; Martin et al. 2010; Steidel et al. 2010). In each pair, the C IV absorption profile roughly follows that of the low-ionisation transitions associated with the DLA, but is relatively weak. Aside from two systems near the J0239-0106 DLA, no additional C IV absorbers are detected within ∼2000 km s^{-1} of the foreground quasar. The C IV absorptions associated with the DLAs are likely due to either the foreground quasar host galaxy or a galaxy in close proximity. Galaxy clustering is augmented near quasars (e.g., Trainor & Steidel 2012), so it is not unexpected that the background line-of-sight could intersect another galaxy in the quasar host environment. However, diffuse gas in the quasar halo, probed with the weaker H I absorptions, does not show evidence of significant C IV enrichment. The cross section of warm gas is apparently small.

The gas in the quasar host galaxy halo may be at too high of a temperature to show absorptions, like C IV, that are associated with intermediate temperature gas (T $\simeq 10^{4-5}$ K). It appears to be in either a cold phase, probed by the DLA, or a hot phase that is difficult to detect in the X-shooter wavelength range. If the majority of the halo gas is at T $> 10^6$ K, a possible test would be to detect X-ray emission and therefore constrain the mass of hot gas extended around the quasar.

Chapter 5

A $\sim$6 Mpc overdensity at $z \simeq 2.7$ detected along a pair of quasar sight lines: Filament or Protocluster? *

5.1 Introduction

Filamentary structures that emerge both from the large-scale distribution of galaxies and in cosmological simulations are iconic of the cosmic web (Bond et al. 1996). Filaments and sheets outline vast extremely underdense regions known as voids, before meeting at nodes that coincide with matter-rich galaxy clusters. Various techniques are used to identify structures in cosmological simulations and trace filaments (e.g., Bond et al. 2010; Cautun et al. 2014; Murphy et al. 2011; Smith et al. 2012; Sousbie et al. 2011), the longest of which span over 100 h^{-1} Mpc. Segments connecting two clusters are relatively straight with typical lengths of $5 - 20$ h^{-1} Mpc and radial profiles that fall off beyond 2 h^{-1} Mpc (Aragón-Calvo et al. 2010; Colberg et al. 2005; González & Padilla 2010).

At low redshift, filament finding techniques applied to the Sloan Digital Sky Survey (SDSS; York et al. 2000) galaxy distribution measure maximum lengths comparable to simulations: $60 - 110$ h^{-1} Mpc (Pandey et al. 2011; Tempel et al. 2014). The majority of galaxies lie within 0.5 h^{-1} Mpc of the filament axis (Tempel et al. 2014). Another strategy is to look for evidence of filamentary structures that connect a particular galaxy

*Accepted 13/08/2014

cluster to the cosmic web. Observations of clusters at $z \sim 0.5$ reveal that they are embedded in filaments extending over 14 h^{-1} Mpc (Tanaka et al. 2007; Verdugo et al. 2012). Complimentary to using galaxies as tracers, filaments can also be directly detected from weak gravitational lensing signals (Mead et al. 2010). Jauzac et al. (2012) unambiguously identify a filament with projected length $\sim$3.3 h^{-1} Mpc (3D length 13.3 h^{-1} Mpc) feeding into a massive galaxy cluster at $z = 0.55$.

At high redshift, diffuse H I in the intergalactic medium (IGM) imprints absorptions in the spectra of background quasars and creates the Lyman-alpha (Lyα) forest. Correlations on scales < 5 h^{-1} Mpc comoving in the Lyα forests of quasar lines-of-sight (LOS) with small angular separations (e.g., Cappetta et al. 2010; Coppolani et al. 2006; D'Odorico et al. 1998, 2006; Rollinde et al. 2003; Saitta et al. 2008) likely arise from filaments. Reconstruction methods applied to simulated and observed IGM absorptions recover the topology of this low-density gas at $z \sim 2$ (Caucci et al. 2008; Cisewski et al. 2014). However, little is known observationally about the topology of the IGM, and the actual H I gas distribution may be less filamentary than simulated structures (Rudie et al. 2012). Currently, the source density limits our ability to resolve cosmic web filaments. Lee et al. (2014) suggest that observing programs with existing $8-10$ m telescopes could achieve the source density necessary to obtain a resolution of $\sim 3-4$ h^{-1} Mpc over cosmologically interesting volumes. However, the next generation of 30 m-class telescopes will best address the challenge of resolving filaments (Evans et al. 2014; Maiolino et al. 2013; Steidel et al. 2009)

It is clear from these studies that quasar LOS intersect structures in the cosmic web. While they most often pass through the filament width, certain LOS foreseeably probe along the length. Here we present H I absorptions indicative of the gaseous environment within a filament. We detect multiple, consecutive absorptions at $z \simeq 2.69$ with log N(H I) (cm^{-2}) > 18.0 that span over 2 000 km s^{-1} and are coincident in *both* LOS toward a pair of quasars separated by about $11''$.

We describe the quasar spectra in Section 2, including how the close LOS pair was identified, and analyze the absorptions in each LOS in Section 3. In Section 4, we discuss evidence for whether the LOS intercept a galaxy protocluster or probe along the length of a filament. We use a ΛCDM cosmology with $\Omega_\Lambda = 0.73$, $\Omega_\mathrm{m} = 0.27$, and $\mathrm{H}_0 = 70$ km s^{-1} Mpc^{-1} (Komatsu et al. 2011).

5.2 Data

The targeted quasars relevant to this work are SDSS J091338.30-010708.7 at $z \sim 2.75$ ($r = 20.49$) and J091338.96-010704.6 at $z \sim 2.92$ ($r = 20.38$). We refer to them as the foreground (FG) and background (BG) quasar accordingly. Their angular separation is $10.74''$, which corresponds to 87.8 ${h_{70}}^{-1}$ kpc proper distance (0.32 ${h_{70}}^{-1}$ Mpc comoving) at $z = 2.69$. These quasars were identified in the publicly available data release 9 quasar catalog (DR9Q; Pâris et al. 2012) from the SDSS-III (Eisenstein et al. 2011) Baryon Oscillation Spectroscopic Survey (BOSS; Dawson et al. 2013).

Initial interest in the pair was due to a damped Lyα absorption (DLA) in the BG LOS at the redshift of FG quasar, which offers an opportunity to study the host galaxy environment in absorption (Finley et al. 2013, and in preparation). In the low-resolution BOSS spectrum, an additional DLA with $\log N(\mathrm{H\,I}) = 21.05$ at $z_{\mathrm{abs}} = 2.680$ is flagged in the BG LOS (Noterdaeme et al. 2012b). A corresponding system appears in the FG BOSS LOS, but the low column density excludes it from the catalog of $\log N(\mathrm{H\,I}) \geq 20$ absorbers. Motivated by the absorption systems, we pursued a higher resolution analysis of these LOS.

The quasars were observed in service mode in spring 2013 with X-shooter on the 8.2m Kueyen (UT2) telescope at the European Southern Observatory as part of a program (ESO 089.A-0855, P.I. Finley) targeting non-binary quasar pairs with small angular separations. The X-shooter spectrograph has UVB, VIS, and NIR arms that allow simultaneous observations across the full wavelength range from 300 nm to 2.5 μm. The total exposure times were 2×3000 s (1.67 h) for the FG quasar and 5×3720 s (5.17 h) for the BG quasar.

The data were reduced with version 2.2.0 of the ESO X-shooter pipeline (Modigliani et al. 2010). The bias level for the raw UVB and VIS frames was corrected by calculating the bias from the overscan region. Cosmic rays in the science exposures were flagged with the van Dokkum (2001) Laplacian edge detection method. After background subtraction, the science exposures were divided by the master flat for the appropriate arm, created from flat frames taken during the same day of observations. Sky emission lines were then subtracted using the technique from Kelson (2003). Each spectral order was rectified from image space to wavelength space, using the 2D wavelength solution obtained from calibration frames. The individual 2D orders were extracted and merged, with pixel values weighted by the inverse variance of the corresponding errors in the overlapping regions. 1D spectra were obtained via standard extraction in the pipeline.

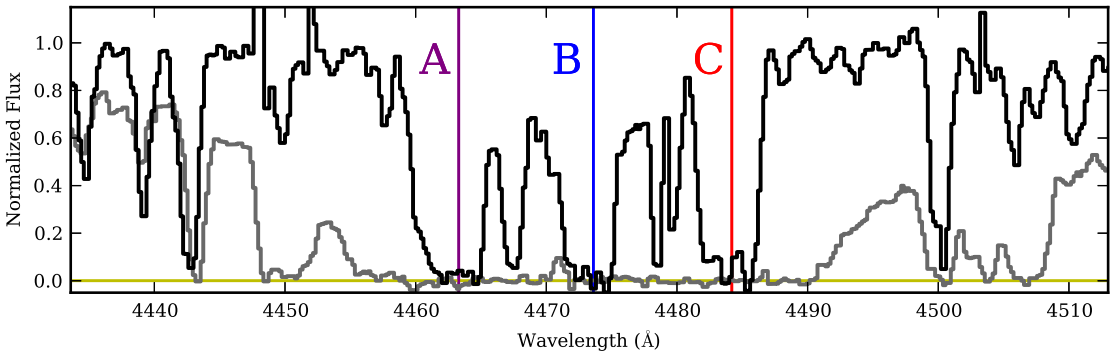

FIGURE 5.1: Portion of the Lyα forest with significant, coincident H I absorptions along both LOS. The FG spectrum (black) is overplotted on the BG spectrum (gray). The main absorption regions are labelled A (purple), B (blue), and C (red).

The extracted 1D spectra from different exposures were shifted to the vacuum-heliocentric reference frame and combined with an inverse variance weighted average. As in Noterdaeme et al. (2012a), we correct a 0.2 Å shift between the UVB and VIS spectra. The signal-to-noise ratio is 47 (21) at 5350 Å and 38 (15) at 8100 Å in the BG (FG) spectrum. We find that the resolution in the VIS spectra (R $\approx$ 11 000), measured from the width of telluric absorption lines, is higher than the nominal resolution (R = 8800), since the seeing was smaller than the 0.9″ slit width. The resolution in the UVB (1.0″ slit width) is likewise approximately R $\approx$ 6400.

5.3 Absorption Systems

We identify consecutive intervening H I absorptions spanning $\Delta v \simeq 2\,000$ km s^{-1} at $z \simeq 2.69$ that are coincident in both LOS toward the J0913-0107 non-binary quasar pair. A proper distance of $\sim$90 ${h_{70}}^{-1}$ kpc at this redshift separates the FG and BG quasar LOS. Three main absorption regions are denoted A, B, and C in the two spectra (Figure 5.1). We fit the entire absorption structure with the VPFIT package[1] to obtain system redshifts and column densities for the components (Figure 5.2). Seven absorptions have log N(H I) (cm^{-2}) > 18.0, and we refer to them by the LOS, absorption region, and component number: BG-A1, BG-A2, BG-B, BG-C, FG-A1, FG-A2, and FG-B. We discuss the absorption systems in each LOS.

[1] http://www.ast.cam.ac.uk/~rfc/vpfit.html

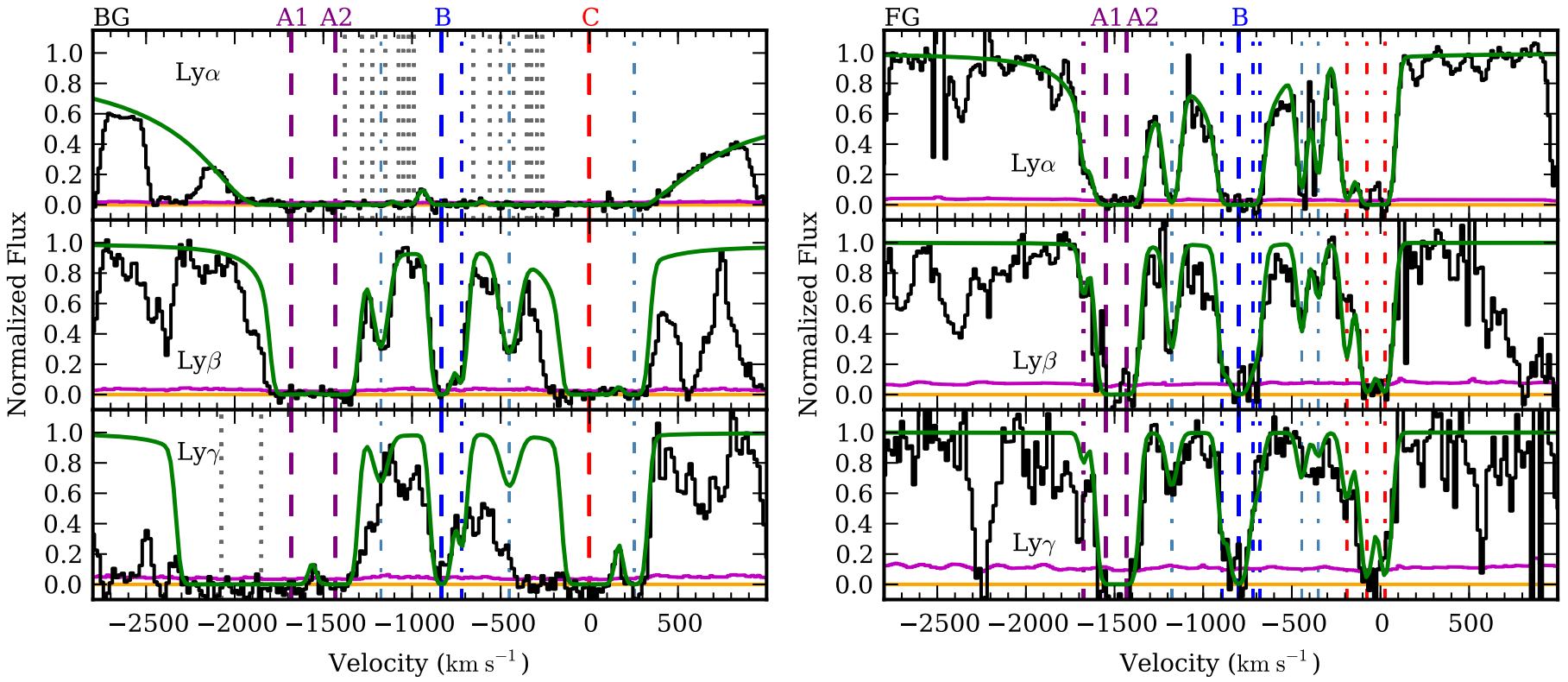

FIGURE 5.2: Fits to Lyα (top), Lyβ (middle), and Lyγ (bottom) H I absorptions in the BG (left) and FG (right) spectra. Dashed purple, blue, and red lines mark the log N(H I) > 18.0 components in regions A, B, and C, while dash-dotted purple, blue, and red lines indicate the weaker components within the respective regions. Dash-dotted blue-gray lines signal low column density components between the three main regions that are also part of the absorption structure. Dotted gray lines in the BG-Lyα panel indicate blended components from Si II λ1190 and 1193 absorptions associated with a $z \simeq 2.75$ DLA.

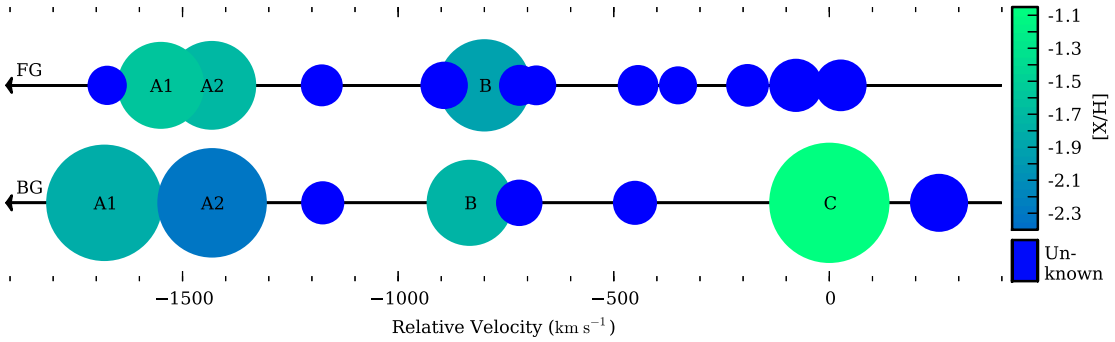

FIGURE 5.3: Diagram of H I clouds distributed along the FG and BG quasar LOS. Circle sizes scale with the H I column density such that twice the area represents eight times as much N(H I) (Area = N(H I)$^{1/3}$). Low column density clouds, for which no metallicity is measured, are dark blue, while brighter, greener colors indicate clouds with higher metallicities. Zero velocity is at $z = 2.6894$.

5.3.1 Background Quasar Line-of-Sight

5.3.1.1 H I Absorption Systems

The H I absorption profiles for the components in regions A, B, and C are constrained from fitting Lyα – Lyδ in the UVB spectrum (Figure 5.2, left). The redshifts for components BG-A1 ($z = 2.6688$), BG-A2 ($z = 2.6718$), and BG-C ($z = 2.6894$) are fixed based on the fits to their associated low ionisation metal transitions (Figure 5.4). The absorption in region C is a log N(H I) = 20.2±0.1 sub-DLA, and the associated metals are fitted with six components. The main absorption, with five components, spans ∼225 km s^{-1}, and the sixth component at 280 km s^{-1} is redshifted relative to the $z = 2.6894$ system redshift. The BG-C redshift is the average of the six components weighted by their Fe II column densities, which are given in Table 5.1.

The flux in the vicinity of Lyα is almost completely absorbed, except for a small peak separating region A from regions B and C at −950 km s^{-1}. Components BG-A1 and BG-A2 are both sub-DLAs, with log N(H I) = 19.9 ± 0.1 and 19.7 ± 0.3 respectively. Strong Si II $\lambda\lambda$1190, 1193 absorptions from a $z \simeq 2.75$ DLA blend with the H I absorptions and contribute to the extended zero-level flux. The components in region B are more apparent in the Lyβ profile, and when they are included the fit to Lyα recovers the small peak near −950 km s^{-1}. The strong component labelled BG-B (Figure 5.2, left) is a log N(H I) = 18.4 ± 0.2 Lyman limit system (LLS). All eight H I absorptions fitted in the BG spectrum are listed with their velocity offsets relative to the BG-C component in Table 5.2.

TABLE 5.1: Column Densities [$\log(N/\mathrm{cm}^{-2})$] for components of the log $N(\mathrm{H\,I}) = 20.2$ cm^{-2} sub-DLA detected in the BG quasar LOS. Velocities (km s^{-1}) are relative to the BG-C system redshift, $z = 2.6894$. The main components of both O I and C II are saturated.

z	v	O I	$\sigma_{\mathrm{O\,I}}$	Si II	$\sigma_{\mathrm{Si\,II}}$	C II	$\sigma_{\mathrm{C\,II}}$	Al II	$\sigma_{\mathrm{Al\,II}}$	Al III	$\sigma_{\mathrm{Al\,III}}$	Fe II	$\sigma_{\mathrm{Fe\,II}}$
2.687165	-180	14.52:	0.04	13.31	0.08	14.75:	0.11	12.22	0.06	11.69	0.35	12.95	0.05
2.688148	-100	15.09:	0.02	14.17	0.02	14.92:	0.03	12.90	0.03	11.93	0.29	13.73	0.01
2.688912	-38	16.23:	0.33	14.11	0.04	15.10:	0.44	13.35	0.10	12.21	0.13	14.16	0.03
2.689329	-4	17.59:	0.44	14.72	0.07	14.61:	0.66	12.95	0.06	12.09	0.17	13.74	0.03
2.689953	47	14.89:	0.03	14.04	0.02	15.07:	0.03	12.76	0.03	11.57	0.90	13.58	0.02
2.692830	280	14.16	0.03	13.44	0.06	14.19	0.02	12.23	0.05	–	–	13.06	0.04

TABLE 5.2: H I column densities [$\log(N/\mathrm{cm}^{-2})$] for components along the BG and FG quasar LOS. Velocities (km s^{-1}) are relative to the BG-C system redshift, $z = 2.6894$.

Comp. Name	v (km s^{-1})	BG log N(H I)	FG log N(H I)
BG-A1	-1681	19.90	–
	-1675	–	14.32
FG-A1	-1550	–	18.46
BG-A2, FG-A2	-1432	19.67	18.57
	-1176	14.82	14.66
	-893	–	15.30
BG-B	-834	18.41	–
FG-B	-800	–	18.77
	-719	15.20	14.54
	-680	–	14.39
	-451	14.92	–
	-444	–	14.50
	-351	–	14.15
	-190	–	14.75
	-78	–	15.90
BG-C	0	20.15	–
	26	–	15.75
	294	16.22	–

5.3.1.2 Abundances

Table 5.3 gives abundances for the LLS and sub-DLA systems in the three regions. The abundances are calculated with respect to solar values (Lodders 2003) following the convention $[\mathrm{X/H}] \equiv \log(\mathrm{X/H}) - \log(\mathrm{X/H})_\odot$.

The BG-A1 and BG-A2 metal absorptions are single-component, and we detect O I, which is a good indicator of the metallicity. Charge transfer processes imply that O I and H I are tightly related (Field & Steigman 1971). Since both the O I λ1302 and O I λ1039 transitions are detected for the BG-A1 component, the absorption line fit is well-constrained. The oxygen abundance is $[\mathrm{O/H}] = -1.19 \pm 0.34$. The Si, Al, and Fe abundances are slightly lower with $[\mathrm{X/H}] = -1.7$, -2.1, and -1.9 respectively. The BG-A1 C II λ1334 absorption is blended with Si II λ1304 from the $z = 2.75$ DLA. We estimate the de-blended C abundance, $[\mathrm{C/H}] = -1.83 \pm 0.59$, by fixing the DLA N(Si II) from other transitions and imposing the same FWHM as for the other BG-A1 absorptions.

The O I λ1039 transition is blended for the BG-A2 component, but the absorptions are non-saturated. The oxygen abundance, $[\mathrm{O/H}] = -1.56 \pm 0.43$, is again slightly higher than the Si, C, Al, and Fe abundances $[\mathrm{X/H}] \lesssim -2.1$. The BG-A2 C II λ1334 absorption is redder than the DLA Si II λ1304 absorption and unaffected by blending.

The [C/O] values, -0.64 ± 0.68 for BG-A1 and -0.54 ± 0.55 for BG-A2, follow the trend where, in low-metallicity systems, [C/O] increases as [O/H] decreases (Cooke et al. 2011; Dutta et al. 2014).

No metal transitions corresponding to the H I absorptions in region B are detected (Figure 5.4) to a limit of log $N(\mathrm{O\,I}) \leq 13.0 \pm 0.1$. To obtain this estimate, we use the average FWHM from the detected BG-A1 and BG-A2 O I components and limit the absorption strength according to the noise in the flux. The upper limit on the [O/H] abundance is -1.80 ± 0.25.

The abundances for the region C sub-DLA, [Si/H] $= -0.71 \pm 0.11$, [Al/H] $= -0.89 \pm 0.08$, and [Fe/H] $= -1.13 \pm 0.18$, are somewhat higher than the average value for intervening DLAs at $z \simeq 2.69$, $\langle Z \rangle = -1.24 \pm 0.12$ (Rafelski et al. 2012). The enhanced [Si/Fe] value, $= 0.41 \pm 0.21$, is typical of intervening DLAs at this redshift and is likely due to dust depletion (Prochaska & Wolfe 2002; Vladilo 2002). Absorptions BG-A1, BG-A2, and BG-B all have abundances approximately an order of magnitude lower than that of BG-C.

5.3.2 Foreground Quasar Line-of-Sight

5.3.2.1 H I Absorption Systems

H I absorptions in the FG quasar Lyα forest have a similar structure as the systems in the same redshift range in the BG quasar spectrum (Figure 5.1). Weaker components separate the main concentrations of H I in regions A, B, and C. We fit thirteen components to the Lyα – Lyϵ transitions for this absorption structure (Figure 5.2, right). Their column densities are listed in Table 5.2, along with the velocity offset relative to the BG-C component redshift. Three components, FG-A1, FG-A2, and FG-B, are in the LLS range, with log $N(\mathrm{H\,I}) = 18.5$, 18.6, and 18.8 respectively, all with $\sigma_{N(H\,i)} \simeq 0.2$. The remaining ten components are all below log $N(\mathrm{H\,I}) = 16.0$. The highest column density components, FG-A1, FG-A2, and FG-B, are aligned with strong absorptions in regions A and B of the BG quasar LOS (Figure 5.3). The FG-A1 component is between the BG-A1 and BG-A2 components, whereas the FG-A2 is exactly aligned with BG-A2 and FG-B is offset from FG-B by less than 35 km s^{-1}. In region C, three lower column density components with log $N(\mathrm{H\,I}) \simeq 14.8$, 15.9, and 15.8 occur within 200 km s^{-1} of the BG-C sub-DLA.

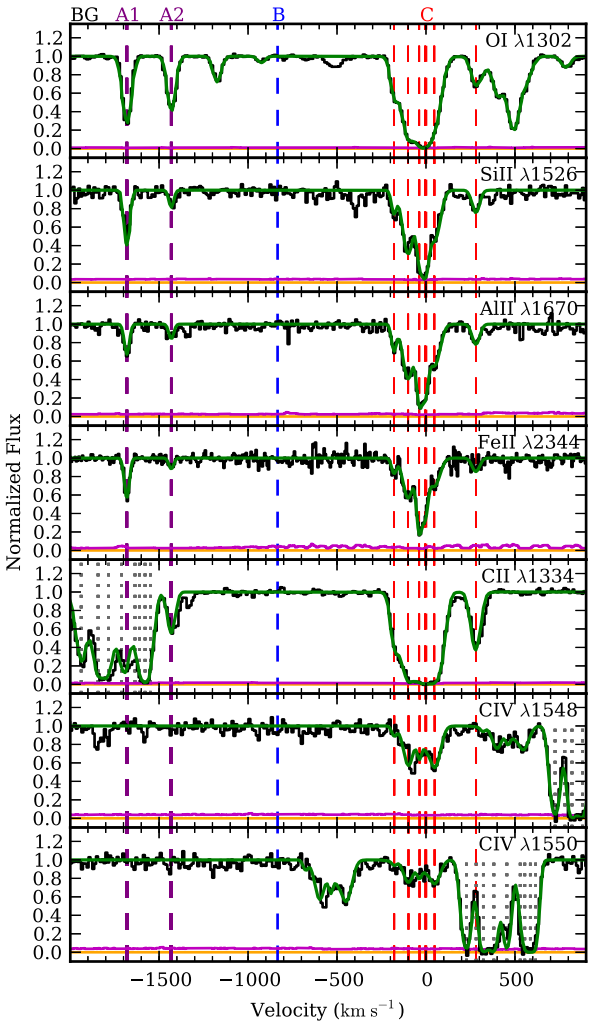

FIGURE 5.4: Fits to metal absorption lines in the BG quasar spectrum. Dashed purple, blue, and red lines mark components in regions A, B, and C. Thin dashed red lines indicate the six individual low-ionization components associated with region C. C IV absorptions are not detected for the BG-A1 and BG-A2 components, and no metal absorption lines associated with the BG-B component are detected. Si II λ1304 absorptions appear directly to the right of the O I λ1302 absorptions in the uppermost panel. The BG-A1 C II component is blended with the Si II λ1304 absorption from a $z \simeq 2.75$ DLA (dotted gray lines), but the BG-A2 component is unaffected. Dotted gray lines in the C IV $\lambda\lambda$ 1548, 1550 panels likewise indicate components from the Si II λ1526 absorption associated with the same $z \simeq 2.75$ DLA. Zero velocity is at $z = 2.6894$, and the 1-σ error on the flux is shown in magenta.

5.3.2.2 Abundances

Low-ionisation metals are detected only for the FG-A2 H I component (Figure 5.5). The C II, Si II, Al II, and Fe II absorptions are fitted with two components, as required to follow the C II profile. The absorptions are weak, however, and often difficult to distinguish from the noise. Upper limits on the abundances are $[\mathrm{C/H}] \leq -0.70 \pm 0.48$, $[\mathrm{Si/H}] \leq -0.48 \pm 0.40$, $[\mathrm{Al/H}] \leq -0.50 \pm 0.45$, and $[\mathrm{Fe/H}] \leq -1.08 \pm 0.47$. Since the FG-A2 H I column density is $\log N(\mathrm{H\,I}) = 18.6$, the gas is not predominantly neutral

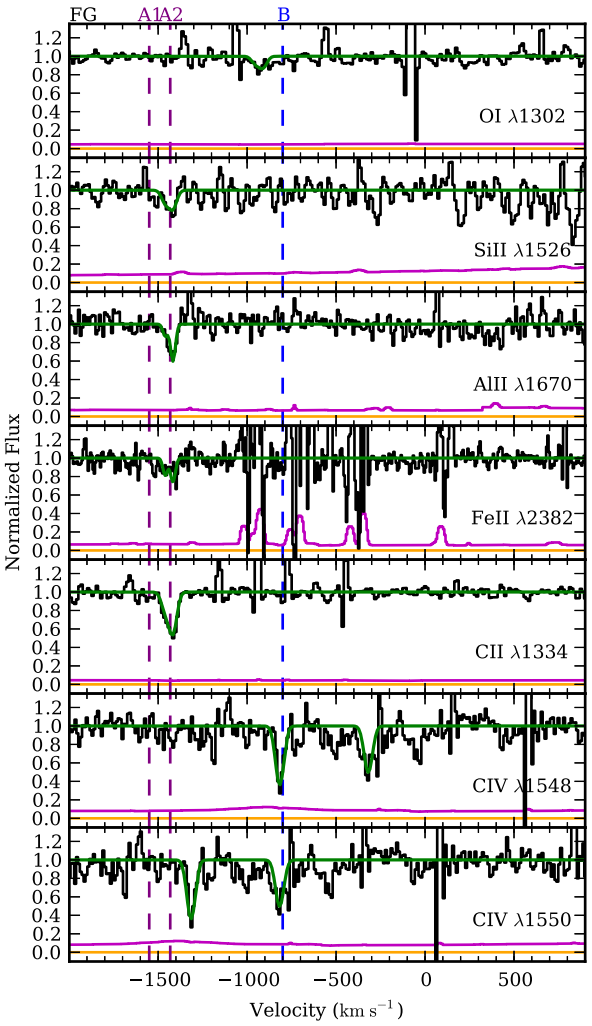

FIGURE 5.5: Fits to metal absorption lines in the FG quasar spectrum. Dashed purple and blue lines mark the strong H I components in regions A and B. Weak low ionisation transitions (C II, Si II, Al II, Fe II) associated with FG-A2 are fitted with two components. No C IV is detected in region A to a limit of log N(C IV) $< 13.2 \pm 0.1$. For FG-B, only C IV is detected. Zero velocity is at $z = 2.6894$, and the 1-σ error on the flux is shown in magenta.

and ionization corrections are likely significant. Both C II and Si II can be associated with the ionized gas.

To obtain a reliable metallicity indicator, we estimate an upper limit of log N(O I) $\leq 13.5 \pm 0.1$ for the three LLS, FG-A1, FG-A2, and FG-B, using the same process as in Section 5.3.1.2. Their corresponding metallicity limits are [O/H] ≤ -1.7, -1.8, and -2.0.

5.4 Discussion and Conclusions

We studied coincident H I absorptions that occur in LOS toward the FG and BG quasars in the J0913-0107 pair. Samples of close quasar pairs have been employed to measure quasar clustering when the redshift differences are negligible (e.g., Hennawi et al. 2010) and to investigate quasar host galaxy environments when the redshifts are offset (e.g., Prochaska et al. 2013a). Despite growing statistics, very few strong coincident absorptions along the LOS have been reported. Ellison et al. (2007) analyzed a binary quasar pair featuring coincident DLA/sub-DLA systems at both $z = 2.66$ and $z = 2.94$ along the two LOS. The transverse distance between the LOS, $\sim 110 h_{70}^{-1}$ kpc, is very similar to that of the LOS presented here; however, the separation between the absorbers along the LOS is an order of magnitude larger than the extent of the coincident absorption region in the J0913-0107 pair. The absorbers also have high [Zn/H] abundances. After comparing with cosmological simulations, the authors determined that the coincident absorptions are more likely due to groups of two or more galaxies than individual large galaxies.

In this work, the velocity separation, metallicities, and kinematics for coincident H I absorptions along the studied region in the two J0913-0107 quasar spectra suggest that their LOS probe the same extended gaseous structure. Examining Figure 5.3, we notice that the absorption system kinematics and metallicities remain similar across the $\sim 90\ {h_{70}}^{-1}$ kpc proper ($0.32\ {h_{70}}^{-1}$ Mpc comoving) distance separating the two LOS. The highest column density absorptions in the FG LOS all have log $N(\mathrm{H\,I}) > 18.5$ counterparts in the BG LOS. The main exception is that the log $N(\mathrm{H\,I}) = 20.2$ BG-C component does not correspond to a high $N(\mathrm{H\,I})$ absorption in the FG LOS.

In region A, the dense gas extends more than $90\ {h_{70}}^{-1}$ kpc in the transverse direction and 250 km s^{-1} along the LOS. The components, which have [O/H] ≤ -1.7 (FG) and [C/O] $\sim$ [Fe/O] ~ -0.5 (BG), are consistent with very metal poor gas (Dutta et al. 2014) and approach what is believed to be the IGM metallicity (Simcoe et al. 2004). Each LOS has one strong component in region B. BG-B and FG-B are closely aligned and also have low metal abundances: [O/H] ≤ -1.8 and -2.0, respectively. Finally, the log $N(\mathrm{H\,I}) \simeq 20.2$ sub-DLA in region C with [Si/H] $= -0.7$ is likely associated with a galaxy. The BG-C abundance is somewhat higher than that of DLAs at the same redshift (Rafelski et al. 2012). If the BG-C sub-DLA galaxy is accreting gas from its surroundings, this could explain the lack of higher column density absorptions in region C of the FG spectrum. Due to accretion, gas in the galaxy halo becomes more sparsely distributed. The A, B, and C regions have distinct properties that are overall consistent in both spectra, but along each LOS the clouds do not appear to be directly in contact.

TABLE 5.3: Abundances relative to solar values (taken from Lodders 2003) for the log $N(\mathrm{H\,I})$ (cm^{-2}) > 18.0 absorption systems detected along the BG and FG quasar LOS. Zero velocity corresponds to $z = 2.6894$.

Comp.	v (km s^{-1})	$N(\mathrm{H\,I})$	$\sigma_{N(H\,i)}$	O	σ_{O}	Si	σ_{Si}	C	σ_{C}	Al	σ_{Al}	Fe	σ_{Fe}
BG-A1	-1681	19.90	0.06	-1.19	0.34	-1.57	0.11	-1.83	0.59	-2.06	0.15	-1.86	0.14
BG-A2	-1431	19.67	0.26	-1.56	0.43	-2.06	0.34	-2.10	0.34	-2.22	0.35	-2.35	0.30
BG-B	-834	18.41	0.23	≤-1.80	0.25	–	–	–	–	–	–	–	–
BG-C	0	20.15	0.05	–	–	-0.72	0.11	–	–	-0.89	0.08	-1.13	0.18
FG-A1	-1550	18.46	0.21	≤-1.65	0.24	–	–	–	–	–	–	–	–
FG-A2	-1432	18.57	0.24	≤-1.76	0.27	–	–	–	–	–	–	–	–
FG-B	-800	18.77	0.20	≤-1.96	0.23	–	–	–	–	–	–	–	–

These absorptions span more than 1 700 km s^{-1} along each LOS, which corresponds to a proper distance of 6.4 $h_{70}{}^{-1}$ Mpc at $z = 2.69$ (23.6 $h_{70}{}^{-1}$ Mpc comoving). Velocity differences at this scale are dominated by the Hubble flow, rather than physical velocities intrinsic to the gas clouds. The A, B, and C absorption regions have a velocity separation of more than 5 000 km s^{-1} from the FG quasar at $z = 2.75$, which makes direct association with the quasar environment unlikely (Ellison et al. 2010).

In addition to the log $N(\mathrm{H\,I}) > 18.0$ components, several weaker absorptions within the ∼2 000 km s^{-1} region are common to both LOS. Corresponding absorptions with log $N(\mathrm{H\,I}) = 14.5 - 15.2$ occur near -1180 km s^{-1}, -720 km s^{-1}, and -450 km s^{-1}. For Lyα forest absorptions in the range log $N(\mathrm{H\,I}) = [14, 17]$ at $z \sim 2.55$, Kim et al. (2013) measured a mean line density $dN/dz = 76.38 \pm 7.32$. The regions where such Lyα absorptions can be detected in both LOS cover a total of 950 km s^{-1}. This is less than the full coincident region, since the log $N(\mathrm{H\,I}) > 18.0$ systems completely absorb the flux in the remaining portion of the coincident region. The expected number of low column density absorptions is therefore 0.89 ± 0.09, whereas three are observed. The probability of such an occurrence is only 6%.

To investigate whether the strong absorption systems imply an overdensity, we evaluate the probability of finding two additional LLS within 2 000 km s^{-1}, given that one LLS occurs along the total path length. O'Meara et al. (2013) determined that the line density, dN/dz, for log $N(\mathrm{H\,I}) \geq 17.2$ cm^{-2} absorptions is 0.92 ± 0.18. For the redshift path between the BG quasar at $z = 2.916$ and the end of the spectrum at 3 000Å ($z = 1.468$), this probability is ∼0.07%. Since the LLS absorptions in the J0913-0107 spectrum all have log $N(\mathrm{H\,I}) \geq 18.0$, the ∼0.07% probability can be considered an upper limit. The LOS clearly probe an overdense region, which may be evidence of a galaxy protocluster, perhaps with a filamentary structure, or a filament in the IGM. We present arguments for the two interpretations.

Following hierarchical structure formation, regions that give rise to galaxy clusters at $z < 1$ have been matter-rich throughout cosmic time. In cosmological simulations, individual galaxies come together along gaseous filaments, creating small groups that in turn merge to form clusters by low redshift. Identifying overdense regions at high redshift that will eventually collapse to form gravitationally bound clusters at $z = 0$ is of particular interest for investigating galaxy cluster evolution. By tracking cluster formation in cosmological simulations, Chiang et al. (2013) were able to predict the $z = 0$ cluster mass from the galaxy overdensity at $2 < z < 5$. The comoving length of the coincident absorption region along the J0913-0107 LOS is consistent with the expected effective diameter for a protocluster. However, to be identified as a protocluster at

$z \sim 2-3$ with 80% confidence, a (25 Mpc comoving)^3 region must exhibit an overdensity of more than twice as many galaxies with $M_* > 10^9\ M_\odot$ than a typical field.

We consider whether is it likely that the absorbers probe gas in the environment of massive galaxies. Rahmati & Schaye (2014) associated log N(H I) > 17 absorptions with galaxies in cosmological, hydrodynamical simulations (see also McQuinn et al. 2011) at $z = 3$ and found that most strong absorbers are most closely related to low mass galaxies with $M_* < 10^8\ M_\odot$. Only log N(H I) > 21 absorptions are routinely associated with $M_* > 10^9\ M_\odot$ galaxies. The mass-metallicity relation similarly suggests that typical DLAs have $M_* \sim 10^{8.5}\ M_\odot$ (Møller et al. 2013). Although the A, B, and C regions in the J0913-0107 LOS are overdense, the galaxies may not be sufficiently massive to directly contribute to the protocluster criterion.

Each quasar LOS can potentially detect C IV gas associated with the circumgalactic medium of massive star-forming galaxies out to a distance of 0.42 h_{70}^{-1} Mpc comoving (Martin et al. 2010). Combining the Schechter mass function for field galaxies (Tomczak et al. 2014) with the factor of 2.2 overdensity necessary for a galaxy protocluster (Chiang et al. 2013), the LOS probe a volume that would encompass only ∼0.1 $M_* > 10^9\ M_\odot$ protocluster galaxies if they are randomly distributed. The possibility that the overdense region intersects a protocluster therefore cannot be ruled out, even if the absorber galaxies are not particularly massive. However, the overdensity of log N(H I) > 18 absorbers is ∼90, which is much higher than the expected overdensity of galaxies in a protocluster. This suggests that the absorbers could be aligned in a filamentary structure.

Cosmic web filaments are expected to consist of clumpy, moderate column density gas distributed over cosmological scales, much like the clouds diagrammed in Figure 5.3. Furthermore, the process of mass build-up that results in galaxy clusters at low redshift is thought to occur along filamentary structures. The metallicity distribution along the overdense A, B, and C regions may indicate a filamentary structure. Absorptions in regions A and B probe very metal poor gas; their metal abundances are nearly an order of magnitude below that of the BG-C component. Lehner et al. (2013) identify a bimodality in the metallicity distribution of $z \lesssim 1$ LLS and argue that the low-metallicity ($\langle$[X/H]$\rangle < -1.57 \pm 0.24$) population traces gas accreting along filaments. Similarly, Bouché et al. (2013) highlight the metallicity difference between a $z = 2.3$ star-forming galaxy and gas detected in a DLA at an impact parameter of 26 kpc. The metallicity and gas kinematics of this system are consistent with a scenario where infalling IGM gas co-rotates in the halo before accreting onto the galaxy disk. The gas in the overdense region may be distributed along the length of a filament, probed by the two parallel quasar LOS.

The observed substructures are likely not in interaction, based on the C IV content of the gas. In an environment where galaxies are interacting, we expect C IV to be conspicuous both because of metal enrichment and higher temperatures. Relatively little C IV absorption associated with the overdense H I region is apparent in the spectra (Figures 5.4 and 5.5), and the C IV absorption associated with the BG-C sub-DLA is relatively weak. Consistent with the metallicity results, the lack of strong C IV absorption implies that the overdense region is not highly enriched. With high resolution, high S/N spectra, Songaila & Cowie (1996) studied the correspondance between H I and C IV absorptions. They found that 90% of log N(H I) > 15.2 absorptions have log N(C IV) > 12.0. In the range log N(H I) $= [15, 17]$, the median C IV/H I value is 3×10^{-3}. The detection limit of log N(C IV) < 12.8 (BG) and 13.2 (FG) may nevertheless be insufficient to reveal C IV absorptions associated with the lower column density H I components.

We favor the interpretation that the gas is distributed in a 6.4 ${h_{70}}^{-1}$ Mpc proper filament at $z \simeq 2.69$. The high concentration of gas clouds along the LOS is difficult to explain with the factor of $\sim$2 galaxy overdensity expected in a protocluster and suggests a clumpy, filamentary structure. The metallicities in regions A and B differ by a factor of ten from the metallicity in region C, and the lack of strong C IV absorption likewise implies that the overdense region is not highly enriched. However, we cannot rule out that this filamentary structure represents the first stages of cluster formation. Imaging this field to search for galaxies associated with the overdensity is essential to unveiling its true nature. Detecting a possible filament in absorption is a step forward in revealing the structure of the IGM on small scales and foreshadows what will be possible with the next generation of 30 m telescopes.

Chapter 6

Conclusions and Prospects

6.1 Conclusions

The properties of quasar host galaxies are of particular interest at the $z = 2 - 3$ epoch, when the quasar luminosity function peaks (e.g., Richards et al. 2006; Ross et al. 2013). Accessing the galactic environments is essential for determining how feedback mechanisms govern the AGN phase of galaxy evolution. Initially, black hole accretion and star formation probably occur together, as both processes are fueled by gas brought to the center via gas-rich mergers and disk instabilities (e.g., Lutz et al. 2008). In one explanation, the AGN phase ends when the two processes have depleted the gas reservoir. Alternatively, AGN outflows blow the gas out of the host galaxy, curtailing star formation (e.g., Fabian et al. 2006). This second scenario requires the outward force from the radiation pressure to exceed the inward gravitational force, implying a minimum luminosity for the AGN.

Observations of high-redshift quasar host galaxies strive to identify evidence of feedback mechanisms and distinguish between these two possibilities. Rauch et al. (2013) obtained spectra of the extended Lyα emission around an obscured quasar at $z = 3.045$ and detected a young stellar population near the quasar that likely formed simultaneous to the AGN activity. Deep NIR imaging aided by adaptive optics has revealed quasar host galaxies at $z = 2 - 3$ with elliptical morphologies and luminosities that are consistent with passive evolution since $z \sim 3$ (Falomo et al. 2008; Wang et al. 2013b). Damped Lyα absorption systems (DLAs) that probe gas in the immediate environment of quasar host galaxies contribute information about the extent of ionization from the AGN, as well as the composition and kinematics of the absorbing gas.

SDSS-III BOSS significantly increased the number of spectroscopically confirmed high-redshift quasars and thereby opened new avenues for studying their host galaxy environments. From the initial 61 931 quasars at $z > 2.15$ in DR9, I identified rare configurations that made it possible to overcome the dominant, blinding radiation from the Broad Line Region (BLR) and access the galactic environment. I implemented two techniques that use DLAs to probe gas at the quasar redshift either along the line-of-sight or in the transverse direction.

Strong DLAs that occur along the line-of-sight at the quasar redshift act as natural coronagraphs, completely absorbing the broad Lyα emission from the central AGN. In some cases, when the absorbing cloud is small compared to the emitting region, it is then possible to observe a narrow Lyα emission line from the quasar host galaxy superimposed on the DLA trough. These absorbers may be dense, compact clouds in the quasar host galaxy. However, when no narrow Lyα emission is detected, the DLA may be due to a neighboring galaxy that acts as a screen, blocking even the more extended emission from the quasar host. To test this scenario, I identified a complete sample of 31 $\log N(\mathrm{H\,I}) \geq 21.3$ DLAs from DR9 within 1 500 km s^{-1} of the quasar redshift, eight of which reveal narrow Lyα emission, and compared the properties, including the velocity offsets, metal absorption line equivalent widths, colors, and reddening, of DLAs with and without narrow Lyα emission detected. Although clouds in quasar host galaxies could be expected to have different properties from neighboring galaxies, due to enhanced kinematics and metal enrichment from the AGN, no clear differences emerged from an analysis with the low-resolution, low-S/N BOSS spectra.

To characterize the narrow Lyα emission, which remains the most striking feature differentiating the DLAs, I supplemented the detections in the complete sample with additional $z_{\mathrm{abs}} \simeq z_{\mathrm{em}}$ DLAs from DR10, accumulating a total of 26 that reveal narrow Lyα emission. Based on the integrated flux (IF) values, the sample can be separated into 11 strong narrow Lyα emission peaks with IF $> 40 \times 10^{-17}$ erg s^{-1} cm^{-2} and 15 moderate ones with IF $< 26 \times 10^{-17}$ erg s^{-1} cm^{-2}. Stacked spectra of both the strong and moderate narrow Lyα emission peaks revealed that the emission profile is symmetric, unlike the profile observed for Lyman Break Galaxies. The symmetric profiles suggests that the emission regions lacks H I gas to scatter the Lyα photons, implying that the DLA gas is not directly associated with the emission regions.

Finally, comparing the Lyα luminosities to those of Lyman-Alpha Emitters (LAEs) and radio galaxies helped constrain the relative sizes of the emitting and absorbing regions. Roughly half of the narrow Lyα emission peaks detected by using DLAs as coronagraphs have luminosities consistent with standard LAEs. For these quasar host galaxies, the DLA is extended enough to cover most of the NLR around the AGN and reduce the

luminosity to a value more typical of a star-forming galaxy. The luminosities for the other half of the narrow Lyα emission peaks are higher than what is typical for LAEs. They are comparable to, but smaller than, those of radio galaxies, whose jets inject energy far from their centers. The luminosities that approach those of radio galaxies are not surprising, given that the AGN ionizes the surrounding gas, which in turn emits Lyα photons. In these cases, the absorber does not significantly obscure the emitting region, and the DLA could arise from a small cloud in the host galaxy.

Complementary to probing the quasar host galaxy along its own line-of-sight with coronagraph DLAs, a second technique makes use of pairs of quasars with small angular separations to investigate their environments at transverse proper distances of $\lesssim 90\ {h_{70}}^{-1}$ kpc. I identified three such close line-of-sight pairs, where a DLA appears in the spectrum of a higher-redshift background quasar coincident with the Lyα emission peak of a lower-redshift foreground quasar, in DR9 and obtained follow-up observations with the VLT/X-shooter. The DLA systems for all three pairs revealed predominantly neutral gas distributed over at least 250 km s^{-1} and grouped into two or three main clumps. The prevalent neutral and low-ionisation gas in the transverse direction suggests that the quasars emit anisotropically, in agreement with previous studies (Hennawi & Prochaska 2007, 2013; Hennawi et al. 2006a; Prochaska et al. 2013a). Surprisingly, diffuse gas in the quasar halo, probed with the weaker H I absorptions, does not show evidence of significant C IV enrichment. The lack of strong C IV absorptions in the vicinity of the quasar host galaxies can be explained if the halo temperatures are too high to show absorptions associated with intermediate temperature gas (T $\simeq 10^{4-5}$ K), like C IV. The halo gas appears to be in either a cold phase, probed by the DLAs, or a hot phase that may be possible to detect via X-ray emission.

Close line-of-sight pairs are also a powerful tool for investigating overdense regions beyond the quasar host galaxy environment by helping to characterize structure in the intergalactic medium (IGM). I serendipitously detected an overdensity of log N(H I) $>$ 18.0 absorbers at $z \simeq 2.69$ along the lines-of-sight toward the close pair separated by $\sim 90\ {h_{70}}^{-1}$ kpc transverse proper distance, J0913-0107. Three main absorption regions spanning $\sim$2 000 km s^{-1} (corresponding to 6.4 ${h_{70}}^{-1}$ Mpc proper) are coincident in the two lines-of-sight. Two regions have [Fe/H] < -1.9 and correspond to mild overdensities in the IGM gas, while the third region is a sub-DLA with [Fe/H] $= -1.1$ that is likely associated with a galaxy. Since the probability of intercepting two additional LLS within 2 000 km s^{-1} of a first LLS along the observed path length is only $\sim$0.07%, the lines-of-sight clearly probe an overdense region that possibly arises from either a galaxy protocluster or a filament in the IGM. The factor of $\sim$90 overdensity of log N(H I) > 18 absorbers suggests that the absorbers could be aligned in a filamentary structure. The very metal poor gas in two of the regions and overall lack of strong C IV absorption

implies that the overdense region is not highly enriched, further evoking an IGM environment. Via the build-up of structure along this possible filament, the overdense region may nonetheless later collapse into a galaxy cluster at low redshift.

6.2 Prospects

6.2.1 Follow-Up Projects

Coronagraph DLAs that reveal narrow Lyα emission are natural candidates for follow-up projects designed to investigate the extent of the NLR in high-redshift quasar host galaxies. I have either obtained or anticipate follow-up observations of several such targets with Magellan/MagE, VLT/X-shooter, and HST/WFC3. For six of the coronagraph DLAs that have strong narrow Lyα emission, MagE spectra were taken at two different position angles. The 2-D MagE spectra reveal narrow Lyα emission that is extended in at least one of the orientations for all six targets. The emission regions span $\sim 10 - 20$ kpc, suggesting that the AGN has a large-scale impact on its environment.

Additional spectra from X-shooter were obtained for two of the quasars observed with MagE, J0953+0349 and J1154-0215. The higher-resolution spectra will give a measure of the metallicity and depletion in the absorbing gas. Furthermore, the X-shooter wavelength range extends into the NIR, where NLR emission from [O II], [O III], Hβ, and Hα may be detected and/or deblended. The emitting and absorbing gas metallicities can then be compared to investigate metallicity gradients, and their relative kinematics may reveal evidence of gas outflow or infall.

One of the narrow-band filters for the HST/WFC3 fortuitously overlaps with the narrow Lyα emission detected in the DLA trough toward the J1154-0215 quasar. For the first time, it is possible to image a $z > 2$ quasar host galaxy while avoiding complications from PSF subtraction. The spatially-resolved observations will probe the distribution of photoionized gas in the host galaxy, potentially giving an indication of the host galaxy morphology, and could also detect fluorescent emission in the surrounding environment. Together, the observations from these three instruments will provide new details about the impact of AGN on their host galaxies.

6.2.2 Future Work

The Multi Unit Spectroscopic Explorer (MUSE), a second-generation instrument installed on the VLT in January 2014, will open new avenues for studying high-redshift

galaxies. One of the primary science goals is to investigate galaxy formation and evolution. Indeed, the simultaneous spectral range covers 4650 - 9300 Å, which means MUSE can detect Lyα emission from galaxies at $2.8 \lesssim z \lesssim 6.7$. By executing deep, 80-hour exposures reaching a limiting flux of 3.9×10^{-19} ergs s^{-1} cm^{-2}, the science collaboration expects to find $300 - 1\,000$ Lyα emitting galaxies in each 1×1 arcmin^2 field of view. The full survey is anticipated to detect ∼15 000 such galaxies and will be an important resource for a variety of scientific endeavors, including:

- improving the Lyα luminosity function.
- determining clustering properties and merger rates.
- probing Lyα emission at the Epoch of Reionization .
- mapping the cosmic web with extended Lyα halos and fluorescent emission.
- searching for late-forming population III stars.
- investigating the physics of Lyman break galaxies by analyzing winds and IGM feedback.
- studying AGN environments at intermediate and high redshifts.

It will be possible to associate galaxies detected in MUSE deep fields with quasar absorption line systems, building on the original Steidel et al. (1997) analysis at $z \leq 1$. In addition to probing higher redshifts, MUSE will provide greater statistical leverage. The IFU observations are also efficient, since they simultaneously accomplish imaging and spectroscopy of objects in the field.

MUSE can likewise target quasar host galaxy environments by mapping Lyα absorption and fluorescent emission. The IFU observations would extend ∼250 kpc around a $z \sim 3$ quasar and compliment studies of the transverse quasar-absorber correlation function measured from pairs of quasar sight lines, which suggest anisotropic absorption (Hennawi & Prochaska 2007; Kim & Croft 2008; Prochaska et al. 2013a). MUSE would be very useful for investigating the distribution of neutral hydrogen and the impact of ionization from the nearby quasar. A proximity effect indicating either increased ionizing flux or higher HI density is observed along the line-of-sight (e.g., Rollinde et al. 2005). Comparing galaxy clustering in a quasar field with a randomly selected field may also provide additional evidence that quasar hosts tend to be in overdense regions.

Additionally, the coronagraph DLAs would be interesting targets for MUSE. The instrument can operate in Narrow Field Mode with a $7.5'' \times 7.5''$ field of view and spatial sampling of $0.025'' \times 0.025''$, making it competitive with current space-based facilities. The

anticipated limiting flux for 1 hour in Narrow Field Mode is 2.3×10^{-18} ergs s^{-1} cm^{-2}. MUSE would therefore be able to image Lyα emission from quasar host galaxies with associated DLAs.

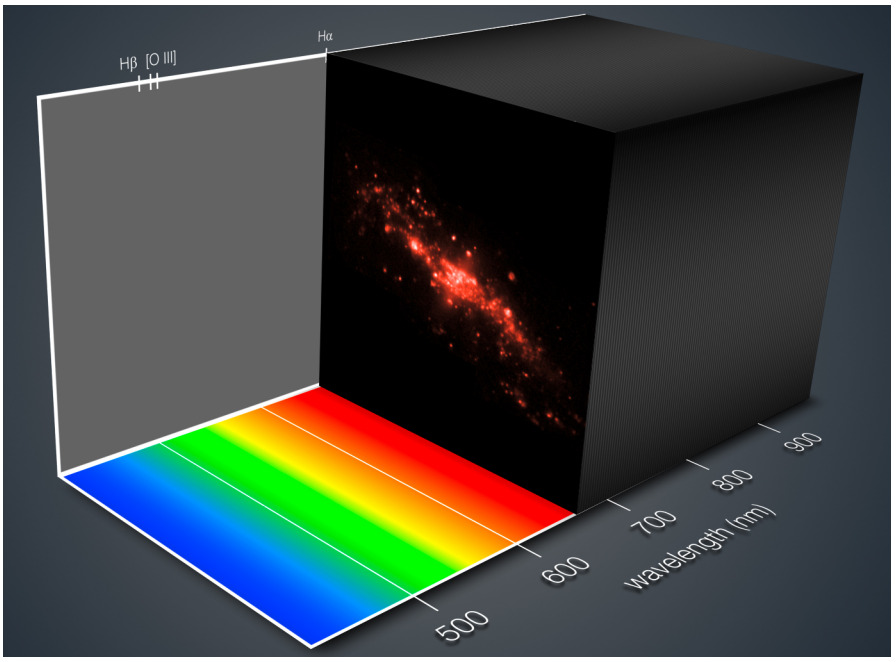

FIGURE 6.1: The IFU obtains an image at each observed wavelength. This image highlights Hα emission from the nearby galaxy NGC 4650A targeted during the MUSE commissioning phase.

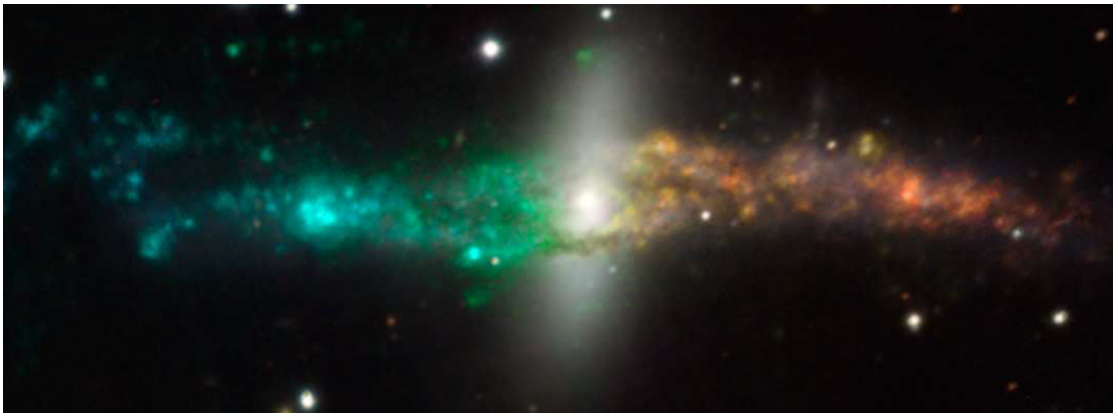

FIGURE 6.2: Star formation regions in this composite MUSE image of NGC 4650A are color-coded based on their velocities, with blue approaching and red receding. The velocity is determined based on how an emission line is offset from its rest wavelength in each spectral pixel (spaxel).

Bibliography

Abazajian, K. N., Adelman-McCarthy, J. K., Agüeros, M. A., et al. 2009, ApJS, 182, 543

Adelberger, K. L., Shapley, A. E., Steidel, C. C., et al. 2005, ApJ, 629, 636

Adelberger, K. L., Steidel, C. C., Kollmeier, J. A., & Reddy, N. A. 2006, ApJ, 637, 74

Adelman-McCarthy, J. K., Agüeros, M. A., Allam, S. S., et al. 2007, ApJS, 172, 634

Ahn, C. P., Alexandroff, R., Allende Prieto, C., et al. 2014, ApJS, 211, 17

Ahn, C. P., Alexandroff, R., Allende Prieto, C., et al. 2012, ApJS, 203, 21

Aihara, H., Allende Prieto, C., An, D., et al. 2011a, ApJS, 193, 29

Aihara, H., Allende Prieto, C., An, D., et al. 2011b, ApJS, 195, 26

Alcock, C. & Paczynski, B. 1979, Nature, 281, 358

Alexandroff, R., Strauss, M. A., Greene, J. E., et al. 2013, MNRAS, 435, 3306

Allen, J. T., Hewett, P. C., Maddox, N., Richards, G. T., & Belokurov, V. 2011, MNRAS, 410, 860

Altay, G., Theuns, T., Schaye, J., Booth, C. M., & Dalla Vecchia, C. 2013, MNRAS, 436, 2689

Altay, G., Theuns, T., Schaye, J., Crighton, N. H. M., & Dalla Vecchia, C. 2011, ApJ, 737, L37

Anderson, L., Aubourg, É., Bailey, S., et al. 2014, MNRAS, 441, 24

Antonucci, R. 1993, ARA&A, 31, 473

Aragón-Calvo, M. A., van de Weygaert, R., & Jones, B. J. T. 2010, MNRAS, 408, 2163

Arav, N., Borguet, B., Chamberlain, C., Edmonds, D., & Danforth, C. 2013, MNRAS, 436, 3286

Bahcall, J. N., Kirhakos, S., Saxe, D. H., & Schneider, D. P. 1997, ApJ, 479, 642

Bahcall, J. N. & Peebles, P. J. E. 1969, ApJ, 156, L7

Balashev, S. A., Petitjean, P., Ivanchik, A. V., et al. 2011, MNRAS, 418, 357

Baldry, I. K., Glazebrook, K., & Driver, S. P. 2008, MNRAS, 388, 945

Barlow, T. A. & Sargent, W. L. W. 1997, AJ, 113, 136

Barnes, L. A. & Haehnelt, M. G. 2009, MNRAS, 397, 511

Becker, R. H., Fan, X., White, R. L., et al. 2001, AJ, 122, 2850

Bell, E. F., McIntosh, D. H., Katz, N., & Weinberg, M. D. 2003, ApJ, 585, L117

Bennert, N., Falcke, H., Schulz, H., Wilson, A. S., & Wills, B. J. 2002, ApJ, 574, L105

Bensby, T. & Feltzing, S. 2006, MNRAS, 367, 1181

Bergeron, J. 1986, A&A, 155, L8

Bergeron, J., Aracil, B., Petitjean, P., & Pichon, C. 2002, A&A, 396, L11

Bergeron, J. & Boissé, P. 1991, A&A, 243, 344

Bergeron, J., Petitjean, P., Sargent, W. L. W., et al. 1994, ApJ, 436, 33

Bi, H. & Davidsen, A. F. 1997, ApJ, 479, 523

Blake, C., Brough, S., Colless, M., et al. 2012, MNRAS, 425, 405

Blake, C., Glazebrook, K., Davis, T. M., et al. 2011, MNRAS, 418, 1725

Blanton, M. R., Lin, H., Lupton, R. H., et al. 2003, AJ, 125, 2276

Bolton, A. S., Schlegel, D. J., Aubourg, É., et al. 2012, AJ, 144, 144

Bond, J. R., Kofman, L., & Pogosyan, D. 1996, Nature, 380, 603

Bond, N. A., Strauss, M. A., & Cen, R. 2010, MNRAS, 409, 156

Borguet, B. C. J., Edmonds, D., Arav, N., Dunn, J., & Kriss, G. A. 2012, ApJ, 751, 107

Bosma, A. 1981, AJ, 86, 1825

Bouché, N., Murphy, M. T., Kacprzak, G. G., et al. 2013, Science, 341, 50

Bouché, N., Murphy, M. T., Péroux, C., et al. 2012, MNRAS, 419, 2

Bouché, N., Murphy, M. T., Péroux, C., et al. 2007, ApJ, 669, L5

Bournaud, F., Dekel, A., Teyssier, R., et al. 2011, ApJ, 741, L33

Bovy, J., Hennawi, J. F., Hogg, D. W., et al. 2011, ApJ, 729, 141

Braun, R. 2012, ApJ, 749, 87

Bunker, A. J., Warren, S. J., Clements, D. L., Williger, G. M., & Hewett, P. C. 1999, MNRAS, 309, 875

Busca, N. G., Delubac, T., Rich, J., et al. 2013, A&A, 552, A96

Cappetta, M., D'Odorico, V., Cristiani, S., Saitta, F., & Viel, M. 2010, MNRAS, 407, 1290

Carswell, B., Schaye, J., & Kim, T.-S. 2002, ApJ, 578, 43

Cattaneo, A., Faber, S. M., Binney, J., et al. 2009, Nature, 460, 213

Caucci, S., Colombi, S., Pichon, C., et al. 2008, MNRAS, 386, 211

Cautun, M., van de Weygaert, R., Jones, B. J. T., & Frenk, C. S. 2014, MNRAS, 441, 2923

Cen, R. 2012, ApJ, 748, 121

Cen, R. & Fang, T. 2006, ApJ, 650, 573

Cen, R., Miralda-Escudé, J., Ostriker, J. P., & Rauch, M. 1994, ApJ, 437, L9

Cen, R. & Ostriker, J. P. 1999, ApJ, 514, 1

Cen, R. & Ostriker, J. P. 2006, ApJ, 650, 560

Charlton, J. & Churchill, C. 2000, Quasistellar Objects: Intervening Absorption Lines, ed. P. Murdin

Chen, H.-W. & Lanzetta, K. M. 2003, ApJ, 597, 706

Chiang, Y.-K., Overzier, R., & Gebhardt, K. 2013, ApJ, 779, 127

Christensen, L., Møller, P., Fynbo, J. P. U., & Zafar, T. 2014, ArXiv e-prints

Christensen, L., Noterdaeme, P., Petitjean, P., Ledoux, C., & Fynbo, J. P. U. 2009, A&A, 505, 1007

Chuang, C.-H. & Wang, Y. 2012, MNRAS, 426, 226

Chun, M. R., Gharanfoli, S., Kulkarni, V. P., & Takamiya, M. 2006, AJ, 131, 686

Churchill, C. W. & Charlton, J. C. 1999, AJ, 118, 59

Churchill, C. W., Mellon, R. R., Charlton, J. C., et al. 1999, ApJ, 519, L43

Cisewski, J., Croft, R. A. C., Freeman, P. E., et al. 2014, MNRAS, 440, 2599

Colberg, J. M., Krughoff, K. S., & Connolly, A. J. 2005, MNRAS, 359, 272

Cole, S., Norberg, P., Baugh, C. M., et al. 2001, MNRAS, 326, 255

Cooke, R., Pettini, M., Steidel, C. C., Rudie, G. C., & Nissen, P. E. 2011, MNRAS, 417, 1534

Coppolani, F., Petitjean, P., Stoehr, F., et al. 2006, MNRAS, 370, 1804

Croom, S. M., Boyle, B. J., Shanks, T., et al. 2005, MNRAS, 356, 415

Dall'Aglio, A., Wisotzki, L., & Worseck, G. 2008a, A&A, 491, 465

Dall'Aglio, A., Wisotzki, L., & Worseck, G. 2008b, A&A, 480, 359

Davé, R., Oppenheimer, B. D., Katz, N., Kollmeier, J. A., & Weinberg, D. H. 2010, MNRAS, 408, 2051

Davis, T. A., Krajnović, D., McDermid, R. M., et al. 2012, MNRAS, 426, 1574

Dawson, K. S., Schlegel, D. J., Ahn, C. P., et al. 2013, AJ, 145, 10

De Breuck, C., Röttgering, H., Miley, G., van Breugel, W., & Best, P. 2000, A&A, 362, 519

Denicoló, G., Terlevich, R., & Terlevich, E. 2002, MNRAS, 330, 69

Dessauges-Zavadsky, M., Péroux, C., Kim, T.-S., D'Odorico, S., & McMahon, R. G. 2003, MNRAS, 345, 447

Djorgovski, S. G., Pahre, M. A., Bechtold, J., & Elston, R. 1996, Nature, 382, 234

D'Odorico, V., Cristiani, S., D'Odorico, S., et al. 1998, A&A, 339, 678

D'Odorico, V., Cristiani, S., Romano, D., Granato, G. L., & Danese, L. 2004, MNRAS, 351, 976

D'Odorico, V., Viel, M., Saitta, F., et al. 2006, MNRAS, 372, 1333

Dutta, R., Srianand, R., Rahmani, H., et al. 2014, MNRAS, 440, 307

Edmonds, D., Borguet, B., Arav, N., et al. 2011, ApJ, 739, 7

Eisenstein, D. J., Weinberg, D. H., Agol, E., et al. 2011, AJ, 142, 72

Eisenstein, D. J., Zehavi, I., Hogg, D. W., et al. 2005, ApJ, 633, 560

Ellison, S. L., Hennawi, J. F., Martin, C. L., & Sommer-Larsen, J. 2007, MNRAS, 378, 801

Ellison, S. L., Prochaska, J. X., Hennawi, J., et al. 2010, MNRAS, 406, 1435

Ellison, S. L., Prochaska, J. X., & Mendel, J. T. 2011, MNRAS, 412, 448

Ellison, S. L., Yan, L., Hook, I. M., et al. 2002, A&A, 383, 91

Epinat, B., Tasca, L., Amram, P., et al. 2012, A&A, 539, A92

Evans, C. J., Puech, M., Barbuy, B., et al. 2014, ArXiv e-prints

Fabian, A. C. 2012, ARA&A, 50, 455

Fabian, A. C., Celotti, A., & Erlund, M. C. 2006, MNRAS, 373, L16

Falomo, R., Treves, A., Kotilainen, J. K., Scarpa, R., & Uslenghi, M. 2008, ApJ, 673, 694

Fan, X., Strauss, M. A., Becker, R. H., et al. 2006, AJ, 132, 117

Faucher-Giguère, C.-A., Lidz, A., Zaldarriaga, M., & Hernquist, L. 2008a, ApJ, 673, 39

Faucher-Giguère, C.-A., Prochaska, J. X., Lidz, A., Hernquist, L., & Zaldarriaga, M. 2008b, ApJ, 681, 831

Ferland, G. J., Porter, R. L., van Hoof, P. A. M., et al. 2013, Rev. Mexicana Astron. Astrofis., 49, 137

Ferrarese, L. & Merritt, D. 2000, ApJ, 539, L9

Field, G. B. & Steigman, G. 1971, ApJ, 166, 59

Filiz Ak, N., Brandt, W. N., Hall, P. B., et al. 2012, ApJ, 757, 114

Filiz Ak, N., Brandt, W. N., Hall, P. B., et al. 2013, ApJ, 777, 168

Finley, H., Petitjean, P., Pâris, I., et al. 2013, A&A, 558, A111

Finn, C. W., Morris, S. L., Crighton, N. H. M., et al. 2014, MNRAS, 440, 3317

Floyd, D. J. E., Dunlop, J. S., Kukula, M. J., et al. 2013, MNRAS, 429, 2

Font-Ribera, A., Arnau, E., Miralda-Escudé, J., et al. 2013, J. Cosmology Astropart. Phys., 5, 18

Font-Ribera, A., Miralda-Escudé, J., Arnau, E., et al. 2012, J. Cosmology Astropart. Phys., 11, 59

Frebel, A. 2010, Astronomische Nachrichten, 331, 474

Fukugita, M., Ichikawa, T., Gunn, J. E., et al. 1996, AJ, 111, 1748

Fumagalli, M., O'Meara, J. M., Prochaska, J. X., & Kanekar, N. 2010, MNRAS, 408, 362

Fumagalli, M., O'Meara, J. M., Prochaska, J. X., Kanekar, N., & Wolfe, A. M. 2014, ArXiv e-prints

Fumagalli, M., Prochaska, J. X., Kasen, D., et al. 2011, MNRAS, 418, 1796

Fynbo, J. P. U., Geier, S. J., Christensen, L., et al. 2013, MNRAS, 436, 361

Fynbo, J. P. U., Laursen, P., Ledoux, C., et al. 2010, MNRAS, 408, 2128

Fynbo, J. P. U., Ledoux, C., Noterdaeme, P., et al. 2011, MNRAS, 413, 2481

Gabel, J. R., Arav, N., & Kim, T.-S. 2006, ApJ, 646, 742

Gallazzi, A., Charlot, S., Brinchmann, J., White, S. D. M., & Tremonti, C. A. 2005, MNRAS, 362, 41

Ganguly, R., Lynch, R. S., Charlton, J. C., et al. 2013, MNRAS, 435, 1233

Gardner, J. P., Katz, N., Hernquist, L., & Weinberg, D. H. 1997, ApJ, 484, 31

Gardner, J. P., Katz, N., Hernquist, L., & Weinberg, D. H. 2001, ApJ, 559, 131

Gebhardt, K., Bender, R., Bower, G., et al. 2000, ApJ, 539, L13

Glikman, E., Urrutia, T., Lacy, M., et al. 2012, ApJ, 757, 51

Glikman, E., Urrutia, T., Lacy, M., et al. 2013, ApJ, 778, 127

González, R. E. & Padilla, N. D. 2010, MNRAS, 407, 1449

Gordon, K. D., Clayton, G. C., Misselt, K. A., Landolt, A. U., & Wolff, M. J. 2003, ApJ, 594, 279

Goto, T., Utsumi, Y., Furusawa, H., Miyazaki, S., & Komiyama, Y. 2009, MNRAS, 400, 843

Graham, A. W., Onken, C. A., Athanassoula, E., & Combes, F. 2011, MNRAS, 412, 2211

Greene, J. E., Zakamska, N. L., Ho, L. C., & Barth, A. J. 2011, ApJ, 732, 9

Guimarães, R., Petitjean, P., de Carvalho, R. R., et al. 2009, A&A, 508, 133

Guimarães, R., Petitjean, P., Rollinde, E., et al. 2007, MNRAS, 377, 657

Gültekin, K., Richstone, D. O., Gebhardt, K., et al. 2009, ApJ, 698, 198

Gunn, J. E., Carr, M., Rockosi, C., et al. 1998, AJ, 116, 3040

Gunn, J. E. & Peterson, B. A. 1965, ApJ, 142, 1633

Gunn, J. E., Siegmund, W. A., Mannery, E. J., et al. 2006, AJ, 131, 2332

Haehnelt, M. G., Steinmetz, M., & Rauch, M. 1998, ApJ, 495, 647

Hainline, K. N., Hickox, R., Greene, J. E., Myers, A. D., & Zakamska, N. L. 2013, ApJ, 774, 145

Hainline, K. N., Hickox, R. C., Greene, J. E., et al. 2014, ApJ, 787, 65

Hall, P. B., Anderson, S. F., Strauss, M. A., et al. 2002, ApJS, 141, 267

Hall, P. B., Brandt, W. N., Petitjean, P., et al. 2013, MNRAS, 434, 222

Hennawi, J. F., Myers, A. D., Shen, Y., et al. 2010, ApJ, 719, 1672

Hennawi, J. F. & Prochaska, J. X. 2007, ApJ, 655, 735

Hennawi, J. F. & Prochaska, J. X. 2013, ApJ, 766, 58

Hennawi, J. F., Prochaska, J. X., Burles, S., et al. 2006a, ApJ, 651, 61

Hennawi, J. F., Prochaska, J. X., Kollmeier, J., & Zheng, Z. 2009, ApJ, 693, L49

Hennawi, J. F., Strauss, M. A., Oguri, M., et al. 2006b, AJ, 131, 1

Herbert-Fort, S., Prochaska, J. X., Dessauges-Zavadsky, M., et al. 2006, PASP, 118, 1077

Hernquist, L., Katz, N., Weinberg, D. H., & Miralda-Escudé, J. 1996, ApJ, 457, L51

Hewett, P. C. & Wild, V. 2010, MNRAS, 405, 2302

Jauzac, M., Jullo, E., Kneib, J.-P., et al. 2012, MNRAS, 426, 3369

Jenkins, E. B. 2009, ApJ, 700, 1299

Jorgenson, R. A. & Wolfe, A. M. 2014, ApJ, 785, 16

Kaplan, K. F., Prochaska, J. X., Herbert-Fort, S., Ellison, S. L., & Dessauges-Zavadsky, M. 2010, PASP, 122, 619

Kashikawa, N., Misawa, T., Minowa, Y., et al. 2014, ApJ, 780, 116

Katz, N., Weinberg, D. H., Hernquist, L., & Miralda-Escude, J. 1996, ApJ, 457, L57

Kelson, D. D. 2003, PASP, 115, 688

Khare, P., vanden Berk, D., York, D. G., Lundgren, B., & Kulkarni, V. P. 2012, MNRAS, 419, 1028

Kim, T.-S., Partl, A. M., Carswell, R. F., & Müller, V. 2013, A&A, 552, A77

Kim, Y.-R. & Croft, R. A. C. 2008, MNRAS, 387, 377

Kirkpatrick, J. A., Schlegel, D. J., Ross, N. P., et al. 2011, ApJ, 743, 125

Komatsu, E., Smith, K. M., Dunkley, J., et al. 2011, ApJS, 192, 18

Kotilainen, J., Falomo, R., Bettoni, D., Karhunen, K., & Uslenghi, M. 2013, ArXiv e-prints

Krogager, J.-K., Fynbo, J. P. U., Ledoux, C., et al. 2013, MNRAS, 433, 3091

Krogager, J.-K., Fynbo, J. P. U., Møller, P., et al. 2012, MNRAS, 424, L1

Kulkarni, V. P., Woodgate, B. E., York, D. G., et al. 2006, ApJ, 636, 30

Lanzetta, K. M., Wolfe, A. M., & Turnshek, D. A. 1995, ApJ, 440, 435

Le Brun, V., Bergeron, J., Boisse, P., & Deharveng, J. M. 1997, A&A, 321, 733

Ledoux, C., Petitjean, P., Bergeron, J., Wampler, E. J., & Srianand, R. 1998, A&A, 337, 51

Ledoux, C., Petitjean, P., Fynbo, J. P. U., Møller, P., & Srianand, R. 2006, A&A, 457, 71

Ledoux, C., Srianand, R., & Petitjean, P. 2002, A&A, 392, 781

Lee, K.-G., Hennawi, J. F., White, M., Croft, R. A. C., & Ozbek, M. 2014, ApJ, 788, 49

Lehner, N., Howk, J. C., Tripp, T. M., et al. 2013, ApJ, 770, 138

Lemaître, G. 1931, MNRAS, 91, 490

Liu, G., Zakamska, N. L., Greene, J. E., Nesvadba, N. P. H., & Liu, X. 2013, MNRAS, 430, 2327

Lodders, K. 2003, ApJ, 591, 1220

Loeb, A. 2006, Scientific American, 295, 46

Lopez, S., Reimers, D., D'Odorico, S., & Prochaska, J. X. 2002, A&A, 385, 778

Lowenthal, J. D., Hogan, C. J., Green, R. F., et al. 1995, ApJ, 451, 484

Lu, L., Sargent, W. L. W., Barlow, T. A., Churchill, C. W., & Vogt, S. S. 1996, ApJS, 107, 475

Lu, L., Wolfe, A. M., Turnshek, D. A., & Lanzetta, K. M. 1993, ApJS, 84, 1

Lutz, D., Sturm, E., Tacconi, L. J., et al. 2008, ApJ, 684, 853

Lynds, R. 1971, ApJ, 164, L73

Ma, C.-P., Greene, J. E., McConnell, N., et al. 2014, ArXiv e-prints

Maiolino, R., Haehnelt, M., Murphy, M. T., et al. 2013, ArXiv e-prints

Márquez, I., Petitjean, P., Théodore, B., et al. 2001, A&A, 371, 97

Martin, C. L., Scannapieco, E., Ellison, S. L., et al. 2010, ApJ, 721, 174

Matteucci, F., Molaro, P., & Vladilo, G. 1997, A&A, 321, 45

McConnell, N. J. & Ma, C.-P. 2013, ApJ, 764, 184

McDonald, P. & Eisenstein, D. J. 2007, Phys. Rev. D, 76, 063009

McQuinn, M., Oh, S. P., & Faucher-Giguère, C.-A. 2011, ApJ, 743, 82

Mead, J. M. G., King, L. J., & McCarthy, I. G. 2010, MNRAS, 401, 2257

Meiring, J. D., Kulkarni, V. P., Lauroesch, J. T., et al. 2008, MNRAS, 384, 1015

Meiring, J. D., Lauroesch, J. T., Kulkarni, V. P., et al. 2007, MNRAS, 376, 557

Ménard, B., Wild, V., Nestor, D., et al. 2011, MNRAS, 417, 801

Milutinovic, N., Ellison, S. L., Prochaska, J. X., & Tumlinson, J. 2010, MNRAS, 408, 2071

Miralda-Escudé, J., Cen, R., Ostriker, J. P., & Rauch, M. 1996, ApJ, 471, 582

Modigliani, A., Goldoni, P., Royer, F., et al. 2010, in Society of Photo-Optical Instrumentation Engineers (SPIE) Conference Series, Vol. 7737, Society of Photo-Optical Instrumentation Engineers (SPIE) Conference Series

Möller, P., Fynbo, J. P. U., & Fall, S. M. 2004, A&A, 422, L33

Møller, P., Fynbo, J. P. U., Ledoux, C., & Nilsson, K. K. 2013, MNRAS, 430, 2680

Moller, P. & Warren, S. J. 1993, A&A, 270, 43

Møller, P., Warren, S. J., Fall, S. M., Fynbo, J. U., & Jakobsen, P. 2002, ApJ, 574, 51

Moller, P., Warren, S. J., & Fynbo, J. U. 1998, A&A, 330, 19

Murphy, D. N. A., Eke, V. R., & Frenk, C. S. 2011, MNRAS, 413, 2288

Myers, A. D., Richards, G. T., Brunner, R. J., et al. 2008, ApJ, 678, 635

Nagamine, K., Springel, V., & Hernquist, L. 2004, MNRAS, 348, 421

Neeleman, M., Wolfe, A. M., Prochaska, J. X., & Rafelski, M. 2013, ApJ, 769, 54

Netzer, H., Shemmer, O., Maiolino, R., et al. 2004, ApJ, 614, 558

Noterdaeme, P., Laursen, P., Petitjean, P., et al. 2012a, A&A, 540, A63

Noterdaeme, P., Petitjean, P., Carithers, W. C., et al. 2012b, A&A, 547, L1

Noterdaeme, P., Petitjean, P., Ledoux, C., & Srianand, R. 2009, A&A, 505, 1087

Noterdaeme, P., Petitjean, P., Pâris, I., et al. 2014, A&A, 566, A24

Noterdaeme, P., Srianand, R., & Mohan, V. 2010, MNRAS, 403, 906

Oh, S., Woo, J.-H., Bennert, V. N., et al. 2013, ApJ, 767, 117

O'Meara, J. M., Chen, H.-W., & Kaplan, D. L. 2006, ApJ, 642, L9

O'Meara, J. M., Prochaska, J. X., Burles, S., et al. 2007, ApJ, 656, 666

O'Meara, J. M., Prochaska, J. X., Worseck, G., Chen, H.-W., & Madau, P. 2013, ApJ, 765, 137

Omont, A., Petitjean, P., Guilloteau, S., et al. 1996, Nature, 382, 428

Ouchi, M., Shimasaku, K., Akiyama, M., et al. 2008, ApJS, 176, 301

Overzier, R. A., Nesvadba, N. P. H., Dijkstra, M., et al. 2013, ApJ, 771, 89

Pagel, B. E. J., Edmunds, M. G., Blackwell, D. E., Chun, M. S., & Smith, G. 1979, MNRAS, 189, 95

Palanque-Delabrouille, N., Magneville, C., Yèche, C., et al. 2013a, A&A, 551, A29

Palanque-Delabrouille, N., Yèche, C., Borde, A., et al. 2013b, A&A, 559, A85

Pandey, B., Kulkarni, G., Bharadwaj, S., & Souradeep, T. 2011, MNRAS, 411, 332

Pâris, I., Petitjean, P., Aubourg, É., et al. 2012, A&A, 548, A66

Pâris, I., Petitjean, P., Aubourg, É., et al. 2014, A&A, 563, A54

Pâris, I., Petitjean, P., Rollinde, E., et al. 2011, A&A, 530, A50

Peng, C. Y., Impey, C. D., Ho, L. C., Barton, E. J., & Rix, H.-W. 2006a, ApJ, 640, 114

Peng, C. Y., Impey, C. D., Rix, H.-W., et al. 2006b, ApJ, 649, 616

Péroux, C., Bouché, N., Kulkarni, V. P., & York, D. G. 2013, MNRAS, 436, 2650

Péroux, C., Bouché, N., Kulkarni, V. P., York, D. G., & Vladilo, G. 2011a, MNRAS, 410, 2237

Péroux, C., Bouché, N., Kulkarni, V. P., York, D. G., & Vladilo, G. 2011b, MNRAS, 410, 2251

Péroux, C., Bouché, N., Kulkarni, V. P., York, D. G., & Vladilo, G. 2012, MNRAS, 419, 3060

Péroux, C., Dessauges-Zavadsky, M., D'Odorico, S., Kim, T.-S., & McMahon, R. G. 2007, MNRAS, 382, 177

Péroux, C., Dessauges-Zavadsky, M., D'Odorico, S., Sun Kim, T., & McMahon, R. G. 2005, MNRAS, 363, 479

Péroux, C., Kulkarni, V. P., & York, D. G. 2014, MNRAS, 437, 3144

Péroux, C., McMahon, R. G., Storrie-Lombardi, L. J., & Irwin, M. J. 2003, MNRAS, 346, 1103

Petitjean, P. & Bergeron, J. 1994, A&A, 283, 759

Petitjean, P., Mueket, J. P., & Kates, R. E. 1995, A&A, 295, L9

Petitjean, P., Pécontal, E., Valls-Gabaud, D., & Chariot, S. 1996, Nature, 380, 411

Petitjean, P., Rauch, M., & Carswell, R. F. 1994, A&A, 291, 29

Petitjean, P. & Srianand, R. 1999, A&A, 345, 73

Pettini, M., Hunstead, R. W., King, D. L., & Smith, L. J. 1995, in QSO Absorption Lines, ed. G. Meylan, 55

Pettini, M., King, D. L., Smith, L. J., & Hunstead, R. W. 1997, ApJ, 478, 536

Pettini, M. & Pagel, B. E. J. 2004, MNRAS, 348, L59

Pieri, M. M., Frank, S., Weinberg, D. H., Mathur, S., & York, D. G. 2010, ApJ, 724, L69

Pieri, M. M., Mortonson, M. J., Frank, S., et al. 2014, MNRAS, 441, 1718

Planck Collaboration, Ade, P. A. R., Aghanim, N., et al. 2013, ArXiv e-prints

Pontzen, A., Governato, F., Pettini, M., et al. 2008, MNRAS, 390, 1349

Prochaska, J. X., Gawiser, E., Wolfe, A. M., et al. 2002, AJ, 123, 2206

Prochaska, J. X. & Hennawi, J. F. 2009, ApJ, 690, 1558

Prochaska, J. X., Hennawi, J. F., & Herbert-Fort, S. 2008, ApJ, 675, 1002

Prochaska, J. X., Hennawi, J. F., Lee, K.-G., et al. 2013a, ApJ, 776, 136

Prochaska, J. X., Hennawi, J. F., & Simcoe, R. A. 2013b, ApJ, 762, L19

Prochaska, J. X., Herbert-Fort, S., & Wolfe, A. M. 2005, ApJ, 635, 123

Prochaska, J. X., O'Meara, J. M., & Worseck, G. 2010, ApJ, 718, 392

Prochaska, J. X. & Wolfe, A. M. 1996, ApJ, 470, 403

Prochaska, J. X. & Wolfe, A. M. 1997a, ApJ, 487, 73

Prochaska, J. X. & Wolfe, A. M. 2002, ApJ, 566, 68

Prochaska, J. X. & Wolfe, A. M. 2009, ApJ, 696, 1543

Prochaska, J. X., Wolfe, A. M., Howk, J. C., et al. 2007, ApJS, 171, 29

Prochaska, J. X. & Wolfe, M. 1997b, ApJ, 474, 140

Rafelski, M., Neeleman, M., Fumagalli, M., Wolfe, A. M., & Prochaska, J. X. 2014, ApJ, 782, L29

Rafelski, M., Wolfe, A. M., Prochaska, J. X., Neeleman, M., & Mendez, A. J. 2012, ApJ, 755, 89

Rahmani, H., Srianand, R., Noterdaeme, P., & Petitjean, P. 2010, MNRAS, 409, L59

Rahmati, A. & Schaye, J. 2014, MNRAS, 438, 529

Rao, S. M., Belfort-Mihalyi, M., Turnshek, D. A., et al. 2011, MNRAS, 416, 1215

Rao, S. M. & Turnshek, D. A. 1998, ApJ, 500, L115

Rao, S. M. & Turnshek, D. A. 2000, ApJS, 130, 1

Rao, S. M., Turnshek, D. A., & Briggs, F. H. 1995, ApJ, 449, 488

Rao, S. M., Turnshek, D. A., & Nestor, D. B. 2006, ApJ, 636, 610

Rauch, M., Becker, G. D., Haehnelt, M. G., Carswell, R. F., & Gauthier, J.-R. 2013, MNRAS, 431, L68

Rauch, M., Haehnelt, M., Bunker, A., et al. 2008, ApJ, 681, 856

Rauch, M. & Haehnelt, M. G. 2011, MNRAS, 412, L55

Reid, B. A., Samushia, L., White, M., et al. 2012, MNRAS, 426, 2719

Reimers, D. & Wisotzki, L. 1997, The Messenger, 88, 14

Richards, G. T., Myers, A. D., Gray, A. G., et al. 2009, ApJS, 180, 67

Richards, G. T., Strauss, M. A., Fan, X., et al. 2006, AJ, 131, 2766

Riess, A. G., Macri, L., Casertano, S., et al. 2011, ApJ, 730, 119

Riess, A. G., Strolger, L.-G., Casertano, S., et al. 2007, ApJ, 659, 98

Rodríguez, E., Petitjean, P., Aracil, B., Ledoux, C., & Srianand, R. 2006, A&A, 446, 791

Rollinde, E., Petitjean, P., Pichon, C., et al. 2003, MNRAS, 341, 1279

Rollinde, E., Srianand, R., Theuns, T., Petitjean, P., & Chand, H. 2005, MNRAS, 361, 1015

Ross, N. P., Hamann, F., Zakamska, N. L., et al. 2014, ArXiv e-prints

Ross, N. P., McGreer, I. D., White, M., et al. 2013, ApJ, 773, 14

Ross, N. P., Myers, A. D., Sheldon, E. S., et al. 2012, ApJS, 199, 3

Rottgering, H. J. A., Hunstead, R. W., Miley, G. K., van Ojik, R., & Wieringa, M. H. 1995, MNRAS, 277, 389

Rudie, G. C., Steidel, C. C., Trainor, R. F., et al. 2012, ApJ, 750, 67

Saitta, F., D'Odorico, V., Bruscoli, M., et al. 2008, MNRAS, 385, 519

Savage, B. D., Kim, T.-S., Wakker, B. P., et al. 2014, ApJS, 212, 8

Savage, B. D. & Sembach, K. R. 1996, ARA&A, 34, 279

Savage, B. D., Sembach, K. R., Tripp, T. M., & Richter, P. 2002, ApJ, 564, 631

Schmitt, H. R., Donley, J. L., Antonucci, R. R. J., et al. 2003, ApJ, 597, 768

Schneider, D. P., Hall, P. B., Richards, G. T., et al. 2005, AJ, 130, 367

Schneider, D. P., Richards, G. T., Hall, P. B., et al. 2010, AJ, 139, 2360

Shapley, A. E., Steidel, C. C., Pettini, M., & Adelberger, K. L. 2003, ApJ, 588, 65

Shen, Y., Hennawi, J. F., Shankar, F., et al. 2010, ApJ, 719, 1693

Simcoe, R. A., Sargent, W. L. W., & Rauch, M. 2002, ApJ, 578, 737

Simcoe, R. A., Sargent, W. L. W., & Rauch, M. 2004, ApJ, 606, 92

Slosar, A., Font-Ribera, A., Pieri, M. M., et al. 2011, J. Cosmology Astropart. Phys., 9, 1

Slosar, A., Iršič, V., Kirkby, D., et al. 2013, J. Cosmology Astropart. Phys., 4, 26

Smee, S. A., Gunn, J. E., Uomoto, A., et al. 2013, AJ, 146, 32

Smith, A. G., Hopkins, A. M., Hunstead, R. W., & Pimbblet, K. A. 2012, MNRAS, 422, 25

Songaila, A. & Cowie, L. L. 1996, AJ, 112, 335

Sousbie, T., Pichon, C., & Kawahara, H. 2011, MNRAS, 414, 384

Srianand, R. & Khare, P. 1994, ApJ, 428, 82

Srianand, R. & Petitjean, P. 2000, A&A, 357, 414

Srianand, R., Petitjean, P., Ledoux, C., Ferland, G., & Shaw, G. 2005, MNRAS, 362, 549

Srianand, R. & Shankaranarayanan, S. 1999, ApJ, 518, 672

Stancil, P. C., Schultz, D. R., Kimura, M., et al. 1999, A&AS, 140, 225

Steidel, C., Martin, C., Prochaska, J. X., et al. 2009, in ArXiv Astrophysics e-prints, Vol. 2010, astro2010: The Astronomy and Astrophysics Decadal Survey, 286

Steidel, C. C. 1993, in Astrophysics and Space Science Library, Vol. 188, The Environment and Evolution of Galaxies, ed. J. M. Shull & H. A. Thronson, 263

Steidel, C. C., Dickinson, M., Meyer, D. M., Adelberger, K. L., & Sembach, K. R. 1997, ApJ, 480, 568

Steidel, C. C., Erb, D. K., Shapley, A. E., et al. 2010, ApJ, 717, 289

Steidel, C. C., Pettini, M., & Hamilton, D. 1995, AJ, 110, 2519

Stocke, J. T., Keeney, B. A., Danforth, C. W., et al. 2014, ArXiv e-prints

Stocke, J. T., Penton, S. V., Danforth, C. W., et al. 2006, ApJ, 641, 217

Tanaka, M., Hoshi, T., Kodama, T., & Kashikawa, N. 2007, MNRAS, 379, 1546

Tapken, C., Appenzeller, I., Noll, S., et al. 2007, A&A, 467, 63

Tempel, E., Stoica, R. S., Martínez, V. J., et al. 2014, MNRAS, 438, 3465

Tescari, E., Viel, M., Tornatore, L., & Borgani, S. 2009, MNRAS, 397, 411

Tomczak, A. R., Quadri, R. F., Tran, K.-V. H., et al. 2014, ApJ, 783, 85

Trainor, R. F. & Steidel, C. C. 2012, ApJ, 752, 39

Tripp, T. M., Giroux, M. L., Stocke, J. T., Tumlinson, J., & Oegerle, W. R. 2001, ApJ, 563, 724

Tripp, T. M., Lu, L., & Savage, B. D. 1996, ApJS, 102, 239

Trump, J. R., Hall, P. B., Reichard, T. A., et al. 2006, ApJS, 165, 1

Tumlinson, J., Thom, C., Werk, J. K., et al. 2013, ApJ, 777, 59

Tumlinson, J., Thom, C., Werk, J. K., et al. 2011a, Science, 334, 948

Tumlinson, J., Werk, J. K., Thom, C., et al. 2011b, ApJ, 733, 111

Turnshek, D. A., Monier, E. M., Rao, S. M., et al. 2014, ArXiv e-prints

Turnshek, D. A., Rao, S., Nestor, D., et al. 2001, ApJ, 553, 288

Turnshek, D. A., Wolfe, A. M., Lanzetta, K. M., et al. 1989, ApJ, 344, 567

Tyson, N. D. 1988, ApJ, 329, L57

Urry, C. M. & Padovani, P. 1995, PASP, 107, 803

van Breugel, W., de Vries, W., Croft, S., et al. 2006, Astronomische Nachrichten, 327, 175

van de Voort, F., Schaye, J., Altay, G., & Theuns, T. 2012, MNRAS, 421, 2809

van Dokkum, P. G. 2001, PASP, 113, 1420

Vanden Berk, D. E., Richards, G. T., Bauer, A., et al. 2001, AJ, 122, 549

Verdugo, M., Lerchster, M., Böhringer, H., et al. 2012, MNRAS, 421, 1949

Vernet, J., Dekker, H., D'Odorico, S., et al. 2011, A&A, 536, A105

Viegas, S. M. 1995, MNRAS, 276, 268

Vladilo, G. 2002, A&A, 391, 407

Wagg, J., Wiklind, T., Carilli, C. L., et al. 2012, ApJ, 752, L30

Wang, R., Wagg, J., Carilli, C. L., et al. 2013a, ApJ, 773, 44

Wang, Y. P., Yamada, T., Tanaka, I., Iye, M., & Ji, T. 2013b, ArXiv e-prints

Watson, W. D. 1978, ARA&A, 16, 585

Welty, D. E., Hobbs, L. M., Lauroesch, J. T., et al. 1999, ApJS, 124, 465

Werk, J. K., Prochaska, J. X., Tumlinson, J., et al. 2014, ArXiv e-prints

Weymann, R. J., Morris, S. L., Foltz, C. B., & Hewett, P. C. 1991, ApJ, 373, 23

Wild, V., Hewett, P. C., & Pettini, M. 2007, MNRAS, 374, 292

Wild, V., Kauffmann, G., White, S., et al. 2008, MNRAS, 388, 227

Willott, C. J., Chet, S., Bergeron, J., & Hutchings, J. B. 2011, AJ, 142, 186

Willott, C. J., Omont, A., & Bergeron, J. 2013, ApJ, 770, 13

Wolfe, A. M., Turnshek, D. A., Lanzetta, K. M., & Lu, L. 1993, ApJ, 404, 480

Wolfe, A. M., Turnshek, D. A., Smith, H. E., & Cohen, R. D. 1986, ApJS, 61, 249

Wootten, A. & Thompson, A. R. 2009, IEEE Proceedings, 97, 1463

Xu, X., Cuesta, A. J., Padmanabhan, N., Eisenstein, D. J., & McBride, C. K. 2013, MNRAS, 431, 2834

Yèche, C., Petitjean, P., Rich, J., et al. 2010, A&A, 523, A14

Yonehara, A. 2006, ApJ, 646, 16

York, D. G., Adelman, J., Anderson, Jr., J. E., et al. 2000, AJ, 120, 1579

York, D. G., Dopita, M., Green, R., & Bechtold, J. 1986, ApJ, 311, 610

Zafar, T., Møller, P., Ledoux, C., et al. 2011, A&A, 532, A51

Zafar, T., Péroux, C., Popping, A., et al. 2013a, A&A, 556, A141

Zafar, T., Popping, A., & Péroux, C. 2013b, A&A, 556, A140

Zhang, Y., Anninos, P., & Norman, M. L. 1995, ApJ, 453, L57

Zhu, G., Ménard, B., Bizyaev, D., et al. 2014, MNRAS, 439, 3139

Zwaan, M. A., van der Hulst, J. M., Briggs, F. H., Verheijen, M. A. W., & Ryan-Weber, E. V. 2005, MNRAS, 364, 1467